NASA CR-165,930

NASA Contractor Report 165930

HYBRID LAMINAR FLOW CONTROL STUDY FINAL TECHNICAL REPORT

ENERGY EFFICIENT TRANSPORT PROGRAM

BOEING COMMERCIAL AIRPLANE COMPANY
P.O. BOX 3707, SEATTLE, WA 98124

CONTRACT NAS1-15325
OCTOBER 1982

NASA

National Aeronautics and
Space Administration

Langley Research Center
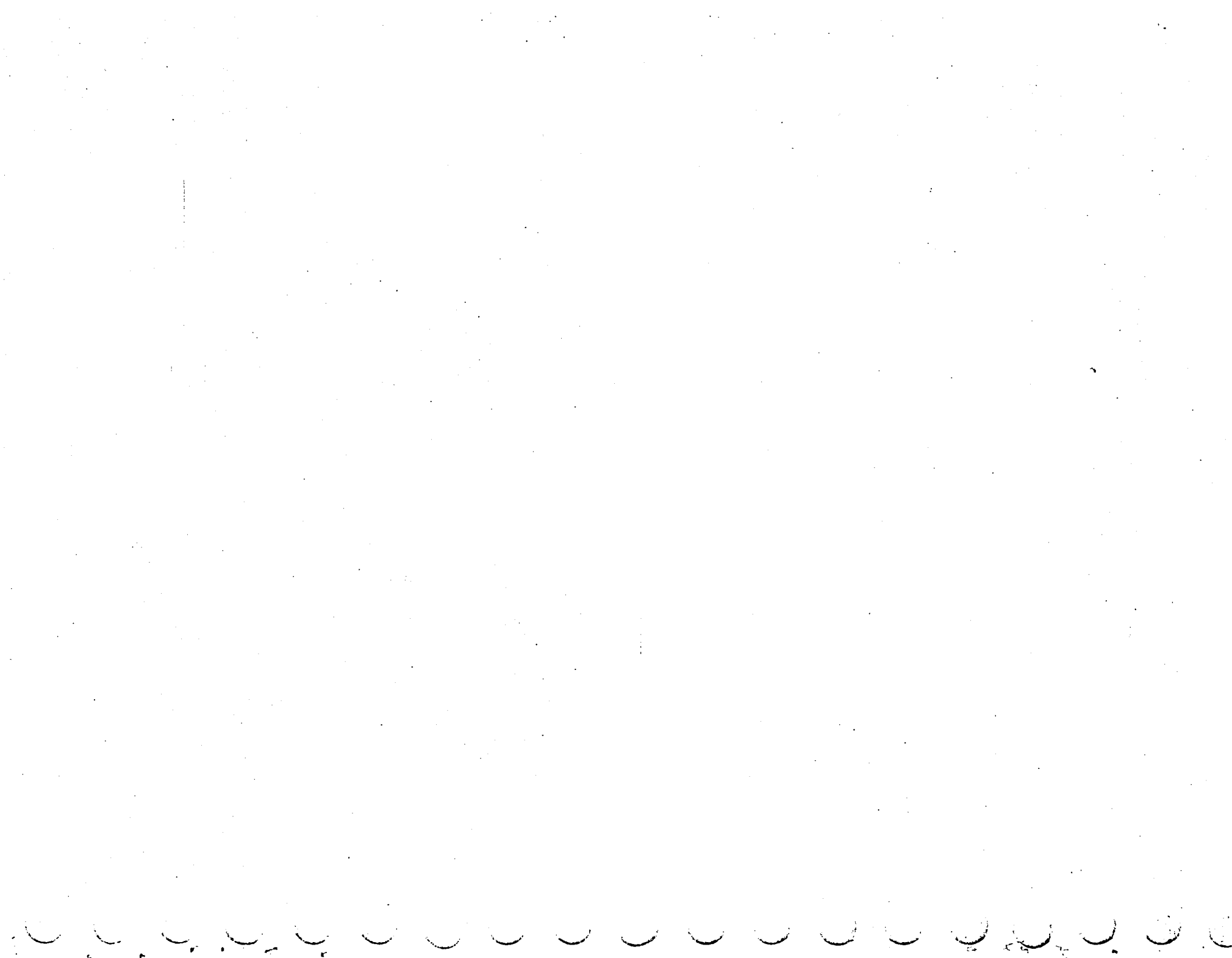Hampton, Virginia 23665

NASA Contractor Report 165930

HYBRID LAMINAR FLOW CONTROL STUDY FINAL TECHNICAL REPORT

ENERGY EFFICIENT TRANSPORT PROGRAM

BOEING COMMERCIAL AIRPLANE COMPANY
P.O. BOX 3707, SEATTLE, WA 98124

CONTRACT NAS1-15325

OCTOBER 1982

NATIONAL AERONAUTICS AND SPACE ADMINISTRATION
LANGLEY RESEARCH CENTER

FOREWORD

This report presents the results of the Hybrid Laminar Flow Control (HLFC) project. The work was conducted under NASA Contract NAS1-15325 from March 1981 through February 1982. The contract was managed by the NASA Energy Efficient Transport Office (EETPO) headed by Mr. R. V. Hood, which is a part of the Aircraft Energy Efficiency (ACEE) program organization at the Langley Research Center. Mr. D. B. Middleton was the technical monitor for the contract. The work was performed by the Preliminary Design department and the Technical Staff of the Boeing Commercial Airplane Company. Key contractor personnel responsible for this effort were:

G. W. Hanks Program Manager	A. E. Moyer Airplane Integration
G. E. Ledbetter Project Manager	A. L. Nagel LFC Technology Integration
F. J. Davenport Design/Documentation Integration	M. J. Omoth Systems Technology
H. A. Dethman Design Management	L. J. Runyan Aerodynamics
D. George-Falvy Aerodynamics	C. J. Thomas Weights Technology
L. B. Gratzer Technology Management	T. C. Versteegh Aerodynamics
E. J. Heineman Configuration	S. Youth Performance
R. N. Johnson Systems Technology	

NOTE: Certain commercial products are identified in this report in order to specify adequately the characteristics of the airplane under investigation. In no case does such identification imply recommendation or endorsement of the product by NASA or Boeing, nor does it imply that the materials are necessarily the only ones available for the purpose.

CONTENTS

FIGURES

ix

TABLES

1.0 SUMMARY

Hybrid laminar flow control (HLFC) is a means of reducing airplane wing friction drag by combining suction laminar flow control near the leading edge (forward of the front spar only) with pressure distribution tailoring in the midchord area. Laminar flow is thus maintained over a significant fraction of wing chord, but the problems of integrating a boundary layer suction system with wing box spar structure are avoided.

A study was conducted to determine the fuel savings potential of the application of HLFC to a modern medium range turbofan transport airplane. The study began with an investigation of the range of sweepback angles and Reynolds numbers over which HLFC should be effective and the wing pressure distribution characteristics required to make it work. It was found that HLFC is theoretically capable of maintaining a laminar boundary layer to 65% of wing chord at 25 deg of sweepback and a Reynolds number of 35 million. Application of HLFC to an airplane in the class of the Boeing 757-200 (180 passengers, 3900-km [2100-nmi] range, Mach 0.8 cruise speed) should therefore be feasible. (This conclusion is stated with the same reservations that apply to the feasibility of any LFC airplane; i.e., the economic aspects depend on manufacturing and operational data that are not available.)

An HLFC airplane was defined to accomplish the 757-200 mission and meet all its design requirements to the extent possible within the constraints of retaining the 757 wing thickness ratio, planform, engines, empennage, and body shape. This airplane would employ body-mounted, electrically driven pumps to remove boundary layer air through a porous titanium sheet covering the wing leading edge. Wing anti-icing and protection from insect roughness contamination (probably necessary for summertime HLFC effectiveness) would be provided by dispensing water/glycol mixtures through portions of the porous leading edge not connected to the suction system.

New wing sections were designed to meet the special pressure distribution requirements associated with HLFC. A 10% chord trailing-edge flap was provided to permit adjustment of the pressure distribution in climb, descent, and off-design cruise conditions. In this way, the full benefits of HLFC can be maintained over a wider range of flight conditions and partial HLFC effectiveness extended to altitudes as low as 3048m (10 000 ft).

Because of the drag reduction afforded by HLFC, it was calculated that a fuel savings of 8.1% over the baseline 757-200 would be obtained in the design mission. Although not studied in detail, it was estimated that the savings could be increased to 12% by applying HLFC to the empennage and adjusting cruise altitude. The takeoff and landing capabilities of the baseline airplane could not be matched within the planform constraints, however, because the suction system could not be integrated with a leading-edge high-lift device. The net effect on fuel savings of adjusting the wing design to meet takeoff and landing requirements and of resizing the wing, empennage, and propulsion system for best HLFC performance was beyond the scope of the study.

The potential fuel savings due to HLFC are significant, and it is recommended that HLFC studies should be continued, with research to resolve questions relating to surface smoothness, insect contamination, and the combined influence of different types of boundary layer instability, followed by design studies to establish the potential of HLFC in an optimized configuration.

1

2.0 INTRODUCTION

The technical feasibility of reducing the friction drag of large, high-speed airplanes with laminar flow control (LFC) by boundary layer suction was demonstrated in the Air Force/Northrop X-21 program in the 1960's (ref. 1). Because of the apparent cost and complexity, however, no LFC-equipped airplanes have been put into service. Interest in LFC revived as a result of the dramatic increases in petroleum prices in the 1970's. NASA's Aircraft Energy Efficiency (ACEE) program has therefore included sponsorship of LFC technology development for application to commercial transport airplanes. The ACEE studies (refs. 2 and 3) have shown that with continuous chordwise suction, disturbances in the laminar boundary layer can be effectively controlled to sufficiently high Reynolds numbers and sweep angles to make LFC potentially feasible for large transport use. The use of suction imposes penalties in weight, systems complexity, and operational compromises, however, that lessen the benefits of drag reduction. With continuous chordwise suction, much of that penalty is associated with the use of suction systems on the upper and lower surfaces integral with the wingbox.

Investigations of natural laminar flow (NLF) (ref. 4) showed that extensive regions of laminar flow can be obtained on wings without suction if the pressure distribution is selected to limit disturbance growth in the laminar boundary layer. This can only be achieved, however, under limitations of Reynolds number and sweep that inhibit the effective application of NLF to large, high-speed transport aircraft. (Later analytical studies [ref. 5] have shown that these limitations may not be as severe as first indicated. Also, flight tests on the variable sweep TACT F-111 airplane at Dryden Flight Research Center have shown laminar flow over a large portion of the test chord of a wing "glove" designed to produce a pressure distribution conducive to laminar flow [ref. 6]. It should be noted, however, that sweep angles typical of modern commercial transports are still somewhat higher than those for which substantial NLF has been demonstrated.)

Hybrid laminar flow control (HLFC) is a concept that combines features of LFC and NLF: suction is only applied forward of the front spar to prevent transition due to crossflow and attachment line instabilities characteristic of sweptback wings. Stabilization aft of the front spar is achieved by tailoring the pressure distribution. The obtainable extent of laminar flow is less than expected from "full-chord" LFC, but conventional wingbox structure may be retained.

To judge whether or not the HLFC concept was worth pursuing further and to plan a program for its exploitation, a quantitative estimate of the range of applicability and the probable benefit of using HLFC on a large, high-speed commercial transport airplane was needed. NASA therefore authorized the Boeing Commercial Airplane Company (BCAC) to conduct the present study as an addition to the Energy Efficient Transport (EET) portion of the ACEE program.

2.1 OBJECTIVES

The objectives of this study were:

● To establish analytically the ranges of chord Reynolds number and wing sweepback angle for which NLF and HLFC can be expected to stabilize the boundary layer on an airfoil suitable for a large, high-speed commercial transport.

3

- To determine the probable fuel savings to be expected from application of HLFC to such an airplane.

- To develop specific recommendations for future research and technology development required for exploitation of the HLFC concept.

2.2 APPROACH

2.2.1 Reynolds Number and Sweepback Study

Given a sweepback angle, a Reynolds number, and pressure distribution and suction quantity distribution, laminar boundary layer profiles can be computed at different points on the airfoil chord. The chordwise location of boundary layer transition may then be estimated by computing the cumulative amplification of small disturbances using methods such as Mack's (ref. 7). By examining the behavior of the predicted boundary layer transition, it is possible to define the ranges of wing sweep and chord for which NLF and HLFC are suitable and the pressure distribution shapes required.

2.2.2 HLFC Fuel Economy Potential

A high-confidence estimate was desired for the potential fuel savings of HLFC, without the expense of a detailed design study of a complete airplane. The stategy adopted in the present study was to consider application of HLFC to an existing modern, turbulent-flow baseline airplane (the Boeing 757-200) for which the depth of design definition and analysis guaranteed high-confidence weight and performance data. The only changes permitted for the HLFC airplane were new airfoil sections (same wing planform and thickness), installation of the HLFC suction system, and modification to other systems and structures required to accommodate it.

3.0 SYMBOLS AND ABBREVIATIONS

3.1 ACRONYMS

APU	auxiliary power unit
ATC	air traffic control
cg	center of gravity
C-F	crossflow
DATAC	digital autonomous terminal access
ECS	environmental conditioning system
EICAS	engine indication and crew alerting system
FAR	federal aviation regulations
FMCS	flight management computer system
HLFC	hybrid laminar flow control
IDG	integrated drive generator
LE	leading edge
LFC	laminar flow control
LRC	long range cruise
MLW	maximum landing weight
NLF	natural laminar flow
OEW	operating empty weight
SFC	specific fuel consumption
TAI	thermal anti-ice
TE	trailing edge
TMC	thrust management computer
TMS	thrust management system
TR	transformer rectifier
T-S	Tollmien-Schlichting
WBL	wing buttock line
WS	wing station
WRP	wing reference plane

3.2 MATHEMATICAL SYMBOLS

a	speed of sound
A	disturbance amplitude
A_0	initial disturbance amplitude
A_w	wetted area
b	wing span
c	chord
$\bar{c}$	mean aerodynamic chord
c_d	section drag coefficient
c_ℓ	section lift coefficient
c_{ℓ_N}	section lift coefficient based on normal chord and normal velocity
c_N	normal chord
c_q	section coefficient of suction flow
c_{q_N}	section coefficient of suction flow based on normal chord and normal velocity
C_D	airplane drag coefficient
C_{D_P}	component profile drag coefficient
C_{D_S}	equivalent suction drag coefficient
C_{D_W}	wing profile drag coefficient
C_L	centerline
C_L	airplane lift coefficient
C_P	pressure coefficient
C_{P_N}	pressure coefficient based on normal velocity
C_Q	wing suction flow coefficient
d	suction hole diameter
D	airplane drag
f	spatial frequency of disturbance wave
h	altitude
H	boundary layer shape factor δ^*/θ
k	waviness or roughness height
ℓ	gap length
ℓ_H	horizontal tail arm
ℓ_V	vertical tail arm
L	airplane lift

6

M	Mach number
M_N	Mach number of normal flow
$M_{N\ell}$	local Mach number of normal flow
n	amplification ratio ($\ell n \, A/A_0$)
P_s	static pressure
Q	suction flow quantity
Q'	suction flow quantity per unit span
R	chord Reynolds number
R_1	unit Reynolds number
R_k	roughness Reynolds number
R_N	normal chord Reynolds number
$R_{\delta*}$	displacement thickness Reynolds number
$R_{\theta_{a\ell}}$	attachment line momentum thickness Reynolds number
s	arc length along wing surface
S_H	horizontal tail area
S_{ref}	wing reference area
S_V	vertical tail area
t	wing or airfoil maximum thickness
tr (subscript)	transition
u	component of boundary layer velocity parallel to flow at edge of boundary layer
u_k	boundary layer velocity at top of roughness element
U	component of freestream velocity normal to leading edge
U_e	velocity at edge of boundary layer
v	equivalent suction velocity
V	freestream velocity
w	component of freestream velocity normal to flow at edge of boundary layer
w (subscript)	at wing surface
W	component of freestream velocity parallel to leading edge
x	distance from wing leading edge
x_L	laminar flow distance from leading edge
y	height above surface (in boundary layer)
z	spanwise distance
δ_F	flap deflection
δ	boundary layer thickness

7

$\delta*$	boundary layer displacement thickness
η	span station (z/semispan)
θ	boundary layer momentum thickness
λ	surface wave length
ν	kinematic viscosity
ρ	air density
Δ	difference
Λ	sweepback angle
Σ	summation

4.0 BASELINE AIRPLANE DESCRIPTION

The baseline airplane used for the HLFC project was the Boeing standard model 757-200. This airplane is a modern, fuel-efficient, high-speed, medium-range transport airplane. The general arrangement, major components, and payload capabilities are illustrated in this section, supplemented by a description of the pertinent systems that would require modification for an HLFC airplane and principal configuration characteristics. The mission rules, speed schedules, performance and noise characteristics, design weights, and center-of-gravity management also are presented.

4.1 CONFIGURATION

Physical data on the baseline configuration are described in this section, which is divided into geometric and characteristic data. The external shape of the airplane and the major internal views (systems, passengers, and cargo) are shown, and the pertinent systems are explained. Finally, the geometric data are supplemented by the applicable characteristics of engines, fuel capacity, and flight crew.

4.1.1 General Arrangement

The Boeing 757-200 is a twin-engine, land-based, low-wing, low-tail airplane designed for commercial passenger and cargo transportation. The standard width (single-aisle) body provides for six-abreast passenger seating and is sized for 178 mixed-class passengers. The lower deck cargo compartments are designed for bulk cargo with an optional telescoping bulk system. The principal dimensions are shown in the general arrangement drawing (fig. 1).

4.1.2 Equipment

An inboard profile drawing of the airplane (fig. 2) shows the locations of the major airplane body components including passenger seats, cargo containers, electric and electronic bays, environmental control packs and mixing bays, and landing gear. Also shown are the door locations for passenger entry, galley, emergency escape, and cargo.

4.1.3 Body Cross Section

The body upper lobe cross section is the same as used on the Boeing 727-200 and provides 3.455m (136 in) seating width (fig. 3). Low density first-class and high density tourist-class seating arrangements also are shown. Two lower-lobe cargo compartments provide 50.12 m^3 (1770 ft^3) of volume, with a structural capacity of 12 020 kg (26 500 lb).

4.1.4 Seating Arrangement

Passenger cabin seating arrangement for the basic two-class, 178-passenger version is shown in the upper part of Figure 4. The locations of galleys, lavatories, cabin attendants' seats, and cabin doors also are shown. In the all-tourist version, seating for 196 passengers is provided in a six-abreast arrangement with one aisle and seats spaced at 0.86m (34 in) seat pitch, as shown in the lower part of the figure.

4.1.5 Design Data

The design data for the baseline airplane are given in this section. Only those items that are to be modified for the HLFC airplane are covered. A structures description of the

9

Configuration

Passengers:	178 mixed class, 196 all tourist
Cargo:	Bulk 50.12 m^3 (1770 ft^3)
Engines:	Two RB 211-535C

Design mission

Cruise Mach:	0.8
Range:	3928 km (2120 nmi)
Takeoff field length:	2094m (6870 ft)
Approach speed:	248 km/h (134 kn) at maximum landing weight
Noise:	FAR 36 stage 3

37.9m
(124 ft 6 in)

15.2m
(49 ft 11 in)

7.3m
(24 ft 0 in)

13.6m
(44 ft 6 in)

46.9m (153 ft 10 in)

47.3m (155 ft 3 in)
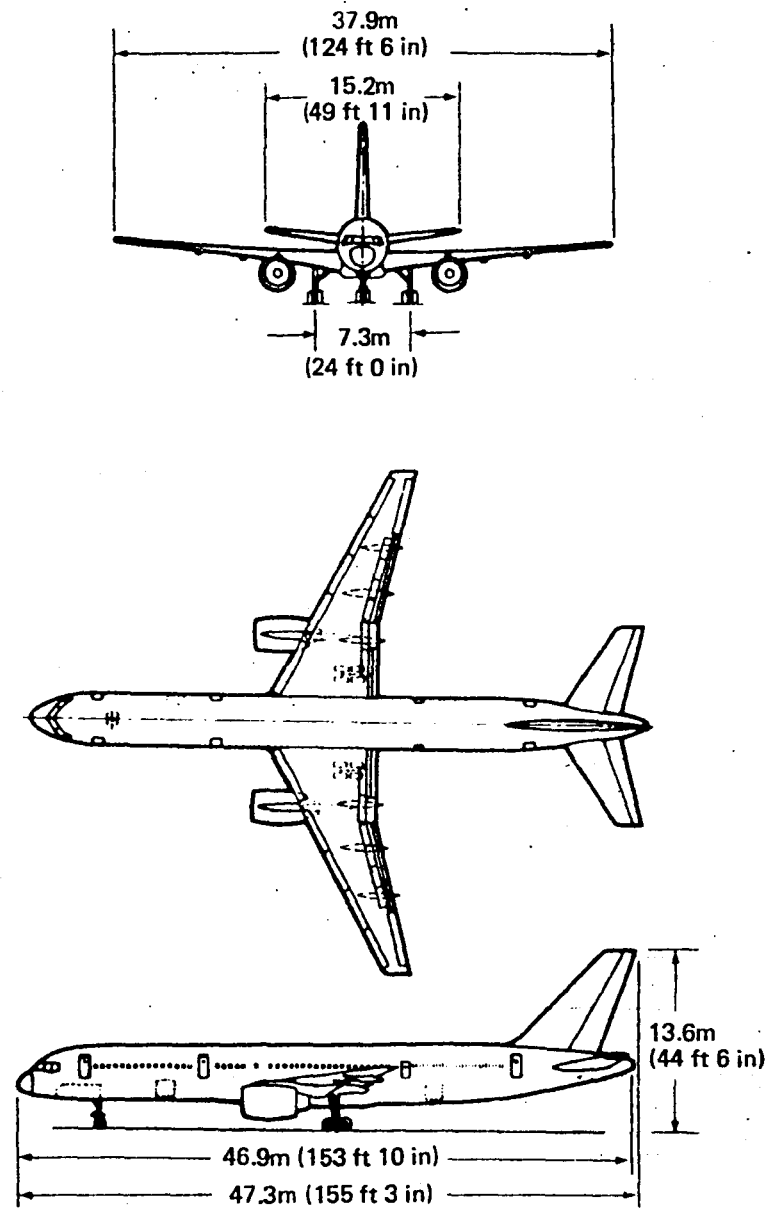
Figure 1. Baseline Configuration, 757-200

10
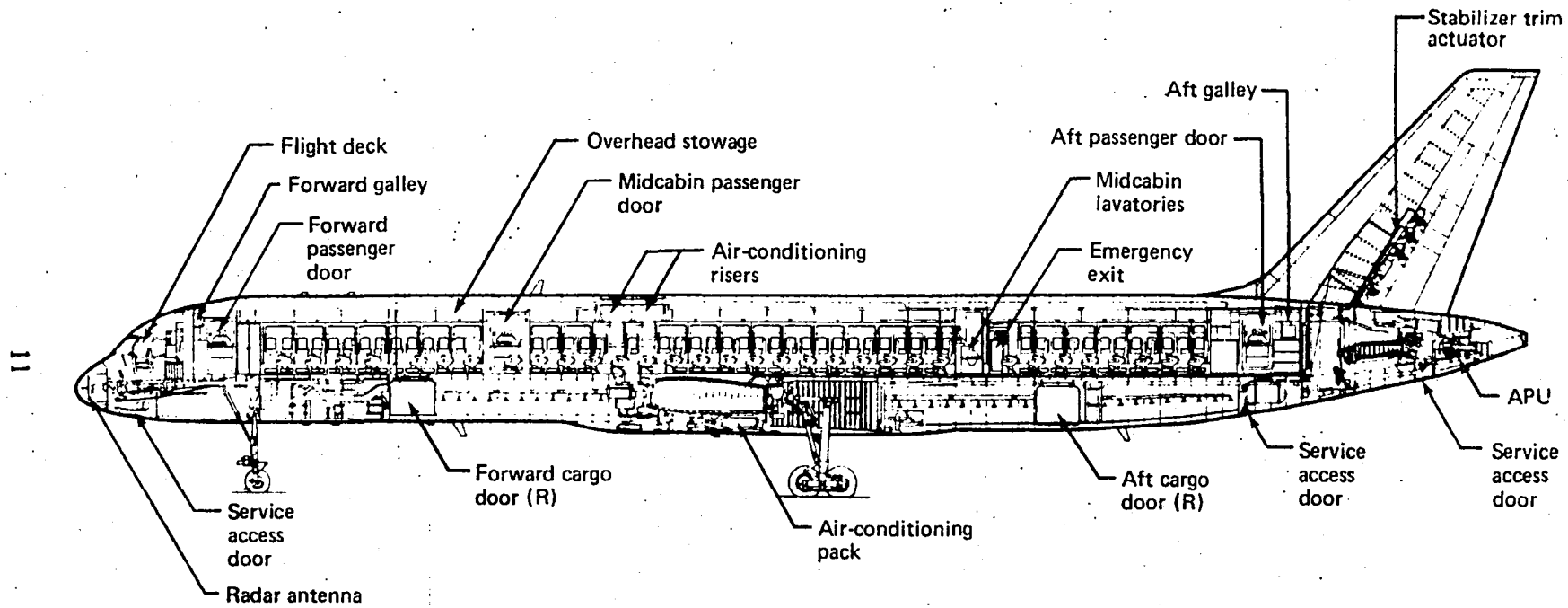
Figure 2. Inboard Profile

Flight deck

Forward galley

Forward passenger door

Overhead stowage

Midcabin passenger door

Air-conditioning risers

Stabilizer trim actuator

Aft galley

Aft passenger door

Midcabin lavatories

Emergency exit

Service access door

Radar antenna

Forward cargo door (R)

Air-conditioning pack

Aft cargo door (R)

Service access door

APU

Service access door

11

First class

Aisle
71.1 cm
(28 in)

← 137 cm (54 in) →

Ceiling panels
with lights
152.4 cm (60 in)

Stowage bins

168.7 cm (66.4 in)

← 149.9 cm (59 in) →

Bin, upward
opening door
152.4 cm (60 in)

PSU

Sidewall
101.6 cm
(40 in)

Tourist class

Minimum 38.1 cm (15 in)
Aisle 45.7 cm (18 in)

Figure 3. Cabin Cross Section
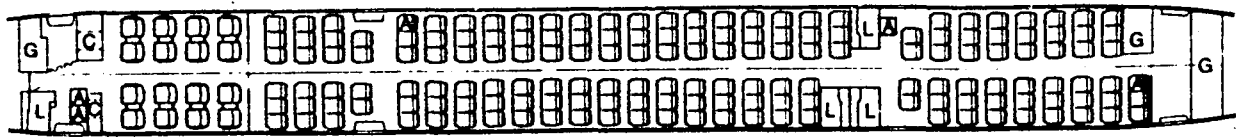
Mixed class, 178 passengers

- 16 first class 96-5-cm (38-in) pitch
- 162 tourist 86.4-cm (34-in) pitch

Legend:

A Attendant
C Closet
G Galley
L Lavatory
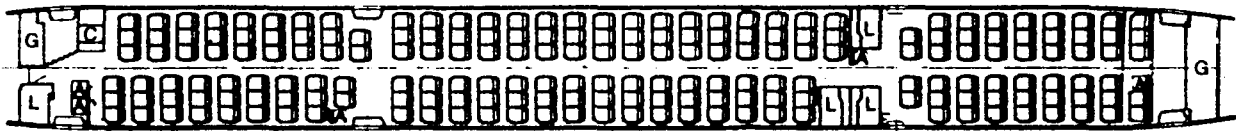
One class, 196 passengers

- 86.4-cm (34-in) pitch

Figure 4. Interior Arrangements

wing is presented in section 4.1.5.1, followed by a description of the major airplane systems that will affect or be affected by HLFC in section 4.1.5.2 through 4.1.5.4.

4.1.5.1 Airplane Wing—The model 757-200 has a $181.25m^2$ (1951 ft^2) wing swept 25 deg at the quarter chord (fig. 5). The wing has advanced airfoil sections, with thickness ratio varying from 13.5% at the side of the body to 10.3% at the tip. In addition to the 5-deg dihedral, the inboard wing is displaced vertically by 40.6 cm (16 in) between the body and the nacelle. This "shear" is distributed so the inboard flap trailing edge is a straight line. Strut-mounted engines are located at 34% of the projected span. The leading edge incorporates slats with chordwise actuation designed to operate in three positions.

The trailing-edge configuration is a track-and-roller-supported, double-slotted flap with a single all-speed aileron located outboard of 75% semispan. The aft portion of the main landing gear trunnion is enclosed in a fairing beneath the wing and is supported by a beam extending from the wing rear spar to the side of the body.

The wing primary structure (fig. 5) consists of two outboard wingboxes cantilevered from a center wingbox, which is contained entirely within the body. The splices occur at body buttock line (BBL) 70.5. Both outboard boxes and the center box are sealed to form integral fuel tanks. The center section tank includes a secondary fuel barrier coating. Each wingbox is built up with a front spar, rear spar, lower panels, and upper panels. In addition, the outboard wingboxes incorporate ribs normal to the outboard rear spar. The spars consist of machined aluminum alloy chords with machined aluminum alloy webs stiffened with mechanically fastened, machined vertical stiffeners. Provision for attachment of fixed leading-edge and fixed trailing-edge structure is incorporated into the spar design.

The upper wingbox panel consists of two machined skin panels with mechanically fastened, machined, spanwise stiffeners. Two of the stiffeners are used for venting the fuel tanks.

13
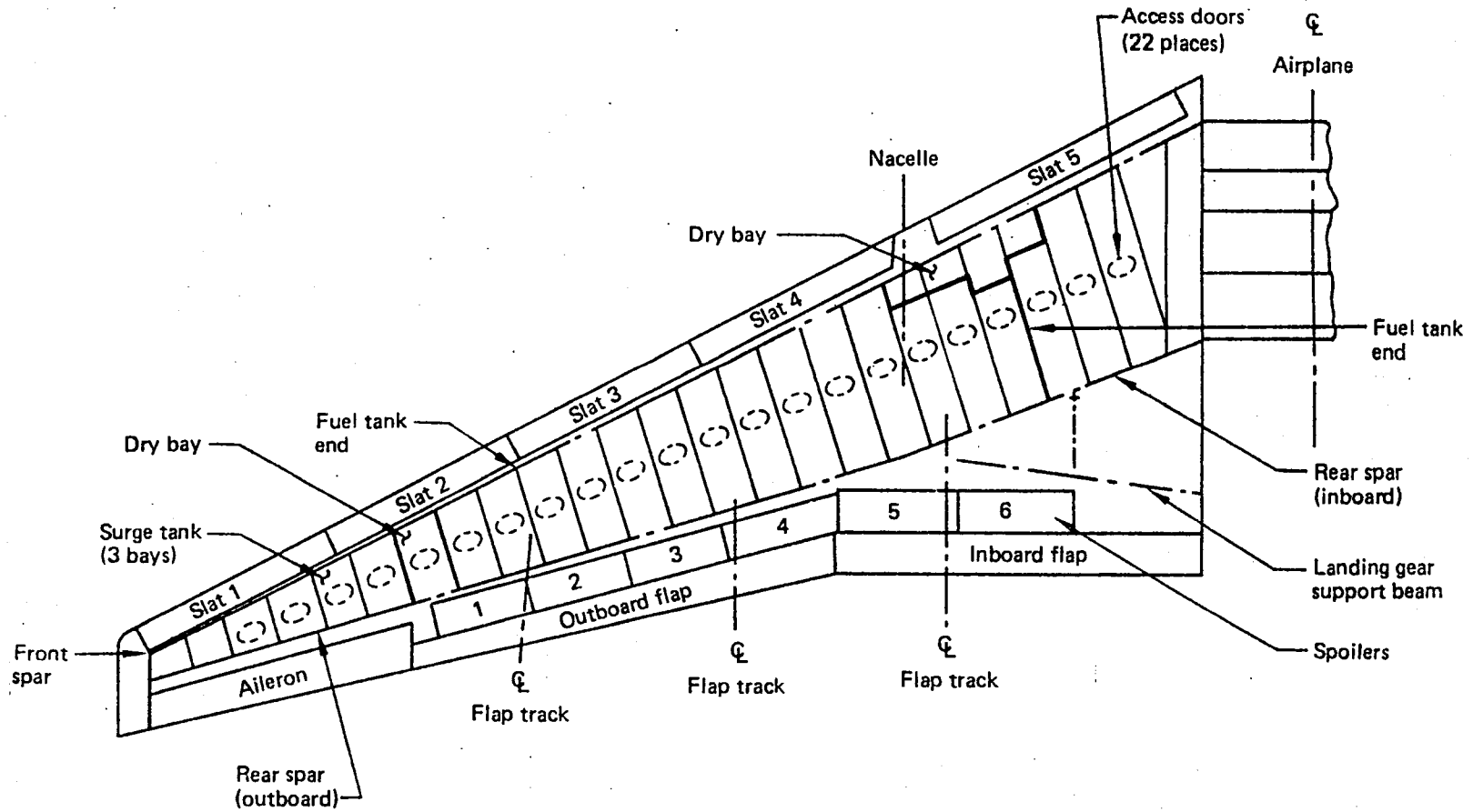
Figure 5. Wing Structural Arrangement

The lower wingbox panel is similar to the upper except it incorporates three machined skin panels with two spanwise splices. The design of the wing structure allows the conversion of the outboard wing dry bays to fuel bays with minimum rework. The dry bays are between wing stations (WS) 565 and 681.1. The provisions will permit the retrofit to be achieved without the need to perform drilling or trimming operations inside the tank. Vent holes and fuel passage holes with covers as required are incorporated in the upper panel stringers, in the fuel dams, and in the rib web together with other minor structural changes. A surge tank is provided at approximately WS 681.5 to 775.5. Both upper and lower machined panels and stiffeners terminate at the outboard wall of the surge tank. Honeycomb-stabilized aluminum alloy panels are used between the surge tank and removable wingtip.

Leading-edge features are shown in Figure 6. Fixed leading-edge structure consists of machined aluminum alloy ribs with bonded fiberglass honeycomb stabilized surfaces. The lower surface is Kevlar laminate panels, removable for access. Four individual tapered chord slats are provided outboard of the engine, and a single 53.3-cm (21-in) constant chord slat is inboard of the engine. Each slat is supported by circular arc steel tracks and is actuated by rotary actuators at two locations. Slat structure is conventional, using machined ribs with stretch-formed skins or bonded aluminum honeycomb.

The trailing-edge flaps are shown in Figure 7. Two flaps consisting of two segments each are provided on each wing. The inboard flap extends from the body to approximately wing buttock line (WBL) 300, and the outboard flap, from WBL 300 to 566.5. Each flap is supported on two forged steel tracks. The inboard track of the inboard flap is attached partly to the main landing gear beam and partly to the body structure. It is enclosed within the wing-body fairing. The remaining tracks are enclosed within flap support fairings of composite structure. Aft flap segments are supported on steel tracks totally enclosed within the main flap segment. Immediately behind the engine, the flap consists of a main segment only (no aft segment). The main flap structure consists of two spars built up from extrusions and sheet metal with machined ribs and square edge honeycomb stabilizing aluminum alloy skins. The aft flap segments are bonded structure consisting of graphite laminated skins and spar and honeycomb core.

Six spoiler panels are located ahead of the trailing-edge flaps (fig. 5). All but panel 4 are used in flight for lateral control. All are used for air brakes on the ground. They are attached to the wingbox by hinge fittings equipped with self-aligning bearings. Spoiler structure consists of graphite-laminate skins and spar and Nomex honeycomb core.

A single, tapered, all-speed, fully powered aileron occupies the remaining trailing edge out to the wingtip fairing. It is hinged to the wing structural box at five locations. All hinges are equipped with self-aligning roller bearings. Support structure for an aileron power control unit is required at approximately 33% of aileron span. Ailerons are mass balanced. Aileron structure consists of graphite-laminate skins and spar and Nomex honeycomb core.

The wingtip is designed as an interchangeable assembly and includes navigation and anticollision lights.

4.1.5.2 Electrical System—The electrical system configuration for the 757-200 is the same as for the 767, using common components wherever possible. The system arrangement is as shown in Figure 8. The main electrical equipment bay is located

Main support track

Emergency downstop

Pinion

Sector gear (bolted to track)

Emergency upstop (integral with track)

Section A-A Support track and drive

Auxiliary track

Auxiliary arm

Section B-B Auxiliary track and arm

High-speed torque input

Rotary actuator

Auxiliary track

Main support track

Wing slat drive—pinion drive concept
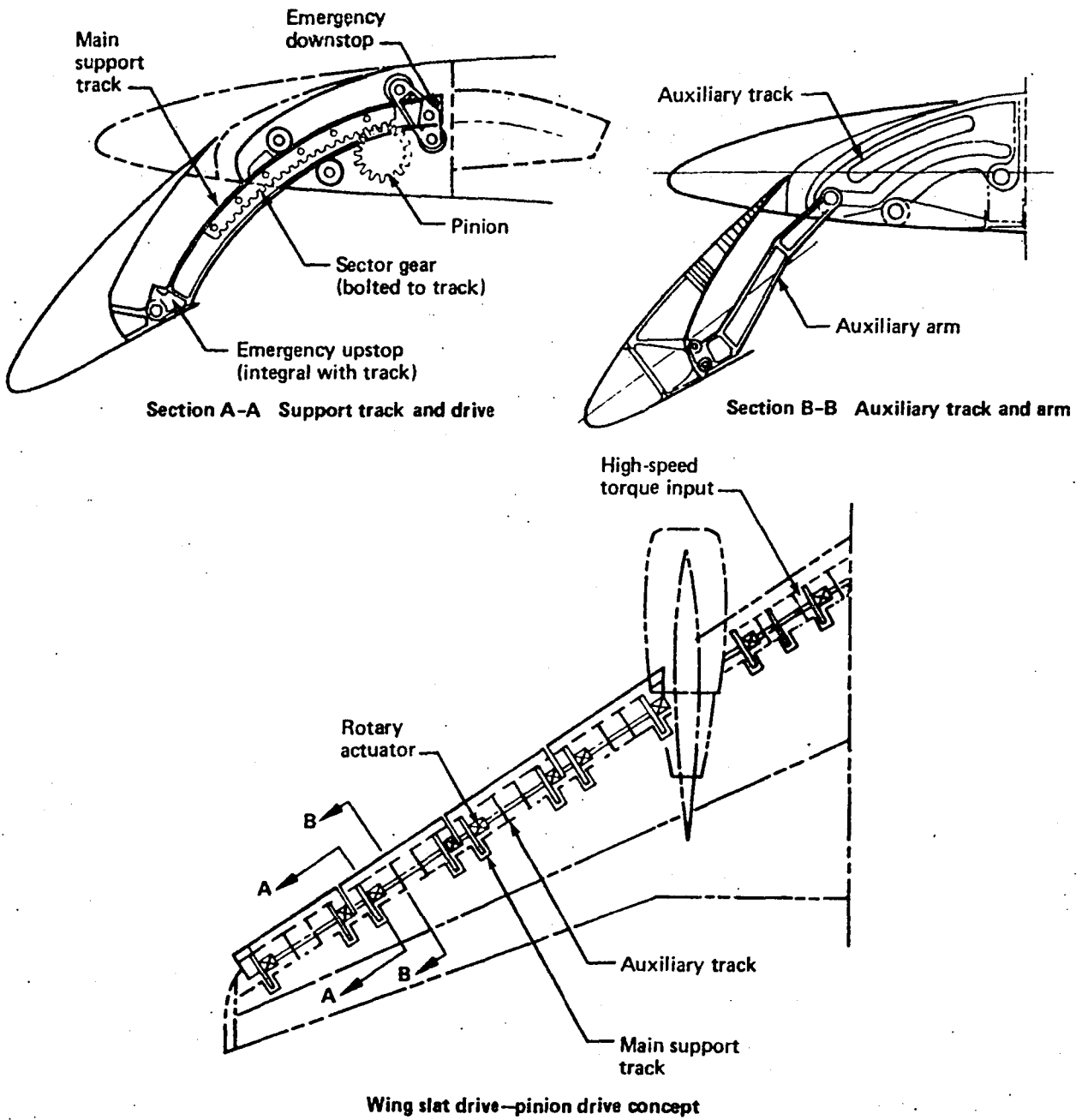
Figure 6. Leading-Edge Slats

16

Plan view

Main flap track and actuator

Main flap

Programming track

Aft flap

Aft flap actuator

Horn aft flap program

Aft flap actuator

Section A-A   Main flap support and drive

Fitting-flap support

Main flap track

Main flap

Aft flap actuating linkage

Fitting-flap support

Drive screw

Flap track fairing

Main flap carriage

Flap track fairing actuating linkage

Aft flap

Section B-B   Aft flap support and drive

Landing gear beam

Main segment

Aft segment

Push rod attachment

Push rod

Push rod

Bellcrank support beam

Section C-C   Aft flap programming track

Aft flap wedge assembly Bonded aluminum full-depth core

Main flap assembly

Aft flap programming track

Figure 7.   Trailing-Edge Flaps

Normal flight configuration:

- Isolated main and standby systems are compatible with triple redundant category III flight controls
- Full capability following dispatch without, or loss of, one power source

- Crew operational participation minimized by auto startup, load transfer, and load shedding features

- Two 90-kVA oil-cooled main ac generators provide reserve power for options plus growth
- APU 90-kVA generator provides ground service power and in-flight backup power for left or right main generators
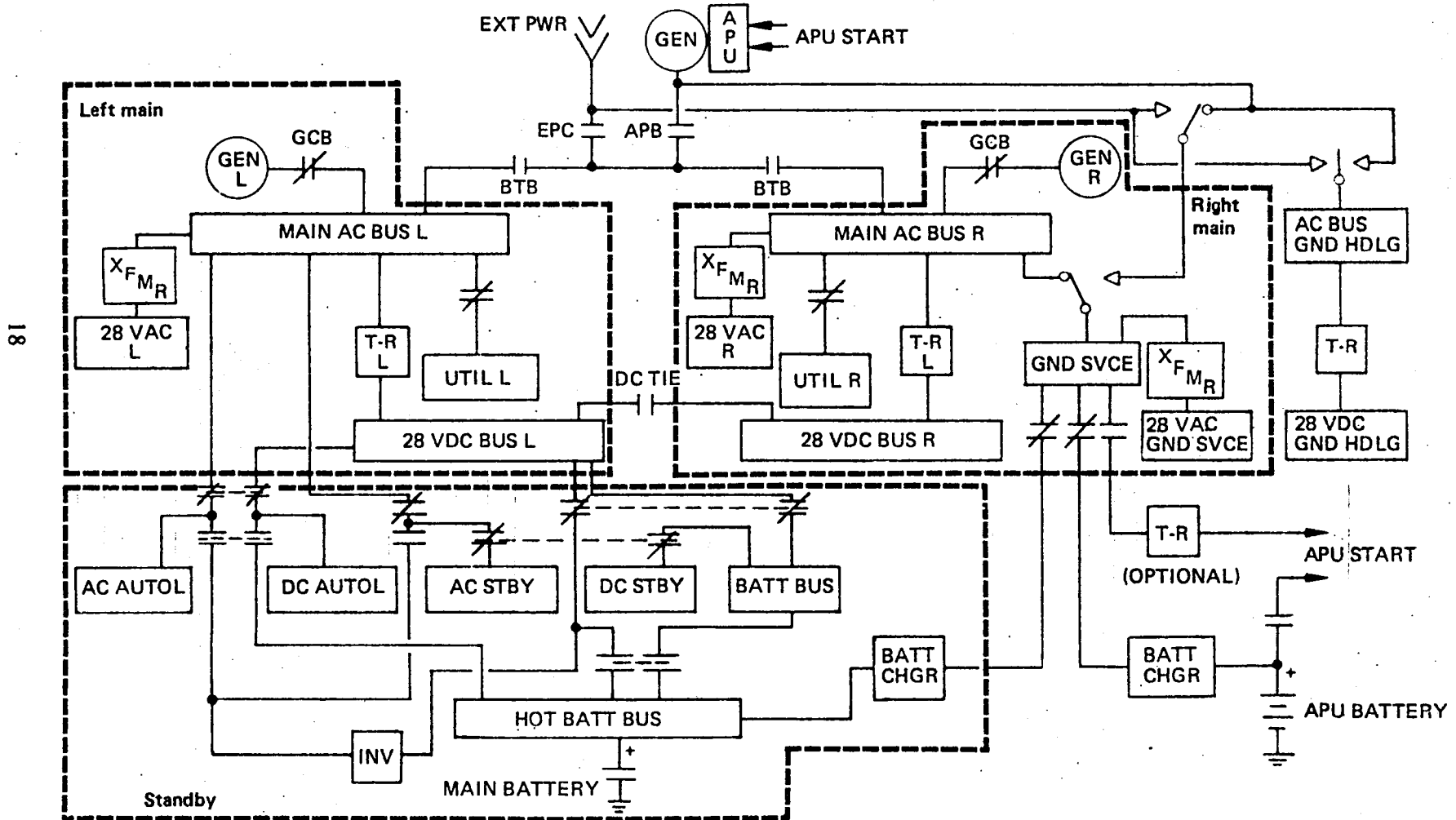
Figure 8. Electrical Power System

between the nosegear wheel well and the forward cargo compartment and includes the area on the right side of the nosegear wheel well. There are smaller equipment areas located forward of the nosegear wheel well, in the aft cargo compartment, and an equipment area located in the flight deck.

Three-phase, 115V, 400-Hz primary power is supplied by two engine-driven 90-kVA, integrated drive generators (IDG). The system operates as two isolated channels, and paralleling of the generators is not possible. A third 90-kVA auxiliary power unit (APU)-driven generator is provided for ground maintenance operations and as an inflight backup for the engine-driven generators. Any single generator has sufficient capacity to supply all flight-essential loads. The electric power load profile is shown in Figure 9.

Twenty-eight-volt dc power is provided by two 120A unregulated transformer-rectifier (TR) units. Each of the two main ac busses supplies its own TR unit. The dc systems operate only in isolation. In the event of a TR unit failure, a dc bus tie contactor enables the remaining TR unit to supply both main dc busses. During ground operation, a 20A TR unit provides dc power for ground handling loads.

A 40-Ah nickel-cadmium battery and a 1000-VA static inverter supply backup power to flight critical loads. A battery charger controls recharge of the battery and operates as a TR unit to supply the standby loads if the main dc source is lost, but ac power is still available. Standby bus transfer is automatic.

A 40-Ah nickel-cadmium battery and a battery charger supply APU start power. The battery and charger are identical to those used in the standby power system. A transformer-rectifier unit is available as a standard option for APU starting when ac power is available from either the main generators or external power.

4.1.5.3 Propulsion—Two Rolls-Royce RB211-535C high-bypass-ratio turbofan engines are installed on pylons extending forward beneath the wings (fig. 10). The nacelles have three-quarter-length fan ducts and have peripheral inlet, fan duct, and primary sleeve acoustical lining. The nacelle components are an inlet, two fan cowls, two fan reverser cowls, and a primary sleeve and plug. A hydraulically actuated fan reverser cowl-opening system is provided. Hold-open rods are provided for the fan cowl and fan reverser cowl.

Accessories are located on a gearbox underneath the fan case. The major airplane-furnished accessories are a hydraulic pump and a 90-kVA IDG. The engine starter fuel flowmeter and tach generators are engine furnished. Firewalls are located to isolate fire zones from the rest of the nacelle and pylon. Fire detection and extinguishing systems are provided for fire zones.

An engine bleed air pneumatic system (fig. 11) supplies air-conditioning (A/C) and thermal anti-icing (TAI) for the inlet lip and wing. Engine compressor bleed air is routed through a precooler to provide the A/C and wing TAI air. The system includes a low-pressure-stage check valve, high-pressure-stage switching valve, and pylon shutoff valve. A precooler modulating valve regulates fan air through the precooler to control beed air temperature. The starter duct is routed from the A/C duct through a starter valve to the starter.

Gearbox pad drains, strut drains, and other miscellaneous drains and vents are provided in the engine section and routed to drains at the bottom of the cowl.
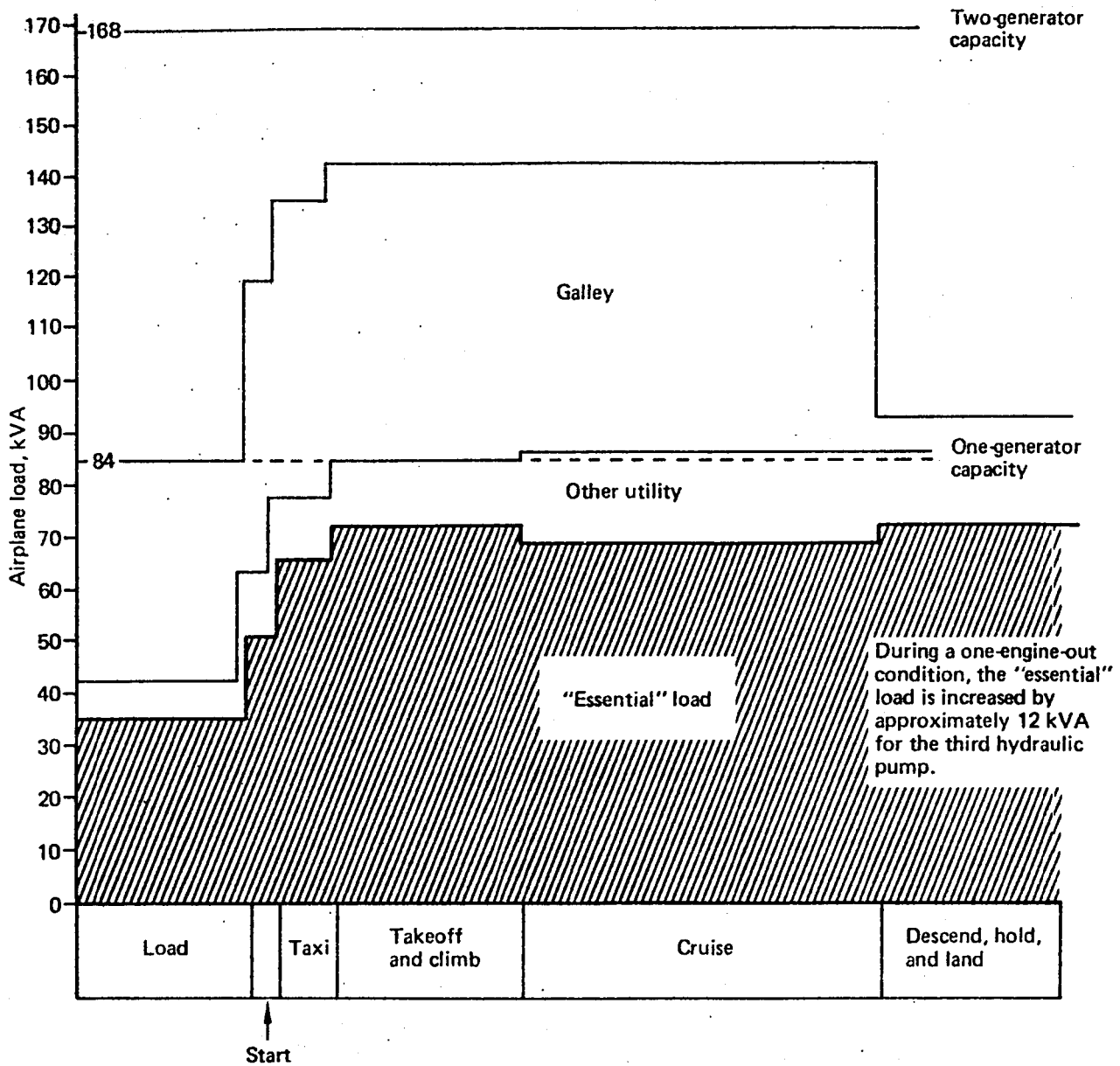
Figure 9. Electric Power Load Profile
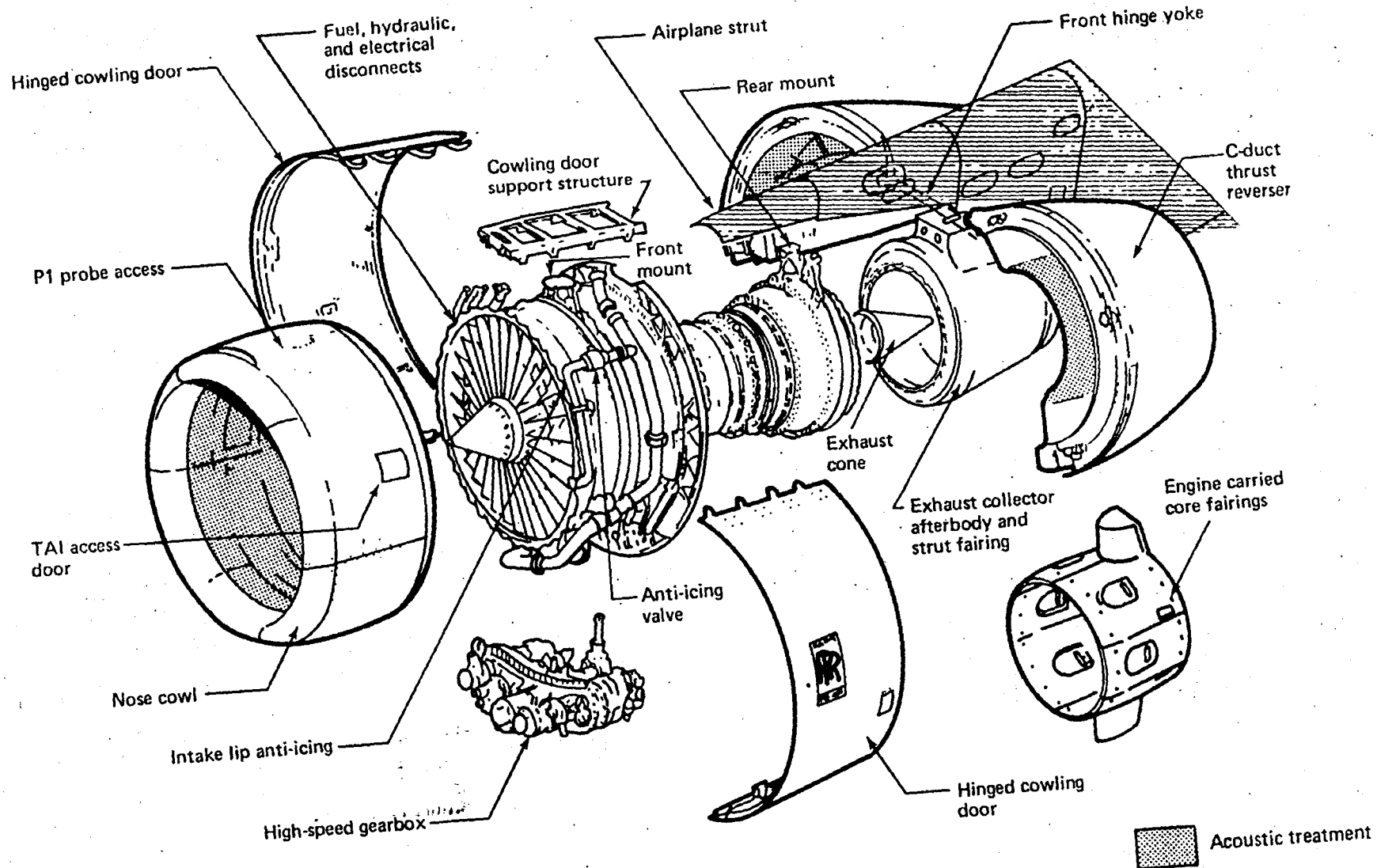
Figure 10. Nacelle Installation, RB211-535C

Hinged cowling door

Fuel, hydraulic, and electrical disconnects

Airplane strut

Front hinge yoke

Rear mount

Cowling door support structure

C-duct thrust reverser

P1 probe access

Front mount

TAI access door

Exhaust cone

Exhaust collector afterbody and strut fairing

Engine carried core fairings

Nose cowl

Anti-icing valve

Intake lip anti-icing

Hinged cowling door

High-speed gearbox

Acoustic treatment

21

Figure 11. Pneumatic System Schematic

4.1.5.4 Wing Thermal Anti-Icing System—The wing TAI system is shown in Figure 12. Hot air is provided by intermediate or high-stage precooled bleed air from both engines. A shutoff valve is installed downstream from the engine bleed air precooler. The shutoff valves are controlled by a single switch on the pilot's overhead panel. A valve position light for each valve is located adjacent to the control switch. The lights indicate disagreement with the selected valve position. A remotely located ground test switch also uses the valve position lights.

A perforated distribution duct feeds air uniformly to the slat leading edge. Telescoping ducts supply TAI air to the wing leading-edge slats when they are extended. The slats are mechanically ganged together, requiring only one telescoping duct per wing.

4.1.6 Characteristics

Principal characteristics of the 757-200 are shown in Table 1.

4.2 WEIGHT AND BALANCE

The 757-200 is designed for a maximum taxi weight of 100 246 kg (221 000 lb), a maximum inflight weight of 99 792 kg (220 000 lb), and a maximum design landing weight of 89 811 kg (198 000 lb). The operating empty weight (OEW) is 59 402 kg (130 960 lb). Center-of-gravity limits are shown in Figure 13.

22

Vibraker coupling
B

Telescoping duct

A—A

Bleed-air manifold

TAI manifold

B

FS

Distribution duct

TAI pressure
regulator
and shutoff
valve
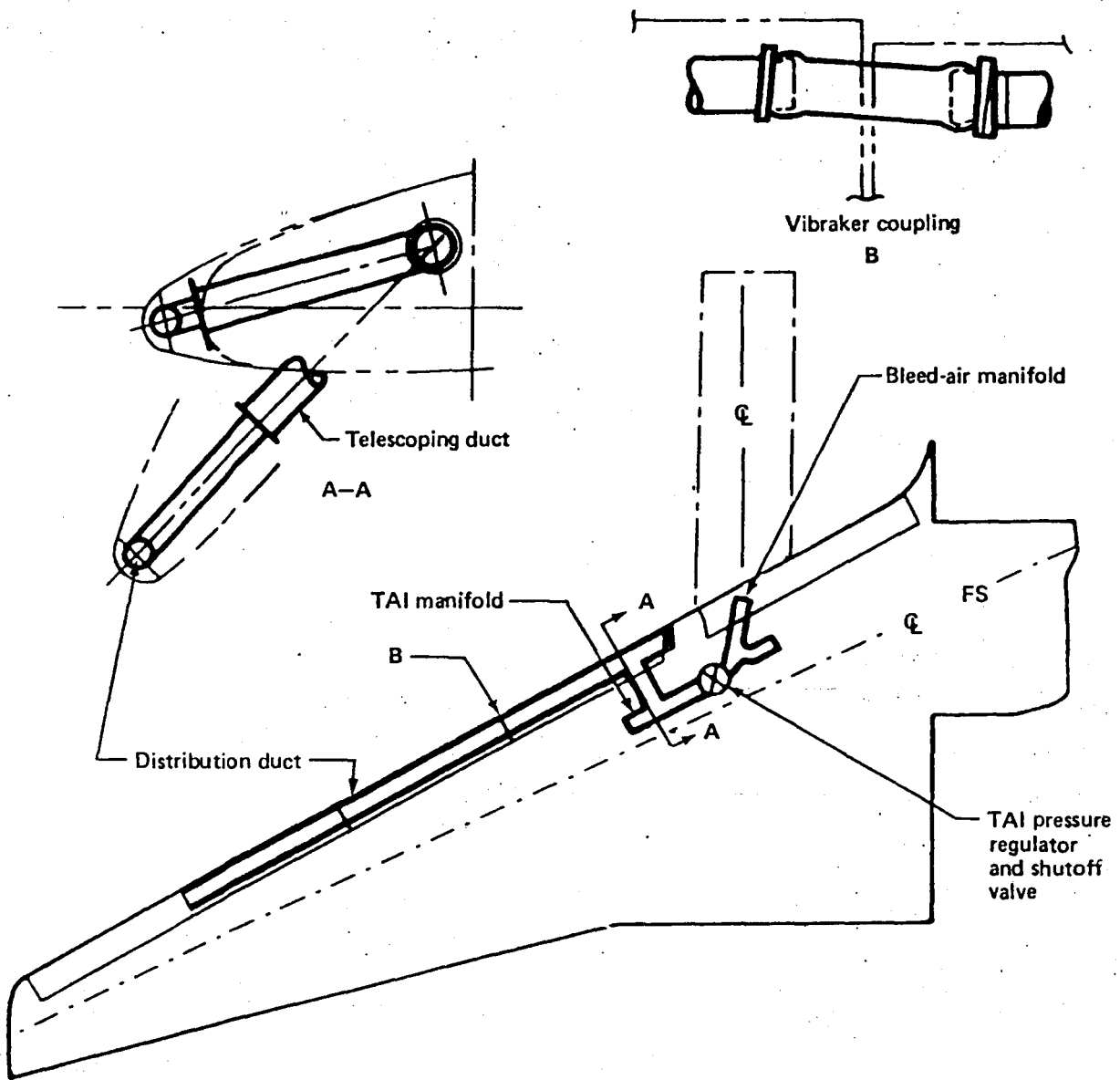
Figure 12. Wing Thermal Anti-Icing System

23

Table 1. Characteristics of 757-200 (Baseline Airplane)

Wing		
Area, m^2 (ft^2)	181.25	(1951)
Span, m (ft)	37.96	(124.5)
Mean aerodynamic chord, m (ft)	5.07	(16.64)
Aspect ratio	7.95	
Sweepback ($c/4$) deg	25.00	
Taper ratio (trapezoidal)	0.24	
Thickness ratio (root/outboard)	0.135/0.103	
Horizontal tail		
Area, m^2 (ft^2)	50.35	(542)
Span, m (ft)	15.05	(49.38)
Aspect ratio	4.50	
Sweepback ($c/4$), deg	30.19	
Taper ratio	0.35	
Thickness ratio (root/outboard)	0.109/0.090	
Volume coefficient ($S_H \ell_H/S\bar{c}$)	1.115	
Vertical tail		
Area, m^2 (ft^2)	34.37	(370)
Span, m (ft)	7.45	(24.45)
Aspect ratio	1.62	
Sweepback ($c/4$), deg	40.00	
Taper ratio	0.35	
Thickness ratio	0.090	
Volume coefficient ($S_V \ell_V/Sb$)	0.0973	
Body		
Length, m (ft)	46.89	(153.83)
Width, cm (in)	375.92	(148)
Maximum depth, cm (in)	440.69	(173.5)
Cabin length, m (ft)	32.51	(106.67)
Engines		
Type	(2) Rolls-Royce RB211-535C	
Thrust (SL static), N (lb)	166 355	(37 400)
Noise level	FAR part 36, stage 3	
Fuel capacity (usable)		
Outboard tanks (both), L (U.S. gal)	14 380	(3 800)
Center tank, L (U.S. gal)	26 800	(7 080)
Weights		
Maximum taxi, kg (lb)	100 246	(221 000)
Maximum takeoff, kg (lb)	99 790	(220 000)
Maximum zero fuel, kg (lb)	83 462	(184 000)
Maximum landing, kg (lb)	89 811	(198 000)
Empty (operating), kg (lb)	59 402	(130 960)
Payload		
Passenger (mixed class)	178	
Cargo (bulk), m^3 (ft^3)	50.12	(1 770)
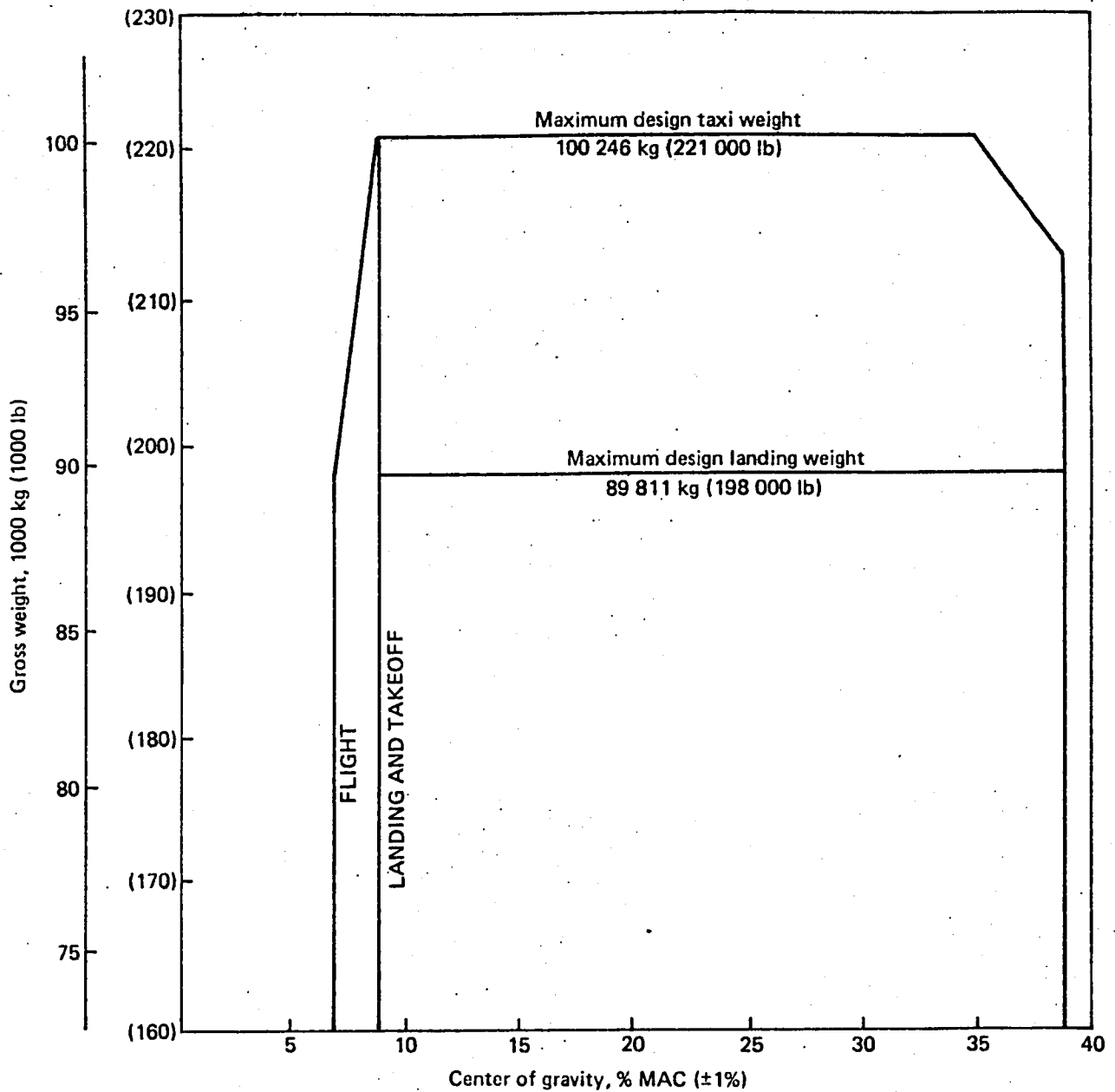
Figure 13. Allowable Center-of-Gravity Limits

4.3 PERFORMANCE

Fuel economy characteristics will be compared for a design mission to transport a 16 148 kg (35 600 lb) payload (consisting of 178 mixed class passengers) over a 3928-km (2120-nmi) still-air distance at a cruise speed of Mach 0.8. Mission rules and profile are presented in detail in Figure 14. Performance of the 757-200 baseline airplane in this mission is given in Table 2. A total of 18 666 kg (41 150 lb) of fuel are burned to accomplish it.

25

RESERVE MISSION

1.0 hr at LRC Mach
(at end cruise altitude and weight)

Missed approach—V_{APP} at 11m (35 ft)
to 463 kg/hr (250 kn) at 457m

Climb

185 km (100 nmi) at LRC

371 km (200 nmi)

Descend to 457m (1500 ft)

Approach and land (5 min)

Reserves

DESIGN MISSION

Taxi out (9 min)

Takeoff—to 11m (35 ft)

Climb to 457m (1500 ft);
accelerate to 463 km/hr (250 kn)

Climb to 3048m (10 000 ft) at
463 km/hr (250 kn)

Accel to climb speed

Climb

Cruise

Descend to 3048m (10 000 ft)

Decel to 463 km/hr (250 kn)

Descend to 457m (1500 ft)

Approach and land (5 min)

Taxi in (5 min) from reserves

Block time, block fuel

Still air range

Note: Standard temperatures used for all mission segments.

Figure 14. Mission Profile—U.S. Domestic Rules

26

Table 2. Mission Summary, 757-200 Baseline

Mission segments	Fuel burn, kg (lb)	Fuel remain, kg (lb)	End segment weight, kg (lb)	Time, hr	Distance, kn (nmi)
① Taxi out, 9 min	184 (405)	24 240 (53 440)	99 790 (220 000)	0.150[a]	—
② Takeoff, sea-level climb to 457m (1500 ft)	376 (829)	23 864 (52 611)	99 414 (219 171)	0.033	8.2 (4.4)
③ Climb to 10 668m (35 000 ft), accelerate to M = 0.8	2 336 (5 150)	21 528 (47 461)	97 078 (214 021)	0.322	225.9 (122.0)
④ Cruise M = 0.8, 10 668m (35 000 ft) to 11 887m (39 000 ft)	15 168 (33 439)	6 360 (14 022)	81 911 (180 582)	4.090	3481.0 (1879.6)
⑤ Descend to 457m (1500 ft)	273 (602)	6 087 (13 420)	81 637 (179 980)	0.323	211.1 (114)
⑥ Approach and land	227 (500)	5 860 (12 920)	81 411 (179 480)	0.083	—
⑦ Taxi in, 5 min	102 (225)[a]	—	—	0.083[a]	—
Total mission	18 666 (41 150)	18 563 (40 925)	—	4.851[b]	3926 (2120)
⑧ Total reserves	5 860 (12 920)	—	—	—	—

[a]Not included in total mission fuel or trip airtime.
Taxi time included in block time.
Taxi-in fuel (from reserves) included in block fuel.

[b]Trip air time.
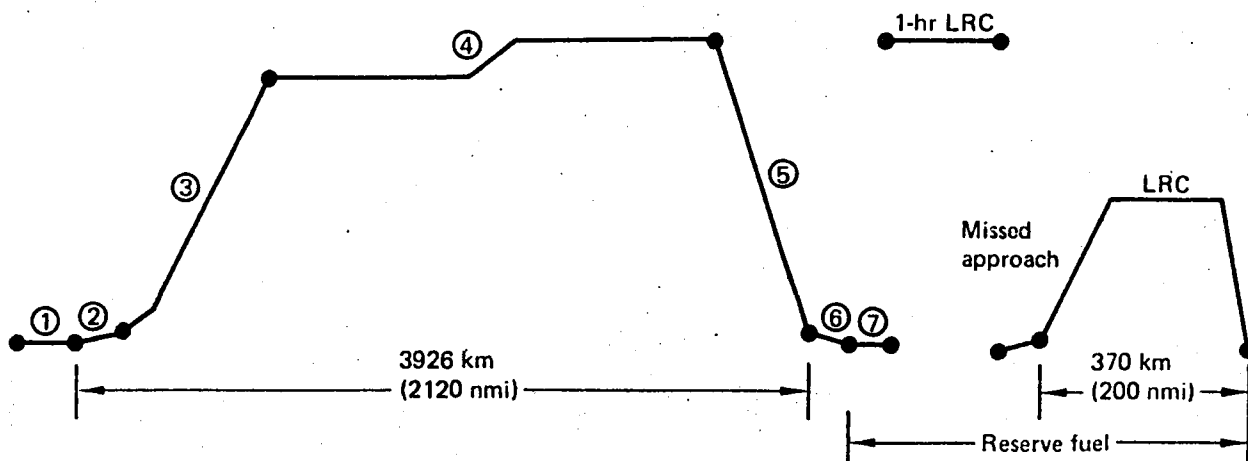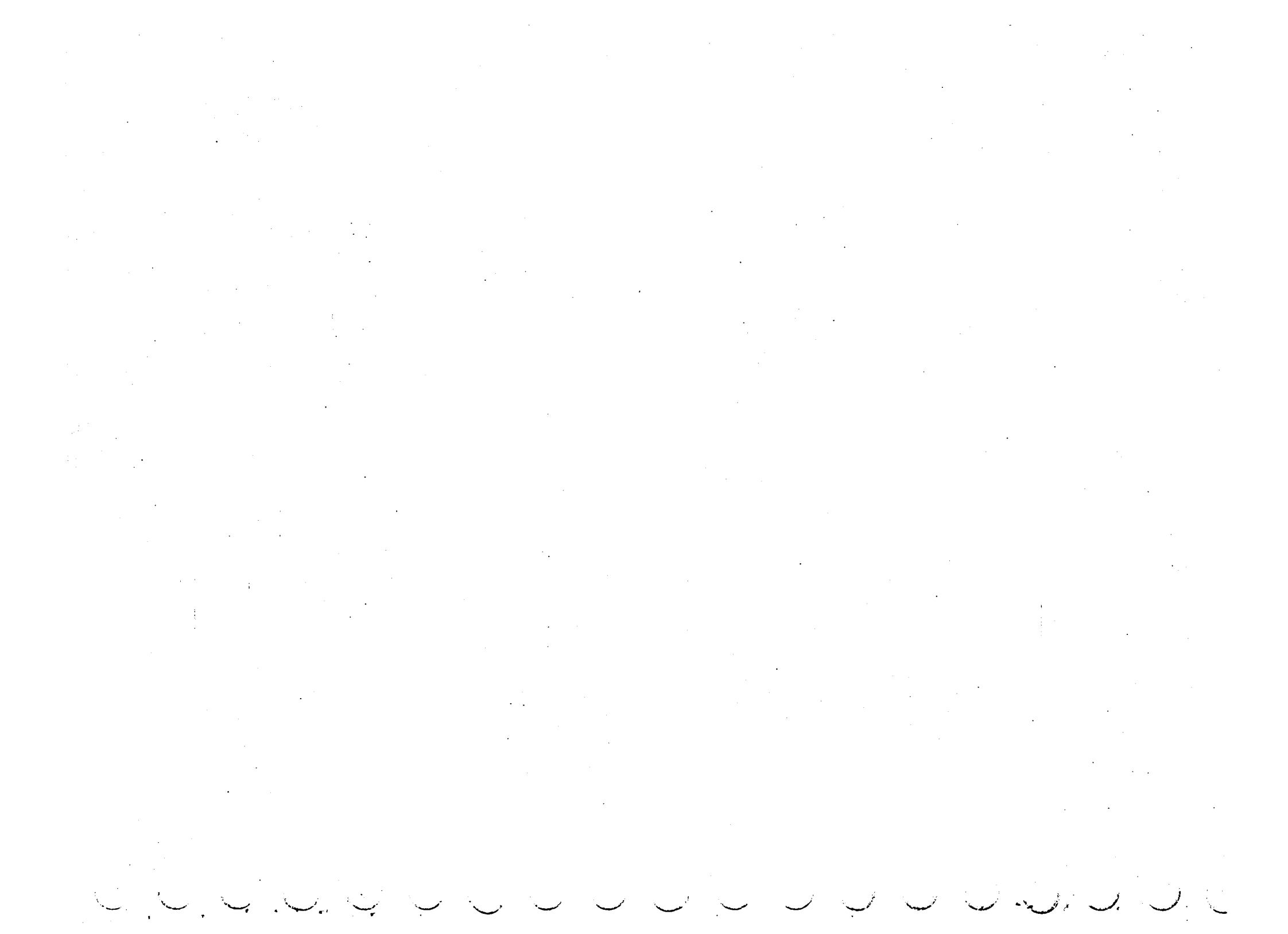
5.0 HLFC ANALYTICAL STUDIES

5.1 AIRFOIL DEVELOPMENT

Development of an airfoil is mainly the selection of the desired pressure distribution. Once this is done, the shape can be computed by a mathematical procedure. However, not all pressure distributions correspond to physically meaningful airfoil shapes; real flow constrains the pressure distribution to have a leading edge stagnation point, low pressure forward, and gradually rising pressure aft, ending somewhat above ambient at the trailing edge. Within these constraints, details must be tailored to meet the specific requirements of HLFC and of low drag rise due to compressibility as indicated in Figure 15. In particular:

- A steep initial gradient (rapidly falling pressure) is helpful in preventing attachment line transition on wings having substantial leading-edge sweepback.

- The midchord pressure distribution affects susceptibility to the two other principal transition mechanisms. Falling pressure tends to suppress the growth of Tollmien-Schlichting disturbances, and rising pressure will generally promote their rapid amplification. Hence, a negative gradient (falling pressure) is often called "favorable," and a positive gradient (rising pressure) is termed "adverse." However, substantial gradients of either sign will combine with sweepback to produce boundary layer crossflow, which tends to amplify disturbances and to promote transition.

  The fundamental technical strategy of HLFC is to confine the unavoidable large negative gradients to the region ahead of the front spar and to use boundary layer suction to suppress disturbance amplification due to crossflow there. Downstream of the front spar, gradients are kept in the weakly favorable to zero range.

- The minimum pressure level on the upper surface must correspond to a slightly supersonic velocity on an efficient high-speed wing. The shock strength at the return to subsonic flow must not be so great as to cause separation of the laminar boundary layer.

- Transition to turbulent flow can be expected early in the region labeled "pressure recovery." The pressure distribution in this region must be designed to ensure that turbulent separation is absent.

- The pressure level on the lower surface is determined by the desired lift coefficient and airfoil thickness ratio. The flow will normally remain subsonic and therefore shock-free. A recovery region having an adverse pressure gradient and turbulent flow must occupy the aftmost portion.

5.1.1 Parametric Study

The purpose of the parametric study was to define the pressure distribution characteristics required for maintaining a laminar boundary layer with HLFC for a range of sweep angles and Reynolds numbers. Only pressure distributions (and not the corresponding airfoil shapes) were required, so the time and cost required to optimize the pressure distribution were minimized. An actual HLFC airfoil shape was then designed to give a pressure distribution close to the best from the parametric study.
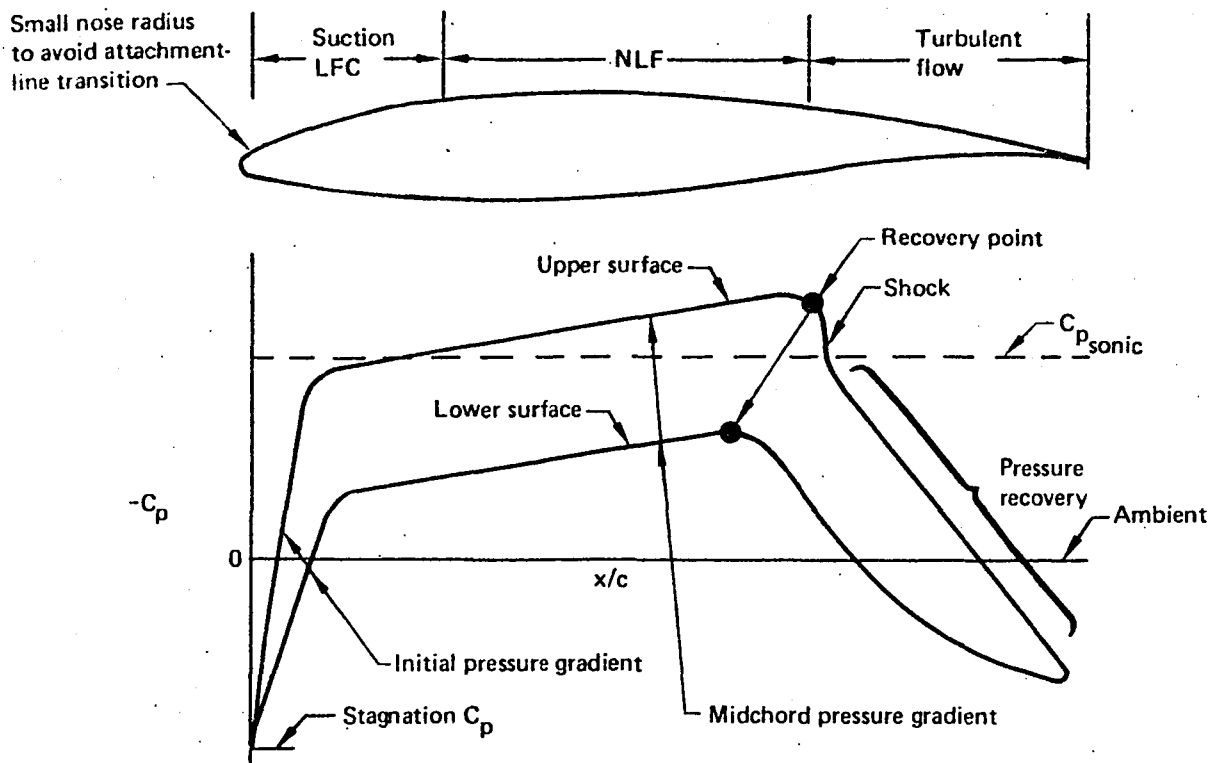
Figure 15. Characteristics of HLFC Airfoil Pressure Distributions

5.1.1.1 Scope and Ground Rules—Twelve pressure distributions were analyzed. (Details are discussed in app. A.) Two cases were designated as baseline distributions. For the upper surface pressure distributions case 1-1 was chosen, and for the lower, case 4-1. These pressure distributions correspond to those of the NLF airfoil described in Reference 4 and provided a convenient starting point for the parametric study. They were used for comparative purposes throughout the study to measure effects of varying pressure distribution shape on the stability of the laminar boundary layer.

Figure 16 shows the upper surface pressure distributions selected to investigate the effect of midchord pressure gradient, initial pressure gradient, and midchord shape on the extent of laminar flow. (Note that pressure coefficient is here plotted against nondimensional arc length on the airfoil surface or s/c, because the boundary layer equations are formulated using that coordinate. The distinction between s/c and x/c [chordwise distance] is important near the leading edge.) The four lower surface pressure distributions included one with a strong favorable pressure gradient from the leading edge to 45% chord (case 4-1), one having a steep initial pressure drop followed by a region of fairly constant pressure (case 4-2), and two in which the pressure drop occurs in two sharp steps (cases 5-1 and 5-2). Two pressure distributions (cases 1-4 and 5-2) were suggested by W. Pfenninger on the basis of studies reported in Reference 8.

The Mach number based on velocity normal to the leading edge was kept fixed at 0.78 for all cases. Each pressure distribution was analyzed at sweep angles of 15, 20, and 25 deg and at Reynolds numbers of 15×10^6, 30×10^6, and 45×10^6 at each sweep angle. (For the purposes of the parametric study, the sweep angle was considered to be constant over the whole chord. For analysis of three-dimensional wing flows, the sweep was varied with

30

Figure 16. Parametric Study Pressure Distributions

31

chord to suit the planform taper.) The analysis was performed both without suction and with suction ahead of 20% chord. In general, the suction quantity and distribution remained the same from case to case. By using a suction distribution that resulted in a small oversuction for most cases, the maximum potential extent of laminar flow for each case could be determined without optimizing the amount of suction. Any suction in addition to that required to damp out the forward crossflow instability will not result in any sig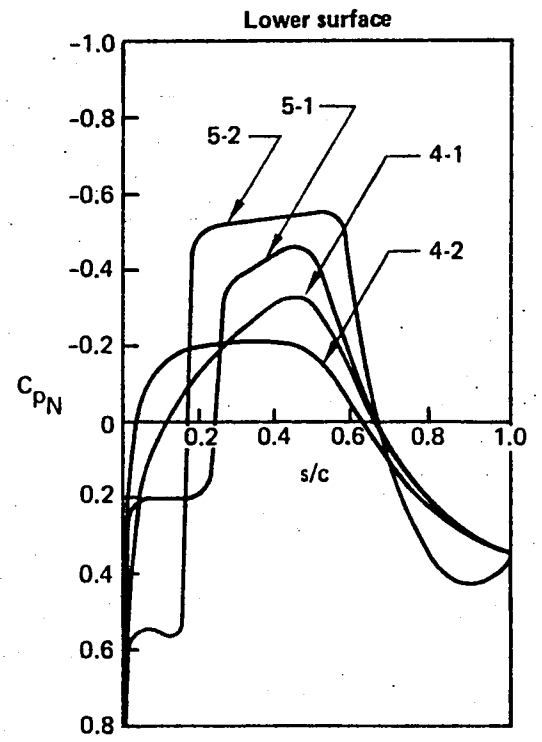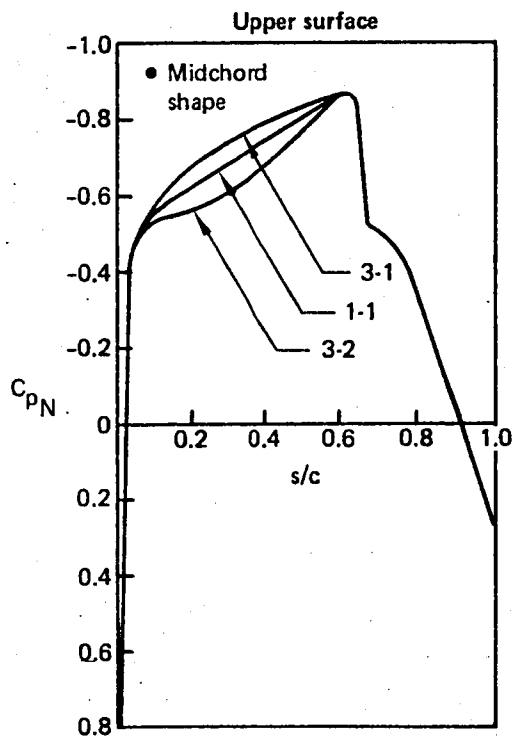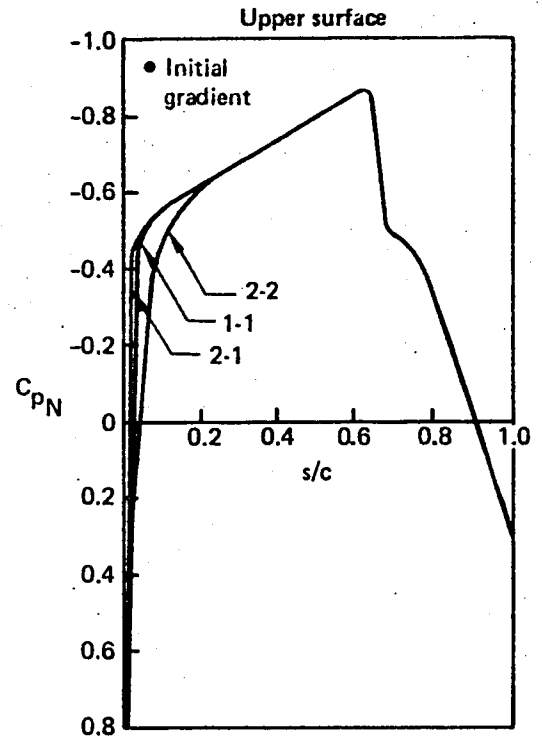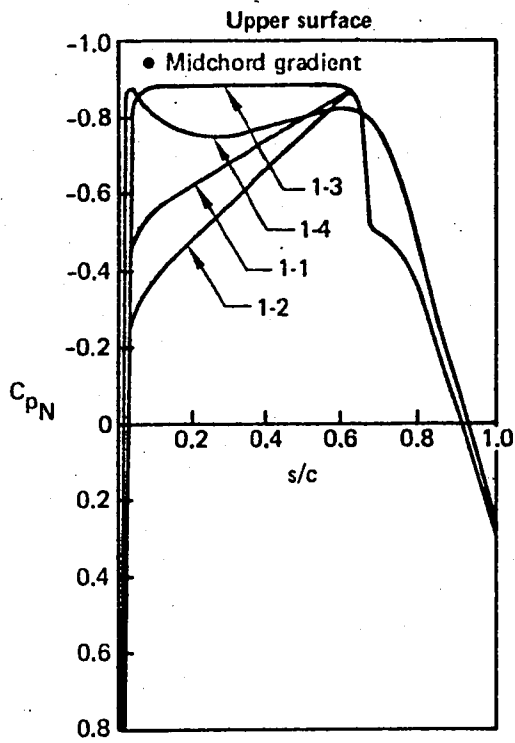nificant increase in the extent of laminar flow (sec. 5.2.3). Therefore, reducing the amount of suction for each case to the optimum level would not result in any significant decrease in the extent of laminar flow.

5.1.1.2 Analysis Method—The objective was to determine the boundary layer transition location (beginning of fully turbulent flow) at each condition. The most accurate methods of predicting boundary layer transition are based on linear boundary layer stability theory. The premise of this theory is that transition is caused by the amplification of initially infinitesimal boundary layer disturbances as they propagate downstream. The rate at which a disturbance is amplified depends on its frequency and propagation direction. When the amplitude of the disturbance grows large enough, it will distort the mean flow profile of the laminar boundary layer and cause transition.

By solving the linearized three-dimensional boundary layer stability equations (ref. 9), the amplification rate at each point along the wing of any disturbance in the boundary layer can be computed. The ratio, A/A_0, of the local disturbance amplitude to the disturbance amplitude at the neutral stability point can be computed by integrating the amplification rate in an appropriate direction along the wing surface. The natural logarithm of this ratio is called the amplification factor. A criterion for transition can be established by correlating the computed amplification ratio with experimentally established transition locations. Transition locations are then identified as the points where the transition amplification factor is exceeded.

There are four basic transition mechanisms on a swept wing. These are: (1) viscous or Tollmien-Schlichting (T-S) instability, (2) inflectional or crossflow (C-F) instability, (3) Taylor-Goertler instability, and (4) leading-edge attachment line contamination.

T-S instability depends on the action of viscosity to transfer energy from the mean boundary layer flow to the disturbance. Its direction of propagation is close to the local freestream direction. Amplification of T-S disturbances is small in regions of negative pressure gradient and large in regions of positive pressure gradient. (For severe positive gradients such as shocks, transition will occur immediately at any practical Reynolds number.)

C-F instability propagates in a direction nearly perpendicular to the local freestream. It is referred to as an inviscid instability because it results from the presence of an inflection point in the C-F velocity profile. C-F in the boundary layer results from the combination of sweep and pressure gradient and is, therefore, most severe in the leading-edge and trailing-edge regions where the pressure gradients are largest.

Taylor-Goertler instability is a centrifugal instability that occurs in viscous flows over concave surfaces. The only two pressure distributions considered in the parametric study that correspond to airfoils having a concave surface in the laminar flow region are the lower surface cases 5-1 and 5-2. Taylor-Goertler instability was not calculated for these cases in the parametric study. If either had been chosen for the final airfoil, however, this kind of instability would have been considered.

Leading-edge attachment line contamination differs fundamentally from the first three transition mechanisms that begin as infinitesimal disturbances that are amplified until they cause transition or are damped out. Leading-edge attachment line contamination, however, refers to the spanwise spread along the wing leading-edge attachment (or stagnation) line of turbulence originating from such sources as leading-edge roughness elements or the fuselage boundary layer. Under some conditions, turbulence can propagate along the wing attachment line and trigger turbulent flow over the entire wing. Attachment line contamination was not considered in the parametric study. It was assessed for the final HLFC wing design, however.

For the present study, a transition criterion for combined C-F and T-S instability was required. Various linear stability methods have been calibrated against wind tunnel and flight test data (refs. 10, 11, 12, and 13) in several studies to date. (Reference 14 is an excellent summary of previous natural laminar flow and laminar flow control studies.) These studies found transition amplication factors for T-S disturbances ranging from 9 to 15 and for C-F disturbances ranging from about 6 to 12. None of the studies assessed the reduction in transition amplification factors that may be caused by the mutual interaction of C-F and T-S disturbances, because at the time there were no suitable experimental data. After consultation with NASA, the line shown in Figure 17 was selected. A sensitivity study (sec. 5.1.1.4) showed that the same type of airfoil would be selected for even stronger T-S/C-F interaction.

The stability analysis procedure is shown in Figure 18. The boundary layer characteristics were first computed using a Boeing program that uses finite difference methods to calculate the compressible boundary layer flow over infinite swept wings. For purposes of the parametric study, only a single sweep angle was used for a given case. In analyzing the final wing design, however, separate analyses were made in the leading-edge and midchord regions because their effective sweep angles differ because of planform taper. Primary inputs to the program are the pressure distribution along a normal to the leading-edge, Reynolds number, and Mach number. The primary outputs are the boundary layer velocity profiles parallel and perpendicular to the local potential flow streamline and the boundary layer temperature profile. These boundary layer profiles then served as the primary input to the stability analysis program, a Boeing modification of a computer program known as the Mack code (ref. 7). This program solves the three-dimensional, linearized, parallel flow boundary layer stability equations for a perfect gas. It is capable of computing either spatial or temporal amplification rates. Spatial amplification was used in the present study. The disturbance growth direction was assumed to coincide with the potential flow streamline. Mack (ref. 9) determined this to be a satisfactory approximation to the actual growth direction. The program can compute either incompressible or compressible stability, and both kinds of computations were made. When the program was used in the compressible mode, the sixth order equations (which neglect dissipation) were used instead of the complete eighth order equations. This saves significant computation time, and as shown by Mack (ref. 9), results given by the sixth order equations for a transonic swept wing differ from those of the eighth order equations by only a few percentage points. The detailed results of the stability analysis for each case are shown in Appendix A. The amplification factor envelopes shown there for the C-F and T-S disturbances were determined as follows:

● The T-S envelope was determined by following a series of T-S disturbances downstream, each having a different frequency. This analysis was performed incompressibly, keeping the wave angle and frequency constant during the downstream march. The envelope of the disturbance growth curves was then adjusted for

33
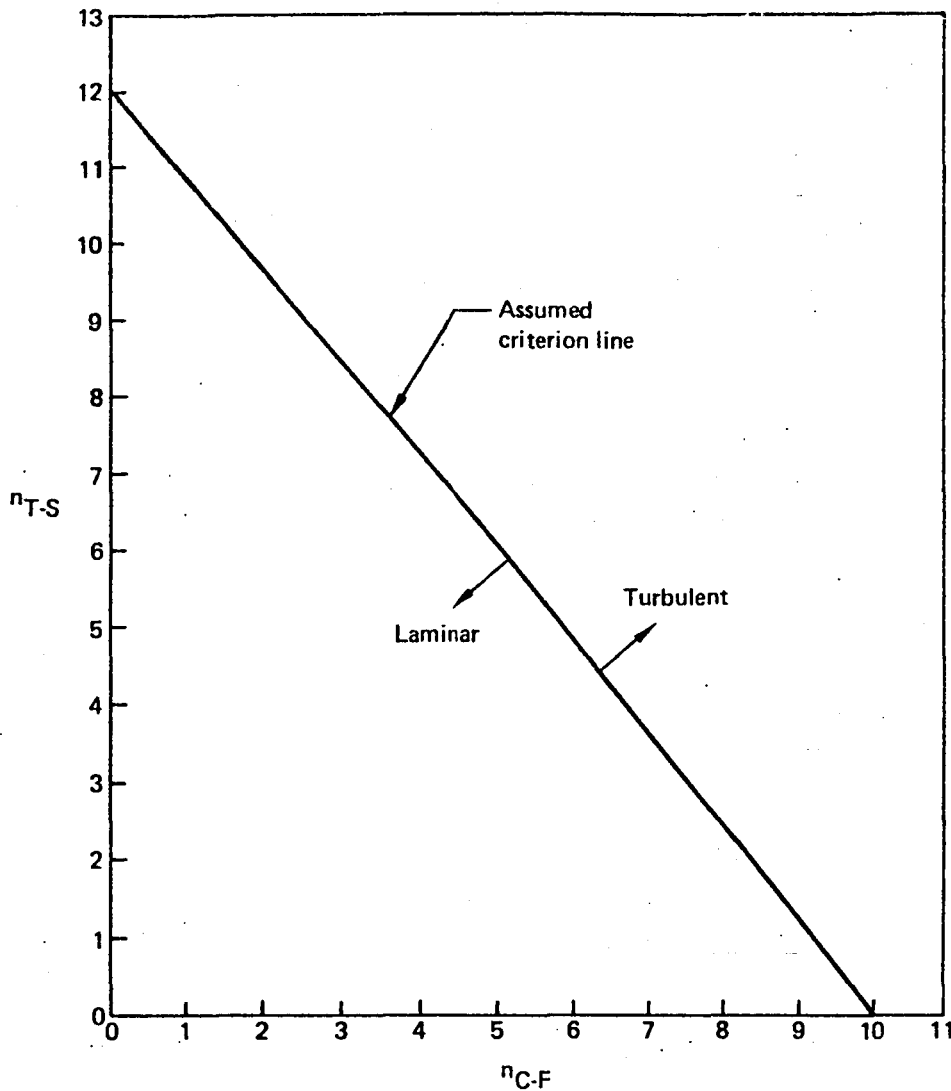
Figure 17. Transition Criterion for Combined Tollmien-Schlichting and Crossflow Instability

compressibility effects by analyzing one of the most highly amplified disturbances compressibly and applying the ratio of the compressible to incompressible maximum amplification factors to the entire envelope.

● The C-F envelope was determined by following a series of C-F disturbances downstream, each having a different frequency. This analysis was performed incompressibly keeping the wave angle and frequency constant during the down-stream march. Previous experience has shown that compressibility effects on crossflow disturbances usually result in about a 10% reduction in amplification factors. Therefore, the envelope of the incompressible C-F disturbances was reduced by 10% to get the compressible envelope.

5.1.1.3 Results—It was found that for the cases with no suction, only six of the nine sweep-Reynolds number combinations had to be analyzed in order to define the influence

34

● Boeing laminar boundary layer code
  ● Infinite swept wing
  ● Compressible

**Boundary layer
velocity profiles**

● Modified Mack stability code (Boeing)
  ● Spatial or temporal stability
  ● Compressible or incompressible

**Boundary layer
stability analysis**
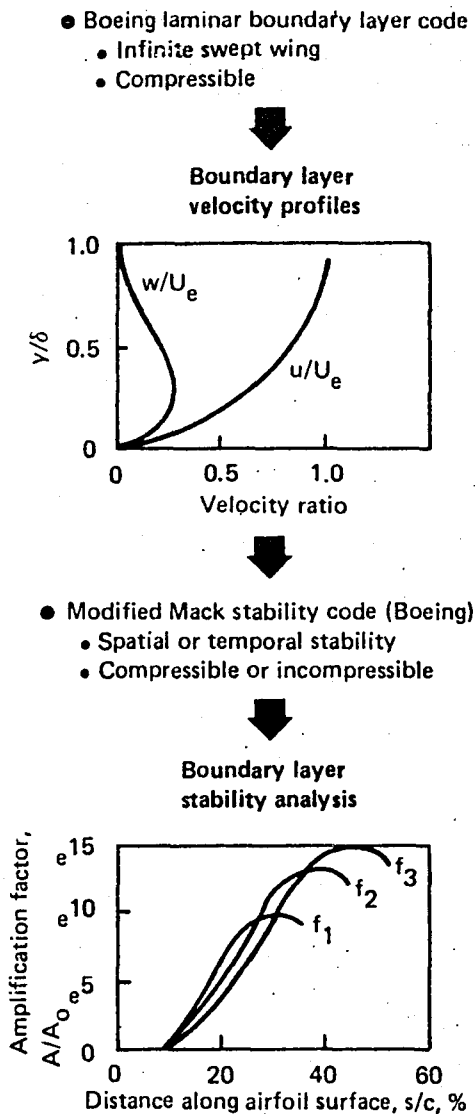
Figure 18. Stability Analysis Procedure

of sweep on transition location. For the cases with suction, even fewer combinations were needed because most of the nine possible combinations reached the point where transition occurs at the shock. It was also found that by calculating just one combination with suction (usually 25-deg sweep and 45×10^6 Reynolds number) and using the combinations where no suction was applied, the remaining suction combinations could adequately be estimated. So for most of the 12 cases analyzed in this study, the compressible stability envelopes were calculated for 5 or 6 combinations of sweep and Reynolds numbers where no suction was applied and 1 combination where suction was applied.

Effect of Upper Surface Midchord Pressure Gradient—Figure 19 shows the extent of laminar flow for cases 1-1 through 1-4 at two sweep angles. At 15-deg sweepback angle, the extent of laminar flow without suction is substantially lengthened by an increasingly favorable pressure gradient. Case 1-2 (most favorable) shows an increase of laminar run over case 1-3 (flat) equivalent to a Reynolds number reduction of 12 million. If suction is applied, all cases showed improvement if their natural transition was forward of 60% chord with cases 1-2 and 1-1 becoming completely insensitive to Reynolds number.

35
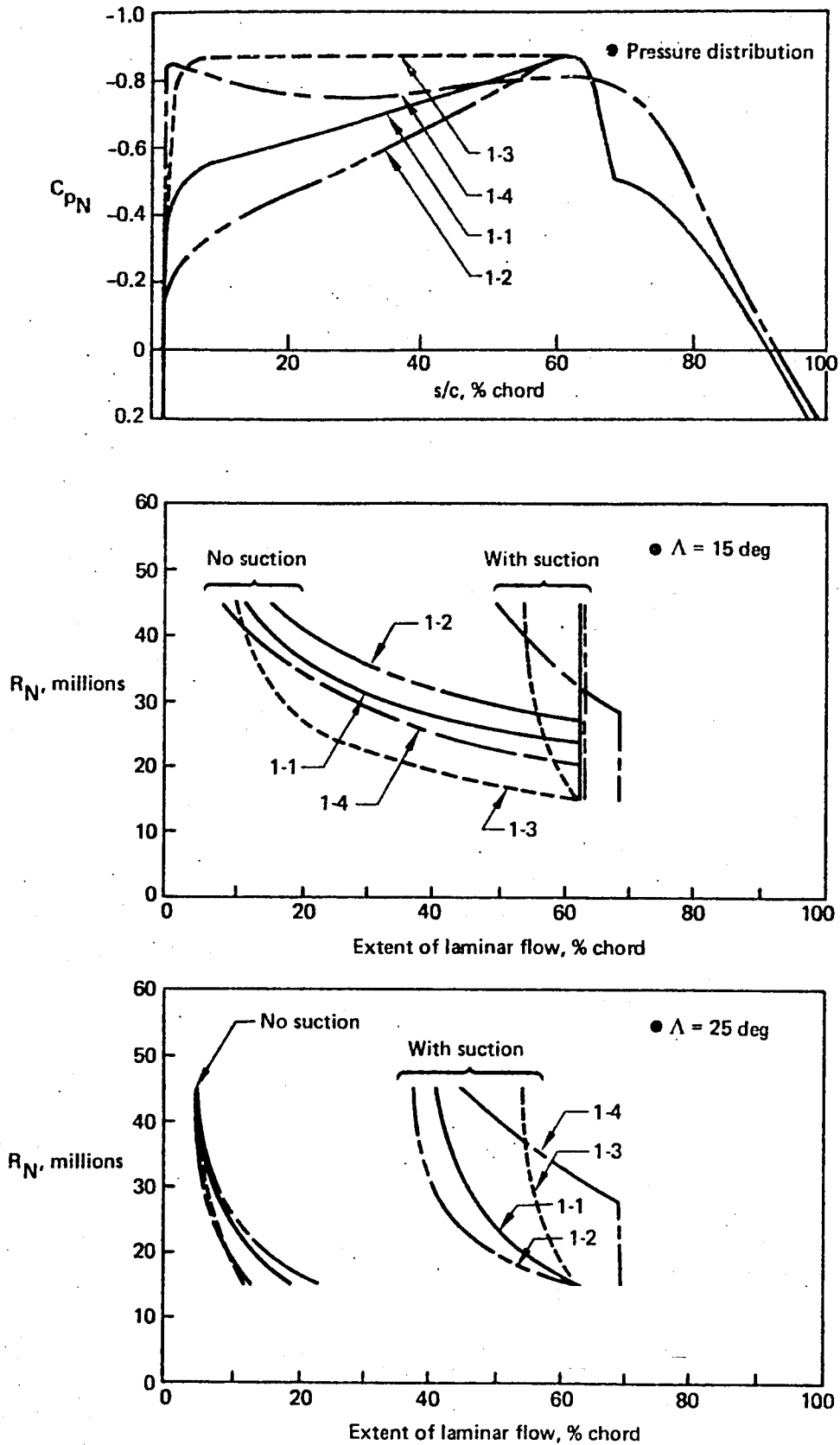
Figure 19. Effect of Midchord Pressure Gradient

For 25-deg sweepback, suction is required to achieve a useful laminar run for all four cases. Furthermore, the steeply favorable midchord gradients (cases 1-1 and 1-2) become a liability, causing C-F instability and transition 15% to 25% chord forward of the other cases (1-3 and 1-4). Case 1-4 gives the best performance of all at Reynolds numbers below 37 million but shows rapid deterioration above that point. (More detailed data, including amplification factors and suction distributions, are presented and discussed for each individual case in app. A.)

Effect of Initial Upper Surface Pressure Gradient—The pressure distributions of cases 1-1, 2-1, and 2-2 are shown in Figure 20, together with the extent of laminar flow as a function of Reynolds number at a sweep angle of 25 deg. These results show that without suction, the steepest initial gradient (case 2-1) is best at low Reynolds numbers and the shallowest initial gradient (case 2-2) is best at high Reynolds numbers. With suction, case 2-1 is the best at all Reynolds numbers, although the differences are not great.
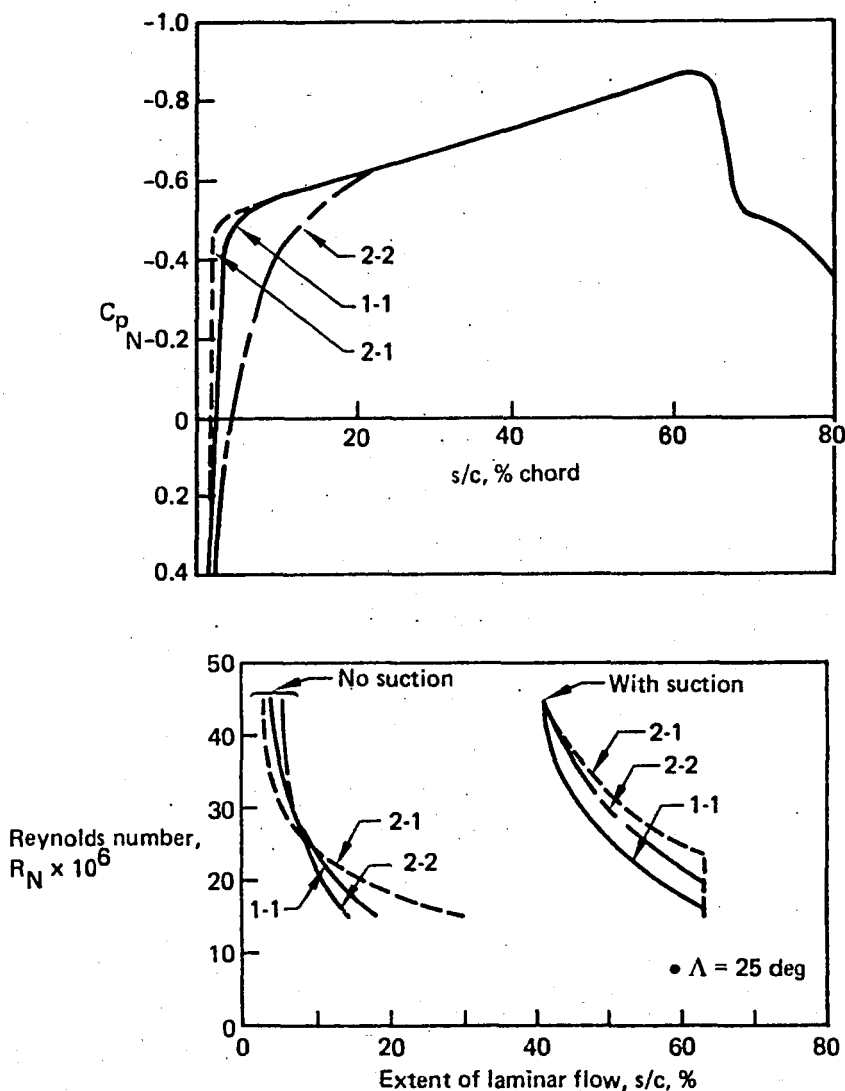
Figure 20. Effect of Initial Upper Surface Pressure Gradient

Effect of Upper Surface Midchord Shape—Figure 21 shows the effect of the midchord shape of the pressure distribution on the extent of laminar flow on the upper surface for sweepback angles of 15 and 25 deg. These cases were analyzed only without suction, because the pressure gradients aft of 20% s/c were similar to those analyzed (with suction) in cases 1-1, 1-2, 1-3, and 1-4. Case 1-1 is the best of the three, but differences are insignificant.

Lower Surface Pressure Distributions—Cases 4-1 and 4-2 are conventional lower surface pressure distributions having relatively low favorable and zero gradients, respectively, over the midchord region. Case 5-1 corresponds to a lower surface contour having a
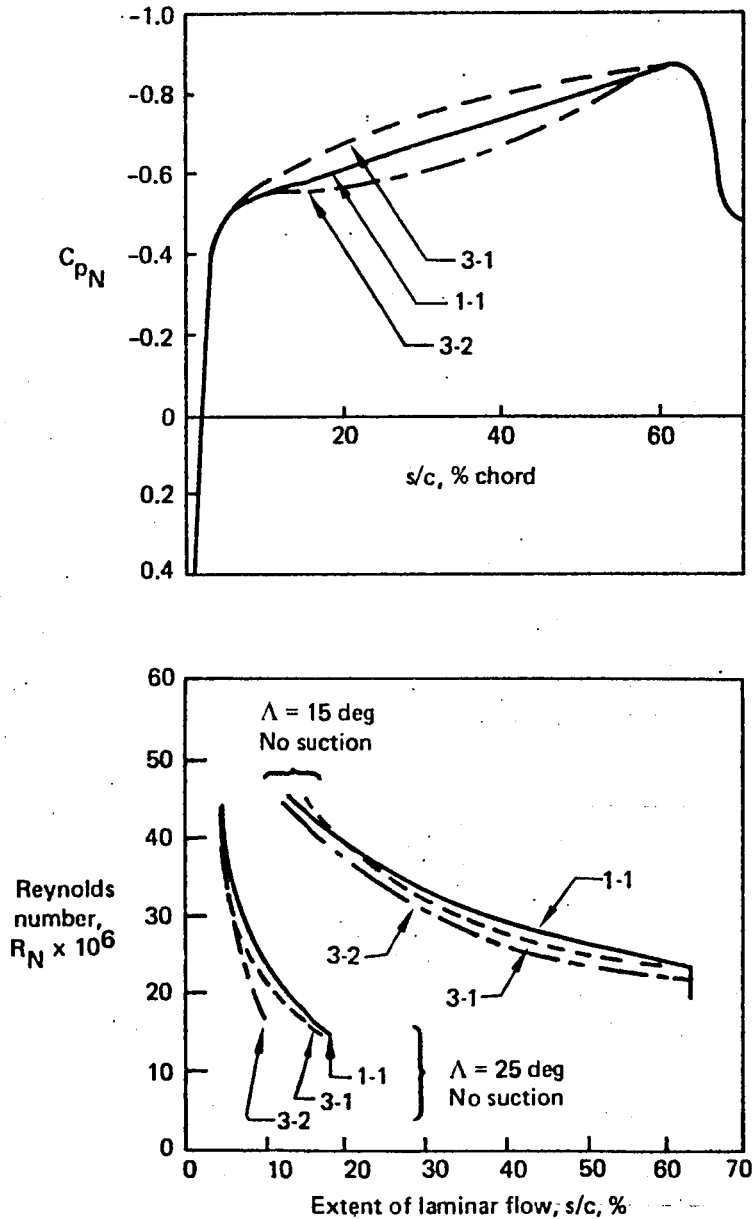
Figure 21. Effect of Midchord Shape

38

loaded, slightly hollow leading edge and a thickened midchord. Case 5-2 corresponds to a contour having its lift concentrated at the leading and trailing edges, and a substantially thickened, reduced lift, midchord. (Thickening the midchord region is of interest because it permits a deeper box spar with structural weight advantages.)

Figure 22 shows these pressure distributions and their calculated transition locations at 25-deg sweepback. Without suction, no significant differences are apparent for Reynolds numbers greater than 25×10^6. At 15×10^6, the flat pressure gradients of cases 4-2 and
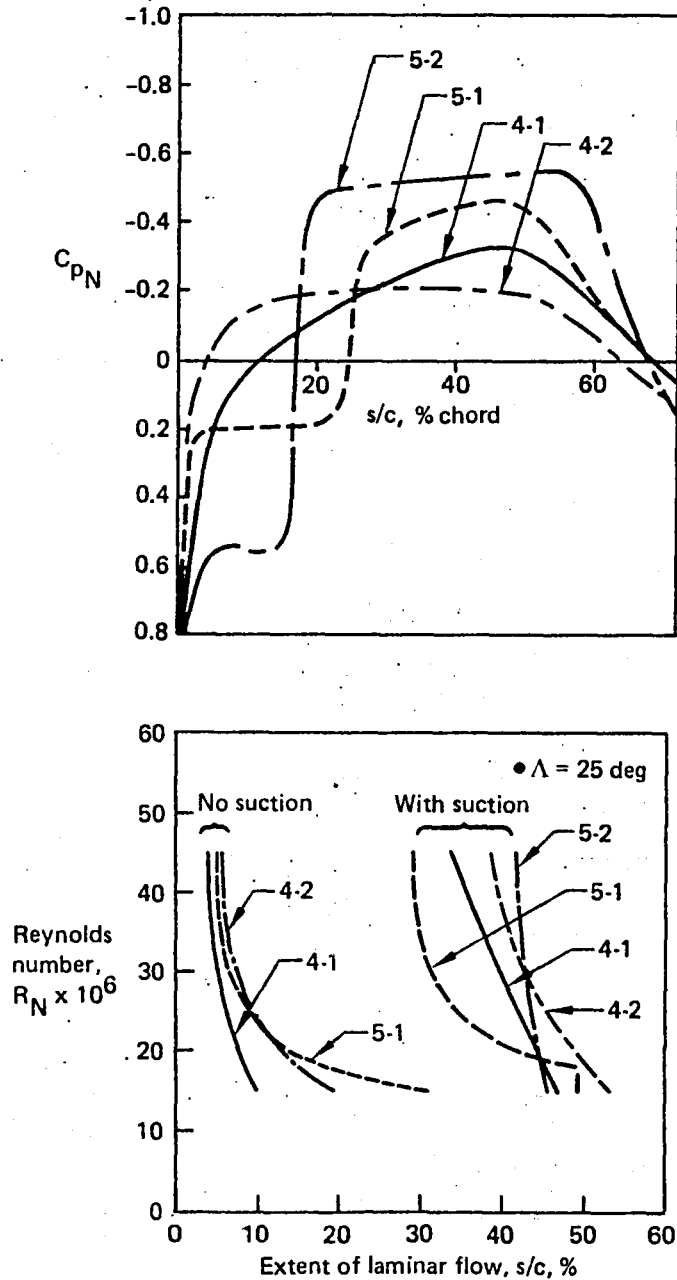
Figure 22. Effect of Lower Surface Pressure Distribution

39

5-1 offer 10% and 20% chord advantages over the "favorable" gradient of case 4-1. (Case 5-2 was not analyzed without suction, because it was designed to use suction to handle the C-F induced by the abrupt pressure rise at 18% chord.)

With suction, case 5-1 is noticeably inferior at Reynolds numbers greater than 15×10^6, and case 5-2 looks best only at 45×10^6.

5.1.1.4 Sensitivity to Transition Criterion Variations—Because the criterion for boundary layer transition under the combined influence of T-S and C-F instability was only assumed to be represented by a straight line in the amplification factor plane (fig. 17), an assessment of the sensitivity of the results of this study to variations in the criterion was required. Therefore, the two best pressure distributions for each surface were analyzed using altered shapes of the criterion curve (fig. 23). In all cases, the end points of the curve were held fixed at the comparatively well-established values for transition due to a
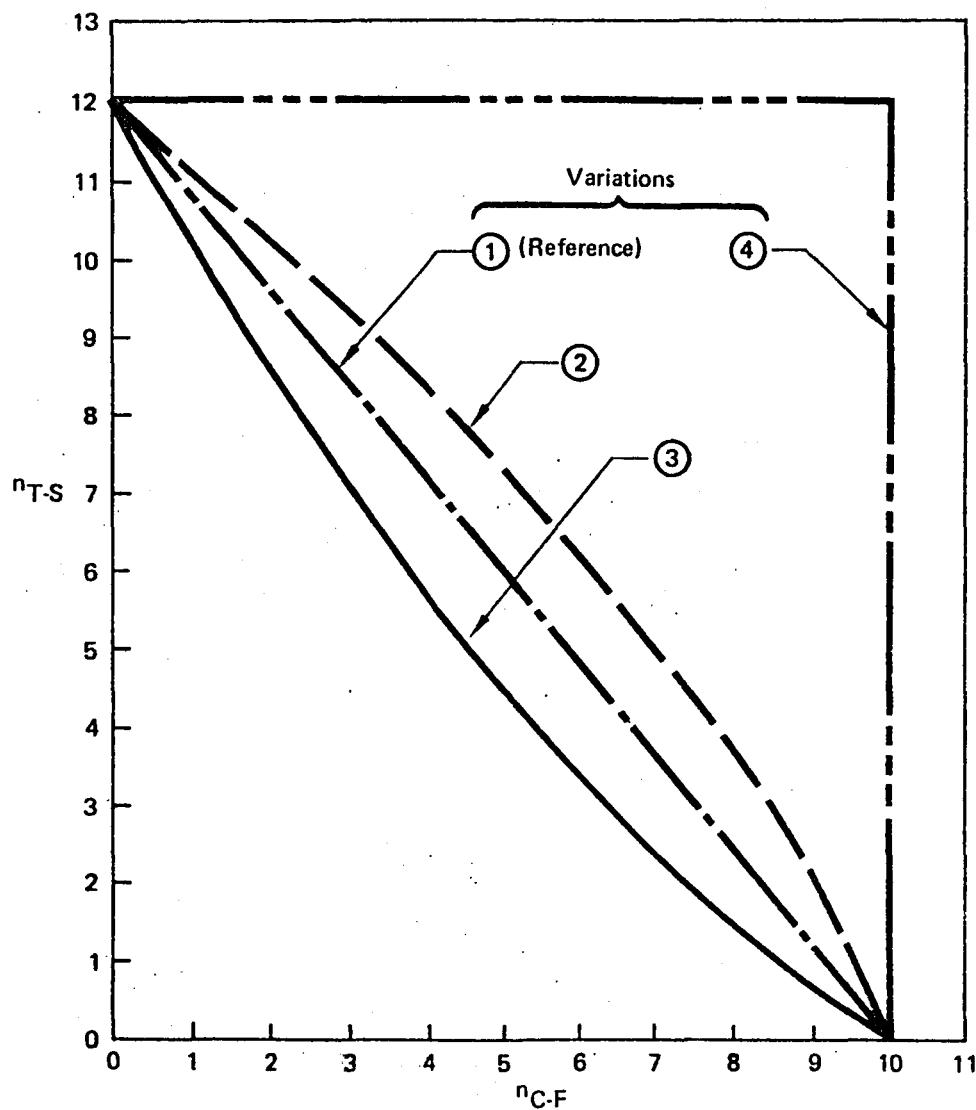
Figure 23. Variations of Transition Criterion

single type of instability. Curve 1 is the straight line used for the main part of the study. Curve 2 corresponds to slightly weaker interaction; curve 3, to slightly stronger interaction; and curve 4, to no interactions at all.

Figures 24 and 25 show transition locations evaluated using the different criteria for 25-deg sweepback, with suction. ($\lambda = 15$ deg was not evaluated because the low C-F level results in domination by T-S instability, with negligible interaction. Similarly, the
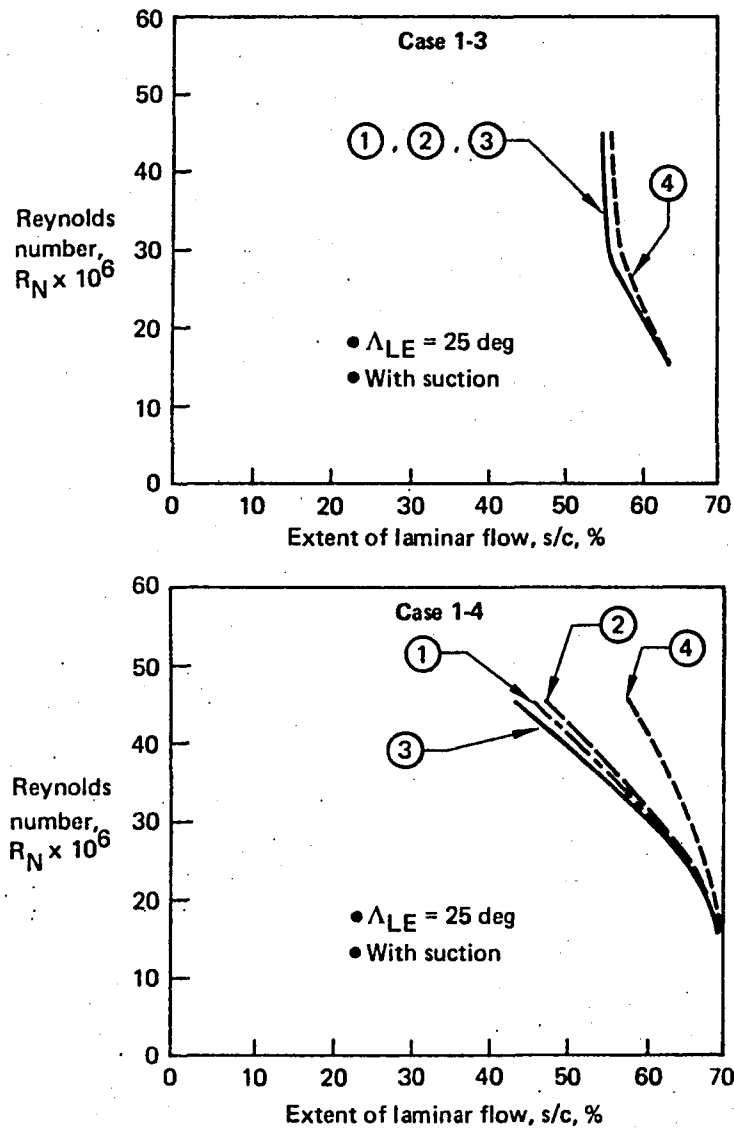
Figure 24. Upper Surface Transition Sensitivity

$\lambda = 25$ deg condition without suction was not of interest because it is strongly dominated by C-F instability near the leading edge.)

For the two flat midchord pressure distributions, cases 1-3 and 4-2, transition is almost unaffected by criterion variations because they do not generate much C-F in the regions not provided with suction and respond almost entirely to T-S instability. Case 1-4 is

41
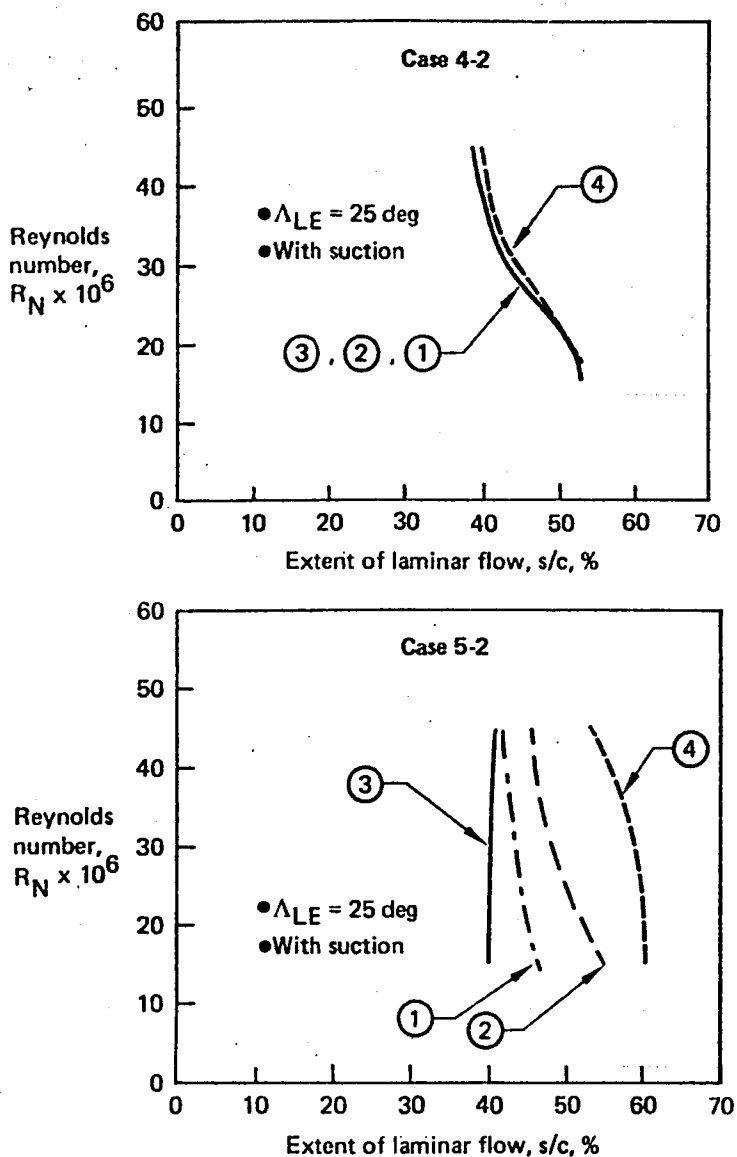
Figure 25. Lower Surface Transition Sensitivity

hardly affected by any variation except the zero-interaction criterion, and then only at high Reynolds number. The unloaded midchord case, 5-2, is the only one showing appreciable sensitivity to small changes in the interaction criterion.

It is therefore reasonable to infer that uncertainty in the transition criterion for combined instability should not affect the conclusions of the present study.

5.1.1.5 Conclusions—Figure 26 shows the sweepback and Reynolds number ranges where these calculations indicate that NLF and HLFC can be expected to operate. (These curves are envelopes of the limiting Reynolds number curves obtained for the various different upper surface pressure distributions.) HLFC greatly increases the size of the airplane where a wing suitable for speeds approaching Mach 0.8 can substantially benefit from skin friction reduction due to laminar flow.

42
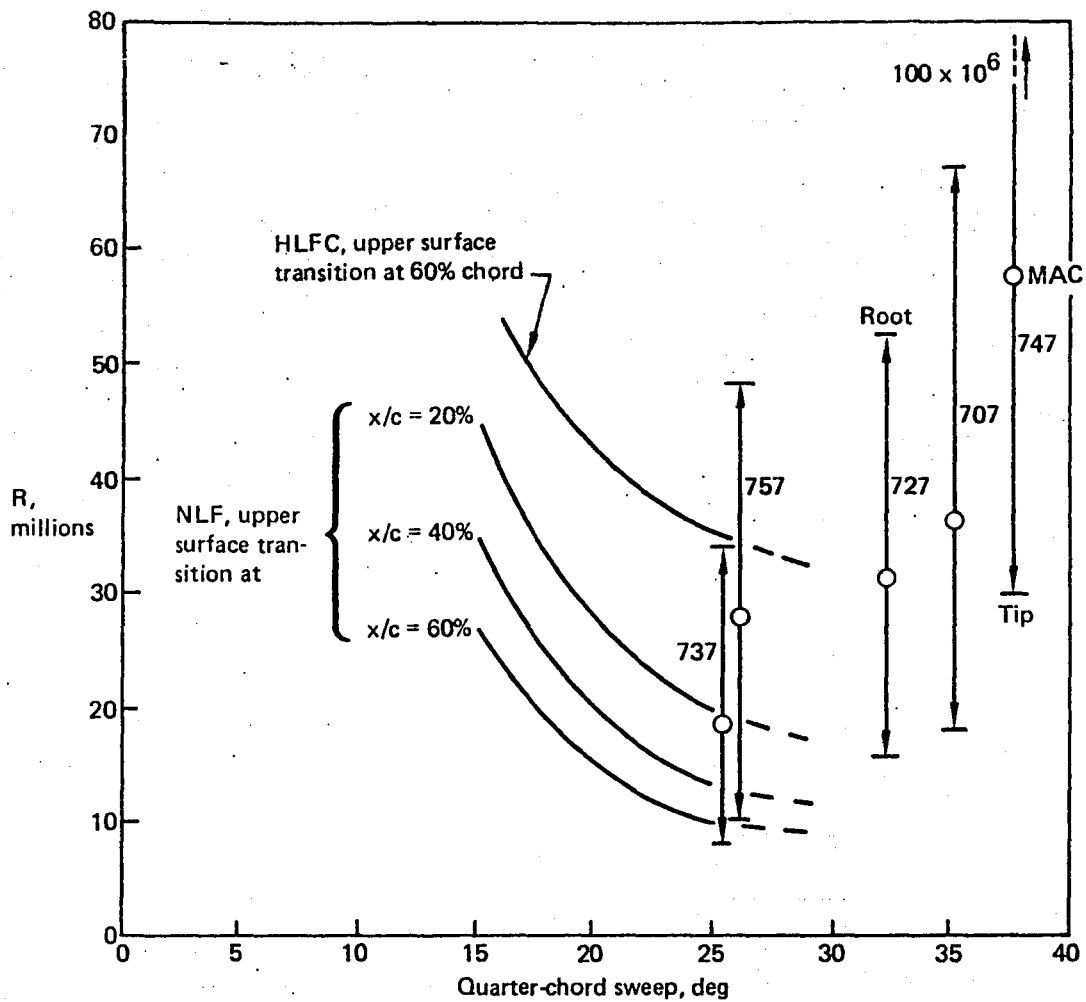
Figure 26. Ranges of Operation of NLF and HLFC

The following comments apply to airfoil pressure distribution features:

• Without suction, steeply favorable midchord gradients on the upper surface are best. With suction, flat or only slightly favorable midchord gradients are best.

• Steep initial gradients result in the most laminar flow without suction and therefore would probably result in lower suction requirements.

• The shape of the midchord pressure distribution (e.g., straight line, convex, and concave) has little effect on the extent of laminar flow without suction. (With suction, this parameter was not analyzed.)

• For pressure distributions with zero midchord gradients, the extent of laminar flow is not sensitive to variations in the shape of the transition criterion curve.

• For pressure distributions with substantial midchord gradients, variations in the shape of the transition criterion curve can result in significant changes in the extent of laminar flow.

5.1.2 Airfoil Selection

Airfoil design goals were: (1) to sustain laminar flow to 55% chord (or more) on the upper

43

surface and to 50% chord on the lower surface with minimum suction quantity and (2) to suffer little or no flow separation or wave drag at Mach 0.8, wing lift coefficient 0.5, and 25-deg quarter-chord sweepback.

As determined by the parametric study in the previous section, a steep initial pressure gradient followed by a flat or weakly favorable region extending to the recovery point will give best HLFC performance by restricting appreciable crossflow to the leading-edge area. Another consideration affecting laminar flow is the nose radius. It should be small to reduce vulnerability to attachment line transition (discussed in sec. 5.2.3.2), but not so small that a slight increase in angle of attack above the design condition will produce a pressure peak.

The desired midchord shape limits the maximum Mach number of the flow and begins the recompression with a weak shock, permitting the second goal to be met. From the recovery point aft, the now-turbulent boundary layer can undergo a smooth subsonic pressure rise without separation.

An airfoil was designed for a typical outboard section at a normal Mach number (M_N) of 0.744, reflecting a sweepback angle of 21.5 deg, corresponding approximately to the 50% chord line outboard. The design lift coefficient (c_{l_N}, based on the normal flow) was 0.64. It also was constrained to a t/c_N of 10.3% to match the 9.6% streamwise t/c of the 757 outboard wing.

The airfoil design process was necessarily iterative. A target pressure distribution was defined to meet the previously discussed requirements. A transonic flow airfoil design computer program was then used to generate the corresponding geometric shape, and a viscous flow computer analysis determined boundary layer displacement thickness. The pressure distributions were adjusted to meet requirements for t/c and to obtain trailing-edge depths consistent with computed boundary layer displacement thickness. The accuracy of the airfoil shape was confirmed using an inviscid flow transonic pressure calculation on the airfoil-plus-boundary layer geometry. Figure 27 shows the pressure distribution and profile so designed.

For the root section, a higher thickness ratio (13%) was required. To keep the same maximum local Mach number on the upper surface, the pressure on the lower surface has to fall, thus reducing c_{l_N}. (Because of the increased chord inboard of the planform break, this was still consistent with smooth and monotonic spanwise loading variation.) Another difference was that maintaining isobar sweepback required shifting the upper surface pressure recovery point forward. Figure 28 illustrates these differences. The design c_{l_N} was 0.40. Note that the resulting profile will not produce this pressure distribution when located close to the fuselage in a real flow. It is only a step in the design of the three-dimensional wing geometry described in the following section.

5.2 WING DEFINITION

5.2.1 Development of Three-Dimensional Geometry

The ground rules of the study required that the planform, thickness, and spanwise lift distribution of the 757-200 baseline airplane be matched by the wing of the HLFC airplane. These constraints are shown in Figure 29.*

---

*The t/c distribution shown in Figure 29 is a simplified approximation to the actual 757 t/c, which varies continuously over the span.

HLFC outboard airfoil at design point
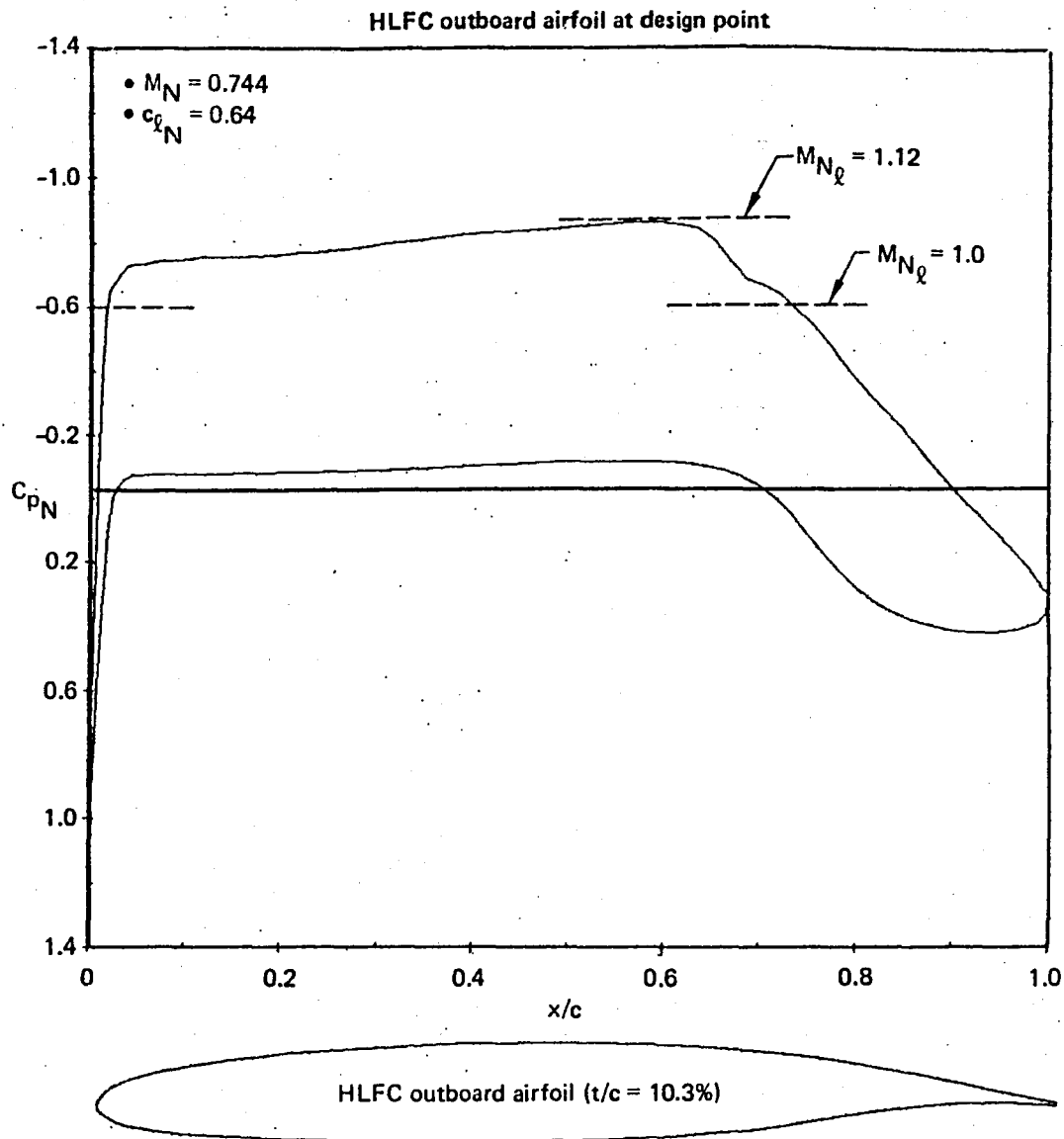
Figure 27. Pressure Distribution and Contour of Outboard Airfoil

To achieve the laminar flow objectives of the design, it also was required that the pressure distributions determined in the previous section (suitably interpolated over the span) should be realized by the three-dimensional wing. Use of computer programs capable of designing swept wings to give specified pressure distributions in transonic flow and in the presence of a fuselage, followed by wind tunnel testing, would be required to develop a final wing design. Experience shows that it is best to begin with a subcritical design. Boeing computer code A236, a linearized theory design/analysis code, was used for this initial design. When applied in the manner described below, the subcritical design will be very close to the final wing geometry. For purposes of the present study, the expense of a transonic analysis was not justified. The shape presented here is defined well enough to ensure the validity of the airplane design and weight analysis presented in section 6.0.

45
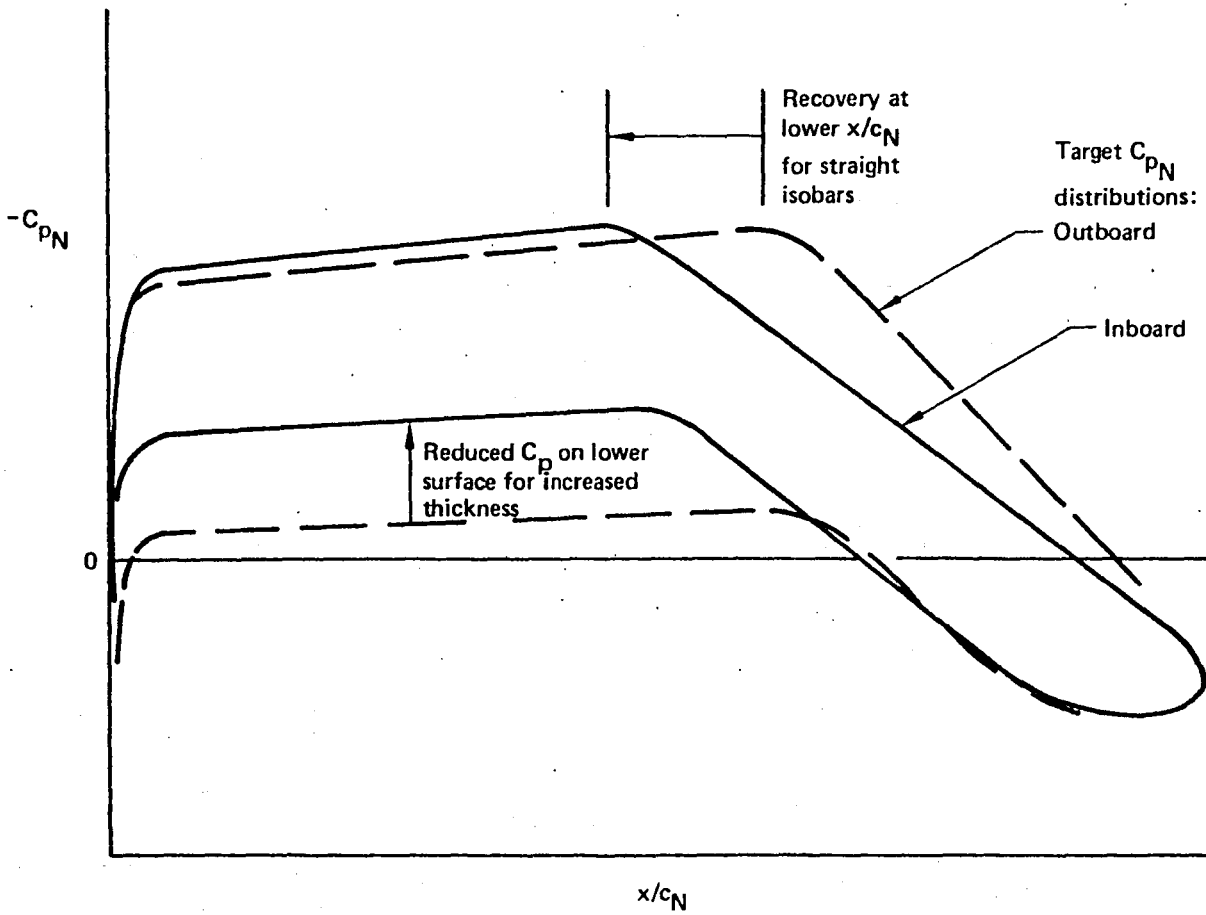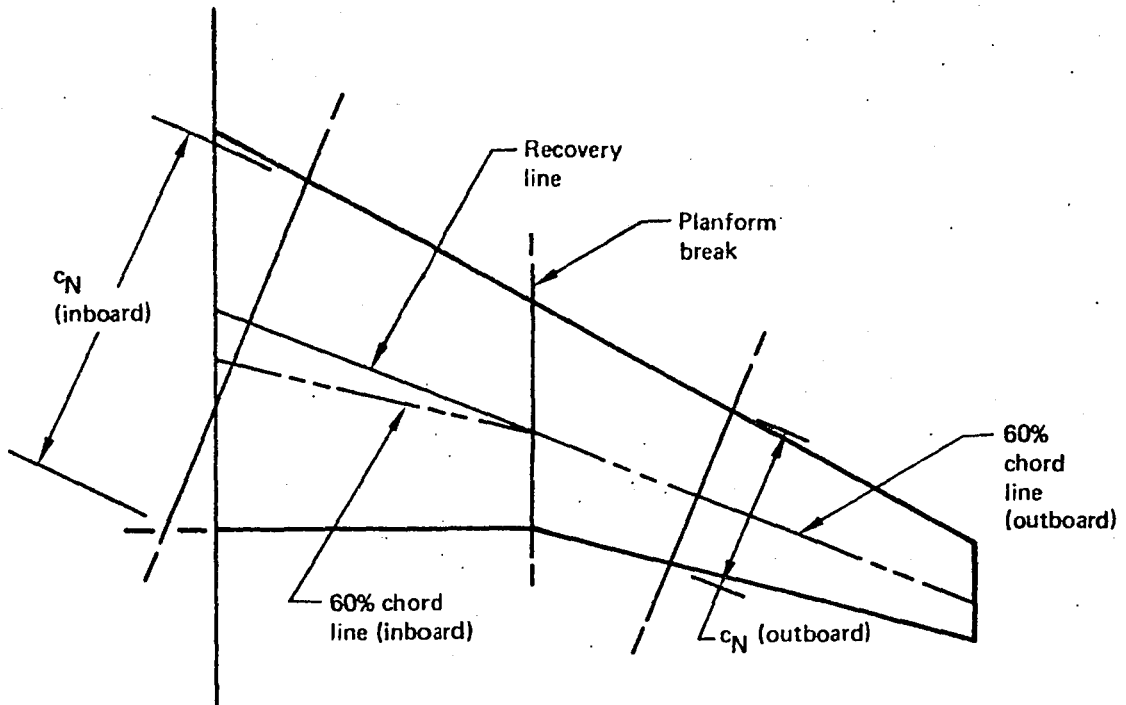
Figure 28. *Inboard Section Pressure Distribution Considerations*

46

Planform

Side
of
body

Plane
of
symmetry

Loading

c_ℓ
or
$\dfrac{cc_\ell}{\overline{c}}$

1.0

0.8

$\dfrac{cc_\ell}{\overline{c}}$

c_ℓ

0.6

0.4

0.2

0

Thickness ratio

Streamwise
t/c, %

16

15.0

14

13.0

12

11.6

10

9.6

9.6

8

0

0   0.2   0.4   0.6   0.8   1.0

Span station, η
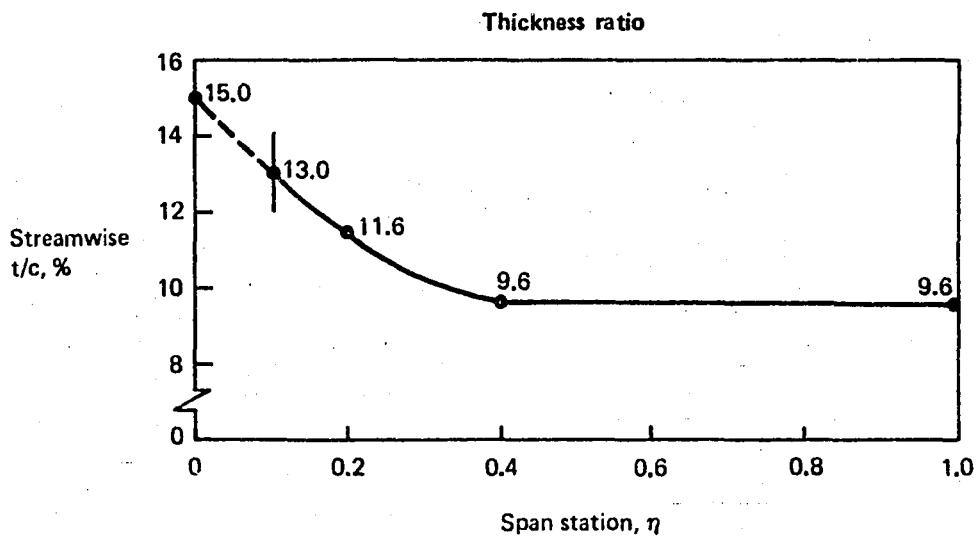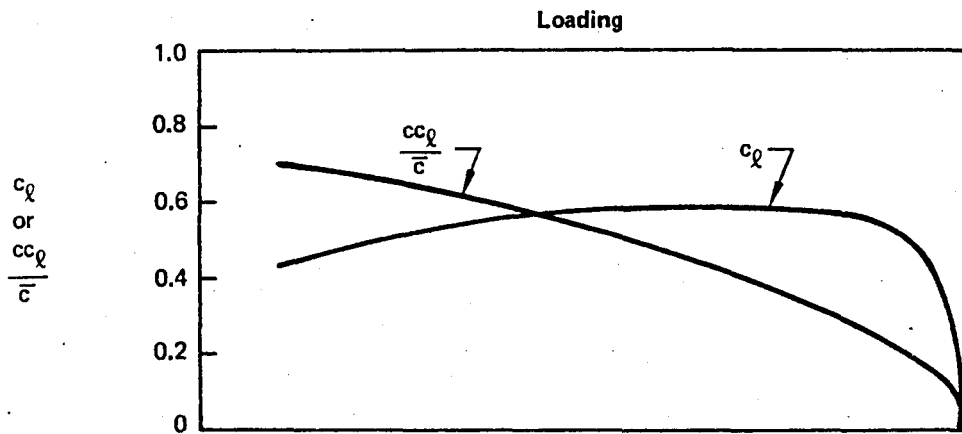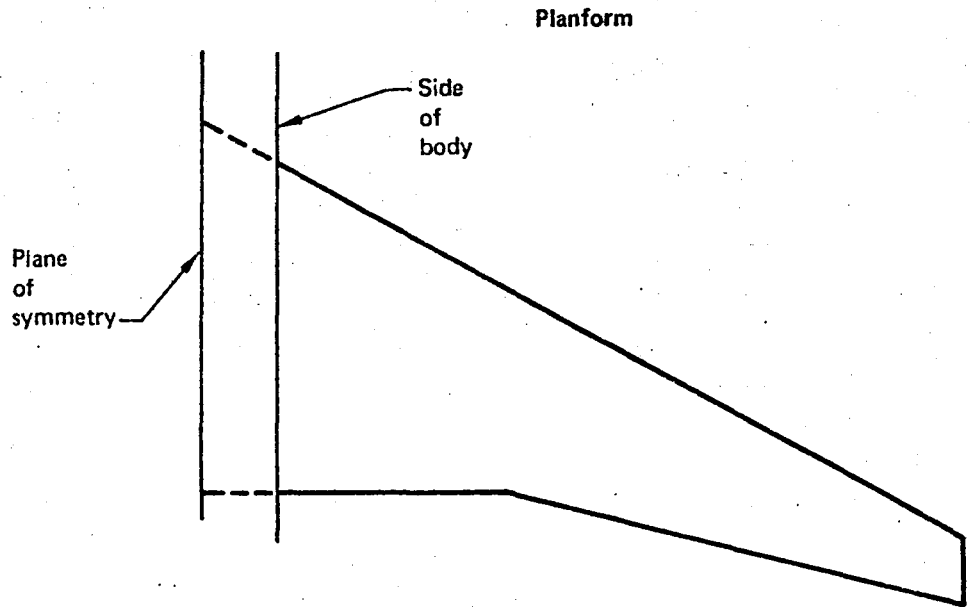
Figure 29. Design Constraints for Three-Dimensional Wing

47

To get good results from a subcritical design code such as A236, the target pressure distribution also must be subcritical. Subcritical pressures for the airfoil of section 5.1.2 were used to define the target pressures. Figure 30 indicates how the subcritical pressures typically differ from the pressures at the design Mach number. Note that the subcritical upper surface C_p distribution has a peak near the nose and an adverse gradient back to the recovery point. The lower surface has an increased favorable gradient.

Despite the simplification afforded by use of a subcritical analysis, it still was necessary to design the wing iteratively. A set of prescribed pressure distributions generally will not meet the required spanwise thickness variation, and in some cases may result in a physically meaningless wing description. The process actually followed was to define an initial geometry using the two-dimensional outboard airfoil and to develop the inboard section with modifications to the two-dimensional root airfoil based on the designer's judgment. Intermediate profiles were interpolated to meet the thickness constraint. Subcritical pressure distributions corresponding to that geometry were then computed by
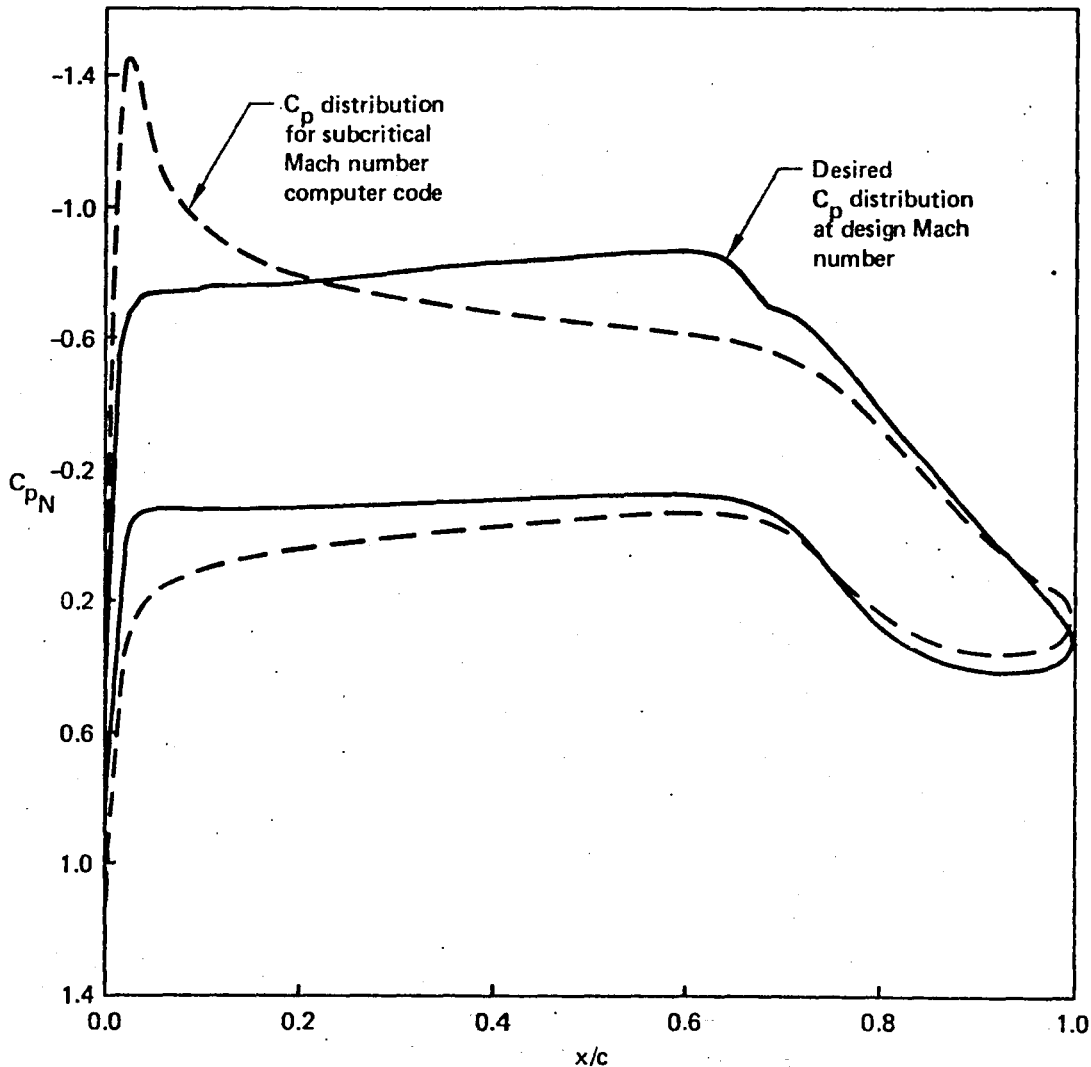
Figure 30. Modifications to Target Pressure Distribution for Subcritical Three-Dimensional Computer Code

48

A236. These pressure distributions were then adjusted to approximate the desired subcritical shapes, and A236 was used to design a set of wing sections plus a twist distribution that gave the required spanwise lift variation.

Figure 31 shows three streamwise cross sections of the resulting three-dimensional wing. From the planform break outboard, the airfoil is the one shown for WBL 299. It is the same as the two-dimensional outboard section (fig. 27) stretched out to reflect the streamwise cut. The root (WBL 72) airfoil differs from the outboard section. In addition to having greater thickness ratio, it has perceptible inverse camber near the leading edge and a lower surface with reduced aft loading. The middle airfoil, at WBL 173.7, illustrates a transition shape in the part of the wing where t/c is decreasing.

WRP

WBL 72 ($\eta = 0.096$) t/c = 13.0%

WRP

WBL 173.7 ($\eta = 0.232$) t/c = 11.3%

WRP

WBL 299 ($\eta = 0.400$) t/c = 9.6%

0.0   0.2   0.4   x/c   0.6   0.8   1.0
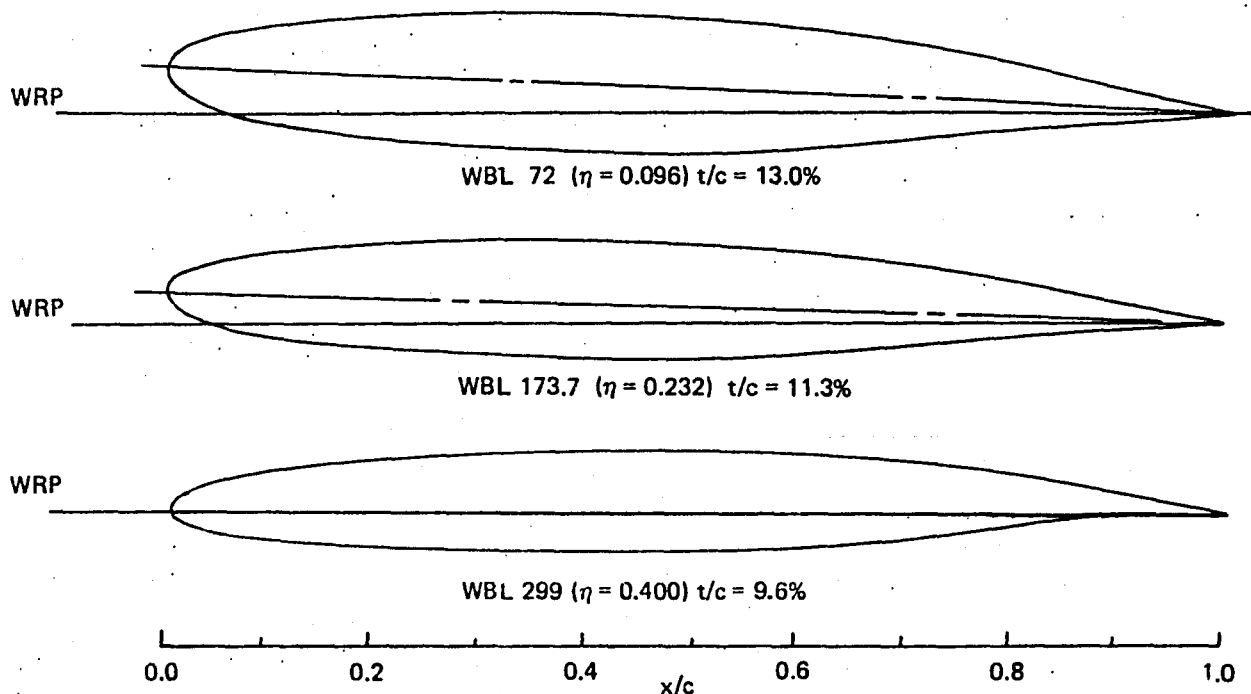
Figure 31. Streamwise Wing Sections

The computed twist distribution, Figure 32, produced a spanwise loading in close agreement with the loading shown in Figure 29.

The subcritical isobar pattern, (fig. 33), computed by A236 from the final geometry, shows satisfactory behavior (no loss of sweepback) in the regions of the wing where supersonic flow at the design Mach number would require it. The pressure distributions implied by these isobars have the subcritical form shown in Figure 30, and therefore do not show the nearly flat, weakly favorable gradients required for satisfactory HLFC performance.

5.2.2 Special Design Considerations

5.2.2.1 Off-Design Operation—Practical use of HLFC requires that laminar flow be maintained through a range of cruise lift coefficients and Mach numbers. Changes in lift coefficient and Mach number will change the wing pressure distributions from the optimum and may result in some loss of laminar flow. Therefore, the use of a trailing-
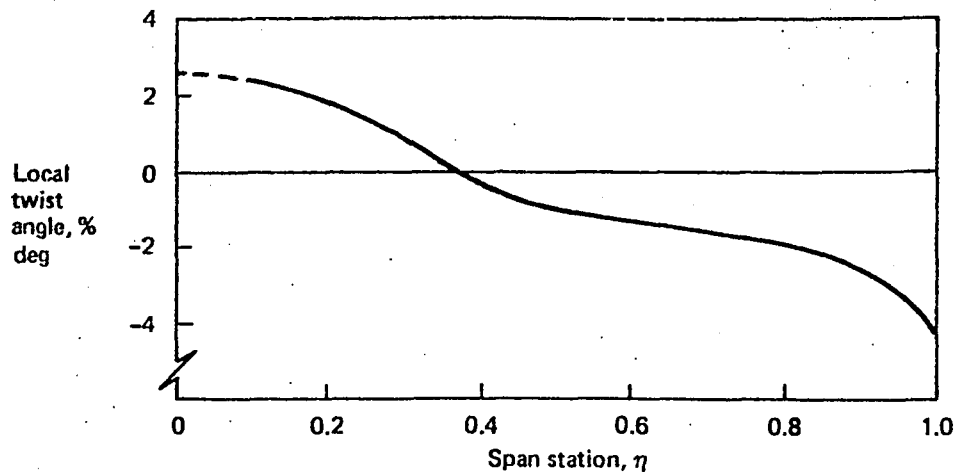
Figure 32. Wing Twist Distribution

edge cruise flap, as proposed earlier by W. Pfenninger (ref. 8) was studied. Deflection of the cruise flap permits controlling the pressure distribution over the forward part of the airfoil, keeping it similar to the design pressure distribution even when the lift coefficient and Mach number differ considerably from the design values. The specific objectives of the study were to determine the behavior of the pressure distributions during the climb and cruise off-design conditions and to define the ranges of M and C_L where laminar flow can be maintained. It was found that the desired pressure gradient control could be achieved not only during cruise, but also during a significant portion of climb and descent.

In this study, deflections of the trailing edge aft of 90% chord were considered. For analysis purposes, pressures were computed using profiles with smoothly deflected trailing edges (as opposed to profiles having abrupt slope changes at the hinge lines.) Figure 34 shows the original airfoil deflected ± 10 deg. Deflections of up to 10 deg during climb and 2 deg during cruise were considered.

Program A423, a Boeing version of the Garabedian-Korn transonic airfoil analysis, including boundary layer effects (ref. 15), was used to analyze both the climb and cruise off-design conditions. The boundary layer transition is assumed at 5% chord for climb series and at 60% chord for cruise. The Reynolds numbers for the airfoil were based on the chord at the planform break. Table 3 shows the climb conditions for which the airfoil was analyzed. Table 4 gives the cruise conditions that were examined.

Figure 35 shows the effect of a typical deflection on the pressure distribution during a climb case. As shown, the basic airfoil has a strong adverse pressure gradient at the chosen flight conditions, but a 5-deg deflection of the trailing edge restores the desired pressure characteristics.

Figure 36 shows the pressure distributions that occur in climb. The two pressure distributions at each altitude correspond to the deflected and undeflected cases. A 10-deg flap deflection is sufficient to suppress the leading-edge pressure peak above 7620m (25 000 ft). (It is estimated, however, that some benefits of laminar flow will be achieved as low as 3048m [10 000 ft]. This point is discussed in sec. 5.2.5.)

Figure 37 shows the pressure distributions at the design Mach number at three lift coefficients corresponding to altitudes of 9144m, 10 668m, and 11 125m (30 000, 35 000,

Upper surface

C_p
-1.0
-0.8
-0.7
-0.65
-0.6
-0.575

-0.55
-0.50
-0.40
-0.20
0

Lower surface

C_p
0.4
0.1
0.08
0.025
0
-0.02
-0.04
-0.06
-0.08
-0.10
-0.12

-0.12
-0.10
-0.08
-0.06
0
0.2
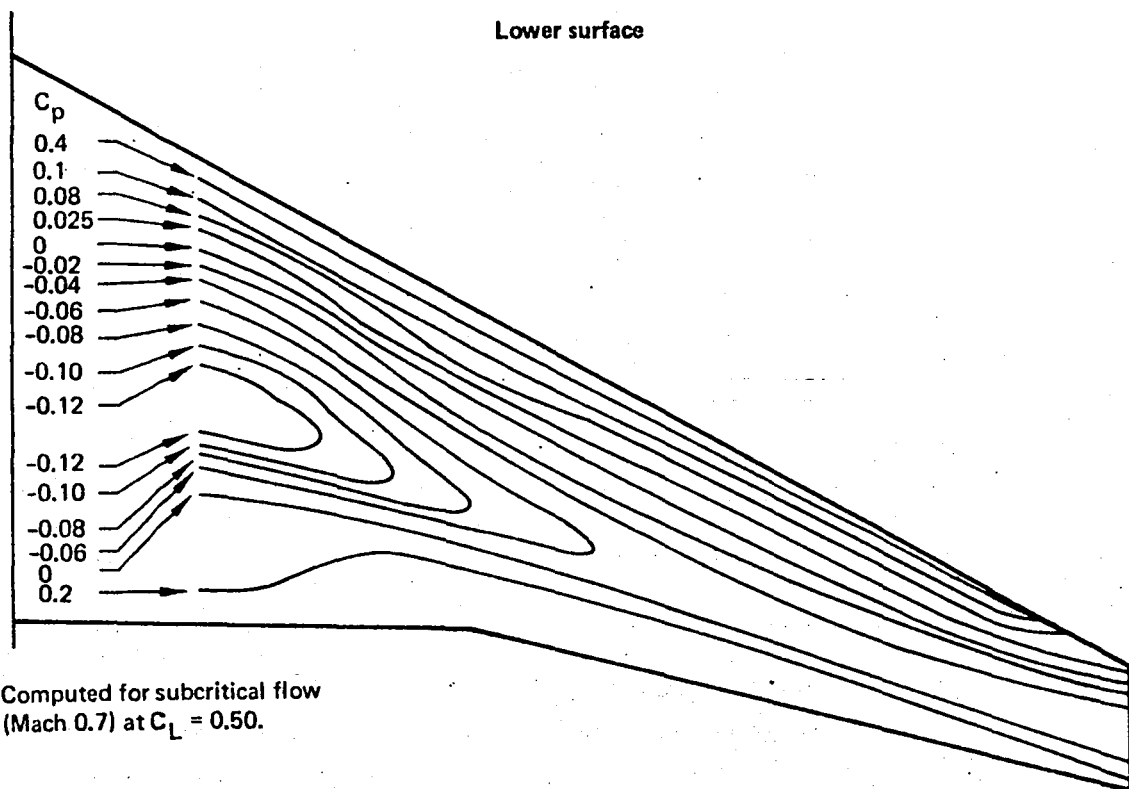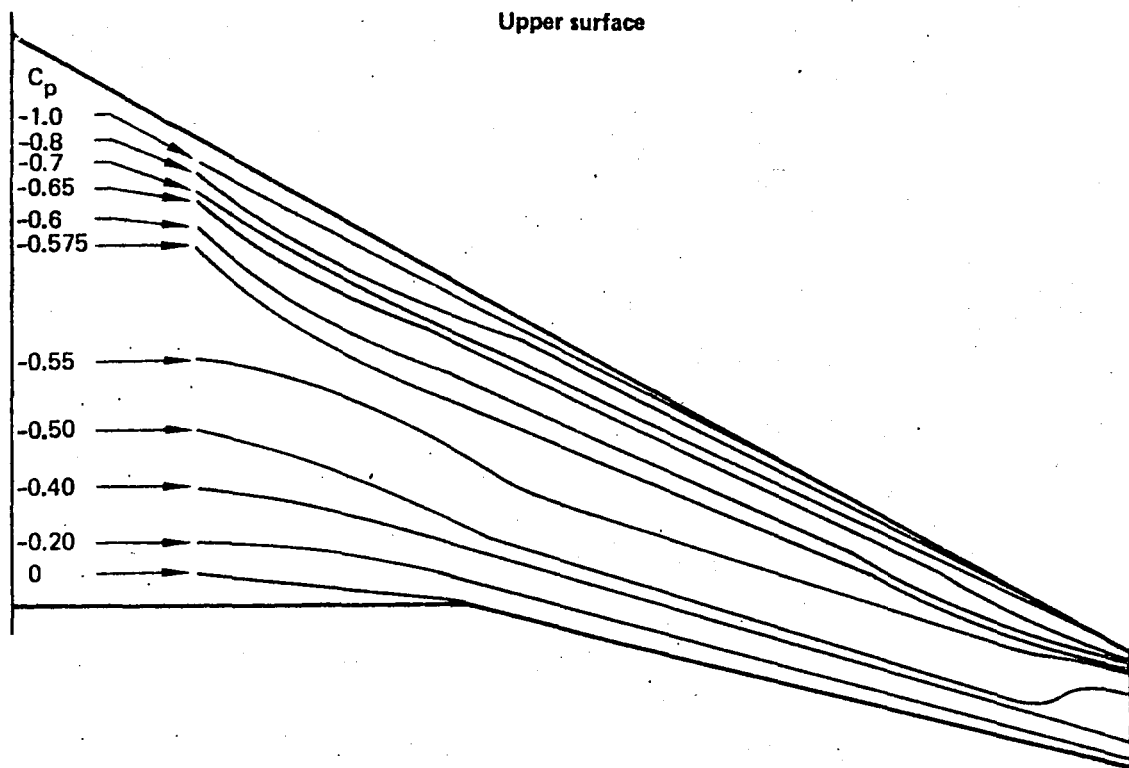
Note: Computed for subcritical flow
(Mach 0.7) at C_L = 0.50.

Figure 33. Wing Isobars at Design Cruise C_L
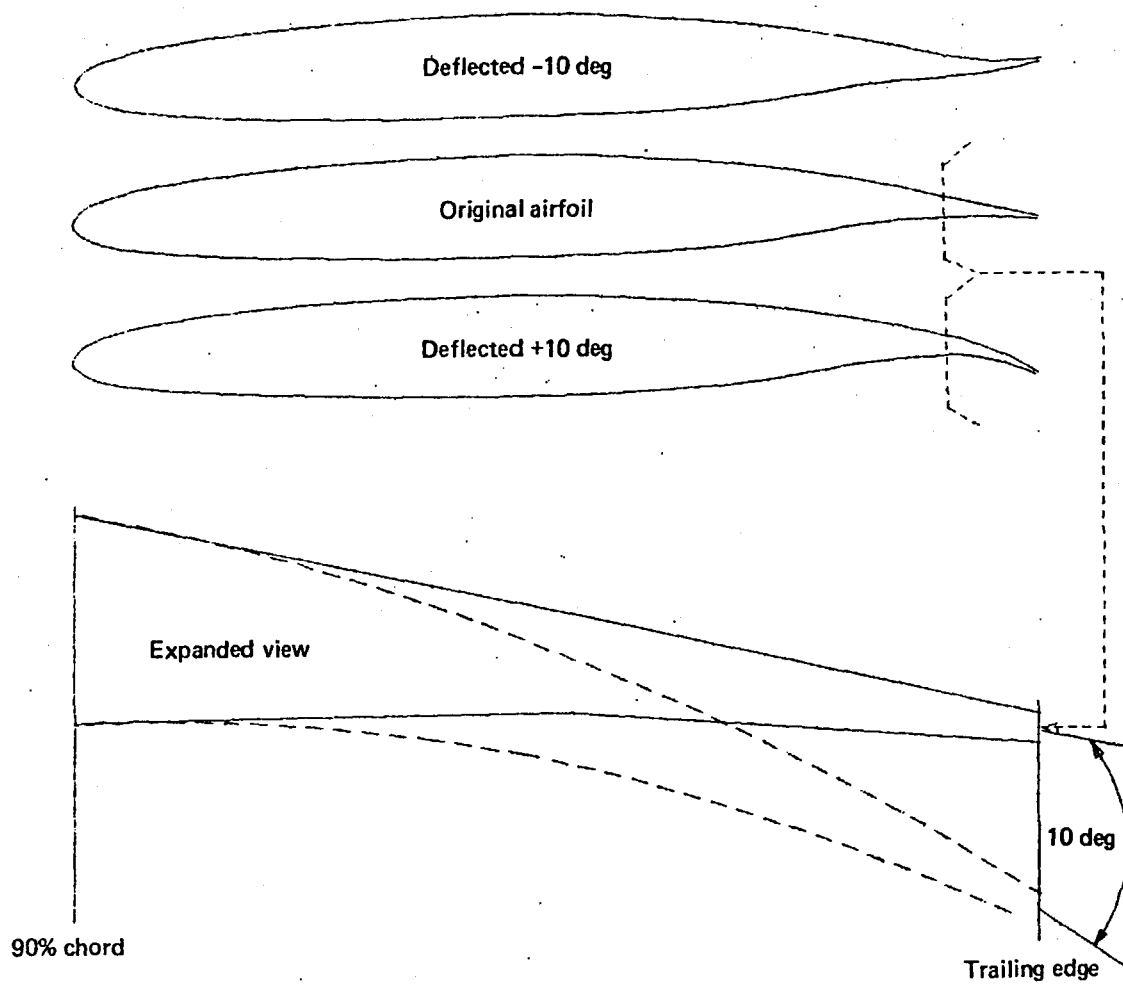
Figure 34. HLFC Airfoil With Deflected Trailing Edge

Table 3. Climb Conditions Analyzed

Condition number	Altitude m	(ft)	R_N	M	M_N	c_ℓ	c_{ℓ_N}
1	3 048	(10 000)	29.6×10^6	0.40	0.370	0.68	0.89
2	6 096	(20 000)	28.8×10^6	0.52	0.480	0.60	0.79
3	9 144	(30 000)	30.8×10^6	0.70	0.650	0.51	0.67
4	10 668	(35 000)	27.0×10^6	0.80	0.744	0.49	0.65

Table 4. Cruise Conditions Analyzed

Type of cruise	R_N	M	M_N	Altitude m	(ft)	c_ℓ	c_{ℓ_N}
Design cruise	31.5×10^6	0.80	0.744*	9 144	(30 000)	0.38	0.50
	27.0×10^6			10 668	(35 000)	0.49*	0.64*
	25.2×10^6			11 125	(36 500)	0.52	0.69
Low-speed cruise	30.8×10^6	0.78	0.725	9 144	(30 000)	0.38	0.50
	26.5×10^6			10 668	(35 000)	0.49	0.64
	24.8×10^6			11 125	(36 500)	0.52	0.69
High-speed cruise	32.1×10^6	0.81	0.753	9 144	(30 000)	0.38	0.50
	27.3×10^6			10 668	(35 000)	0.49	0.64
	25.5×10^6			11 125	(36 500)	0.52	0.69

*Design point.
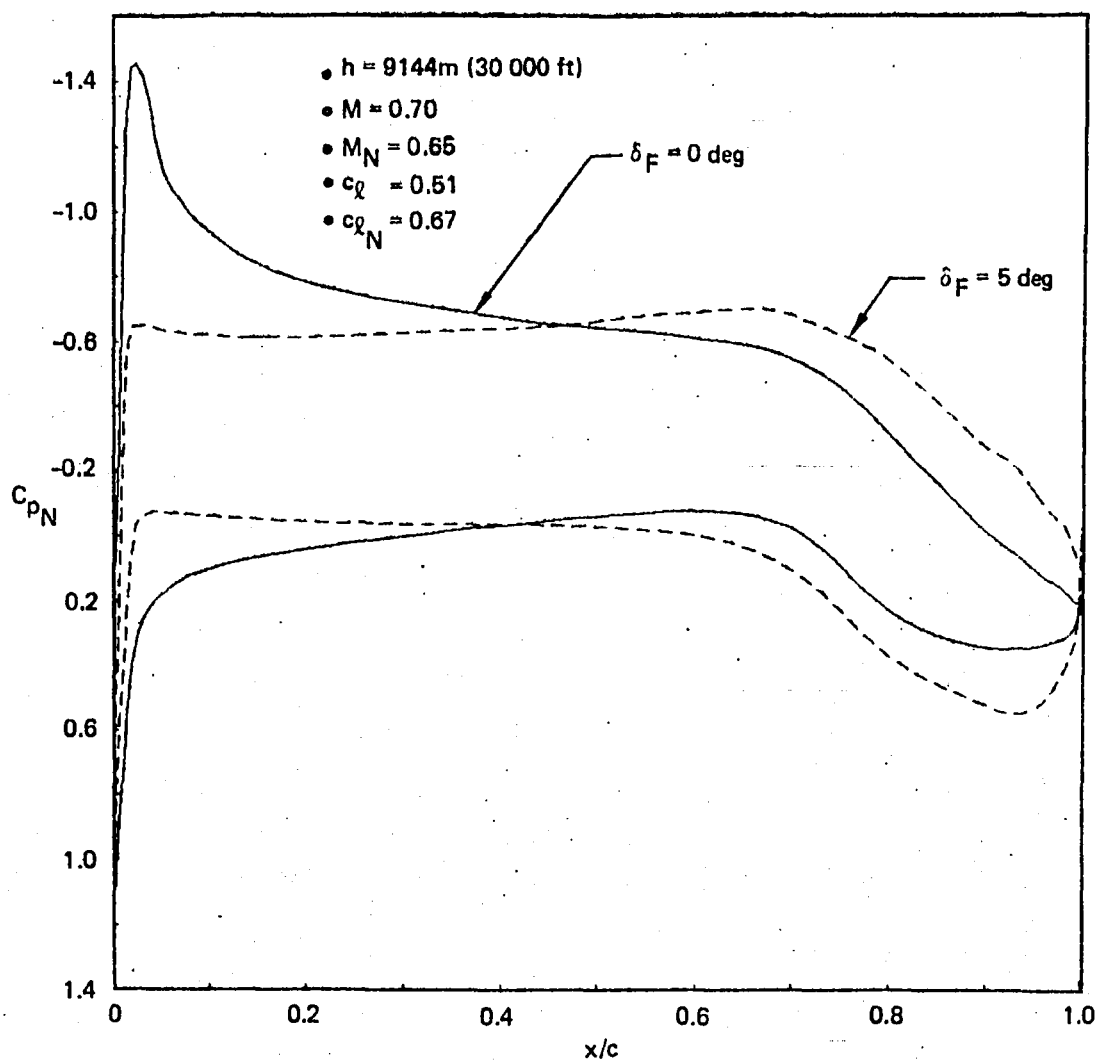
Figure 35. Effect of Cruise Flap Deflection on Pressure Distributions

53
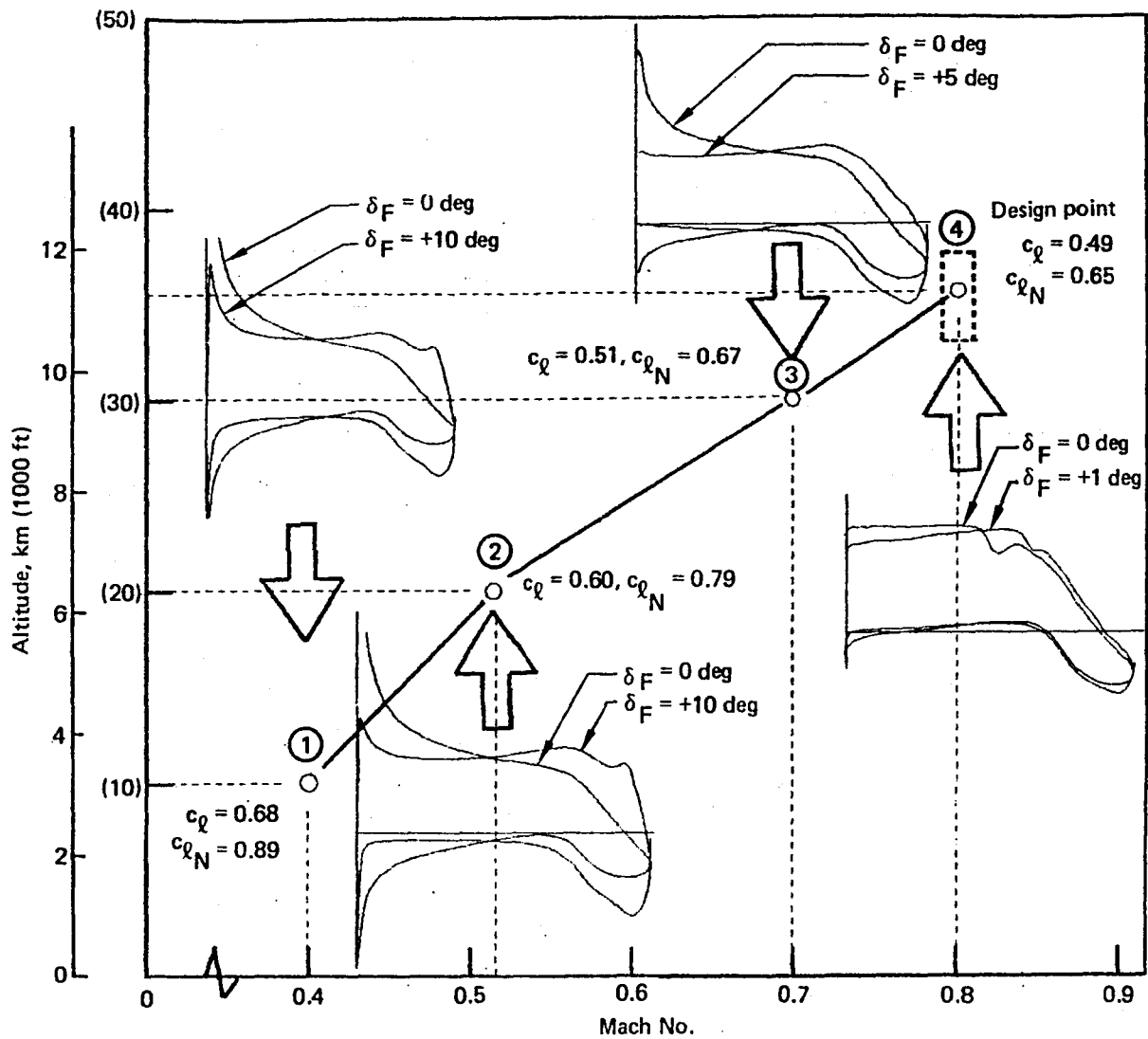
Figure 36. Pressure Distributions in Climb

Figure 37. Effect of Cruise Flap at Off-Design Cruise Conditions
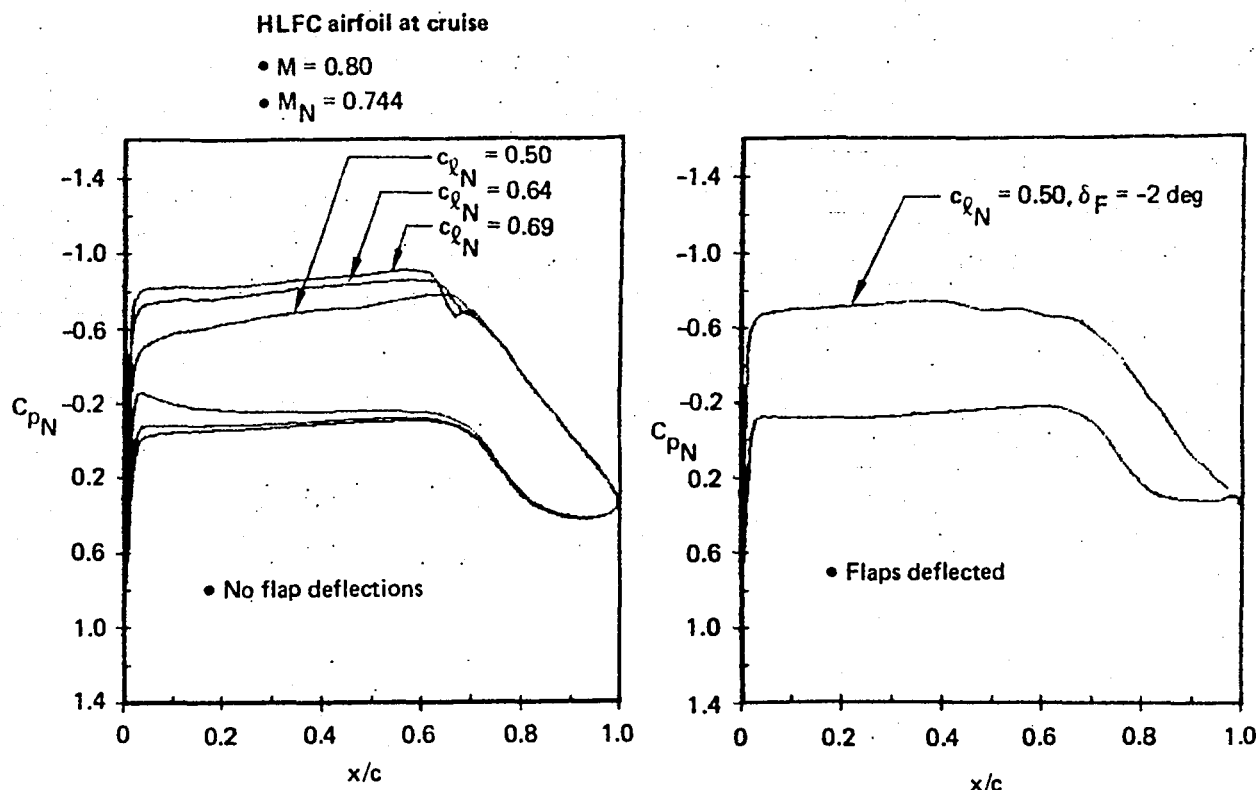
and 36 500 ft). No flap deflections were required at the two higher altitudes. Even for the lowest altitude (off-design C_ℓ = 0.5), a flap deflection of -2 deg restores desirable pressure characteristics on both surfaces.

Figure 38 shows the pressure distributions at the off-design Mach numbers of 0.78 and 0.81 (low-speed and high-speed cruise). A negative (trailing-edge-up) deflection of about 2 deg is required to suppress the pressure gradient at the high-speed cruise condition. For the low-speed cruise case, an angle from -1 to +2 deg is required.

It is concluded that a cruise flap can provide an important degree of operational flexibility in cruise plus added laminar flow capability in climb. It is therefore a significant design feature for HLFC airplanes.

5.2.2.2 Prevention of Attachment Line Transition—In addition to the Tollmien-Schlichting and crossflow instabilities previously discussed, there is a third mechanism that can cause premature boundary layer transition. It arises at the leading edge of sweptback wings, where the local flow is outward along the attachment line rather than across the wing. This flow develops its own boundary layer, also susceptible to transition. If the attachment line boundary layer becomes turbulent, laminar flow is lost over the downstream regions as well.

Attachment line transition caused the loss of laminar flow over all but the far outboard wing in the early flights of the X-21 LFC airplane. Subsequently, it was shown that leading-edge transition depends on the attachment line boundary layer momentum thickness Reynolds number, $R_{\theta_a\ell}$ and on the magnitude of disturbance present. For very low disturbance levels, $R_{\theta_a\ell}$ can be as large as 200 or higher, but if disturbances are present, $R_{\theta_a\ell}$ must be 100 or less to maintain laminar attachment line flow.

55

Figure 38. *Pressure Distributions at Off-Design Cruise Mach Number*

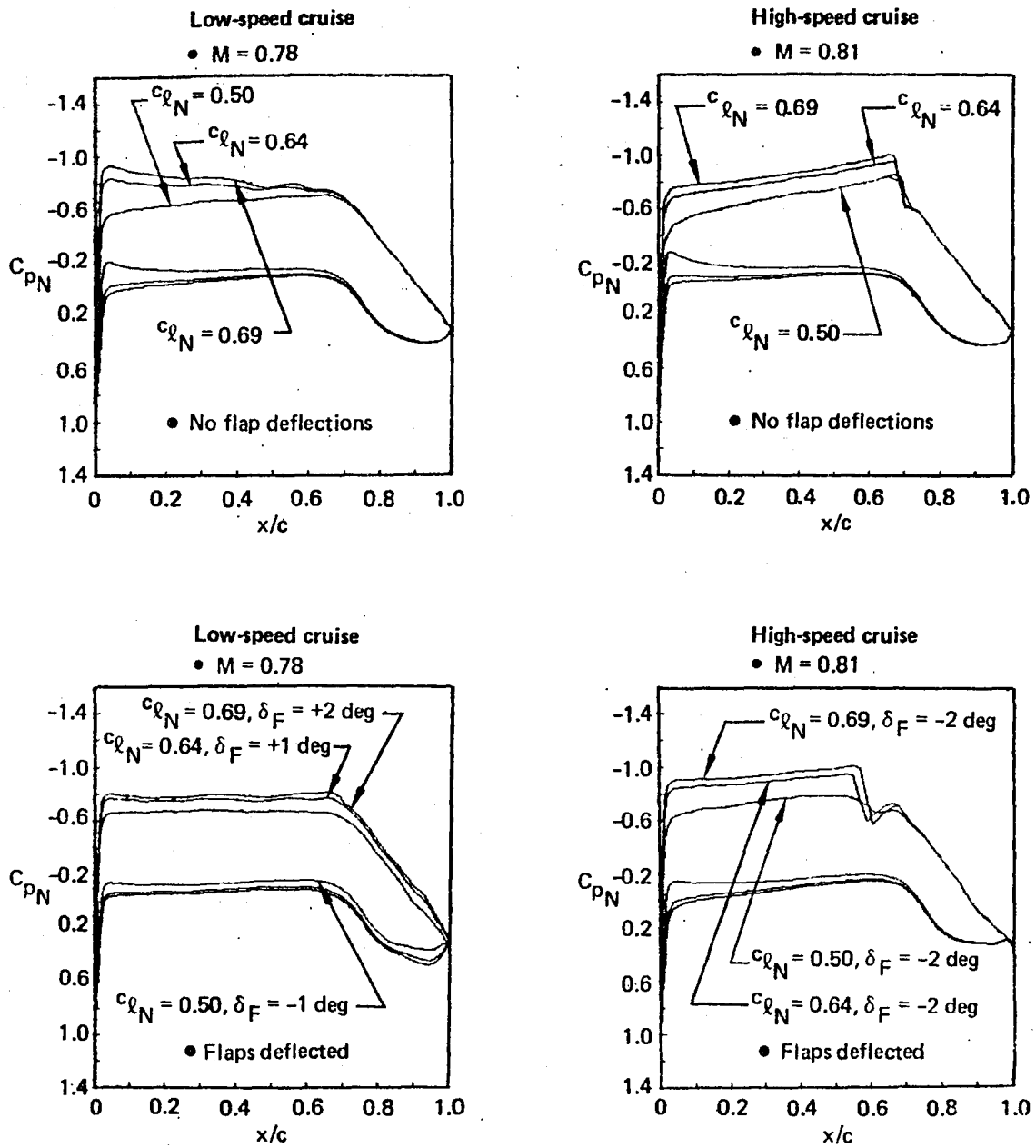Figure 39 shows how $R_{\theta a \ell}$ is defined and gives an approximate formula based on section geometry that can be used if the normal velocity gradient, dU_e/ds, is not known. Because $R_{\theta a \ell}$ is proportional to the square root of the leading-edge radius, one way to prevent attachment line transition is to use a relatively sharp-nosed airfoil. The leading-edge design, however, is constrained by the requirement for operating over a reasonable angle-of-attack range without a pressure peak on either surface. Suction can also be used to thin the attachment-line boundary layer; $R_{\theta a \ell}$ can then be reduced to any desired value independently of the leading-edge radius.

For the current wing, $R_{\theta a \ell}$ was determined using the exact formula, where the initial velocity gradient (dU_e/ds) was evaluated from transonic flow computations performed for the root airfoil section and for the outboard wing airfoil section. Figure 40 shows the initial velocity gradients. For the root airfoil, the initial gradient is less steep than for the outboard airfoil. This implies higher values of $R_{\theta a \ell}$ and greater susceptibility to attachment-line transition. $R_{\theta a \ell}$ was calculated for three spanwise locations and several altitudes as shown in Figure 41. On the outboard wing, $R_{\theta a \ell}$ is always below 1000. On the inboard wing, $R_{\theta a \ell}$ is in the intermediate range and some method of either controlling $R_{\theta a \ell}$ or preventing disturbances will probably be necessary. In any case, it is desirable to reduce $R_{\theta a \ell}$, because the sensitivity to unpredictable disturbances such as insect contamination is reduced.

Initial tests on the X-21 showed that fuselage boundary layer turbulence caused attachment line transition near the wing root, which then propagated outward along the leading edge. Near the wingtip, however, laminar flow was maintained because $R_{\theta a \ell}$ had fallen below the critical value (approximately 100). Later, several inboard wing modifications were demonstrated that prevented contamination of attachment line flow and/or excessive disturbance growth leading to premature transition. One of these was a fence near the wing root to isolate the fuselage boundary layer. Although the fence (especially with suction) effectively prevented leading-edge contamination, it was also necessary to reduce the leading-edge radius inboard on the wing in order to prevent attachment line transition. A short chordwise extension with smaller leading-edge radius was applied in an extended spanwise region substantially reducing $R_{\theta a \ell}$. Thus the critical disturbances were effectively damped and the entire attachment line remained laminar. (A related approach would be to use an undercut airfoil shape, as proposed by Pfenninger [ref. 8] and shown in fig. 42.) Another alternative, also shown to be effective, was boundary-layer suction applied to the leading edge to maintain $R_{\theta a \ell}$ below the critical value.

In the X-21 LFC airplane program, several approaches were tried to prevent attachment-line transition. The most effective was the application of suction in the leading-edge region through chordwise slots to control the spanwise growth of the attachment line-boundary layer. Another was the revision of the airfoil contour near the leading edge, which provided a reduced nose-radius and increased the initial velocity gradient. A related approach would be to use an undercut airfoil shape, as proposed by Pfenninger (ref. 8) and shown in Figure 42.

In the current study, an undercut airfoil was the first method considered for preventing attachment line transition. However, the location of the front spar on the baseline airplane limited the extent of undercut that could be used. When area suction through perforated skin (as opposed to slot suction) was selected, it was found simplest to reduce $R_{\theta a \ell}$ by extending the suction surface to the airfoil nose on the inboard wing.

$$R_{\theta_{a\ell}} = \frac{W\theta_{a\ell}}{\nu} \leqslant 100$$
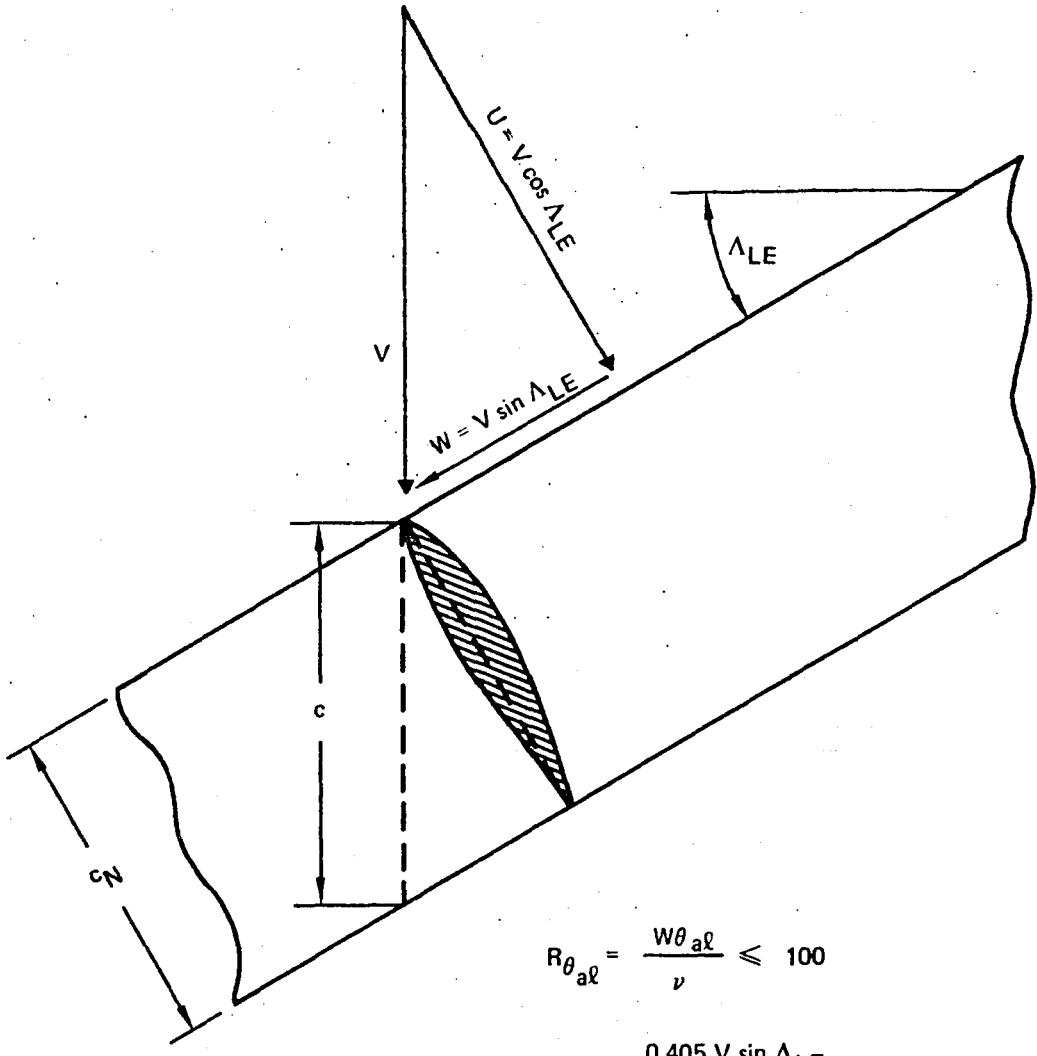
$$R_{\theta_{a\ell}} = \frac{0.405\ V\ \sin \Lambda_{LE}}{\sqrt{\nu\ (dU_e/ds)}}$$

$$\approx 0.405\ \underbrace{\frac{\sin \Lambda_{LE}}{\sqrt{\cos \Lambda_{LE}}}}_{\text{Sweep}}\ \underbrace{\sqrt{R_1}}_{\text{Unit Reynolds No.}}\ \sqrt{\frac{r_0}{1 + \tau}}$$

LE radius

Inscribed ellipse thickness ratio

Figure 39. Attachment Line Transition Criterion

58

- Initial velocity gradient: $\dfrac{dU_e}{ds} = \dfrac{a}{c_N}\left(\dfrac{dM}{ds/c}\right)$

Outboard section, $\eta = 0.4$ to 1.0

Root section, $\eta = 0.10$
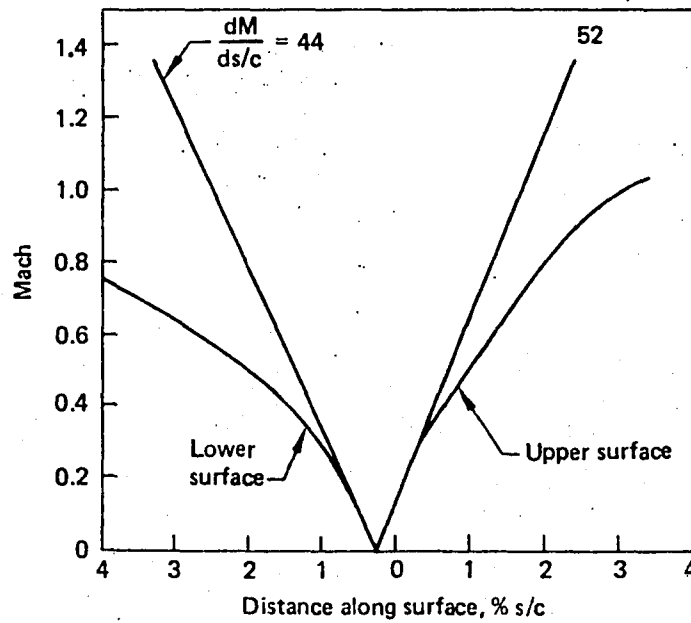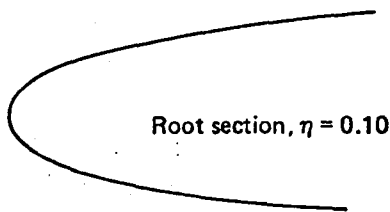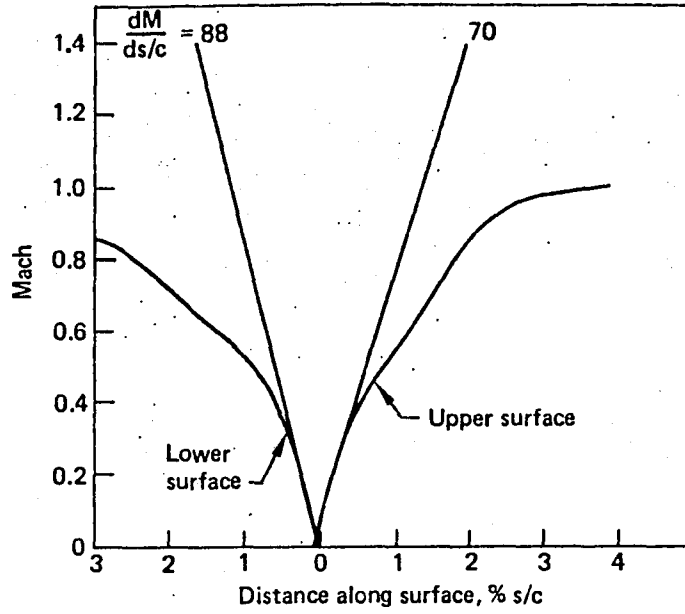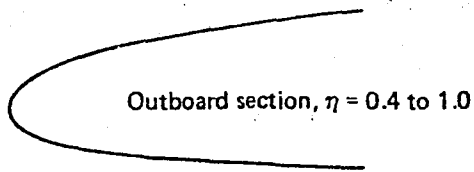
Figure 40. Attachment Line Velocity Gradients

59

$$R_{\theta_{a\ell}} = 0.405 \, \frac{V \sin \Lambda_{LE}}{\sqrt{\nu \, (dU_e/ds)}}$$

Design limit: $R_{\theta_{a\ell}} = 100$

h = 9 144m (30 000 ft)
h = 10 668m (35 000 ft)
h = 11 277m (37 000 ft)
h = 11 887m (39 000 ft)
h = 12 802m (42 000 ft)

● M = 0.80
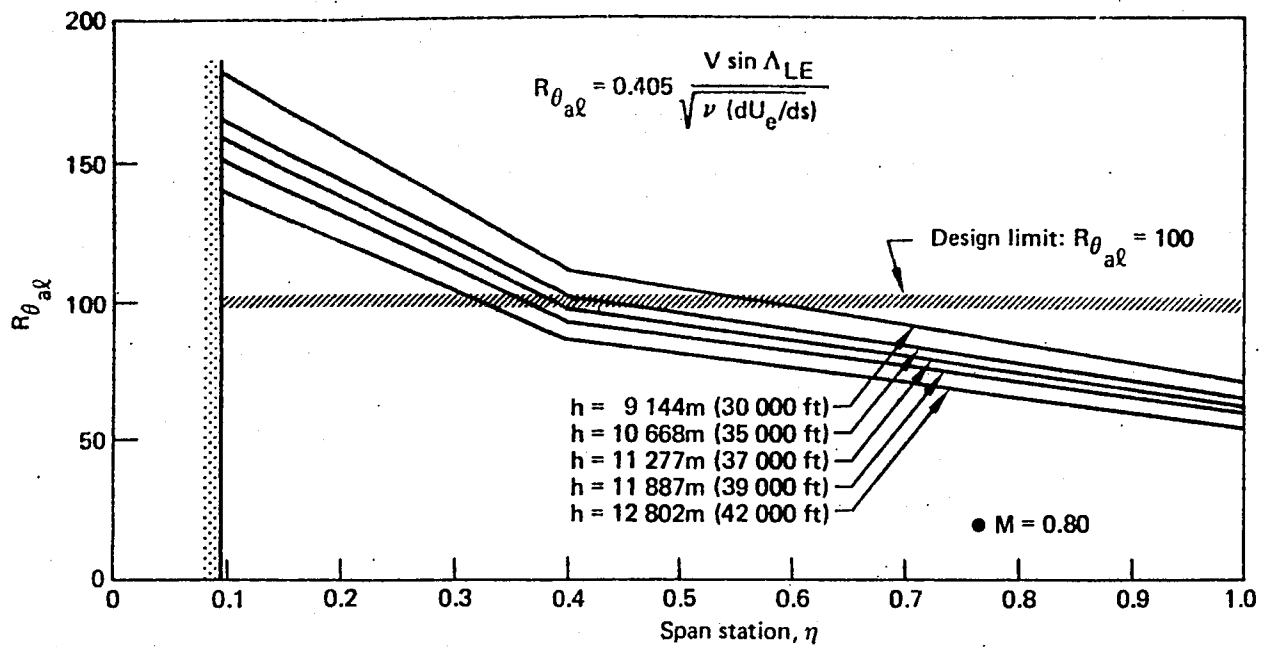
Figure 41. Attachment Line Momentum Thickness Reynolds Number

Original shape

Undercut lower surface

(a) Geometric tailoring of leading edge

(b) Suction at nose
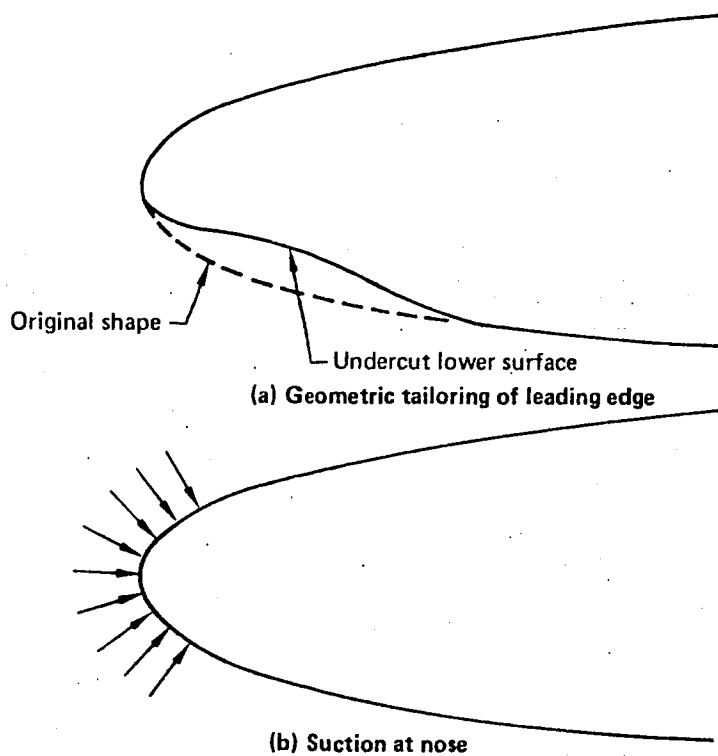
Figure 42. Two Ways to Prevent Attachment Line Transition

60

5.2.2.3 Wing Surface Smoothness Requirements—An HLFC wing will require a smoother surface than a turbulent airplane in terms of both waviness and discontinuities. Guidelines for surface quality were established during the Northrop X-21 LFC research program (ref. 16) using the extensive data base of previous boundary layer research and the results of specific LFC-related experiments. These guidelines are still regarded as valid and have been used in subsequent studies, incuding the present one. The principal results are reproduced here. Typical surface waviness tolerance criteria, developed on the basis of low-speed wind tunnel test results, are shown in Figure 43. The wave amplitude limits shown are applicable to multiple spanwise waves. For chordwise waves, the amplitude limits can be doubled, and for single waves (in either direction), tripled. Criteria for surface roughness and for discontinuities such as steps and gaps are shown in Figure 44.

The above criteria are believed to be representative of areas in which the protuberance height is relatively small in comparison to the boundary layer thickness, which is generally the case over the aft 75% of a chord. However, there is mounting evidence that in the forward region (up to 25% chord), where the boundary layer is relatively thin, more stringent surface-quality requirements are needed, particularly on swept wings where crossflow effects become more significant. In this case, the admissible height of surface protuberances can be determined by empirical criteria. The critical protuberance height is defined as the value at which the transition starts to move forward from its natural (no
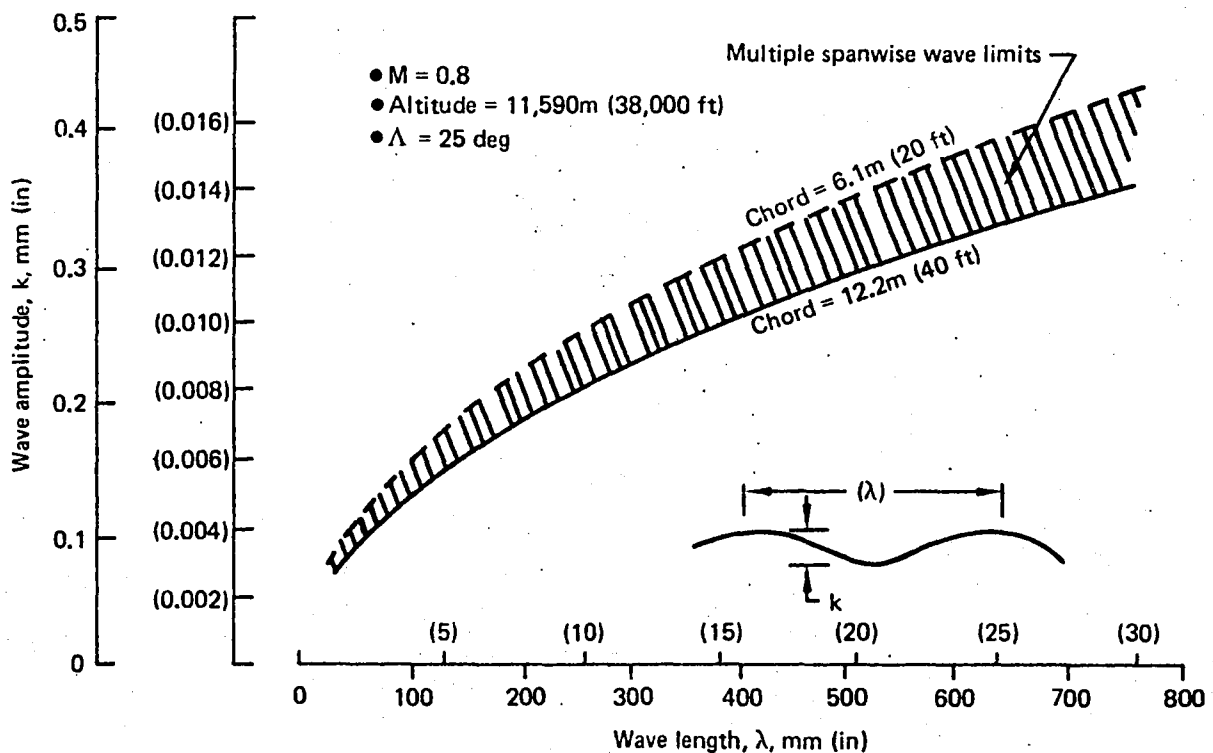
Figure 43. Typical Surface Waviness Criteria for an LFC Wing
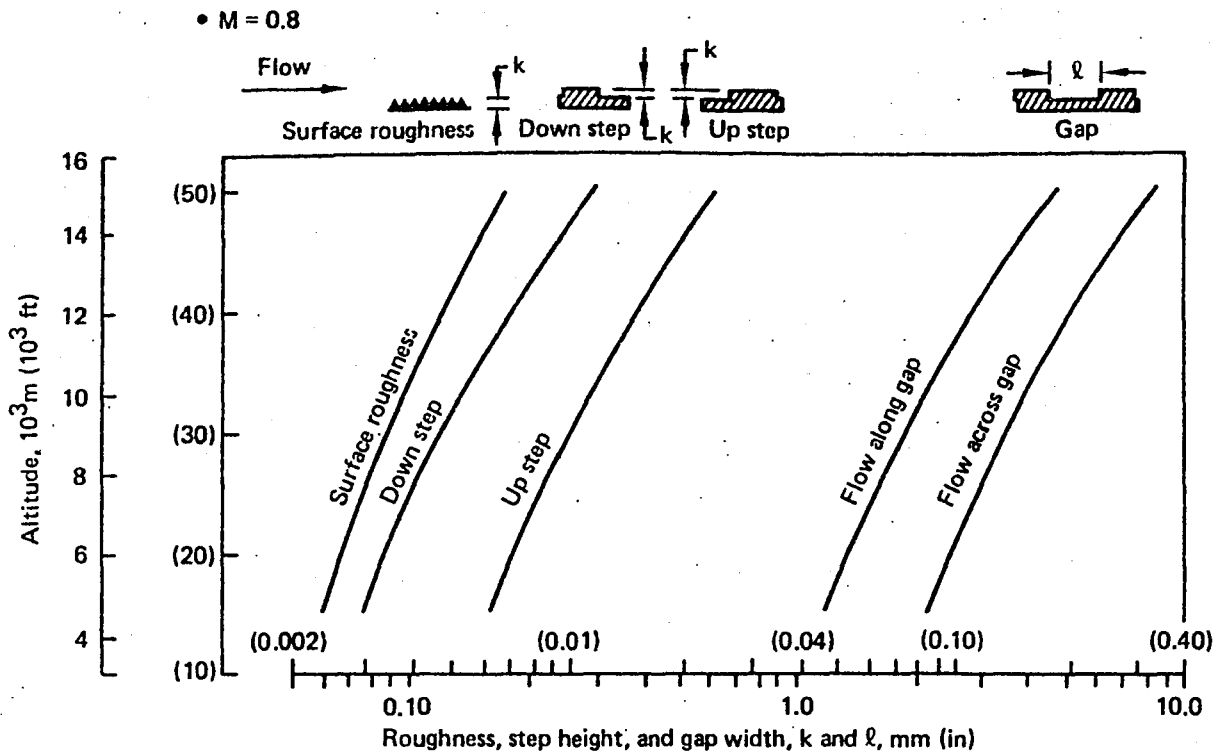
Figure 44. Typical Surface Roughness, Step Height, and Gap Width Criteria for an LFC Wing

protuberance) position. The applicable criteria are expressed in terms of the roughness Reynolds number, defined as

$$R_{k_{crit}} = \frac{U_k \, k_{crit}}{\nu}$$

where k is the height of the protuberance, U_k is the local velocity in the boundary layer at height k, and ν is the kinematic viscosity.

For two-dimensional protuberances, such as steps, grooves, or ridges, the critical roughness Reynolds number ranges between from 100 to 300, depending on the shape (ref. 17). For three-dimensional surfaces, such as rivet heads, dents, or insect contamination, the Reynolds number varies between 200 and 600, again depending on the shape (ref. 18). In the current study, mean values of $R_{k_{crit}}$ = 200 for two-dimensional protuberances, and $R_{k_{crit}}$ = 400 for three-dimensional protuberances were assumed to be applicable.

The calculation scheme is illustrated by an example involving the forward lower surface of the wing for which a detailed study was made to determine the tolerance requirements for a leading-edge device (Krueger flap). Figure 45 shows the calculated boundary layer velocity profiles along the forward lower surface between s/c_N = 1% to s/c_N = 30%. Figure 46 shows R_k as a function of s/c_N for three k values. The R_k curves peak at about s/c_N = 4% indicating that this is the most critical area of the wing with respect to surface

62
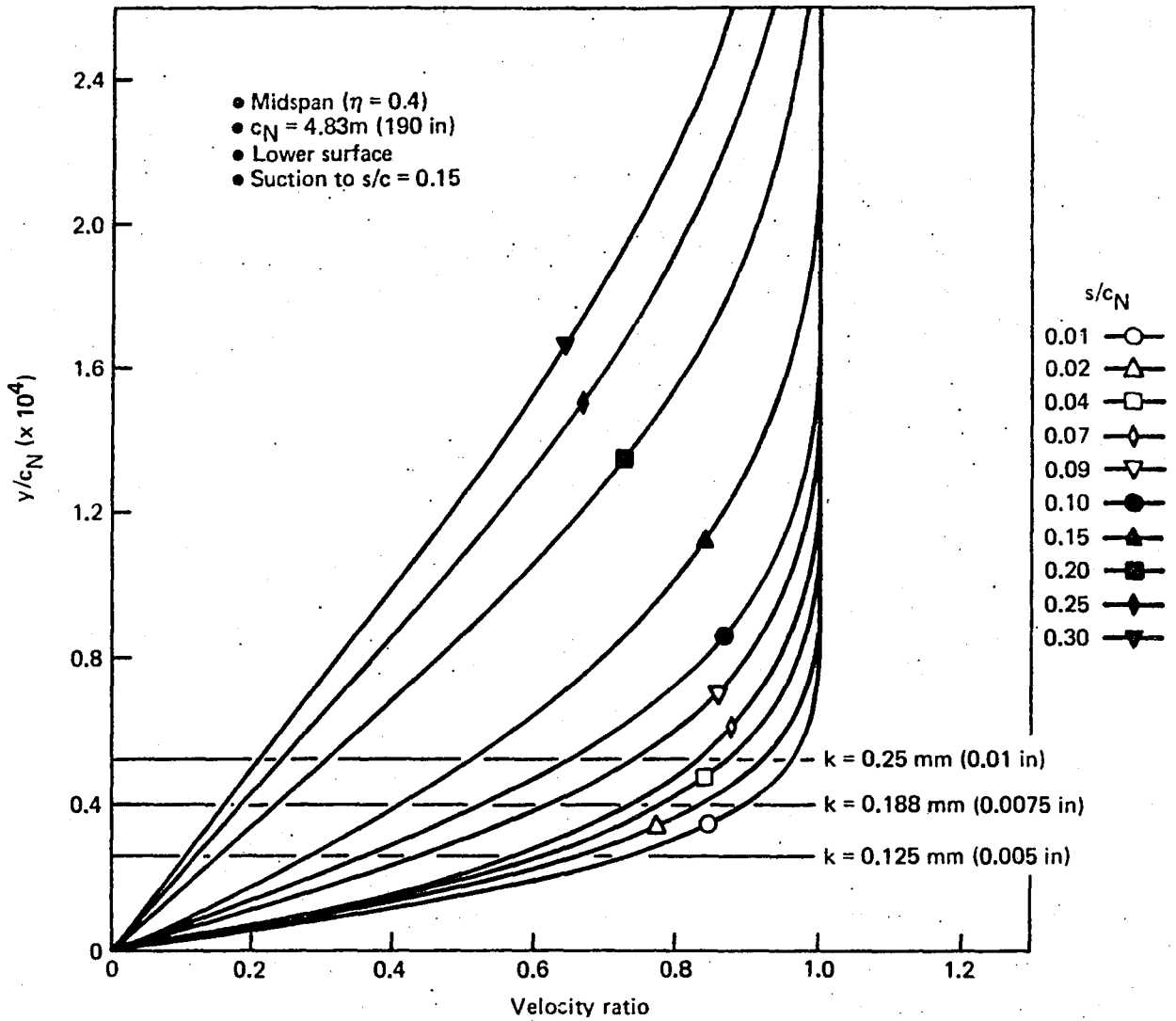
Figure 45. Calculated Boundary Layer Profiles

tolerances. For three-dimensional discontinuities, using $R_{kcrit} = 400$, the critical protuberance height is about 0.1 mm (0.004 in) in the vicinity of $s/c_N = 4\%$, increasing to about 0.25 mm (0.01 in) at $s/c_N = 25\%$. For two-dimensional discontinuities, using $R_{kcrit} = 200$, the corresponding critical protuberance heights are 0.05 mm (0.002 in) at $s/c_N = 4\%$ and 0.19 mm (0.0075 in) at $s/c_N = 25\%$, respectively.

It should be noted, however, that more recent experiments (ref. 19) have indicated that the allowable height of a down-step can be increased by 2 to 2-1/2 times by appropriate suction. This means that the aerodynamic design may compensate to some extent for an unavoidable surface discontinuity by a properly administered suction. If an upper limit of $R_{kcrit} = 1200$ can be attained (also indicated in fig. 46), the surface discontinuities in the critical region of $s/c_N \approx 4\%$ could be as large as 0.22 mm (0.0085 in). Even this requirement would be difficult to meet, however.

63
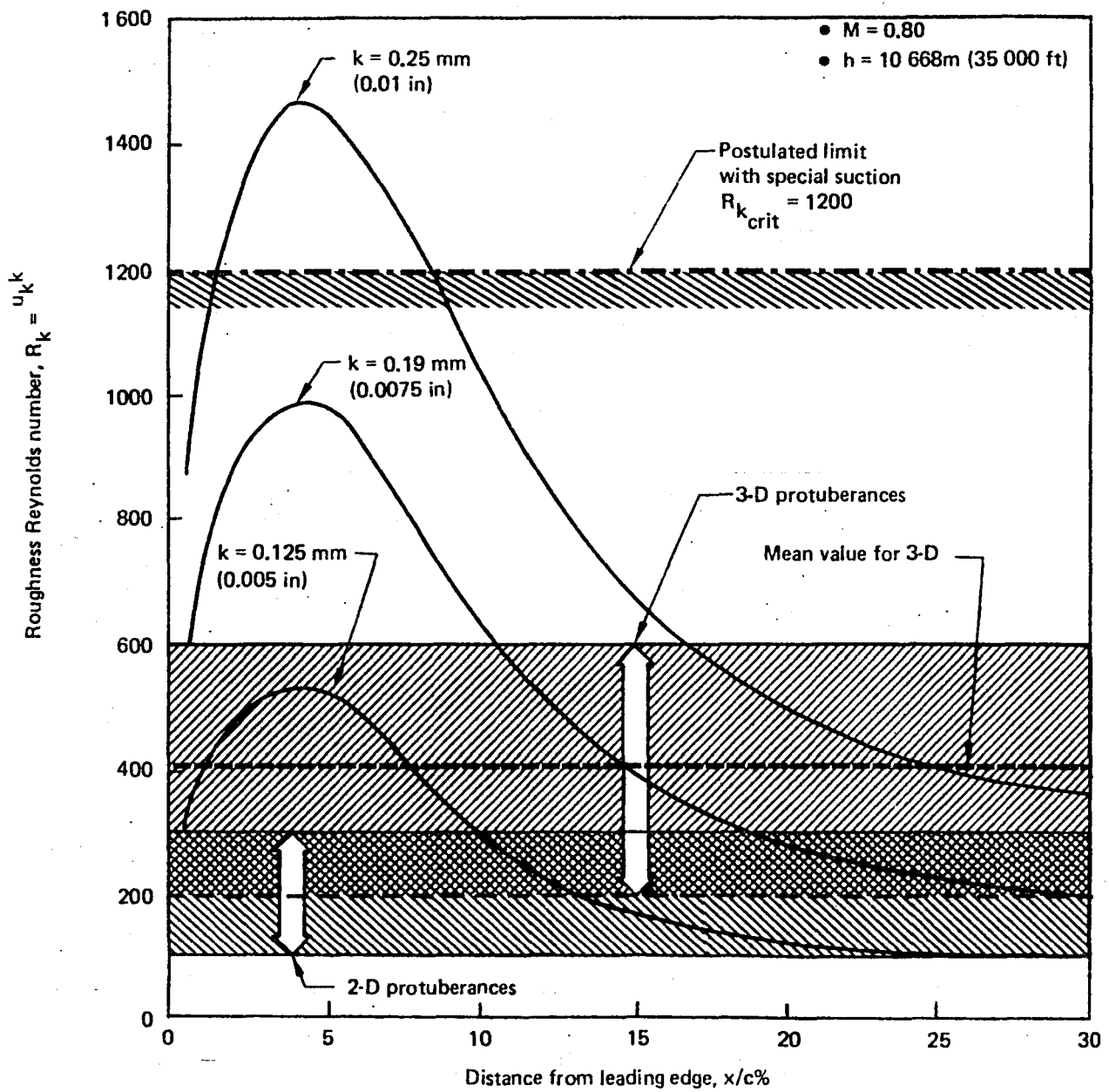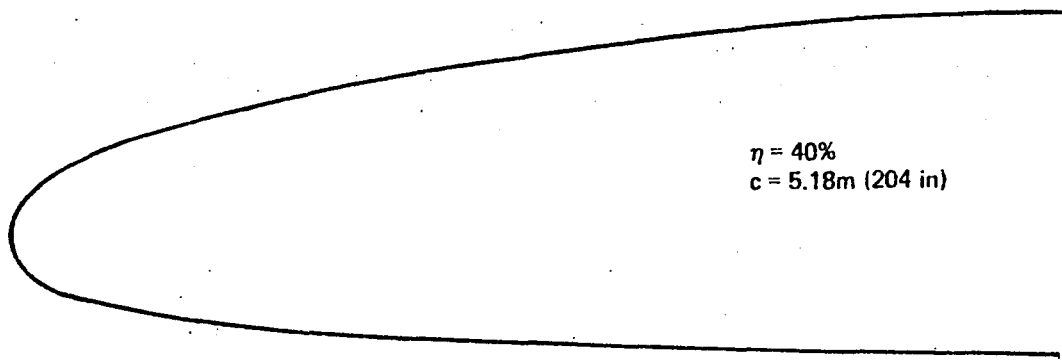
Figure 46. Roughness Reynolds Numbers on Lower Forward Surface

64

These calculations are relevant to the major configuration question of whether or not to use a leading-edge flap to improve low-speed stall performance. The tolerance requirements are too stringent to be met with current technology flap design without locally increased suction. Laminarization of the lower surface behind a Krueger flap would require invention of a scheme to ensure very small discontinuities at the edges of the retracted flap, as well as specifically tailored suction.

5.2.2.4 Leading-Edge Insect Contamination—Insect remains adhering to the leading edge can constitute roughness elements large enough to cause boundary layer transition. Therefore, a device to shield the wing or a system to prevent the impinging insects from sticking probably must be provided. This device or system must be operable whenever the airplane is moving at appreciable speed on the ground and in flight at altitudes to 1500m (5000 ft) above ground level.

Based on the data of reference 18, the critical roughness heights are plotted versus chordwise position in Figure 47 for the representative wing section and the range of critical roughness Reynolds numbers as shown in Figure 46. Figure 47 also shows typical
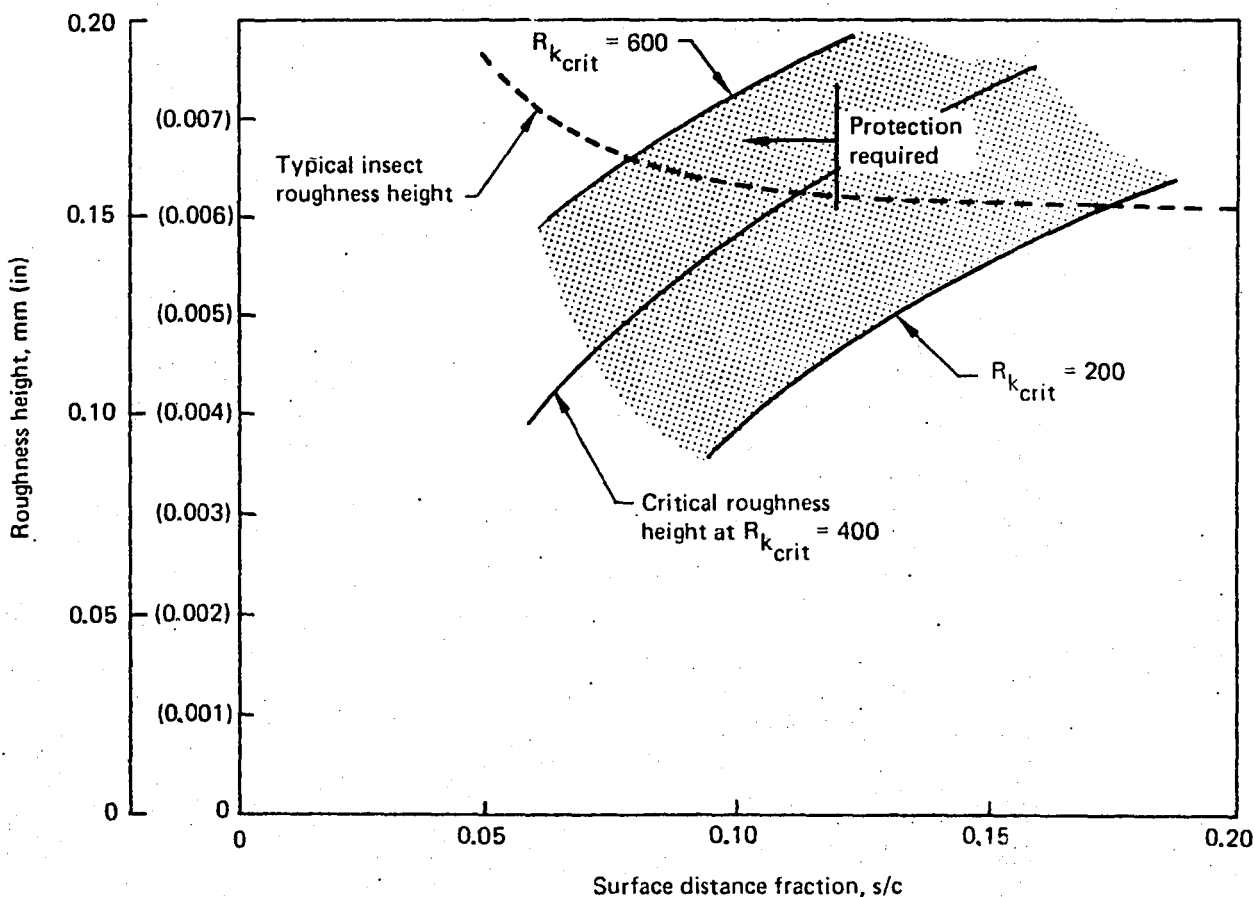
Figure 47 Leading-Edge Cleaning Requirements

roughness heights produced by impinging insects as determined by wind tunnel tests (ref. 20) as a function of chordwise location. A value of 400 for $R_{k_{crit}}$ was selected as the criterion for estimating the extent of chord requiring insect protection. Because the roughness heights corresponding to the selected criterion are below typical insect heights forward of 12% chord, the protection system used should be effective at least back to that point.

Figure 48 shows the Krueger flap used on one configuration considered in the present study and shows the region of the leading edge that it can be expected to shield. (The straight-line trajectories assumed for the insects are probably optimistic for the lower surface and conservative for the upper.) Thus, if the wing lower surface is to be laminarized, a washing system on the leading-edge flap is essential, and washing on other portions of the leading edge cannot be ruled out without detailed analysis and testing.

Details of the proposed insect contamination protection system are discussed in section 6.1.3.2.

5.2.2.5 Acoustic Disturbances—The influence of engine noise on the wing lower surface boundary layer is an area of concern. High-bypass-ratio fans typically radiate frequencies that coincide with the most critical T-S frequencies. These could excite rapidly amplified boundary layer oscillations and cause premature transition at high Reynolds numbers. Acoustic treatment of the engines or increased suction in affected areas may therefore be required. Detailed evaluation of the influence of noise on HLFC was beyond the scope of this study.

Insect impingement during takeoff roll (x/c = 0.02)

Insect impingement during initial climb

Typical limit of critical insect deposits

10 deg

(A) Surface probably requiring protection by washing system (for lower surface laminarization)

(B) Surfaces possibly requiring protection by washing system

Figure 48. Leading-Edge Flap as Protection From Insect Contamination

5.2.3 Suction Requirements

5.2.3.1 Suction Quantity—Suction requirements were determined using the method described in section 5.1.1. The suction distribution was optimized at the root, midspan, and tip at an off-design condition (altitude = 9144m [30 000 ft]).

Because the boundary layer analysis method assumes an infinite yawed wing, a sweepback of 28 deg was used for the leading edge to account for taper. Aft of the quarter chord, 25 deg was used, except at the wing root, where a value of 14 deg reflected the effect of the fuselage in straightening the streamlines.

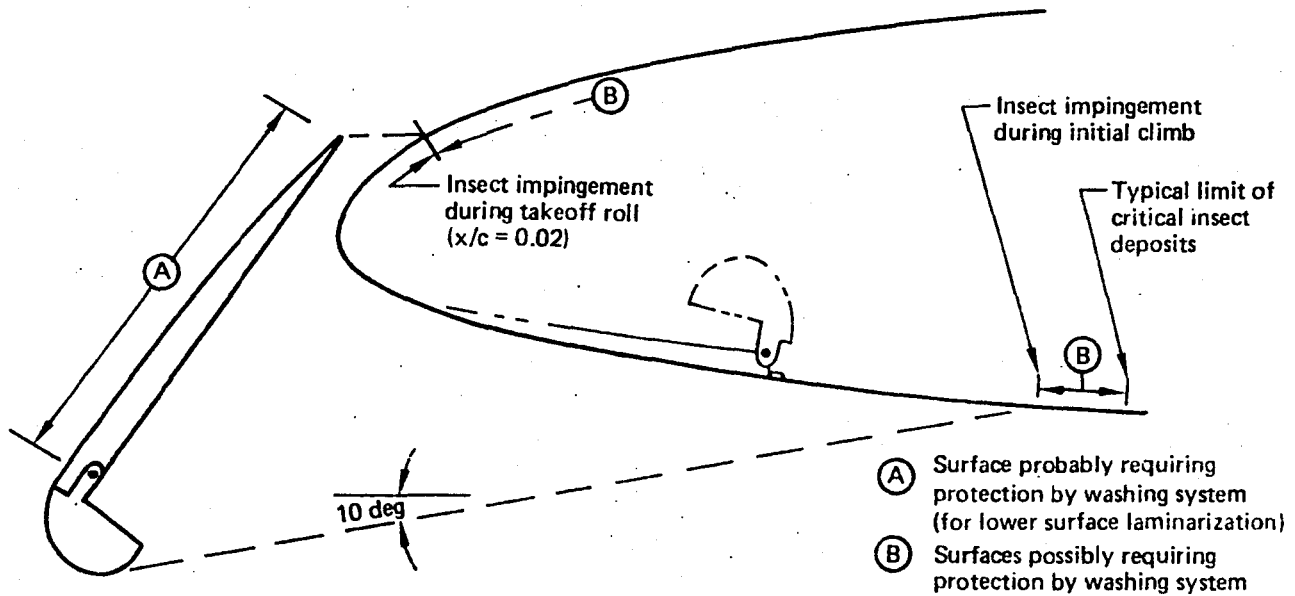Crossflow stability envelopes were computed using the more economical incompressible-flow procedure, and then were reduced by 10% to account for compressibility. (This approximation is supported by refs. 5 and 9.)

The T-S disturbance amplification rates also were first computed incompressibly. Since compressibility effects are more important in the case of T-S disturbances, however, one of the most highly amplified disturbance frequencies also was analyzed compressibly. The ratio of the maximum compressible amplification factor to the maximum incompressible amplification factor (typically about 0.5) for this disturbance then was applied to the entire incompressible disturbance envelope.

Pressure distribution 1-3 was used for the upper surface calculation and 4-2 for the lower surface. These were selected for two reasons: (1) Both distributions were used extensively in the parametric study and several points were available to define the curves. (2) They are similar to the selected pressure distribution in both shape and level. Note that the most inboard is sucked from the nose aft to keep $R_{\theta a \ell}$ below 100.

Figure 49 shows the chordwise suction distributions of the three wing locations. These suction levels and the resulting shapes were determined to maximize laminar flow for the selected airfoils. Each shape has an initial high suction level dropping to a lower level at about 10% s/c. The initial high-level suction damps out the disturbances that would otherwise be amplified in the strong crossflow due to the high negative pressure gradient near the swept leading edge. Aft of 10% s/c, the pressure gradient eases, so that both T-S and crossflow disturbance require less suction. Figure 50 shows the computed transition point as a function of the suction quantity for a midspan section. Pressure distribution 1-3 was used for the upper surface calculations and 4-2 for the lower surface. These were selected for two reasons: (1) Both distributions were used extensively in the parametric study and several points were available to define the curve. (2) They are similar to the selected pressure distributions in both shape and level. The well-defined "knee" in the curve provides an obvious basis for selecting the amount of suction.

The resulting extent of laminar flow is shown in Figures 51 and 52 for Mach 0.8 at 9144m and 10 668m (30 000 ft and 35 000 ft), respectively.

5.2.3.2 Suction Surface Details—The boundary layer profiles for which the stability was analyzed were computed on the basis of a uniformly porous suction surface. Available structural materials suitable for aircraft skins are impermeable, so discrete slots or holes must be used instead. There is a substantial data base for both of these approaches, and both have been demonstrated successfully in LFC experiments. In the present study, holes were chosen because the structural design is more straightforward and because modern electron-beam drilling techniques permit economical fabrication of sheet metal with

67

- M = 0.8
- Altitude = 9144m (30 000 ft)

Upper root

$\eta = 0.1$
$R_N = 50 \times 10^6$
$c_{q_N} = 14.9 \times 10^{-5}$

$\dfrac{(\rho v)_w}{\rho_\infty U} \times 10^4$

s/c

Upper midspan

$\eta = 0.4$
$R_N = 33 \times 10^6$
$c_{q_N} = 11.94 \times 10^{-5}$

$\dfrac{(\rho v)_w}{\rho_\infty U} \times 10^4$

s/c

Upper tip

$\eta = 0.76$
$R_N = 20 \times 10^6$
$c_{q_N} = 6.60 \times 10^{-5}$

$\dfrac{(\rho v)_w}{\rho_\infty U} \times 10^4$

s/c

Lower root

$\eta = 0.10$
$R_N = 50 \times 10^6$
$c_{q_N} = 11.08 \times 10^{-5}$

$\dfrac{(\rho v)_w}{\rho_\infty U} \times 10^4$

s/c

Lower midspan

$\eta = 0.4$
$R_N = 33 \times 10^6$
$c_{q_N} = 8.45 \times 10^{-5}$

$\dfrac{(\rho v)_w}{\rho_\infty U} \times 10^4$

s/c

Lower tip

$\eta = 0.75$
$R_N = 20 \times 10^6$
$c_{q_N} = 7.83 \times 10^{-5}$

$\dfrac{(\rho v)_w}{\rho_\infty U} \times 10^4$

s/c
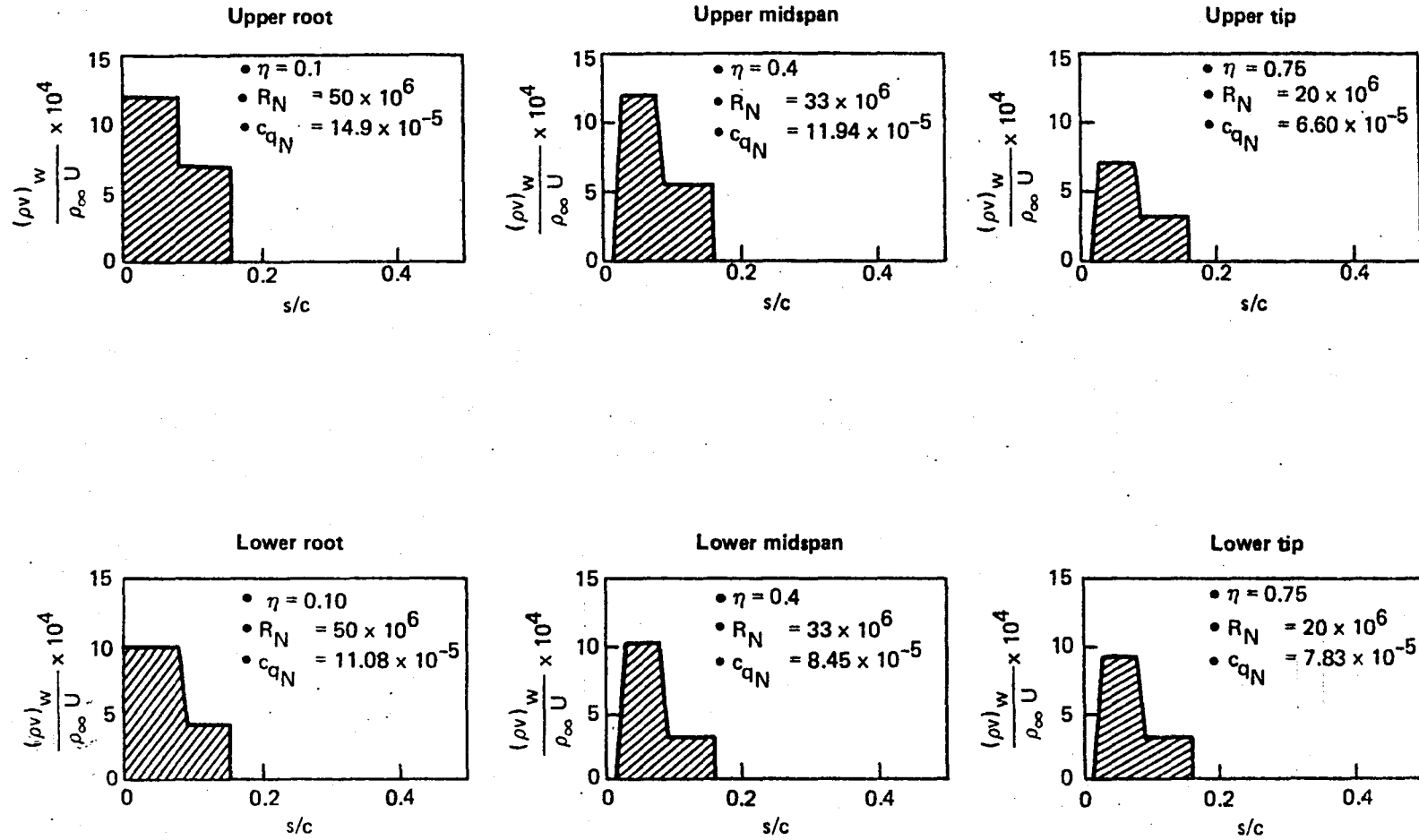
Figure 49. HLFC Maximum Suction Requirements
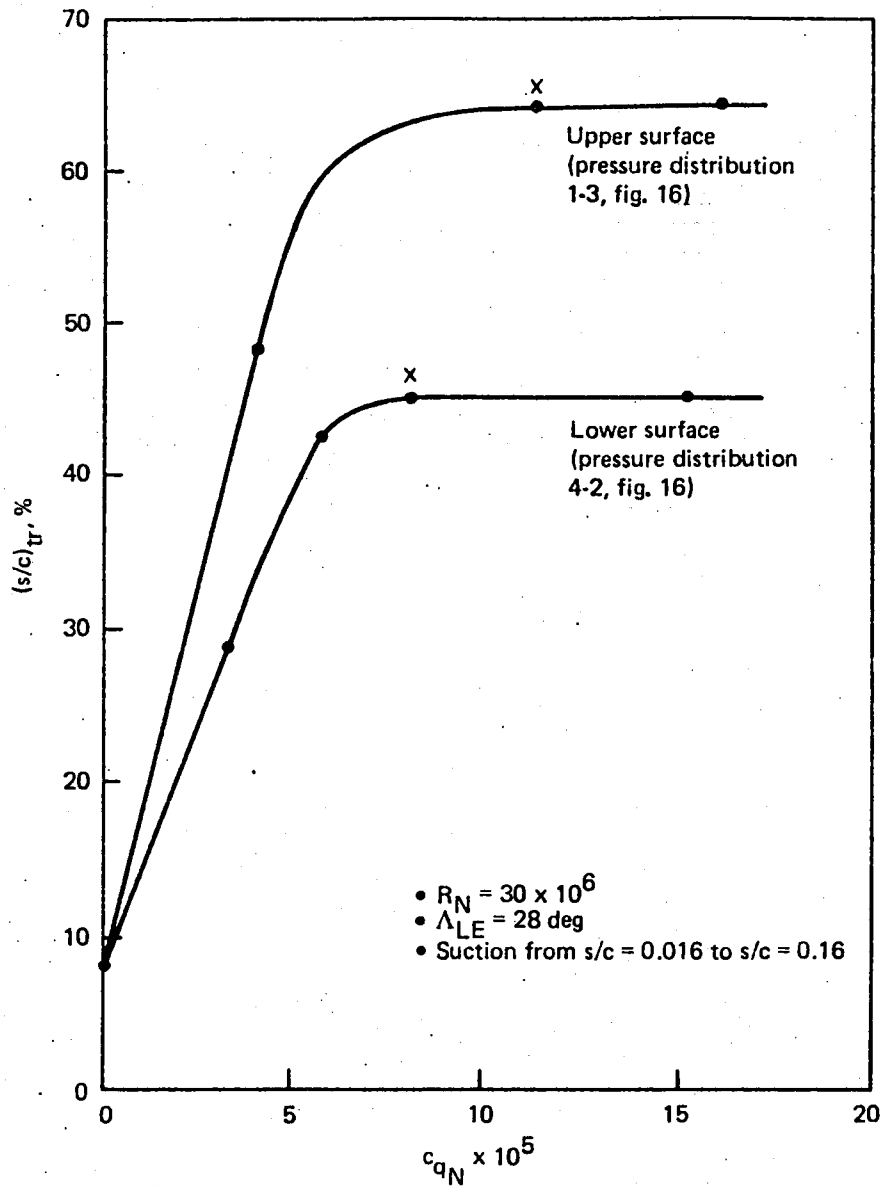
89

Figure 50. Effect of Suction Quantity on Transition Location

large numbers of small, uniform, evenly spaced holes. To establish pressure drops for suction system designs, a tentative selection of hole sizes and spacing must be made. The subject of design criteria for suction holes is involved and unsettled. The remainder of this section presents the analysis used to make that selection. It is not an endorsement of, or comment on, the criteria used.

To prevent the streamline pattern of the flow into an individual hole from becoming a transition-producing disturbance in itself, both the hole size and the hole spacing must be small compared to the boundary layer thickness. According to Reference 21, a hole suction surface will function satisfactorily if the suction velocity ratio (u_{hole}/U_e) is kept

Figure 51. Extent of Laminar Flow—Off-Design Condition

Figure 52. Extent of Laminar Flow—Cruise Condition

71

below the critical value shown in Figure 53. Each hole behaves as if it were isolated. Holes measuring 0.064 mm (0.0025 in) on 0.64-mm (0.025-in) centers have been wind-tunnel tested successfully, and flight tests are planned (ref. 22). These dimensions were chosen here. They provide a porosity of 0.758% of the surface area.

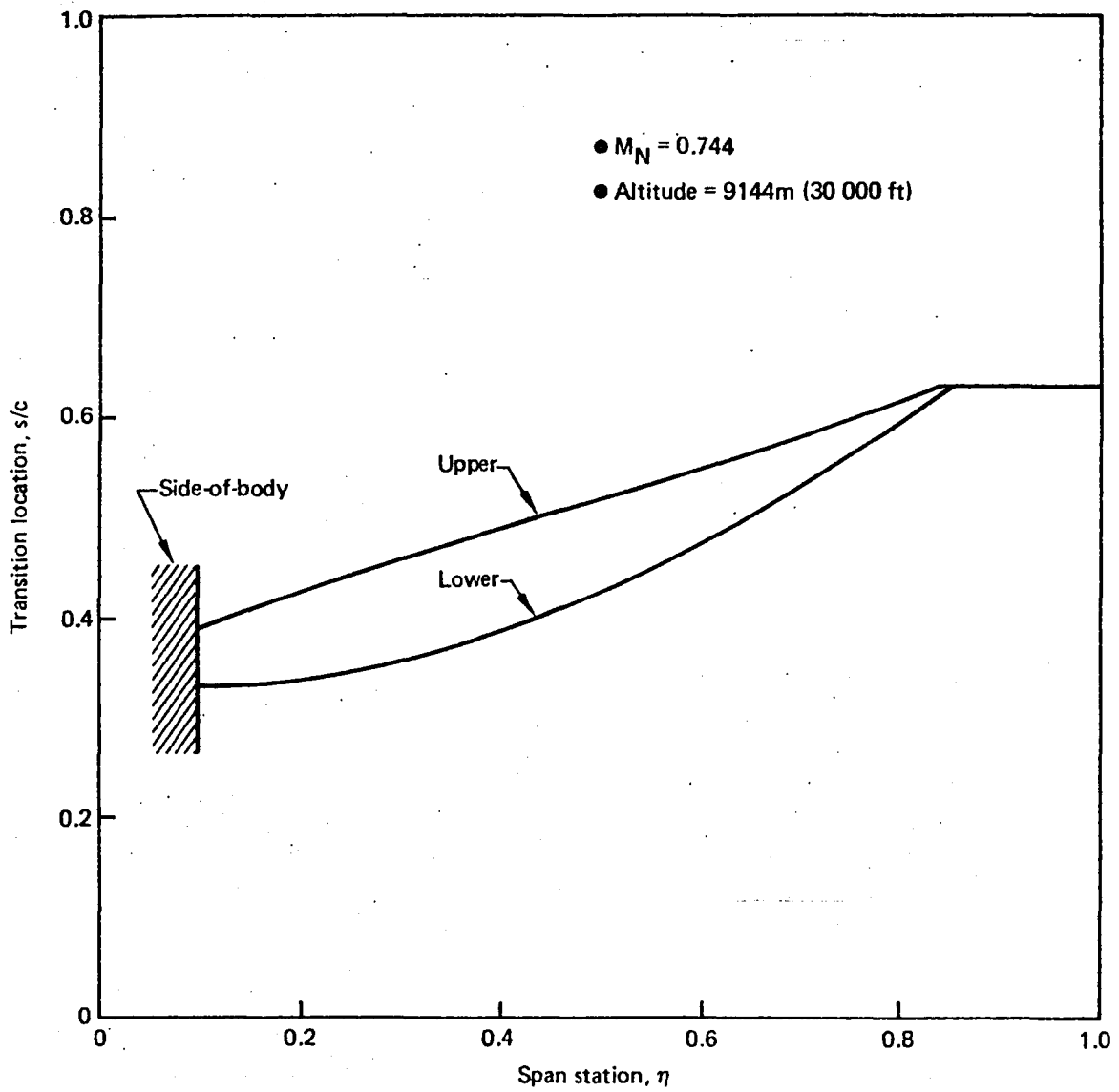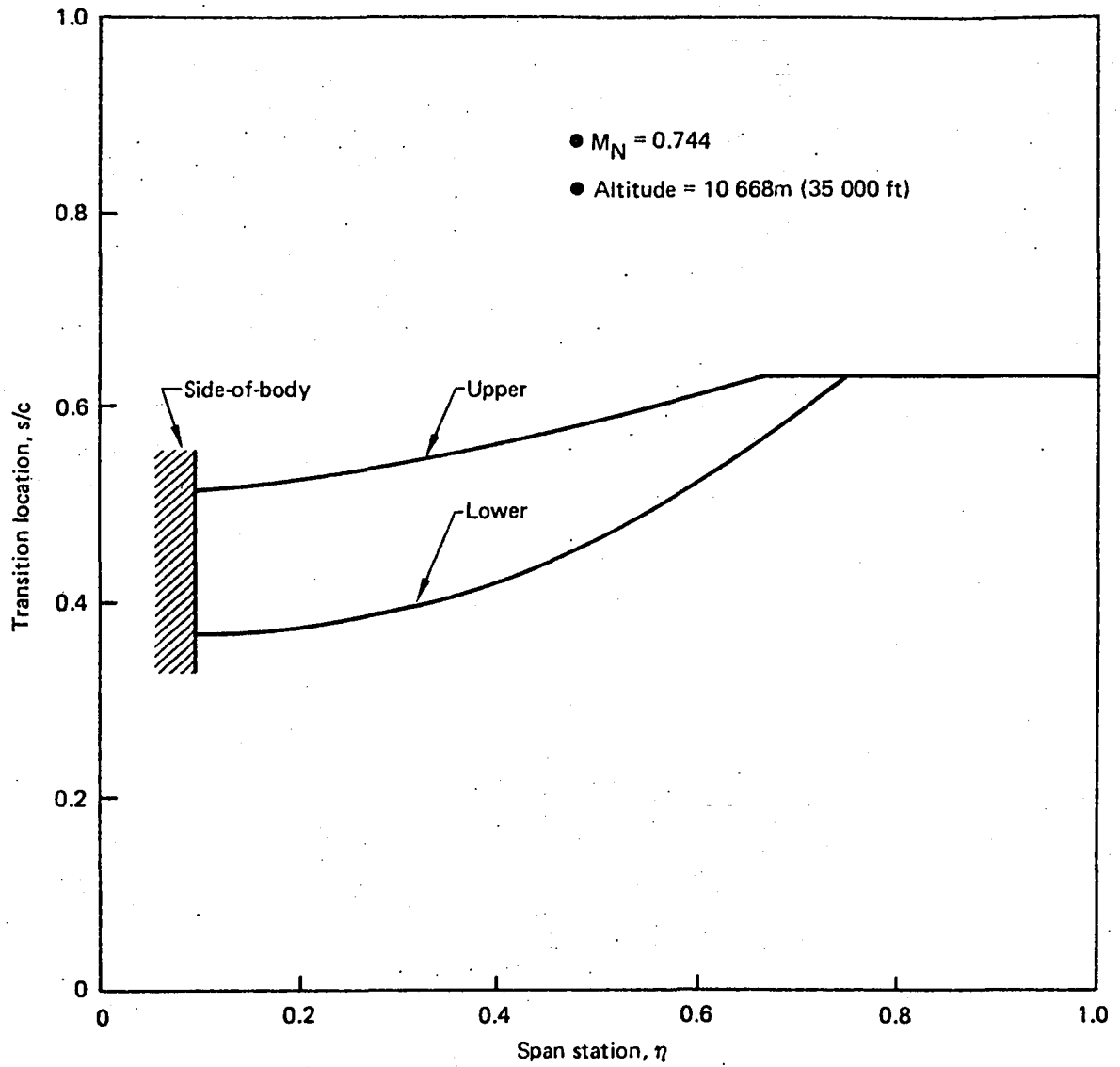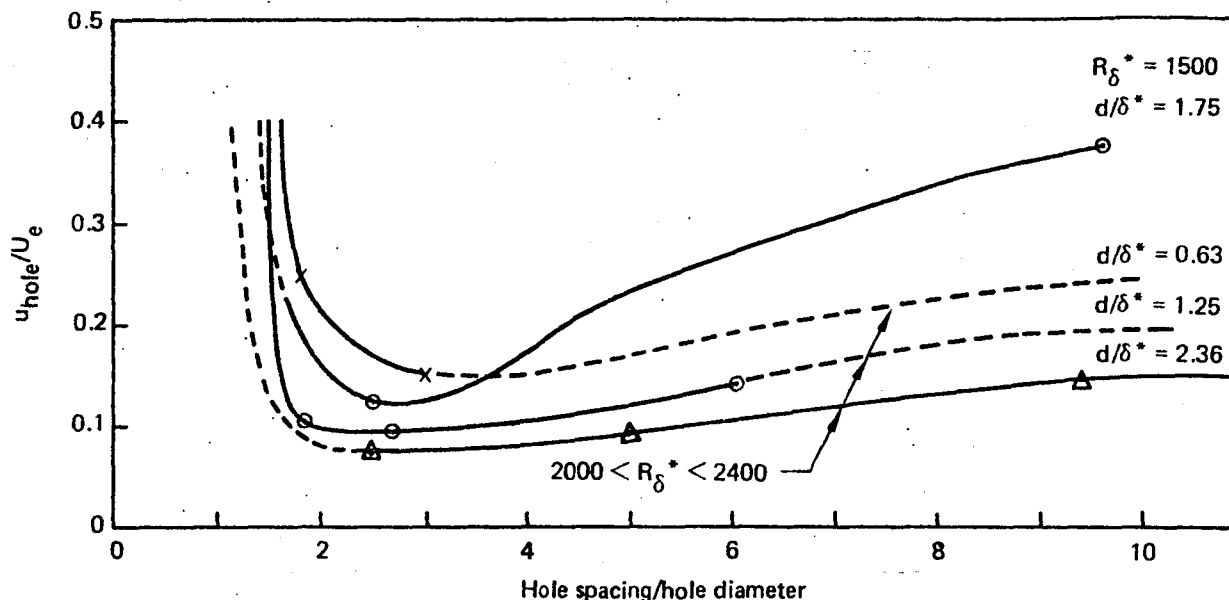**Figure 53. Hole Spacing Criterion**

The suction velocity ratio was checked for upper surface locations at the wing root and tip, where it reaches its highest and lowest values. Figure 49 shows $(\rho v)_w/\rho_\infty U$ requirements of 12×10^{-4} and 7×10^{-4}. The suction velocity ratio is

$$\frac{u_{hole}}{U_e} = \frac{(\rho v)_w}{\rho_\infty U} \cdot \frac{U}{U_e} \cdot \frac{\rho_\infty}{\rho} \cdot \frac{\text{surface area}}{\text{hole area}}$$

For a local Mach number of 1.1 at a freestream Mach number of 0.8, the density ratio, ρ_∞/ρ, is 1.272, giving maximum suction velocity ratios of 0.135 at the root and 0.083 at the tip, back to s/c = 0.08.

Figure 54 shows the boundary layer displacement thicknesses computed for these locations at the design flight condition, together with the corresponding Reynolds numbers. For the root, the $R_{\delta*}$ = 1500 line of Figure 53 is conservative over the entire sucked surface and shows a u_{hole}/U_e limit of 0.37 for d/δ* = 1.75. The s/c = 0.08 point will be critical, since the suction is sharply reduced further downstream. There, δ* = 0.18 mm (0.007 in) so d/δ* is only 0.36, and there is ample margin. At the tip, the variation of δ* over the first 8% of s/c is similar to that of the root, so the same conclusions apply.

In summary, a uniform, hole-type suction surface that has a hole diameter of 0.063 mm (0.0025 in) and a hole spacing of 0.63 mm (0.025 in), both chordwise and spanwise, satisfies the applicable criteria in all areas. In addition, there is adequate margin to allow up to 50% of the holes in a given region to be blocked off (if necessary for structural purposes) without violating the criteria.

72
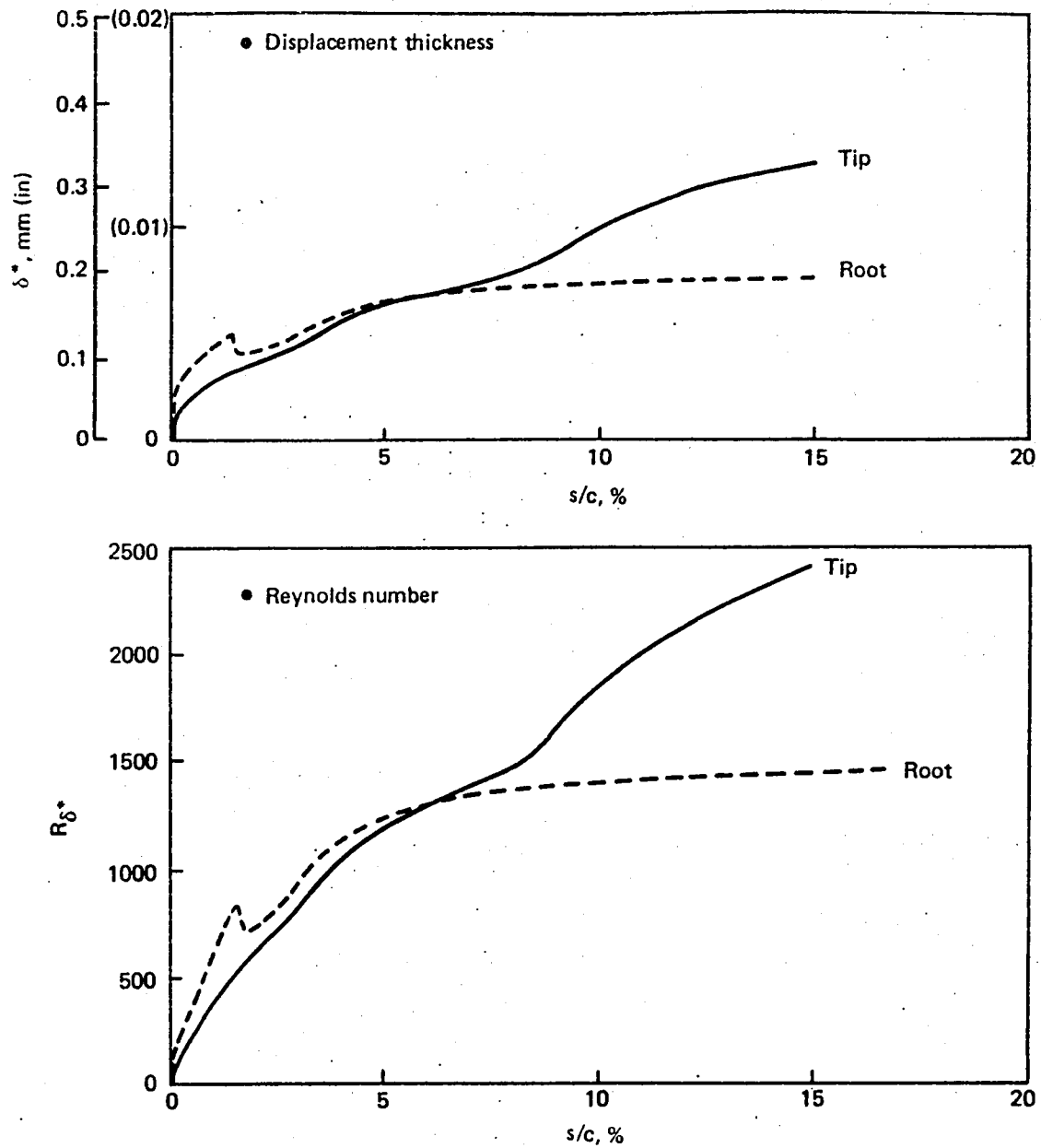
Figure 54. Characteristics of Upper Surface Boundary Layer in Suction Area

5.2.3.3 Pumping Power Requirements—The principal design requirements for the complete suction system were established on the basis of local suction inflow specifications discussed in section 5.2.3 and summarized in Figure 50. The required ideal pumping power was determined from the total suction flow quantity, Q, and the required pressure rise, Δp_s. That is,

$$\text{Pumping power} = Q \times \Delta p_s$$

The total suction flow quantity was obtained by integrating local values along the span, as shown in Figure 55. That is,

$$Q = 2 \int_{Root}^{Tip} Q'dz$$

where $Q' = c_q c V$

The resulting figures, for cruise at 10 668m (35 000 ft) altitude, are

$$Q_{upper} = 3.94 \ m^3/s \ (139 \ ft^3/s) \text{ for the upper surface}$$
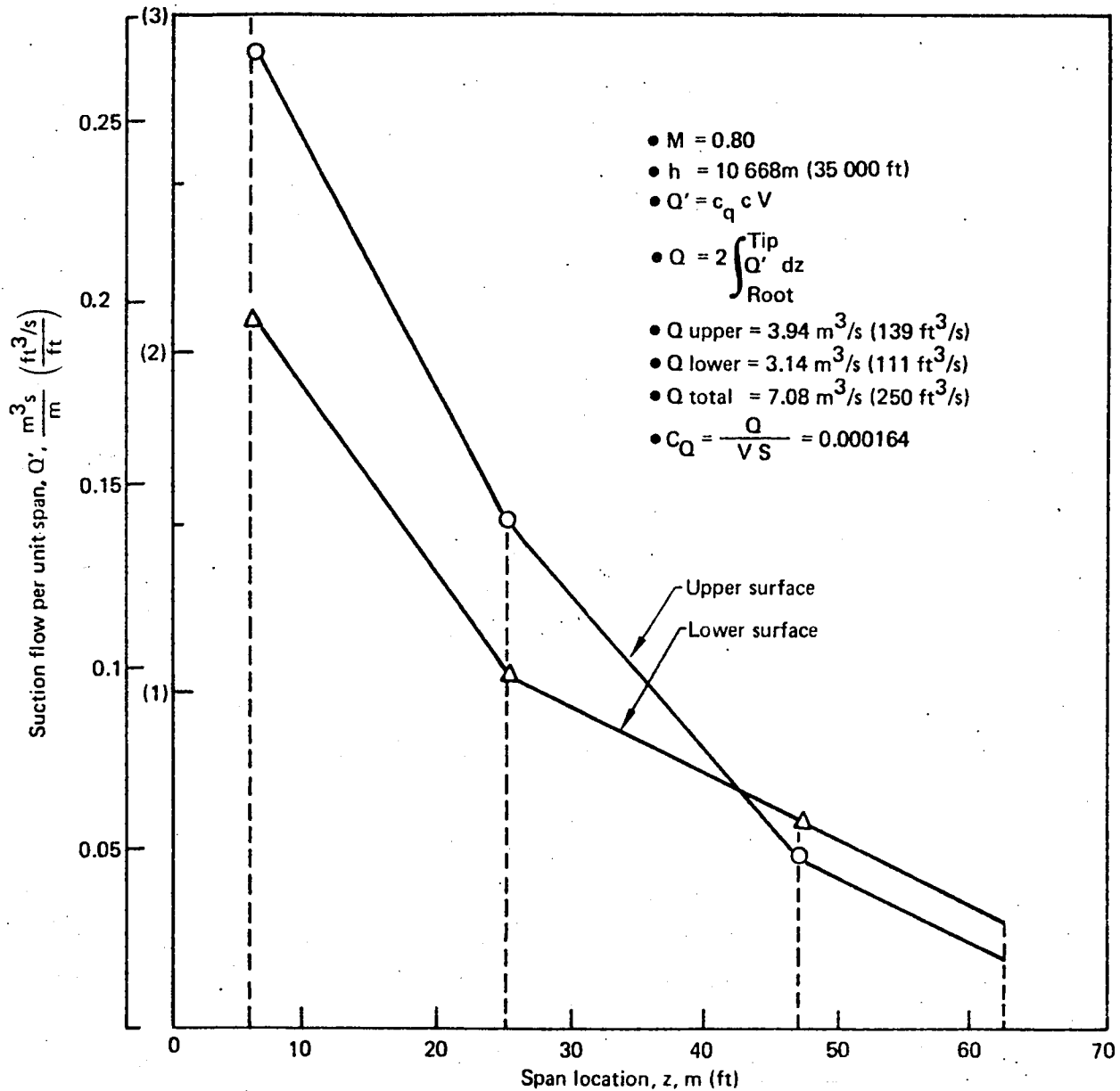
Figure 55. HLFC Wing Suction Quantity

74

and Q_{lower} = 3.14 m³/s (111 ft³/s) for the lower surface

totaling Q = 7.08 m³/s (250 ft³/s) for the entire wing

This corresponds to a mean suction flow coefficient of

$$C_Q = \frac{Q}{V \ S_{ref}} = 1.64 \times 10^{-4}$$

The pressure rise that the suction pump must provide was established by assuming suction duct pressure levels lower than the external local static pressure by a margin of C_p = -0.2, as shown in Figure 56. Based on past experience, this pressure differential is adequate to move the sucked air mass through the suction surface and the ducting. Best performance is obtained if the suction air mass is pumped back up to freestream total
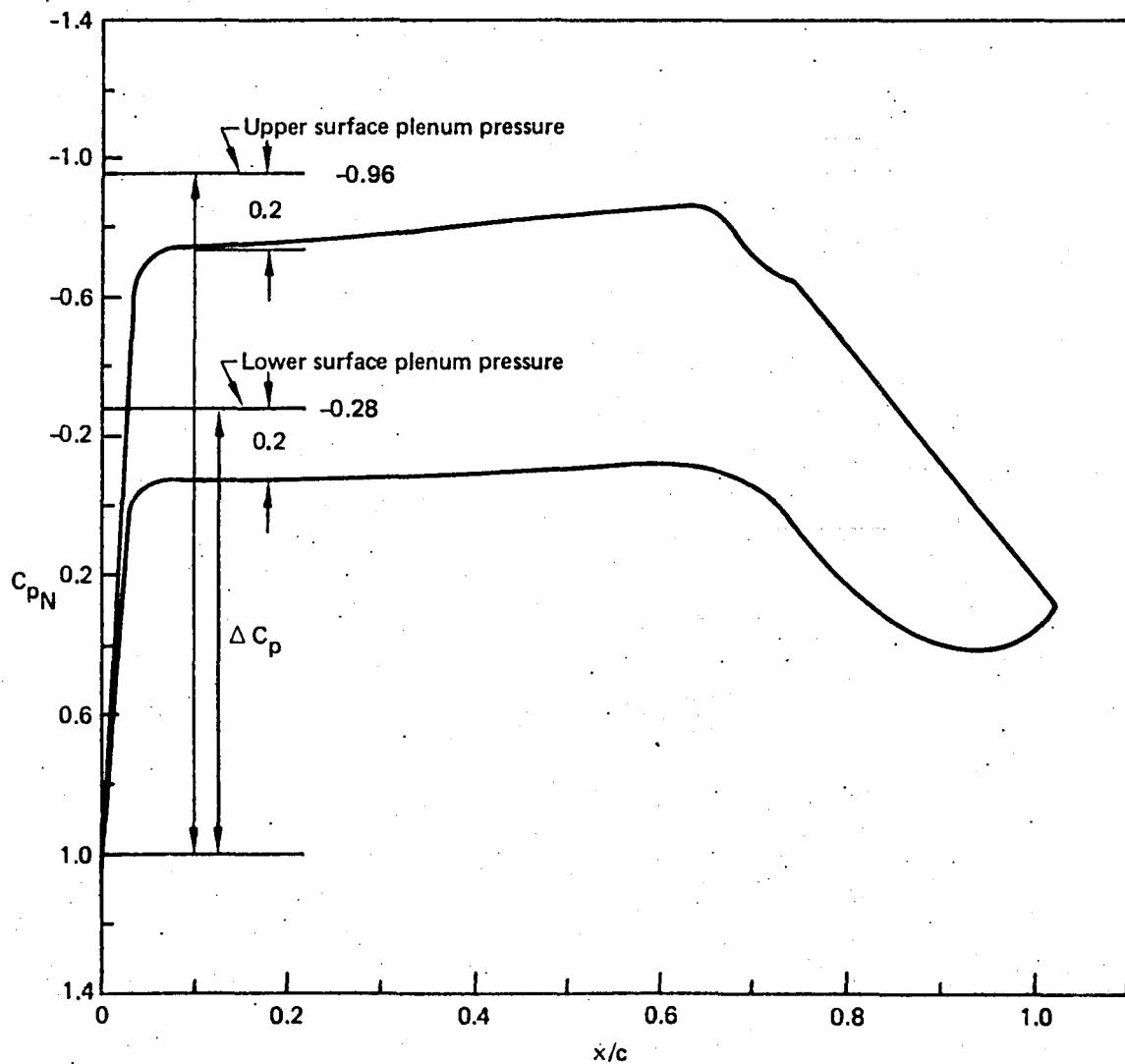
Figure 56. Suction Flow Pressure Rise Requirements

pressure. Thus, the suction pressure differentials applicable to the upper and lower surfaces were

and

$$\Delta C_p = -1.96 \text{ (upper surface)}$$

$$\Delta C_p = -1.28 \text{ (lower surface)}$$

The results of the required suction pumping power calculations are summarized in Table 5. The suction system must be sized for the 9144m (30 000 ft) condition, requiring 7.23 m^3/s (255.4 ft^3/s) capacity and an ideal pumping power of 161.4 kW (216.5 hp).

Table 5. Suction Power Requirements

| h, m (ft)		9 144 (30 000)	10 668 (35 000)	11 277 (37 000)	12 192 (40 000)
q, kPa (lb/ft^2)		13.45 (281.0)	10.67 (223.0)	9.67 (202.0)	8.40 (175.6)
Q, m^3/s (ft^3/s)	Upper	4.02 (142.0)	3.93 (139.0)	3.91 (138.3)	3.91 (138.3)
	Lower	3.21 (113.4)	3.14 (111.0)	3.12 (110.4)	3.12 (110.4)
	Total	7.23 (255.4)	7.08 (250.0)	7.04 (248.0)	7.04 (248.7)
Δp_s, kPa (lb/ft^2)	Upper	26.4 (551.3)	20.92 (437.0)	19.00 (397.0)	16.47 (344.0)
	Lower	17.23 (360.0)	13.64 (285.0)	12.40 (259.0)	10.76 (224.8)
Pump power, kW (hp)	Upper	106.1 (142.3)	82.4 (110.5)	74.5 (100.0)	64.1 (86.0)
	Lower	55.3 (74.2)	42.8 (57.5)	38.7 (52.0)	33.5 (45.0)
	Total	161.4 (216.5)	125.2 (168.0)	113.3 (152.0)	97.7 (131.0)

- $C_Q = 0.000164$
- $C_{D_S} = 0.000272$
- $M = 0.8$

5.2.4 Drag Estimation

The drag reduction due to HLFC was estimated on the basis of boundary layer calculations performed at three spanwise locations on the wing (app. B). These gave the local section profile drag coefficients for fully turbulent flow and for partly laminar flow. Interpolation of the three local section profile drag coefficients gave the spanwise drag distributions from which the total wing profile drag was obtained by integration. The drag prediction procedure is summarized in Figure 57.

$$c_d = \frac{2\theta}{c}\left(\frac{U_e}{V}\right)^{\frac{H+5}{2}}$$

Spanwise profile drag distribution

$(c\, c_d)$

$$C_{D_W} = \frac{2}{S_{REF}} \int (c\, c_d)\ dz$$

Wing profile drag coefficient C_{D_W}

Drag reduction:

$$\Delta C_{D_W} = C_{D_{TURB}} - C_{D_{HLFC}}$$
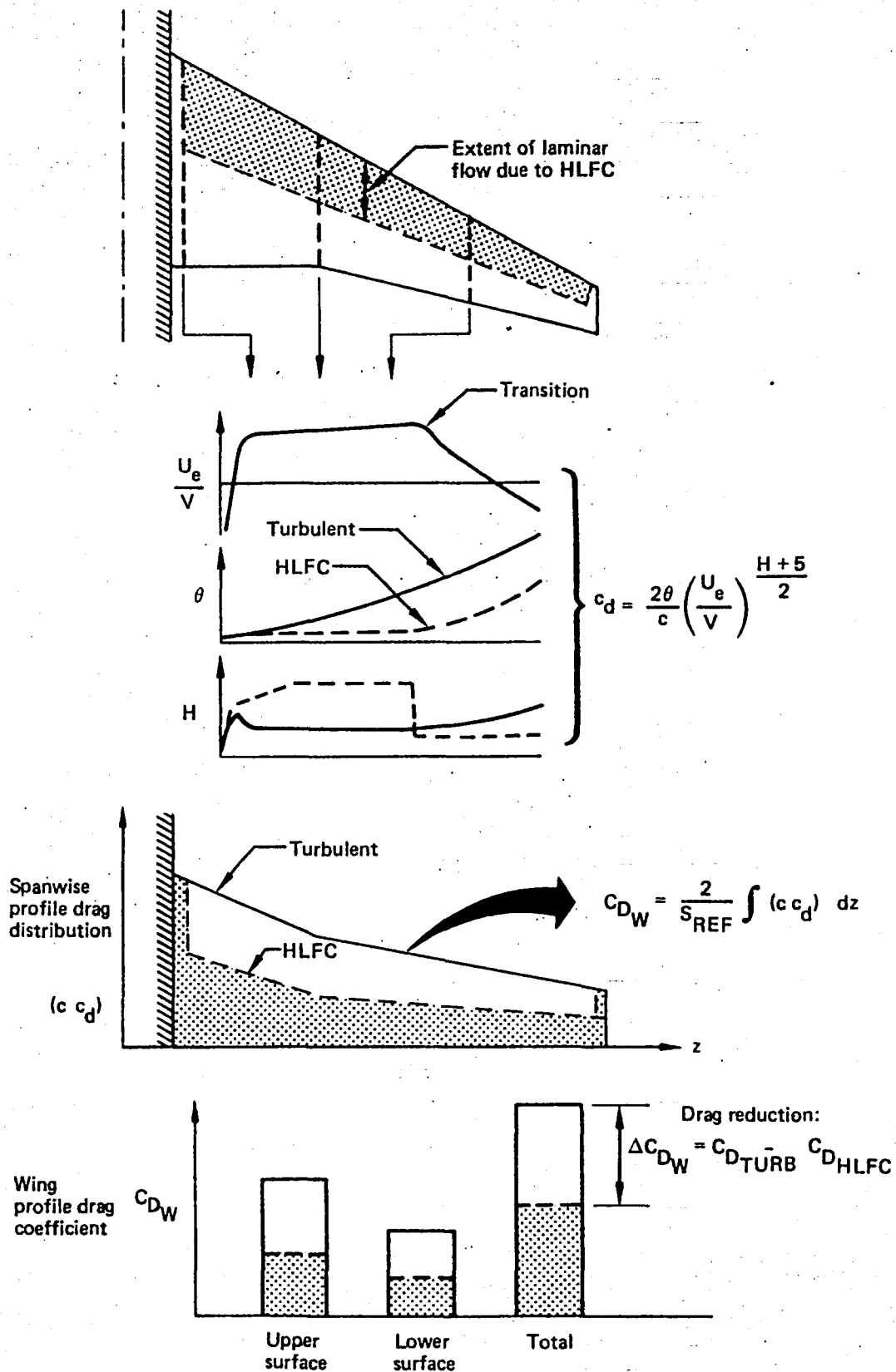
Upper surface   Lower surface   Total

Figure 57. Summary of Drag Prediction Procedure

77

Figure 58 shows the extent of laminar flow used for these calculations. This is based on the boundary layer stability calculations described in section 5.2.3. Allowance was made for loss of laminarization due to turbulent contamination from the body, wingtips, nacelle struts, and flap track fairings. Credit was taken for the favorable effect of increasing cruise altitude (i.e., decreasing Reynolds number) on the extent of laminar flow. Typical values of momentum thickness (θ) and shape factor (H) are shown in Figure 59. The local section profile drag coefficients were calculated from the boundary layer parameters at the trailing edge by the Squire-Young formula (ref. 23). That is,

$$c_d = \left(\frac{2\,\theta}{c}\right)\left(\frac{U_e}{V}\right)^{\frac{H+5}{2}}$$

The spanwise variation of profile drag is shown in Figure 60 for turbulent flow and partly laminarized flow.

Overall wing profile drag is shown in Figure 61. Drag reduction due to HLFC is clearly apparent: the upper surface drag is reduced by $\Delta C_D = 0.00225$ (54.5%) and the lower surface drag is reduced by $\Delta C_D = 0.0011$ (50%). The total reduction is $\Delta C_D = 0.00335$ (53%). (In considering various options for leading-edge high-lift devices, one possibility was to use a Krueger flap and give up the laminarization of the lower surface. In this case, the wing profile drag reduction would drop from 53% to about 35%.)

Since the wing profile drag constitutes only about 37% of the entire profile drag and only about 20% of the total airplane drag, the percentage of reduction is less dramatic for the total airplane. Figures 62 and 63 illustrate this by showing the component wetted areas and the corresponding component profile drag coefficients. Note that if HLFC also were applied to te empennage (assuming 50% chord laminarization), an additional $\Delta C_D = 0.0013$ drag reduction would be obtainable.

The potential drag reductions due to application of HLFC to the baseline airplane for cruise at M = 0.80, h = 37 000 ft, and $C_L = 0.50$, are:

	C_D	ΔC_D	(L/D)	Δ(L/D), %
Baseline airplane (w/turbulent flow)	0.0308	—	16.28	—
HLFC applied to wing and empennage	0.0261	0.0047	19.23	18.0
HLFC applied to wing only	0.0274	0.0034	18.11	11.2
HLFC applied to wing upper surface only	0.0285	0.0023	17.48	7.3

It should be noted, however, that the present baseline airplane has a relatively small wing (optmized for turbulent flow), and that an HLFC airplane designed for the same mission probably would have a larger wing; hence, the impact of laminarization could be larger.

Upper surface

$x_L/c, \%$
39
51
60

h = 9 144m (30 000 ft)
10 668m (35 000 ft)
12 192m (40 000 ft)

60%

Side of body

Lower surface

$x_L/c, \%$
33
38
44

h = 9 144m (30 000 ft)
10 668m (35 000 ft)
12 192m (40 000 ft)

60%
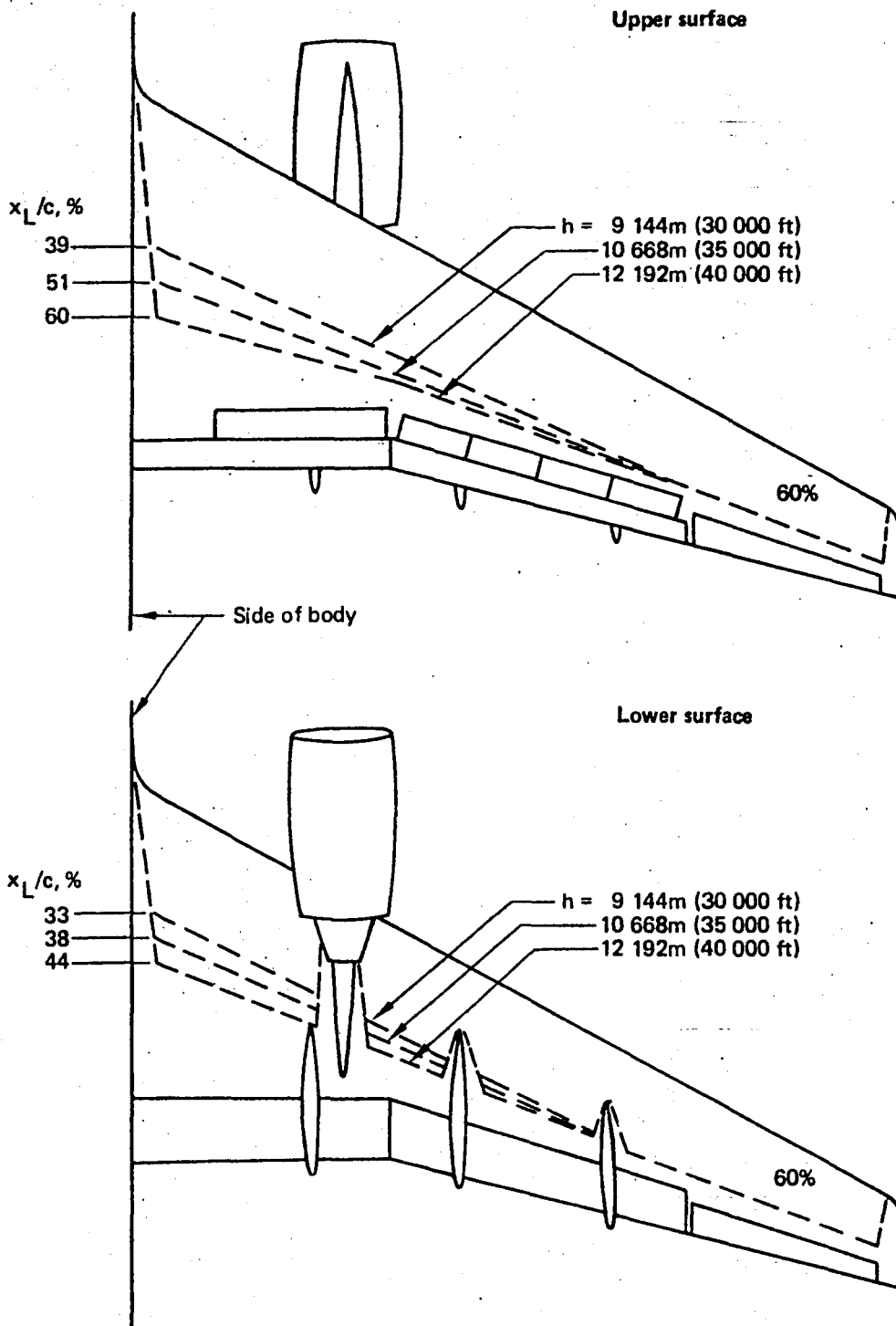
Figure 58. Effect of Cruise Altitude on Extent of Laminar Flow
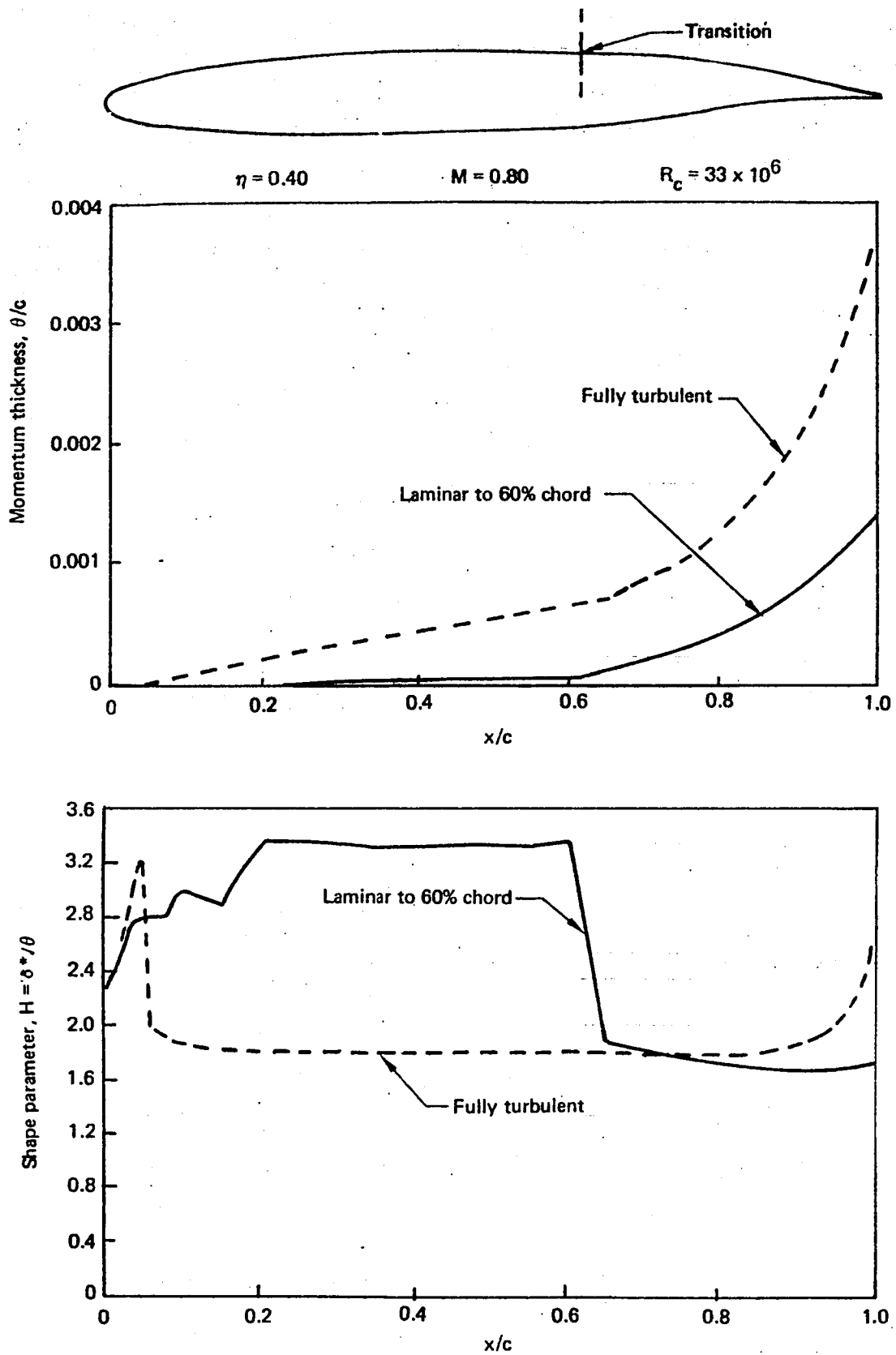
Figure 59. *Typical Results of Boundary Layer Calculations for Drag Estimation*
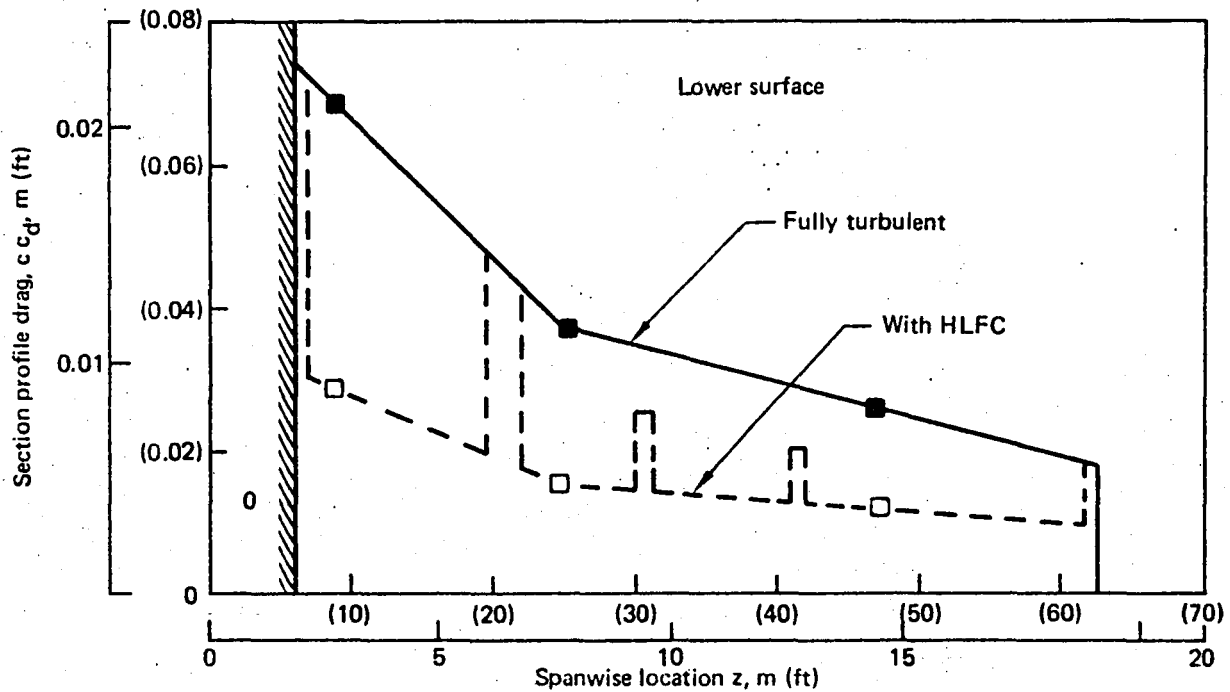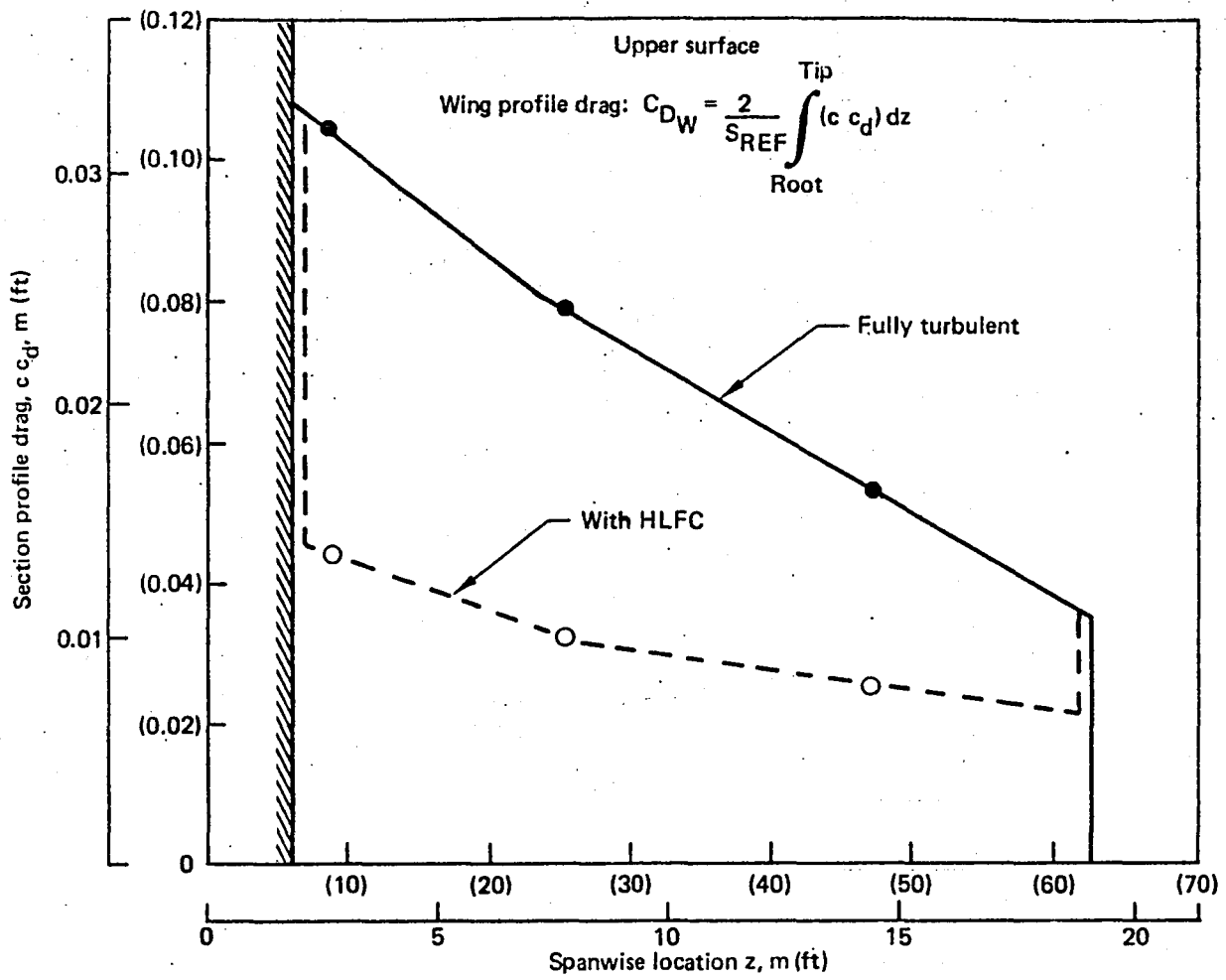
Figure 60. Spanwise Variation of Section Profile Drag, M = 0.8, C_L = 0.5

81
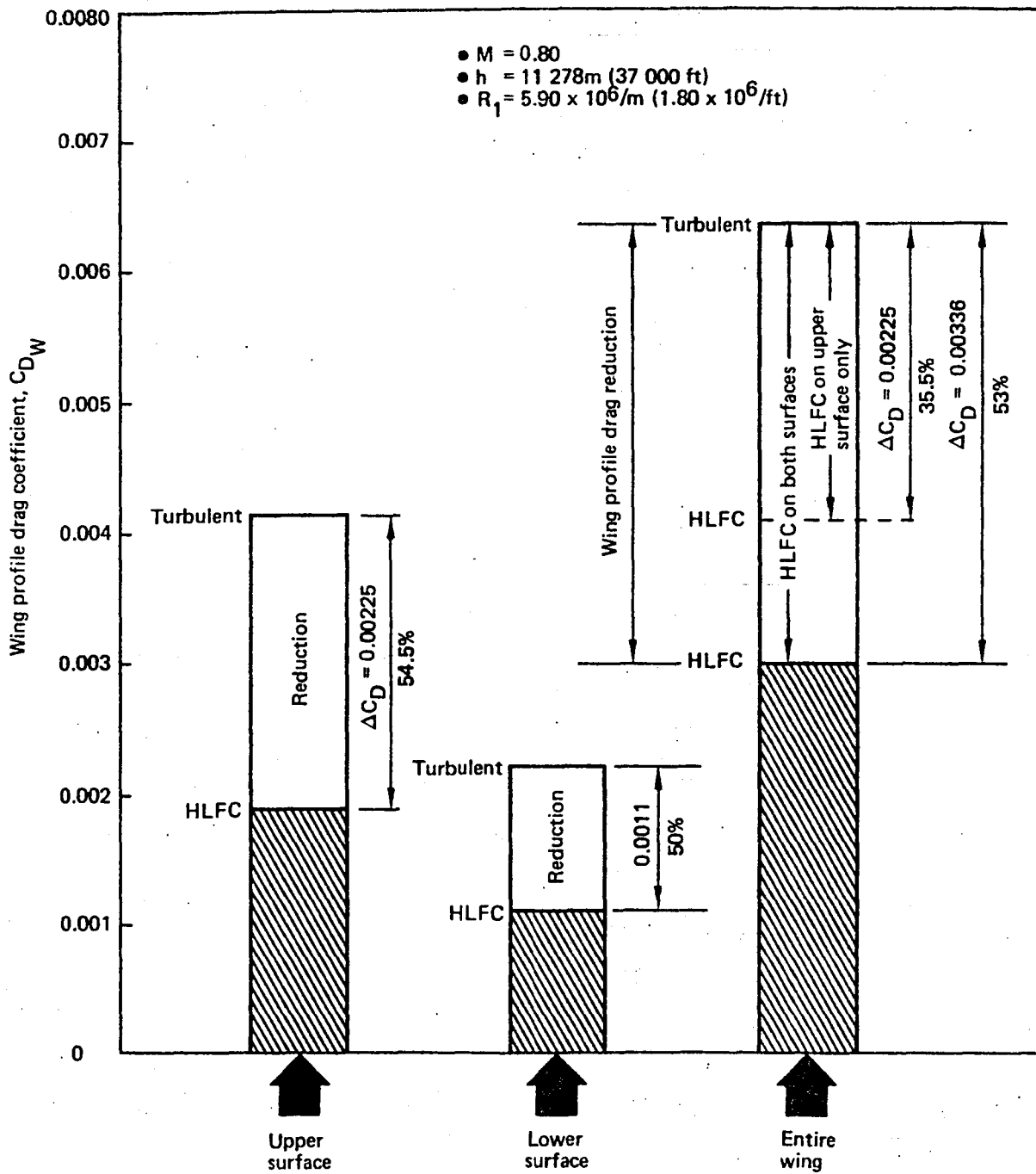
Figure 61. *Effect of HLFC on Wing Profile Drag*

$$S_{REF} = 181.25 \text{ m}^2 \text{ (1951 ft}^2\text{)}$$

	A_W, m^2 (ft^2)
Wing	312.0 (3358)
Body	520.3 (5601)
Vertical tail	70.8 (762)
Horizontal tail	83.0 (893)
Nacelles	57.8 (622)
Struts	11.8 (127)
Flap tracks	20.9 (225)
Total	1076.6 (11 588)

Total wetted area, %
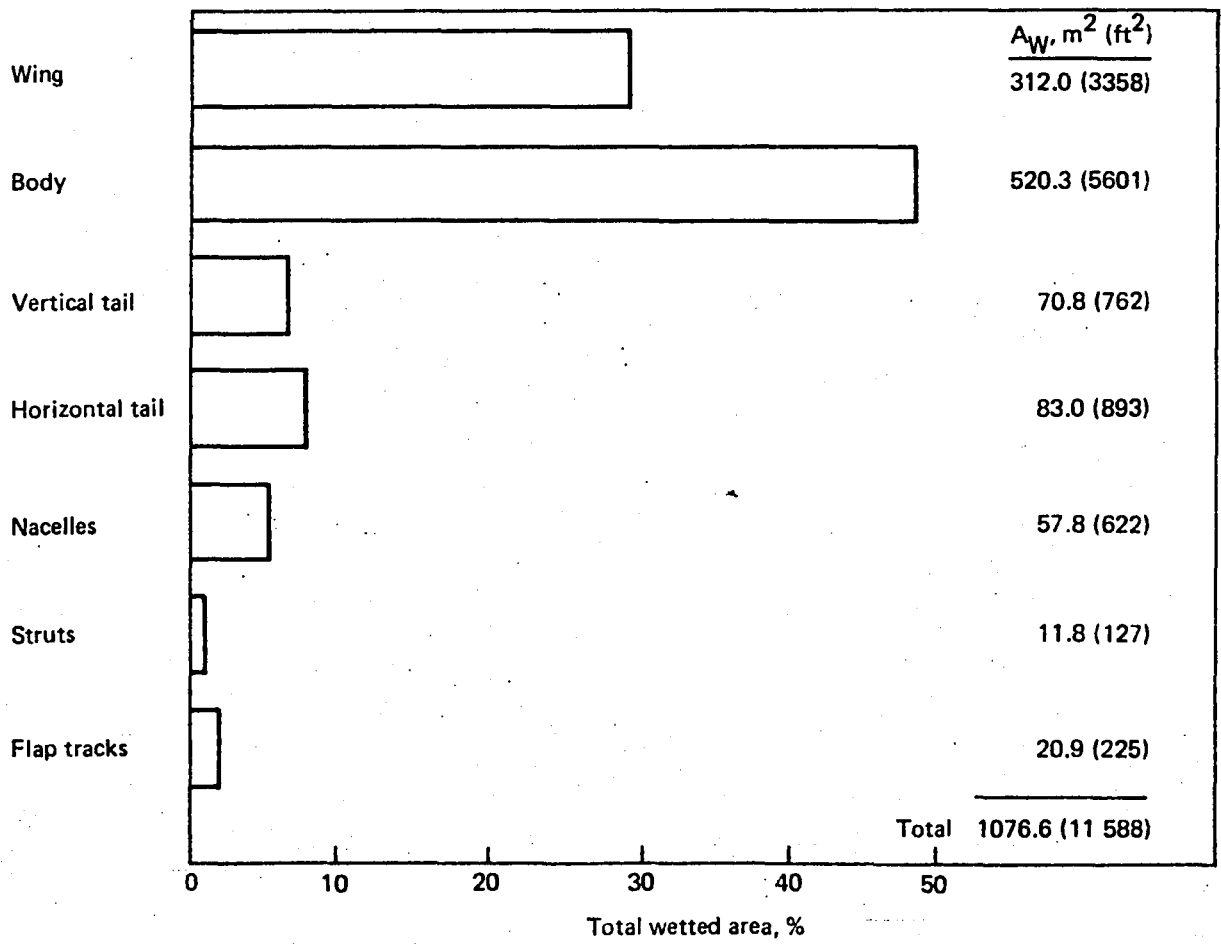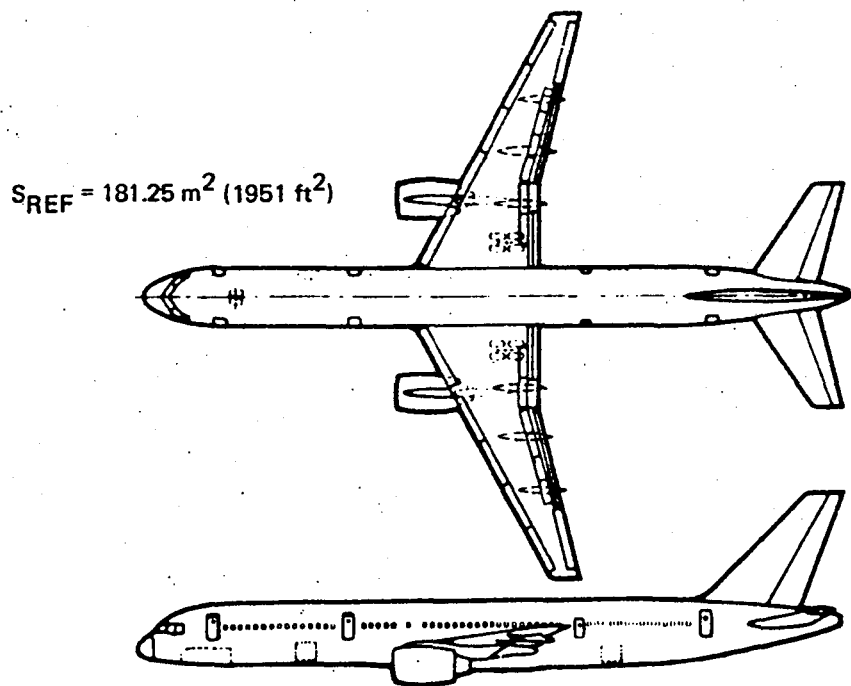
Figure 62. Wetted Area Breakdown, 757-200

83

$S_{REF} = 181.25\ m^2\ (1951\ ft^2)$ $R_1 = 5.50 \times 10^6/m\ (1.675 \times 10^6/ft)$

		%, C_{D_P}
	Reduction due to HLFC	
Wing	$\Delta C_D = 0.0034$	36.9
Body		34.7
Vertical tail	ΔC_D $\Delta C_D = 0.0005$	6.8
Horizontal tail	ΔC_D $\Delta C_D = 0.0008$ } 0.0013	9.6
Nacelles		8.7
Struts	$\Sigma C_{D_P} = 0.01875$	1.3
Flap tracks		1.6

Component profile drag, $C_{D_P} \times 10^4$

Figure 63. Component Drag Buildup, 757/HLFC

84

Full effectiveness of HLFC can be expected only at cruise conditions. However, partial effectivness may be achieved at off-design operations such as climb and descent. As shown in section 5.2.2.1, the use of a short trailing-edge flap permits controlling the pressure distributions on the wing to extend the range of flight conditions where some laminarization would be possible. For the lower surface, extended laminar flow is probably possible in climb above 3048m (10 000 ft) and for the upper surface above 7620m (25 000 ft). Based on these assumptions, estimates were made of the potential drag reduction due to HLFC during climb. Figure 64 shows the drag reduction as a function of altitude. Credit was taken for this reduction in the fuel-burned calculations (sec. 6.2).

So far, discussion has concerned only the viscous drag of the HLFC wing represented by the momentum loss of the wake. In the evaluation of the complete HLFC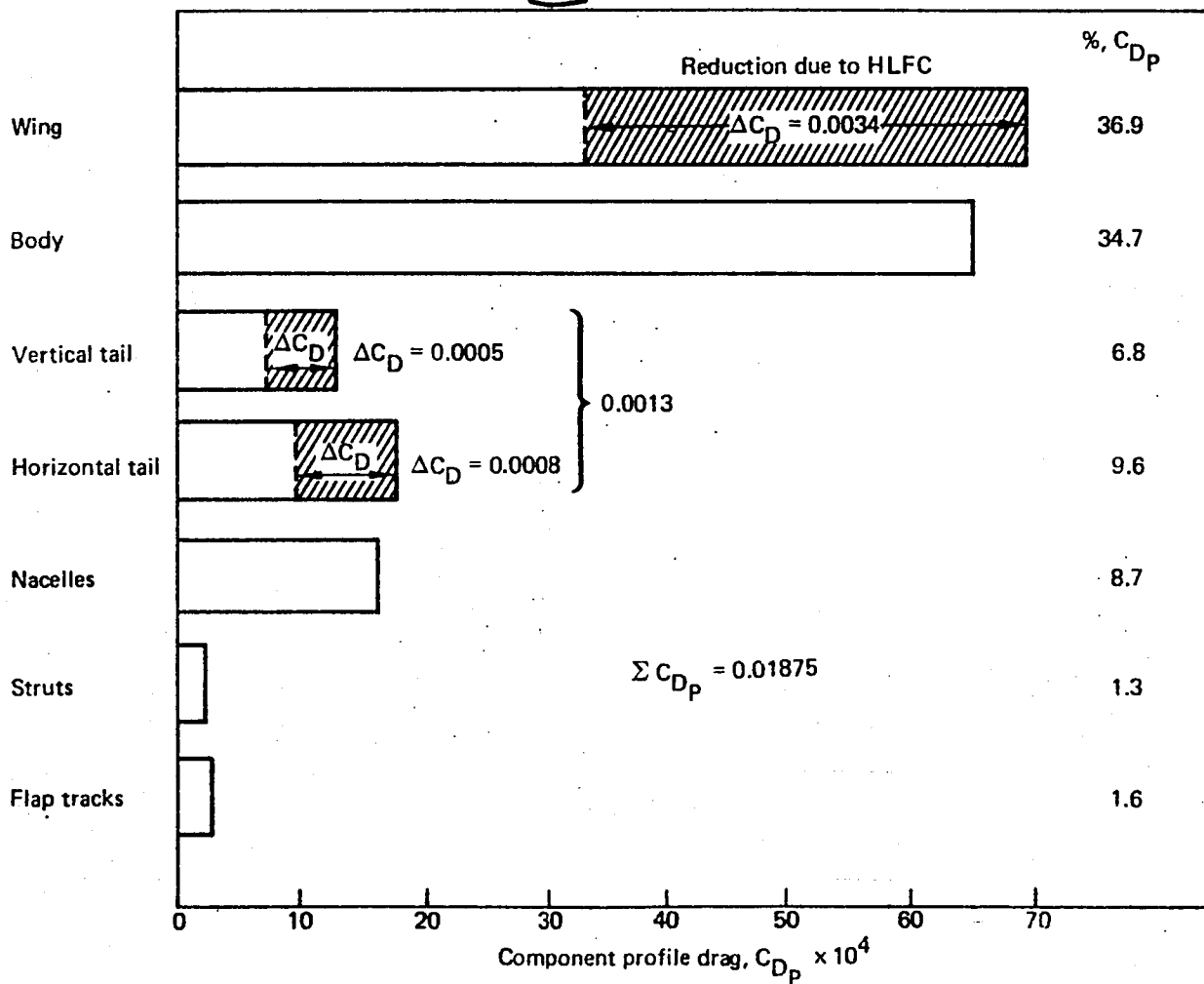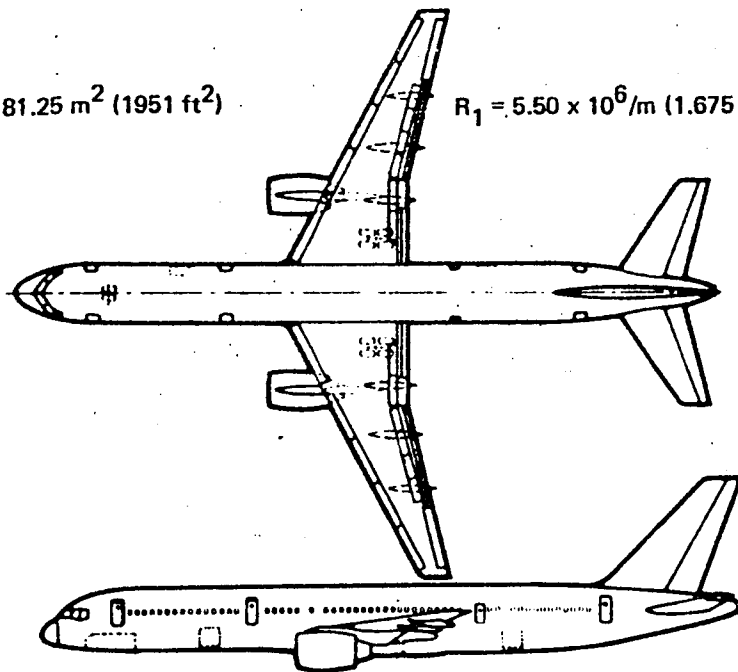 system, however, the power required to drive the suction pump also must be considered as an additional drag term. The total drag reduction due to HLFC is therefore somewhat less than indicated by the reduction in wake drag. Assuming equal efficiencies for the propulsion system and the suction pumps, an equivalent suction drag coefficient can be defined:

$$C_{D_s} = C_Q \text{ (average } \Delta p \text{ suction)}/q$$

This is not large on the current airplane. At the nominal cruise condition, $C_{D_s} = 0.00027$, which represents about 9% of the total wing profile drag. (C_{D_s} puts into perspective the energy expended in suction, but was not included in the drag coefficient for the fuel burned calculations in section 6.0. Instead, the engine fuel flow was increased as required to account for the power extracted to drive the suction pumps.)

Figure 65 illustrates the estimated variation of the wake, suction, and total wing profile drag coefficients as a function of suction flow coefficient. The curve between the points representing fully turbulent flow and fully operative HLFC is drawn intuitively, based on past experience that showed a certain suction level must be exceeded before substantial laminarization is obtained.

Figure 64. Drag Reduction due to HLFC in Climb
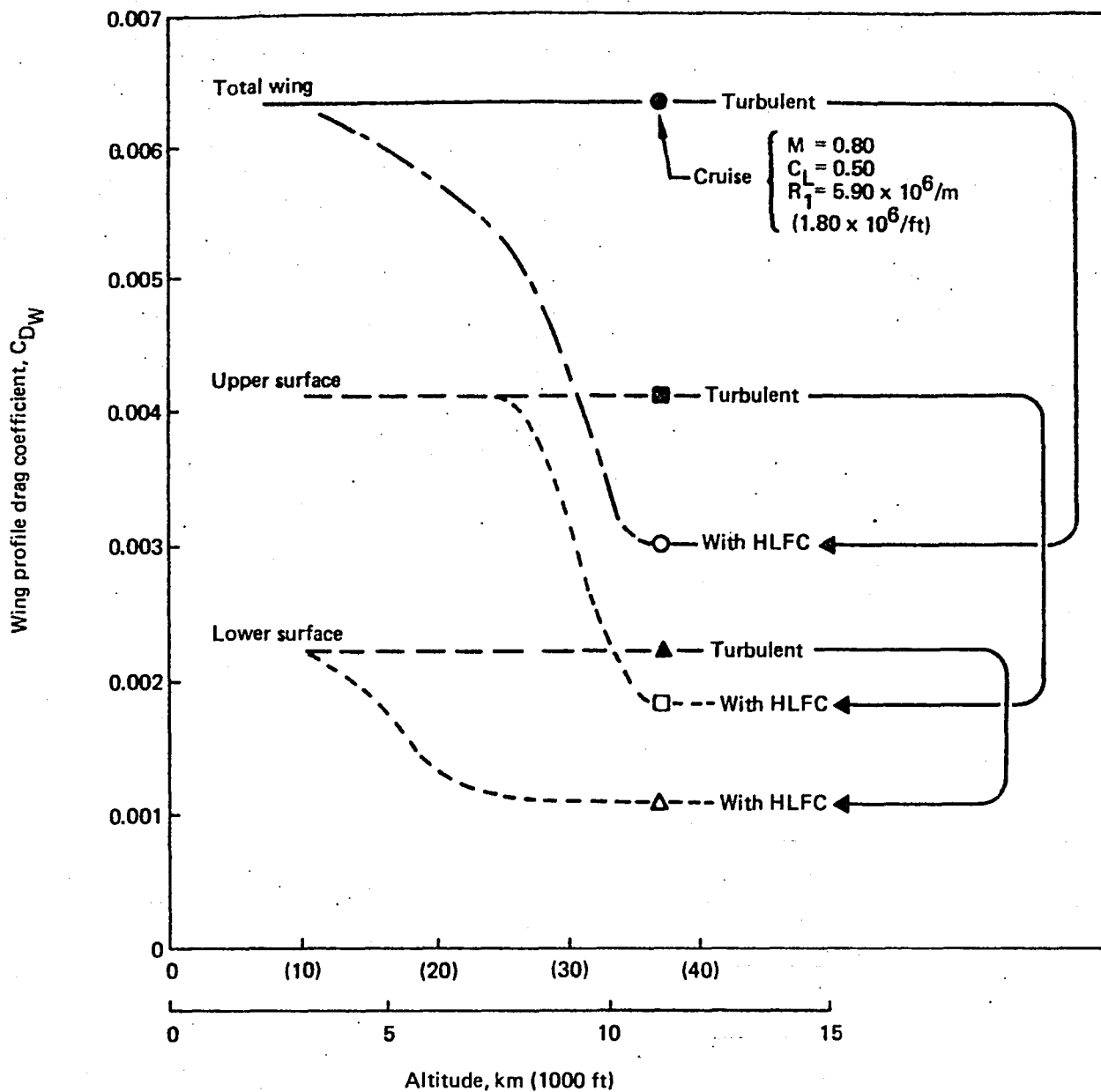
Note:

• These data are applicable to normal climb where Mach No., lift coefficient, and Reynolds No. vary with altitude.

• Cruise flap deflections are varied with altitude to keep the C_p distributions conducive to laminar flow.

86
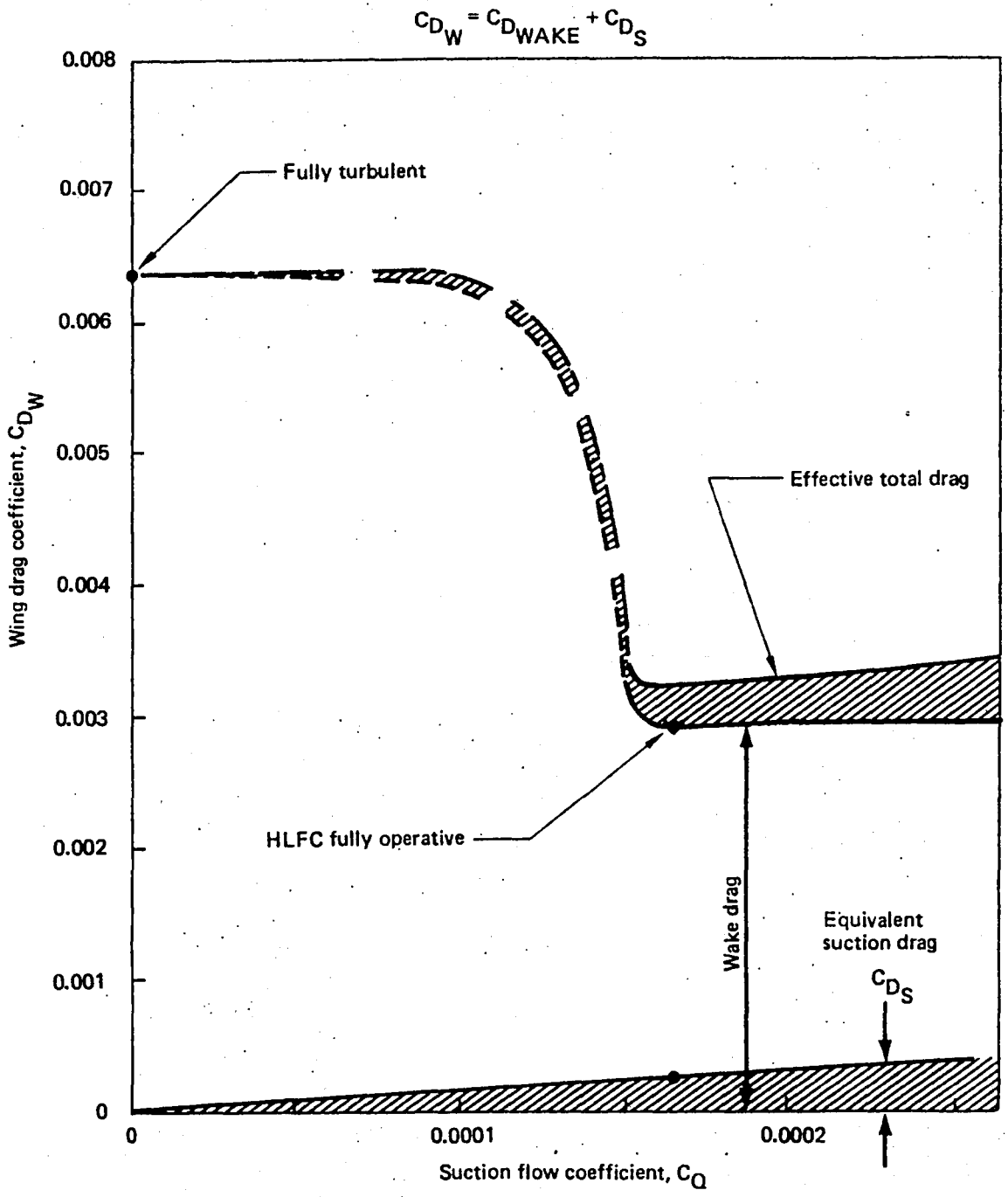
Figure 65. Components of Wing Profile Drag With HLFC

6.0 AIRPLANE APPLICATIONS

This section examines how to implement the HLFC aerodynamic design on a practical airplane and how much fuel savings can be expected to result.

6.1 AIRPLANE INTEGRATION

The airplane integration task consisted of selecting one of three major configuration concepts and then defining the structural and systems changes required to accommodate the HLFC system while continuing to provide all necessary airplane functions.

6.1.1 Configuration Selection

Section views of the three wing configurations considered are shown in Figure 66. Configuration I has both upper and lower surface suction, from the front spar forward to

Suction on both surfaces

Triple-slotted flap with increased Fowler motion

No leading-edge flap

Configuration I

Suction on upper surface only

Leading-edge Krueger flap

Configuration II

757-type flaps

Suction on both surfaces

Leading-edge Krueger flap with suction system

Configuration III

Figure 66. Cross Sections of Candidate Wing Configurations

1.6% s/c. Because it has no leading-edge device, it requires triple-slotted flaps with extended Fowler motion to reduce the approach speed. Leading-edge washing is required. Configuration II replaces the baseline wing slats with full-span Krueger flaps, which, with the baseline flap deployment, provide equivalent high lift capability. The Krueger flaps also shield the fixed leading edge from insect accumulation. Only the upper surface, however, has suction panels.
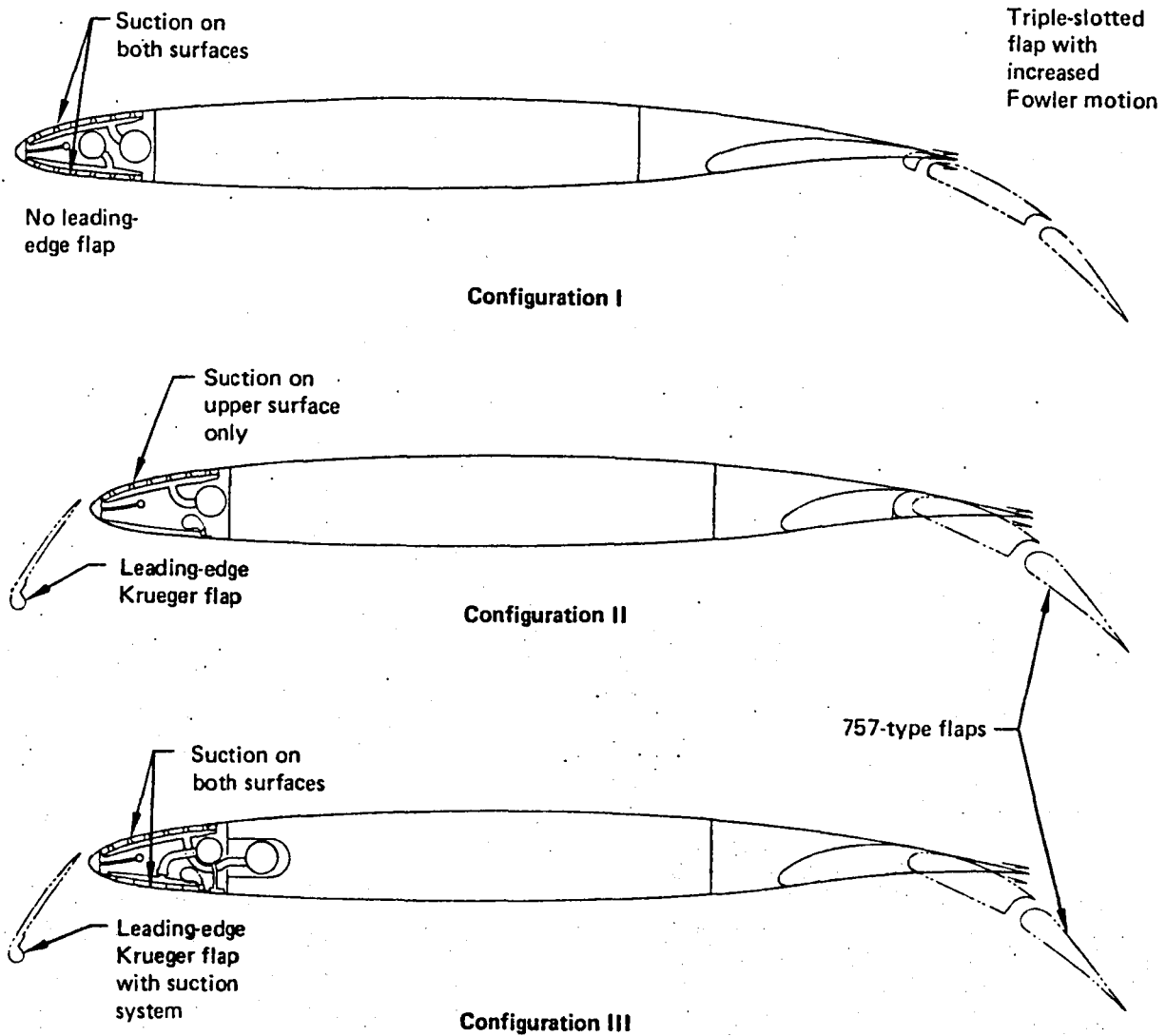
Configuration III is similar to configuration II but provides suction through the Krueger flaps and an additional suction surface between the retracted Krueger flaps and the front spar chord. Make and break connections are necessary at each flap to carry the suction plumbing to the flap. A washing system is installed in each Krueger flap to prevent insect contamination of the extended flap. The flap itself protects the fixed leading edge. Trailing-edge flaps are identical to those of the baseline airplane. The Krueger flaps and the two-surface suction system would not both fit in the wing leading edge forward of the front spar. To comply with the study ground rule of minimum deviation from 757 primary structural arrangement, weights were estimated for configuration III on the basis of providing a suction duct behind the front spar as shown at the bottom of the figure. If configuration III were studied in greater depth, the front spar would be moved to accommodate the added space requirement.

Preliminary estimates indicated cruise drag reductions of about 11% for configurations I and III, while the reduction for configuration II was only 7%.

The high lift configuration proposed for configuration III was equivalent to that used for the baseline; therefore, no change in low-speed performance relative to the baseline was anticipated. Two additional technical risks applicable to configuration III were noted:

- To maintain laminar flow, transverse downsteps must be kept small (<0.01 cm [0.004 in] at 5% chord, < 0.025 cm [0.01]in at 25%). Upsteps also must be limited (<0.03 cm [0.012 in]). While concentrated suction is known to increase allowable step size substantially, it was still considered that learning how to meet these tolerances without excessive weight penalty would have required an extensive examination of how the Krueger system could accommodate flexing while ensuring positive surface contact. This examination was not performed.

- Insect protection is provided only for the upper surface. Washing fluid is injected over the Krueger outer surface only and washes back over the upper wing. The wing lower surface and fixed leading edge are assumed to be shielded by the Krueger. This arrangement, therefore, requires only 50% of the fluid used for configuration I, where both surfaces are washed. The mechanism by which insect accretion occurs in a complex flow field is not well understood, and this arrangement would require verification.

Since both configurations I and III result in approximately equivalent reductions in fuel burn, the selection criteria were mainly risk and complexity. A summary of the advantages, risks, and disadvantages are:

- Configuration I: the advantages are (1) a simple system with no leading-edge device and (2) upper and lower surface laminar flow for least drag. The disadvantages and risks are (1) high approach speeds and landing field lengths and/or more complex trailing-edge high lift system, (2) longer takeoff field lengths, particularly for hot, high-altitude conditions, and (3) a trim penalty due to the extended Fowler flap.

90

- Configuration III: the advantages are (1) upper and lower surface laminar flow for least drag and (2) low-speed performance/field length the same as the baseline. The disadvantages and risks are (1) a stepwise tolerance requirement of from 0.015 cm (0.006 in) to 0.03 cm (0.012 in), (2) a complex suction system, (3) a weight increment for the leading-edge Krueger, (4) questionable insect protection, and (5) possible ice formation on the Krueger.

The deficiencies noted for configuration I are related to low-speed performance. This was limited by arbitrary baseline geometry constraints. The potential exists for high lift performance improvements if the wing were specifically designed for the HLFC task. The primary concern relating to configuration III is the ability to maintain the specified step tolerances without an undue weight penalty. The risks appeared to favor configuration I. It therefore was selected for further study.

6.1.2 Wing Modification

6.1.2.1 Trailing-Edge Flaps—Figure 67 shows the high lift system of the selected configuration. It was designed to retain as much of the high lift capability of the baseline airplane as practical, within the constraints of the baseline rear spar and landing gear arrangement. An additional 5% in extended wing area (Fowler motion) relative to the baseline is provided. The 757's double-slotted configuration is replaced by a triple-slotted design. The aft segment deployment mechanisms incorporate rotary actuators to provide 2-deg up, 5-deg down aft segment motion for pressure distribution adjustment in climb and cruise. Actuators are multi-geared, fail-passive assemblies. The spoiler actuators are modified to permit upward motion of the aft flap segment.

Maximum lift capability was estimated using wind tunnel data for the 757 with leading-edge slat retracted, adjusting for the additional Fowler motion, triple-slotted flap, and scale effects, yielding a FAR stall lift coefficient of 2.33. This value corresponds to an approach speed of 273 km/hr (147 kn), well above the baseline approach speed of 250 km/hr (135 kn).

Some configuration options are possible, however, to improve the maximum lift capability of configurtion I to make up for deleting the leading-edge slats. They include:

- Adjustments to the flap settings (inboard and outboard) for tailoring the span load distribution to the unprotected leading-edge situation.
- Use of the HLFC suction system for low-speed leading-edge boundary layer control.
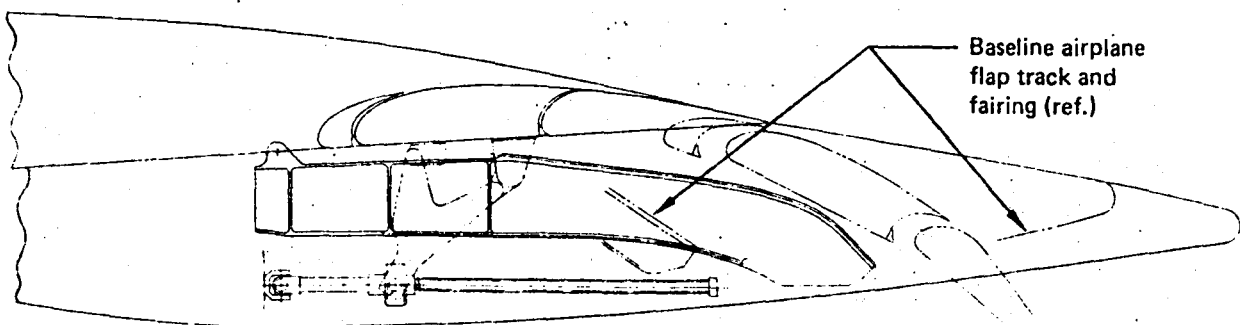- Increased flap chord and/or Fowler motion (weight penalty trade).

Baseline airplane flap track and fairing (ref.)

Figure 67. Trailing-Edge Flaps

- Reshaping of the leading edge with a possible attendant increase in HLFC suction for cruise (suction power trade).
- Drooped ailerons and flap cove (weight penalty trade).
- Increased wing area (weight penalty trade).

In addition, resizing the configuration may result in a lower wing loading for the HLFC airplane, which would result in reduced approach speed. (Optimum cruise lift coefficient for a laminar flow airplane tends to be lower than for a turbulent airplane because of its lower profile drag.)

Evaluation of takeoff field length requirements would have required developing flaps down drag polars, which was beyond the scope of the present study, but deletion of the leading-edge high-lift device can be expected to degrade takeoff performance. The configuration changes that would be considered for approach speed reduction are generally applicable to takeoff as well, and the two problems would be considered together.

6.1.2.2 **Structures**—The wing planform is identical to that of the turbulent flow baseline airplane. The center section was shortened 50.8 cm (20.0 in) (one fuselage frame), however, to accommodate suction system motors and compressors. The front spar centerline between the engine and the side-of-body was moved in conformity. Figure 68 shows the spar centerlines and indicates suction duct routing. Sizing of some structural elements near the rear spar was revised to reflect increased local loads due to larger trailing-edge flaps. At the same time, deletion of the leading-edge device permitted sizing for the absence of point loads in the leading-edge area.

The leading edge consists of upper, lower, and nose skin panels, supported by a built-up aluminum nose beam and lightweight built-up aluminum ribs. Skin panels are individually removable for replacement. Section views of inboard and outboard leading edges are shown in Figures 69 and 70. Typical upper and lower panels consist of titanium outer sheets chem-milled from the maximum thickness required at fastener locations to 0.030 over the remainder of the panel. These are bonded to individual trapezoidal section graphite-epoxy tubes, which are bonded in their turn to graphite-epoxy inner skins. The panels, in addition to their function as LFC suction conduits, are stiff structural assemblies that maintain the aerodynamic contour and carry air loads to the support ribs. Kevlar-epoxy collector plenums, two per panel, run chordwise the width of the panel and are connected to the main suction duct for reach surface.

Outboard of the engine nacelle, the perforated titanium nose skin is backed by porous plates in sealed chambers forward of the nose beam, with washing fluid injected as required. (Fluid for anti-icing is injected into the same chambers by a separate supply system. Separate fluid-supply systems were used to maintain the glycol concentrations at 50% for the washing fluid and 80% for the anti-icing fluid. When this study was made, data were not available to confirm that a common fluid could perform both functions satisfactorily.)

From the engine nacelle inboard, the nose skin is bonded to Kevlar-epoxy hat sections filled with porous medium. The hat sections are bonded to an inner Kevlar-epoxy skin. Fluid for washing or anti-icing is injeted into the hat sections as required. The spaces between hats are conneced to plenums connected in turn to the suction ducts.
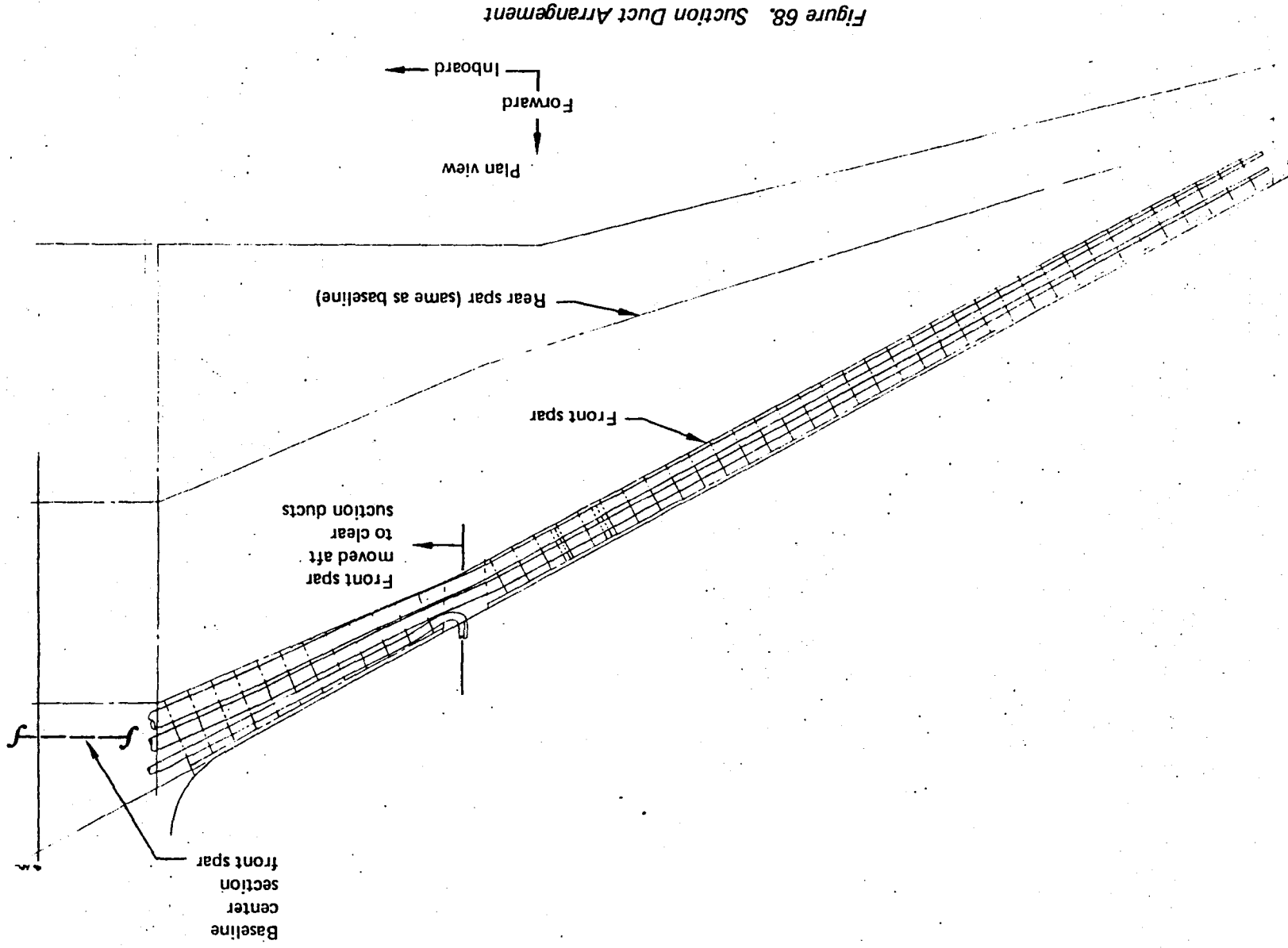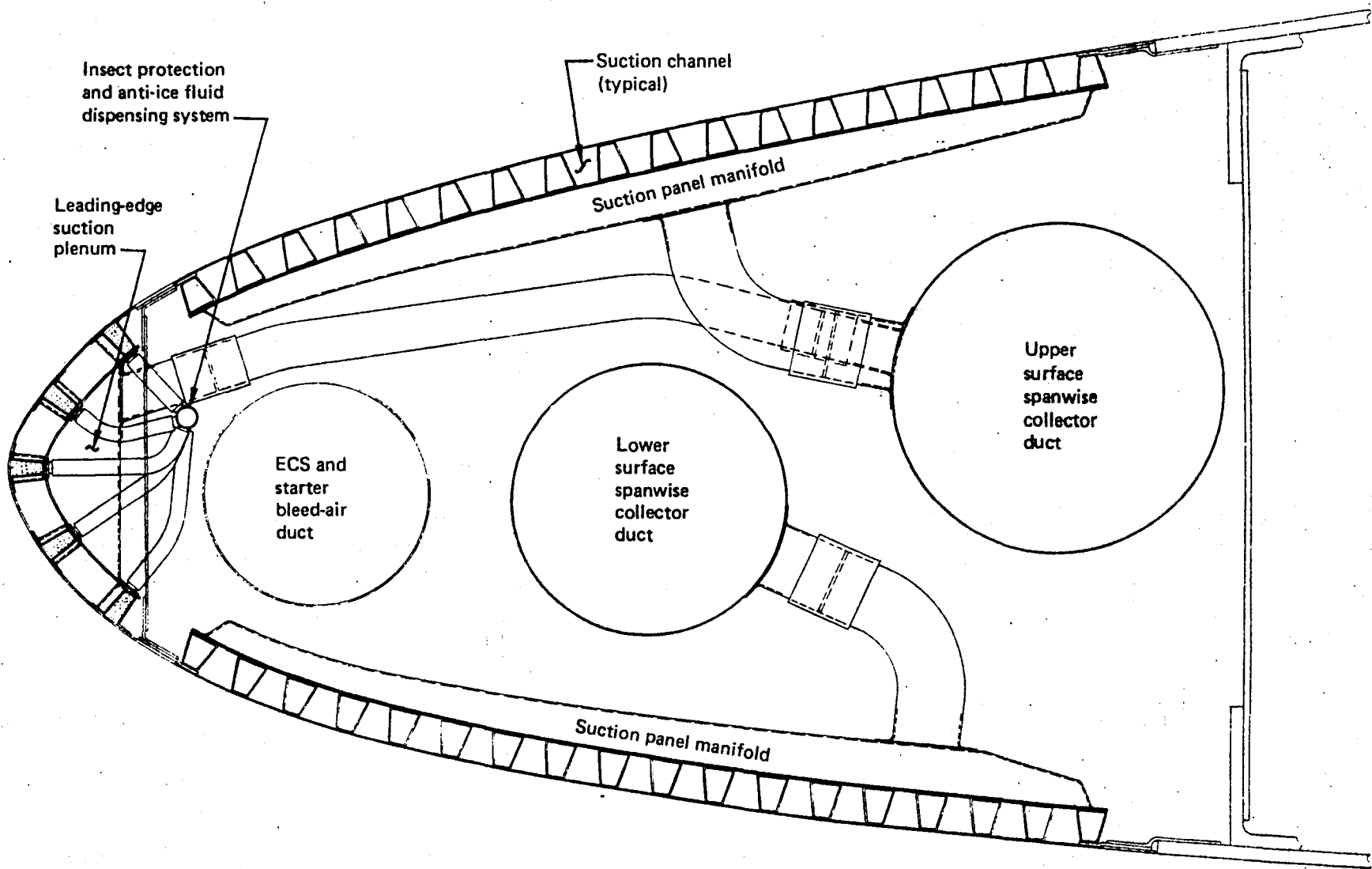
Figure 68. Suction Duct Arrangement

Inboard →

Forward

Plan view

Rear spar (same as baseline)

Front spar

Front spar
moved aft
to clear
suction ducts

Baseline
center
section
front spar

93

Insect protection
and anti-ice fluid
dispensing system

Leading-edge
suction
plenum

Suction channel
(typical)

Suction panel manifold

Upper
surface
spanwise
collector
duct

ECS and
starter
bleed-air
duct

Lower
surface
spanwise
collector
duct

Suction panel manifold

94

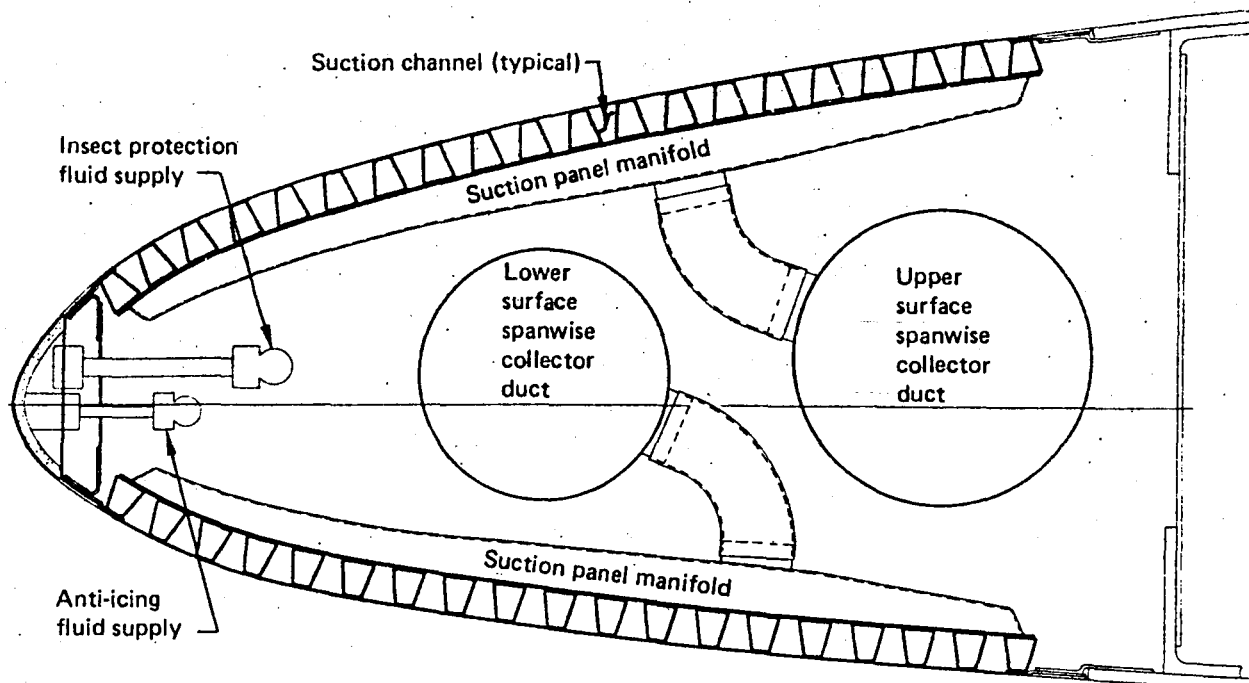*Figure 69.   Inboard Leading-Edge Arrangement*

Figure 70. Outboard Leading-Edge Arrangement

6.1.3 Systems Modification

Suction, cleaning, and anti-icing systems were sized for the three wing leading-edge configurations defined in section 6.1.1. The system ground rules for each configuration were:

- Configuration I
    - Suction—forward of front spar, upper and lower surfaces
    - Cleaning—liquid distribution on upper and lower surfaces
    - Anti-icing—liquid TKS* system
- Configuration II
    - Suction—forward of front spar, upper surface only
    - Cleaning—none
    - Anti-icing—liquid TKS system
- Configuration III
    - Suction—forward of front spar, upper and lower surfaces
    - Cleaning—Krueger flap only
    - Anti-icing—liquid TKS system

Table 6 summarizes the evaluation criteria and results. Suction, cleaning, and anti-icing system concepts are presented for configuration I. Summary data comparing the system designs for the three leading-edge configurations are presented where appropriate.

6.1.3.1 Suction System—Three suction zones were selected to meet the HLFC airfoil performance requirements defined in section 5.1.2. Outboard of 40% span, suction is applied between 1.6% and 16% on both wing surfaces. Inboard of 40% span, this is supplemented by nose suction to control attachment line boundary layer growth. Suction flow requirements are shown in Figure 55.

---

*TKS is a trade name for a type of anti-icing system using a glycol and water mixture dispensed from the leading edge.

Table 6. HLFC Systems Evaluation Matrix

Evaluation item	Configuration		
	I	II	III
Weight			
Suction	2	1	3
Cleaning system	2	—	1
Anti-icing system	1	2	2
Technical risk			
Suction	1	2	3
Cleaning system	1	2	3
Anti-icing system	1	1	2
Performance			
Suction system	1	2	3
Cleaning system	1	2	3
Anti-icing system	1	1	1
Installation complexity			
Suction system	1	2	3
Cleaning system	1	—	2
Anti-icing system	2	1	3
Total	15	16	29

Evaluation numbers are from 1 (best) to 3 (worst) on the basis of these criteria:

● Weight—based on data in section 6.2.1.

● Technical Risk—based on the ability to meet the operating conditions without added penalties

● Performance—based on the confidence that the performance calculations, duct losses, and compressor horsepower represent the actual system.

●, Installation complexity—based on the ability to integrate the several systems in the wing leading edge.

Suction Ducting—Figure 71 shows the schematic arrangement of the suction ducting network. Surface boundary layer air is drawn through the perforated skin into suction channels. The suction channels are connected to suction panel manifolds through metering holes, which are varied in spacing and diameter to produce the desired flow distribution along the wing chord. The suction panel manifolds then feed into spanwise collector ducts through connector tubes equipped with flow-limiting nozzles to establish the pressure gradients required to maintain the desired spanwise suction flow distribution.

Suction duct segment sizes are defined in Table 7. Duct diameters were determined based on selected Mach numbers for each segment. The suction plenum Mach number was set at 0.05 to minimize the pressure gradient in the plenum channels. The plenum suction duct Mach number was set at 0.1, and the suction duct Mach number, at 0.2. The plenum suction duct nozzle accelerates the plenum suction flow to match the air velocity in the spanwise collector duct. (This study did not attempt to size each orifice and nozzle, as their size would have to set by calibration tests.) Maximum duct run lengths were used to predict the overall pressure losses for each duct segment. Figure 72 shows the pressure drops for each segment and the pressure rise necessary to achieve the desired flow. Because of the difference in the suction pressure needed to provide the desired flow, the upper and lower surface ducts were kept separate from each other.
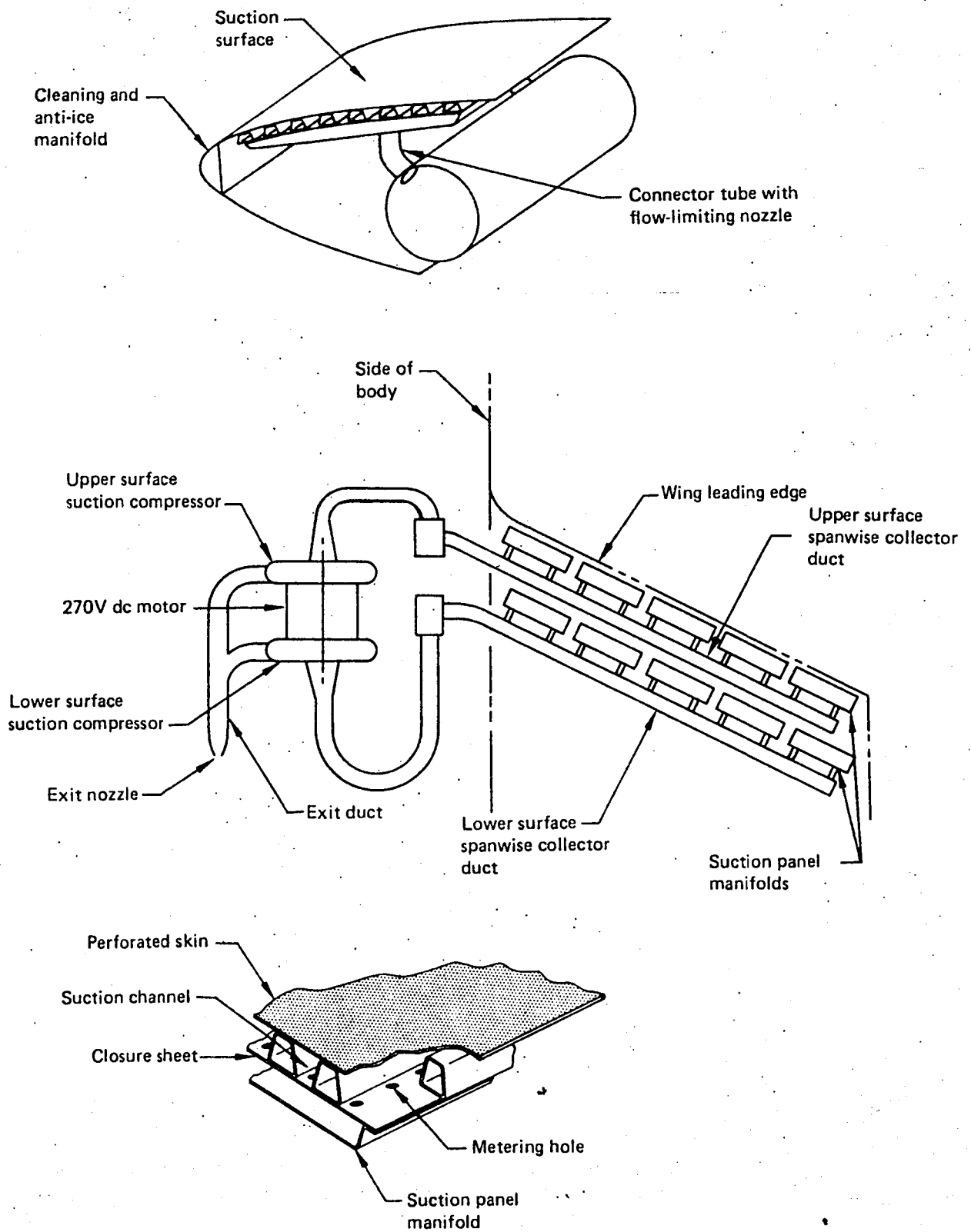
96

Figure 71. Suction System Schematic

Table 7. Suction System Sizing Characteristics

Item	Upper surface		Lower surface	
Suction plenum				
Depth, cm (in)	2.54	(1.0)	2.54	(1.0)
Length	See Figure 68		See Figure 68	
Average Mach number	0.05		0.05	
Area/wing, m² (ft²)	11.67	(125.6)	12.11	(130.3)
Average span per panel, m (ft)	1.1	(3.6)	1.1	(3.6)
Plenum suction duct				
Depth, cm (in)	1.3 to 2.6	(0.5 to 1.0)	1.3 to 2.6	(0.5 to 1.0)
Width, cm (in)	5	(2)	5	(2)
Length	See Figure 68		See Figure 68	
Average Mach number	0.1		0.1	
Tube diameter, cm (in)	1.9	(0.75)	1.9	(0.75)
Number of tubes/panel	2		2	
Spanwise collector duct				
Diameter, cm (in)	21.6	(8.5)	17.8	(7.0)
Length, m (ft)	18.3	(60.0)	18.3	(60.0)
Overall diameter, cm (in)	15.2	(6.0)	15.2	(5.0)
Compressor				
Wheel diameter, cm (in)	29	(11.4)	21.5	(8.45)
Overall diameter, cm (in)	55.6	(22.0)	40.6	(16.0)
Overall length, cm (in)	81.3	(32.0)	58.4	(23.0)
Design pressure ratio	3.35		1.68	
Design inlet pressure, kPa (lb/ft²)	8.52	(178.00)	16.95	(354.00)
Design power, kW (hp)	51.3	(68.8)	33.9	(45.4)
Shaft speed, r/min	23 000		23 000	
Exit duct				
Diameter, cm (in)	15.2	(6.0)	15.2	(6.0)
Length, m (ft)	6.1	(20.0)	6.1	(20.0)

Inboard Leading-Edge Suction Ducting—Inboard wing leading-edge suction is applied to control the attachment line boundary layer growth. A suction zone was estabished (fig. 73) based on the maximum extent the stagnation line traveled over the airfoil leading edge during cruise. The quantity of suction necessary to keep the attachment line boundary layer laminar is not precisely known. Suction sizing sensitivity studies showed that a 10% increase in the inboard suction flow would not result in a significant compressor or duct segment size change. Therefore, the suction flow requirement defined in section 5.2.3.1 was not changed to account for the additional leading-edge suction. The pressure in the leading-edge suction plenum is referenced to the upper surface suction channel collector duct. The channel collector duct is connected to the leading-edge plenum as shown in Figure 69. Metering orifices set the leading-edge plenum pressure with respect to the channel collector duct.
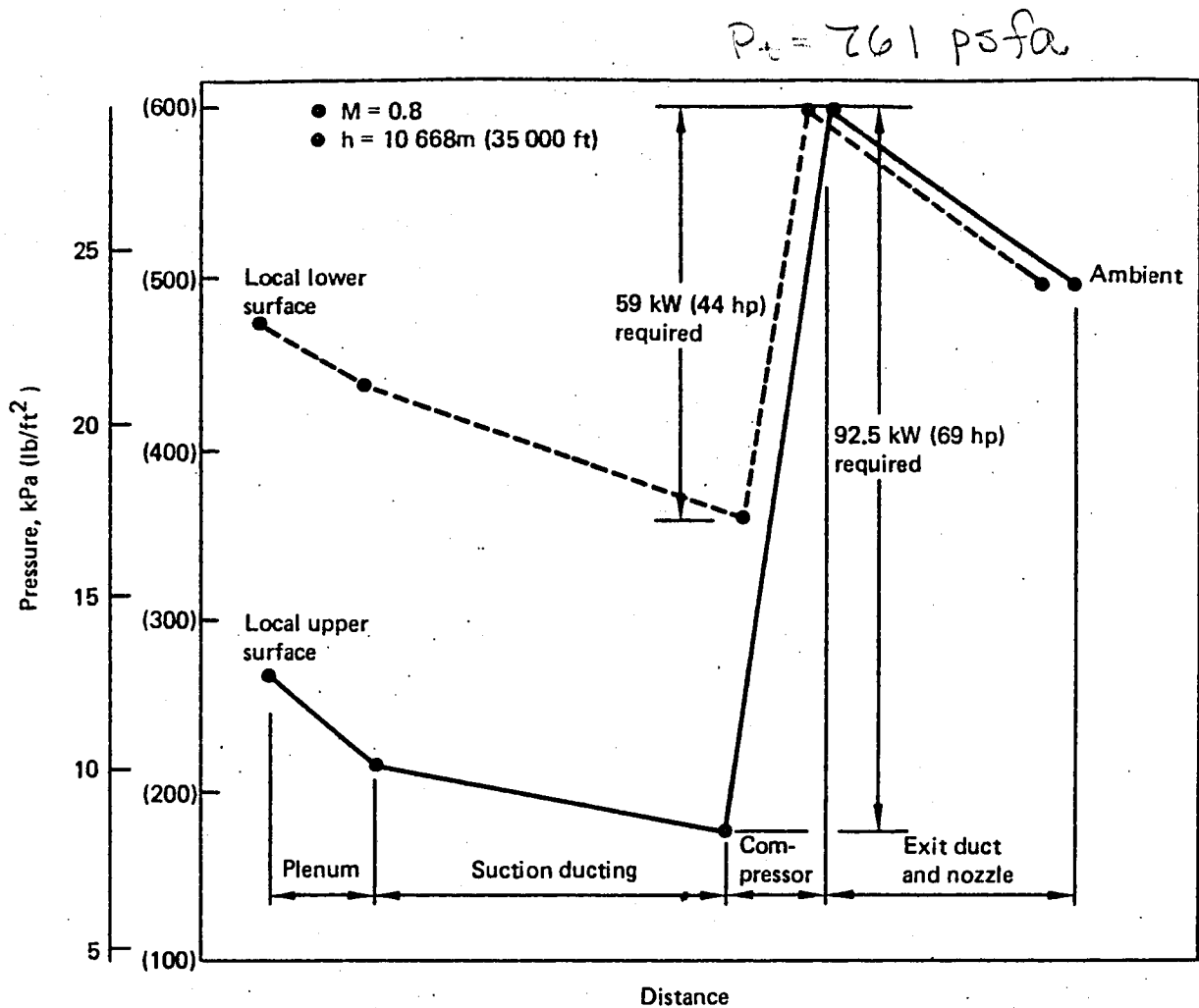
$P_t = 761 \text{ psfa}$

Figure 72. Hydraulic Gradient for Suction System

Suction Compressors—Suction pressure is provided by two suction compressors for each wing. They are driven by a single electric motor. The compressor size was set to meet the flow and pressure requirements of Figures 55 and 72. Compressor characteristic dimensions were determined from the specific speed and specific diameter criteria of Reference 24. The optimum speed for the upper surface suction compressor set the design speed for the compressor/motor set.

Upper and lower surface suction compressors were matched based on the optimum speed for the upper surface compressor and the best corresponding specific speed for the lower surface suction compressor. Design results show that the upper surface suction compressor should incorporate a radial outflow wheel. The lower surface suction compressor should incorporate a mixed flow wheel. Weight and volume of the compressors were based on the correlations reported in Reference 25. Table 7 also gives the upper and lower surface suction compressor characteristic dimensions for the design point suction flow at a flight Mach number of 0.8 and an altitude of 10 668m (35 000 ft). Off-design compressor performance characteristics were not determined in this study. The maximum rotational speed was set at 30 000 r/min, based on a tip speed limit of 457 m/s (1500 ft/s) for the upper surface compressor wheel.

99
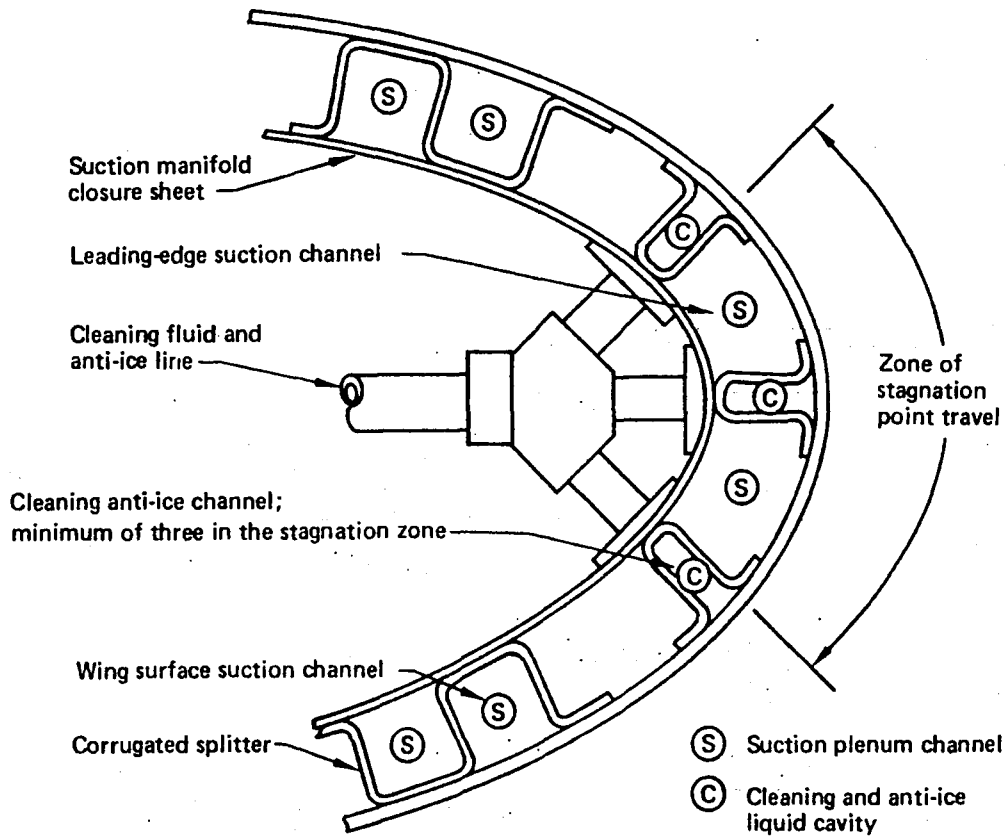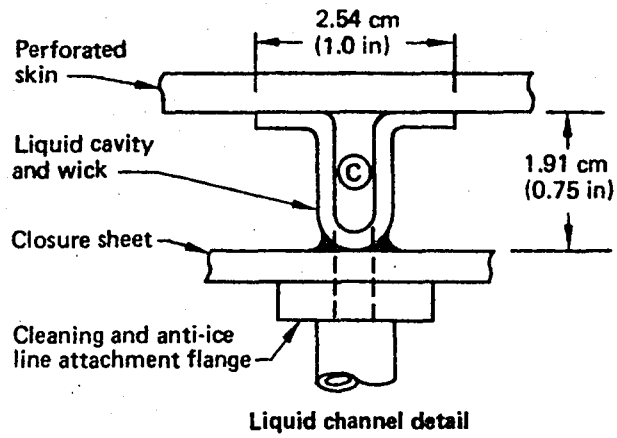
Figure 73. Inboard Leading-Edge Cleaning Anti-Ice and Suction Channel

Operation of the suction system is based on use in climb, cruise, and descent at altitude above 1524m (5000 ft) only. No specific purge or cleaning system is proposed. The suction system was not designed for low altitude or simultaneous operation with either the suction or cleaning system on. Ground checkout is possible although the high air density will greatly reduce suction flow. Any water entering the suction plenum will be removed via plenum drains and scuppers in the suction ducting upstream of the suction compressors. The perforated surface selected for this configuration is expected to prevent significant quantities of water from entering the suction system.

Electric Motor—A 270V dc electric motor was selected to drive both compressors. The motor input power was set to allow for a 5% increase in the suction flow coefficient. The characteristic dimensions for the motor are shown in Table 8. While the motor has not been designed in detail, similar motors have been evaluated under the Reference 26 Air Force contract. The motor design objectives are:

- Weight-to-power ratios of 0.3 kg/kW (0.5 lb/hp) or less
- Use of gas film bearings
- Integral motor winding cooling
- Liquid-cooled stator

Table 8. Drive Motor Size Summary

Size	Configuration	
	I and III	II
Output power, kW (hp) (includes 5% compressor power margin)	103 (138.0)	63 (84.5)
Rotor speed, r/min	23 000	23 000
Diameter, cm (in)	15.2 (6.0)	12.7 (5.0)
Length, cm (in)	38.1 (15.0)	30.4 (12.0)
Motor weight, kg (lb)	26.7 (59.0)	16.3 (36.0)
Inverter weight, kg (lb)	13.6 (30.0)	8.1 (18.0)

Actual motors, AiResearch Manufacturing Company

44.8 kW (60 hp), 40 000 r/min, 13.6 kg (30 lb) =95%, D = 14.0 cm (5.5 in),
L = 25.4 cm (10.0 in)
134.3 kW (180 hp), 27 000 r/min, 33.1 kg (73 lb) = 95%, D = 15.2 cm (6.0 in),
L = 30.4 cm (12.0 in)

Note: Either dc or ac power generators can be used; however, ac power would require rectification to 270V dc.

Control—Control of the suction system would be based on developing a suction plenum pressure schedule that can be correlated against flight parameters such as altitude, Mach number, and wing angle of attack. The suction compressor then can be operated to maintain the desired suction pressure by varying the shaft speed. Speed control can be accomplished by varying the pulse frequency of the dc motor. Further compressor design work is needed, however, to establish if speed control alone can povide the necessary operating range or if inlet guide vanes (IGV) are needed to meet off-design suction flow demands. The compressor weights include an allowance for the suction compressor IGVs and associated controls.

6.1.3.2 Cleaning System—A liquid intercept system (fig. 74) was selected in preference to dispensing a cleaning agent on the airfoil after it was contaminated. A film of liquid is exuded near the stagnation point and covers the wing surface, intercepting any debris or insects the wing encounters. This film is maintained during takeoff and climb to 1524m (5000 ft). (It also can be maintained on approach and landing to obviate the need to clean the leading-edge during a stop.) Flow rates necessary to establish the liquid film were based on the wind tunnel results presented in Reference 3. Figure 74 shows the routing of the liquid from the storage tank to the wing leading edges. This system incorporates a proportioning unit to control the pressure drop to each distribution manifold. The distribution manifold contains a porous stainless steel wire mesh that ensures even distribution of the fluid over the length of the manifold. Two manifold configurations are used on the wing. Figure 73 shows the inboard fluid distribution manifold that permits leading-edge suction during cruise operation. Figure 74 shows the wing distribution manifold outboard of the engines. Both manifolds allow either cleaning fluid or anti-ice fluid to be dispensed on the wing surface.
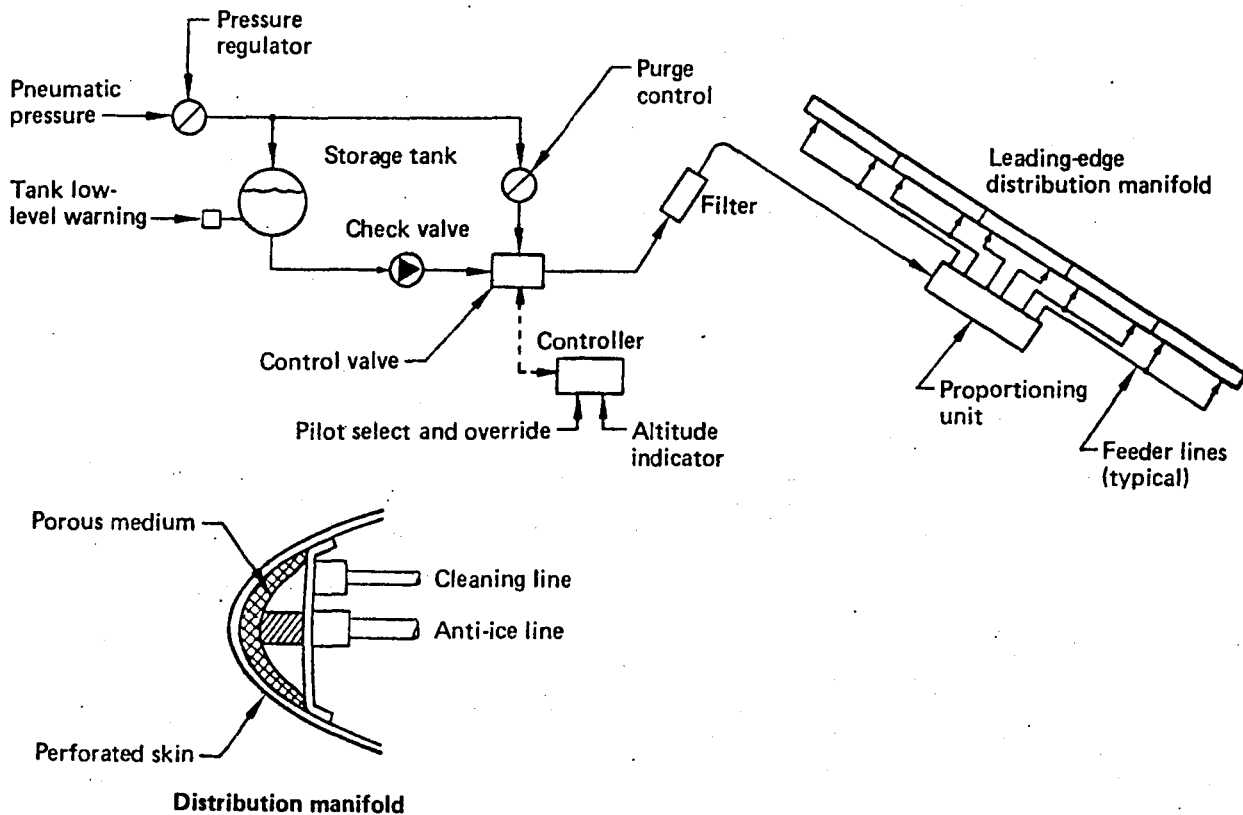
Figure 74. Cleaning System

Data were not available to assess the extent of the wing chord protected for liquid flow rates defined in Reference 3. The reference photographs, however, did show that uniform surface protection was produced at the lowest flow rate tested. The sizing estimates for this study were based on a 0.0102 kg/min/cm (0.057 lb/min/in) value. Line sizing was based on a liquid Reynolds number of 10^4 or greater to minimize pressure drop.

102

Table 9 lists the liquid system characteristic dimensions. The system can be operated on either pneumatic or electric power, with manual and automatic control options. A purging capability eliminates the liquid from the manifolds after use and flushes foreign material out of the system.

The cleaning system operation protects the wing for 13 min of flight during takeoff, climb, descent, and landing flight segments. A maximum required operational altitude of 1524m (5000 ft) above ground level has been selected based on insect aerial dispersion data in Reference 20. The flow rate of the washing liquid was held constant for this study; however, it is likely that lower rates may be sufficient out of immediate ground vicinity. Additional tests are needed to determine the extent of chord protected and the film thickness needed to intercept insects and other debris.

6.1.3.3 Anti-Icing System—A liquid anti-icing system was chosen as the only suitable one for an HLFC airplane after traditional bleed air and electric-powered anti-ice systems had been considered. The liquid system offered the least complexity and the lowest weight. The system is based on a design by TKS, Ltd. (ref. 27). The operating principle of the liquid anti-ice system is to allow ice to shear off the wing surface. A similar system currently holds transport category airworthiness certificates in both Britain and Canada for the British Aerospace Corporation HS-125 business jet.

Table 9. Cleaning System Summary

Item	Requirement	Characteristic dimensions	Material
Storage tank	454 kg (1000 lb)	1.4m (4.5 ft) diameter sphere*	Carbon filament
Fluid, Configuration I and Configuration III	454 kg (1000 lb)	1126 kg/m^3 (70.3 lb/ft^3)	Glycol/ water
Distribution lines	$R_N > 10^4$	1.6 cm x 49.4m (5/8 in x 162 ft)	Plastic—0.21 kg/m (0.14 lb/ft)
Feeder lines	$R_N > 10^4$	0.8 cm x 49.4m (5/16 in x 162 ft)	Plastic—0.052 kg/m (0.035 lb/ft)
Valve and control	Modulate flow	7.62-cm (3-in) cube	Aluminum
Manifold Configuration I	Distribute cleaning fluid	7.62 cm x 5.08 cm x 34.10m (3 in x 2 in x 112 ft)	Fiberglass + stainless steel
Configuration III		3.81 cm x 5.08 cm x 34.10m (1.5 in x 2.0 in x 112.0 ft)	Fiberglass + stainless steel

*Maximum capacity 1315 kg (2900 lb).

Figure 75 shows the functional schematic of the anti-icing system. All components shown represent developed hardware. Dispensing the liquid through the perforated skin requires addition of the porous medium behind the perforated skin to distribute the liquid evenly along the wing span by capillary action. Liquid pressure is controlled by the proportioning block, which ensures that the proper flow is available to each anti-ice panel.

Single manifold concept
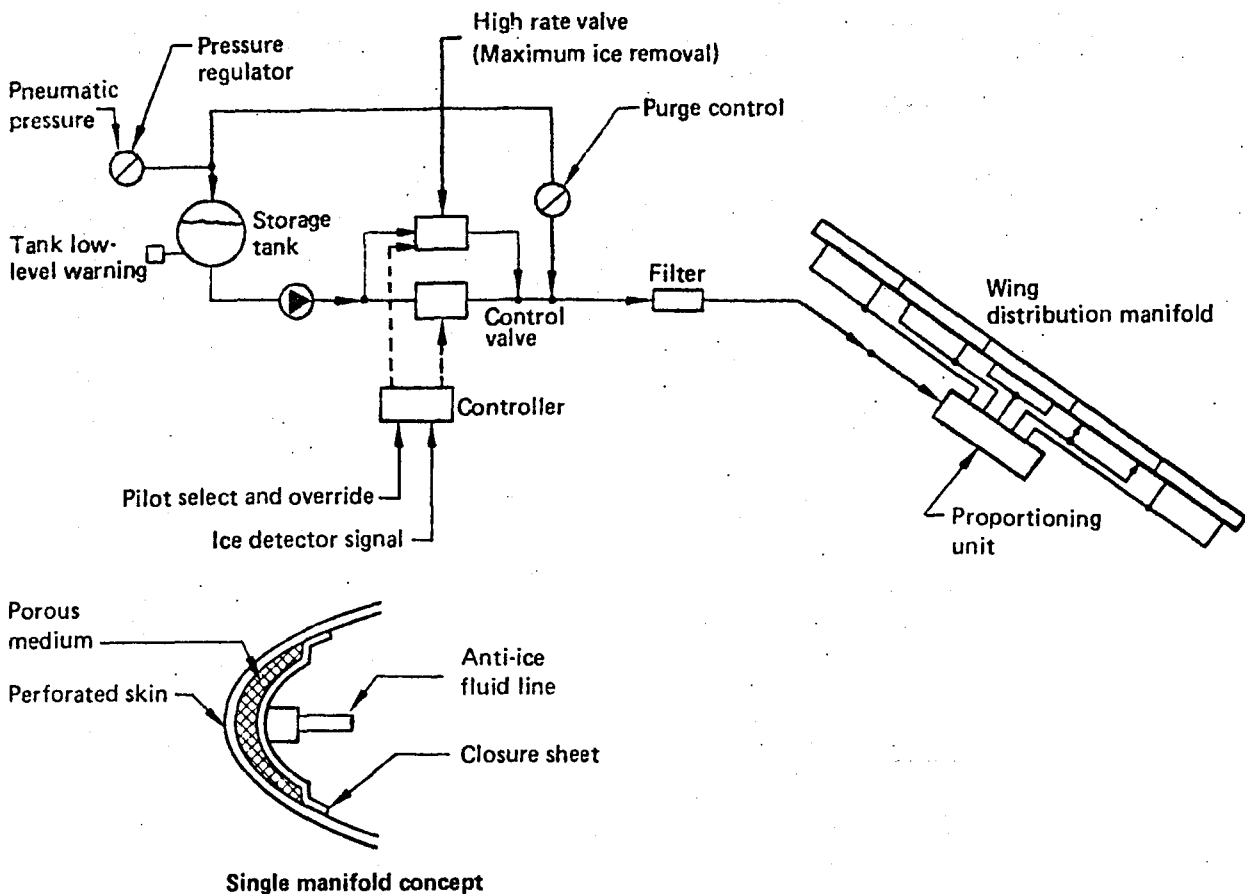
(Figure 73 shows a possible three-manifold configuration.)

Figure 75. Anti-Icing System

Table 10 lists anti-icing system component sizes. Anti-icing system operation is controlled by traditional icing detection methods and procedures. Either pneumatic pressure or electrically driven pumps can be used to force the anti-ice fluid through the wing surface. The anti-ice fluid consists of an 80% glycol and water mixture. A small amount of a wetting agent is used to achieve uniform distribution of the fluid over the wing surface.

6.1.3.4 Power Generation— Power for the HLFC suction system is generated by a dedicated 270V dc electrical system, completely independent of the existing 115/200V, 400-cycle, three-phase system. The samarium cobalt generators supply 103 kW for configurations I and III and 63 kW for configuration II. The 120-kW (75-kW for configuration II) generator is driven from a core-mounted gearbox located in the area between the fan bypass duct and the compressor casing aft of the fan frame. Because of the simplicity and low heat rejection of the generator, the cooling oil supply is shared with the engine oil system. This avoids the need to provide pressure pumps, scavenge pumps, or dedicated heat exchangers for the HLFC power system.

Table 10. Anti-Icing System Summary

Item	Requirement	Characteristic dimensions	Material
Storage tank	63.5 kg (140 lb)	50.8-cm (20-in) diameter sphere	Carbon filament wound
Fluid	63.5 kg (140 lb)	–	80% glycol/20% water
Lines	$R_N > 10^4$	0.8 cm x 49.4m (5/16 in x 162 ft) 0.48 cm x 49.4m (3/16 in x 162 ft)	Plastic 4.052 kg/m (6.034 lb/ft) Plastic 0.019 kg/m (0.0126 lb/ft)
Valve and control	Regulate and shutoff	7.62-cm (3-in) cube	Aluminum
Manifold	TKS design (ref. 27)	7.62 cm x 1 cm x 34.1m (0.3 in x 0.4 in x 112 ft)	Stainless steel
Supports Configurations II & III	Structural integrity	Unknown	–
Configuration I	Structural integrity	Unknown	–

The engine indication and crew alerting system (EICAS) controls and monitors the dedicated electrical system. Monitor and control signals are transmitted by a digital data bus. A block diagram of the system is shown in Figure 76.

6.1.3.5 Flight Displays—The following systems were evaluated:

Flight Management Computer System (FMCS)—The FMCS computes guidance parameters for each phase of the lateral and vertical navigation flight profile. The FMCS software furnishes an appropriate set of performance modes and allows the pilot to select any performance mode by manually operating the control display unit.

The output parameters for each of the performance guidance modes are constrained by operating limits for stall protection, maximum operating speeds, flap placards, maneuver margins, maximum thrust, and other operating limitations such as ATC constraints. Manual and automatic operation of the HLFC system must be implemented in the FMCS software. It must be reprogrammed to reflect the changed operating characteristics due to operation of the HLFC system in cruise.

Thrust Management System (TMS)—The TMS operates in conjunction with the inertial reference system, air data system, angle-of-attack sensors, flap and elevator sensors, flight management computer, caution and warning system, and air/ground logic to provide full flight regime autothrottle and display of thrust-setting limits.

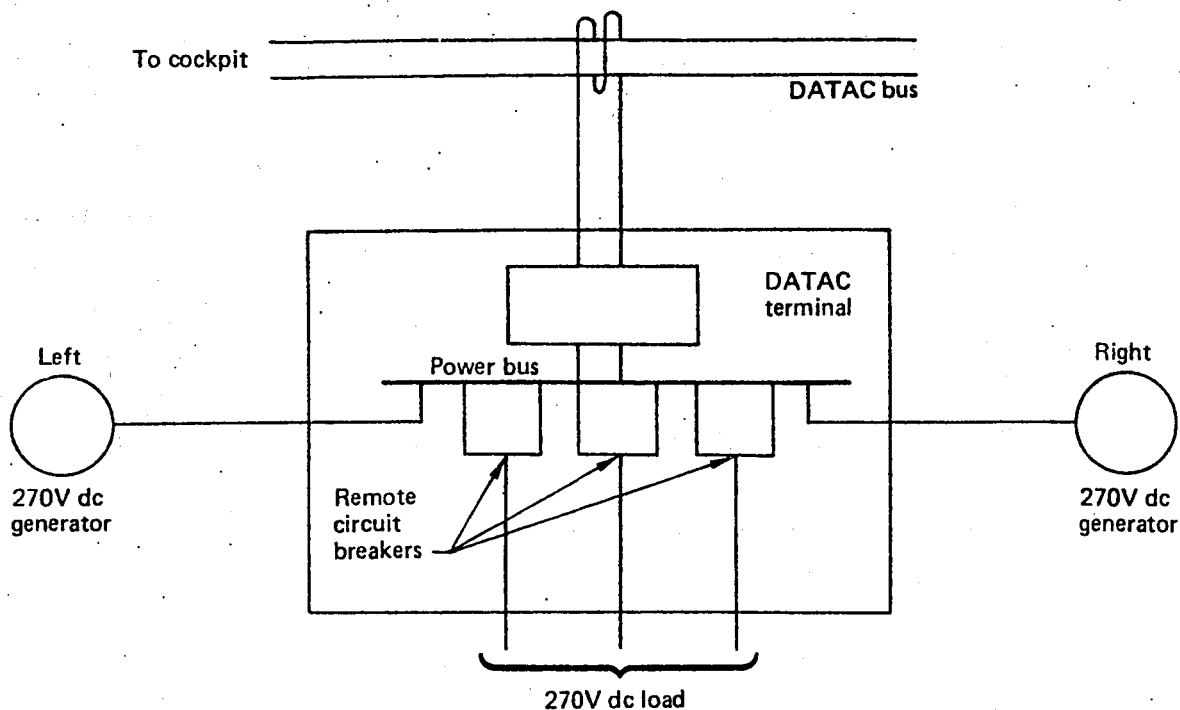The TMS consists of the thrust management computer (TMC), the autothrottle servo, and the thrust mode select panel.

Figure 76. Block Diagram—HLFC Electrical System

In the HLFC airplane, TMS autothrottle operation will be affected by the suction system mode (on or off), and possibly by the state of the boundary layer itself, which can be detected by flush-mounted sensors.

The software resident in the TMC will require programming to reflect the additional parameters and the different operating characteristics of the propulsion system when the HLFC is functioning.

Engine Indication and Crew Alerting System (EICAS)—The EICAS is an integrated system that displays engine data and caution and warning messages for accurate and rapid interpretation by the flight crew. The system must be modified to provide monitoring of the suction system, using data from laminar flow sensors, fuel flow, Mach, and the dedicated electric system. EICAS software may require modification to monitor the different operating charateristic of the propulsion system that result when the HLFC system is operating.

6.2 BENEFITS ASSESSMENT

This section presents an evaluation of the weight changes and fuel savings of the HLFC system.

6.2.1 Weight Analysis

Preliminary weight estimates for the three candidate configurations were made using statistical/parametric methods. The results are summarized in Table 11.

Table 11. Weight Comparison—HLFC Configurations

Item affected	Configuration I		Configuration II		Configuration III	
	kg	(lb)	kg	(lb)	kg	(lb)
Leading edge	Fixed -704	(-1550)	Slotted Krueger -150	(-330)	Slotted Krueger -150	(-330)
Trailing edge**	Extended Fowler +290	(+640)	Same as 757		Same as 757	
Cleaning system	Liquid-wing LE +572	(+1260)	None		Liquid-wing LE +345	(+760)
Anti-icing system	Liquid-wing LE +72	(+160)	Liquid-wing LE +132	(+290)	Liquid-wing LE +132	(+290)
Suction system	Upper and lower surface +399	(+880)	Upper surface +268	(+590)	Upper and lower surface +517	(+1140)
Supply power	120 kVA system +150	(+330)	90 kVA system +122	(+270)	120 kVA system +150	(+330)
Total weight*	+779	(+1720)	+372	(+820)	+994	(+2190)

*Weights shown are deltas applied to the baseline 757-200.

**No weight increment for the pressure distribution control flap (movable aft segment) was included.

When configuration I had been selected and defined in greater detail, incremental weights (from the 757-200 baseline) were estimated for each identified change, as discussed below.

6.2.1.1 Leading Edge—The 757-200 leading edge (with movable slat) was replaced by a fixed leading edge made of perforated titanium skin over a conventional aluminum backup structure (rib webs, chords, and stiffeners). The proposed new leading-edge structure weighs 481 kg (1060 lb) versus 1129.5 kg (2490.0 lb) for the baseline.

6.2.1.2 Trailing Edge—The Fowler motion of the trailing-edge flaps was increased to 80% of the flap chord. The new flap concept has a small foreflap, a main flap, and an aft flap. The aft flap acts as a third slotted flap when deployed at takeoff and landing. It also is used for pressure distribution control in cruise, with a deflection range of 2 deg up and 5 deg down. The existing 757-200 trailing-edge flap system has double-slotted flaps both inboard and outboard. The increased flap motion would cause excessive gap between the leading edge of the foreflap and the trailing edge of the spoilers and fixed trailing edge. The lengths of the spoilers and fixed trailing edge were therefore increased. As a result, the flap thickness had to be reduced.

The designing force on the flap is the force normal to the flap when extended to its maximum deflection. The design dynamic pressure and the longest unsupported length of flap (used to determine the structural deflections of the flap) were the same as the baseline. The new normal force for each new segment was determined by assuming that the lift-to-chord ratio for each flap segment was the same as the baseline. The resulting

flap segment weights are higher than the baseline values, both because of the higher normal forces and because of reduced structural depth.

Weights of the new main flap supports, which transfer the flap system load to the torque box of the wing, were determined by the change in moment that the supports must transfer. The auxiliary flap support weights were correlated to the moments they transfer to the main flap.

Flap fairings are non-load-carrying structure, so a unit weight in pounds per square foot was used to account for the lengthening of the flap fairings.

Spoilers and the fixed trailing edge between the spoilers were also increased in weight because of the increase in chord due to the increased gap caused by the extended Fowler motion of the flaps.

A weight summary of the trailing edge structure is included in the operating empty weight (OEW) summary, Table 12.

6.2.1.3 Systems—Both upper and lower surfaces have suction in conjunction with a liquid cleaning system and a liquid anti-icing system. The channel collector ducts are made of Kevlar, and there are four per panel. A description of the system is in section 6.1.3. The suction channels are made of graphite and run the length of the panels.

The cleaning and anti-icing systems are also described in section 6.1.3. The storage tanks are carbon filament wound. The cleaning fluid weight is not carried in the operational

Table 12. Operating Empty Weight Summary

Item	kg	(lb)
Existing 757-200 OEW	58 891	(129 830)
Delete existing leading edge	-1 129	(-2 490)
Add new leading edge	+481	(+1 060)
Delete existing trailing-edge flaps	-1 392	(-3 070)
Add new trailing-edge flaps	+1 583	(+3 490)
Delete existing flap fairings	-168	(-370)
Add new extended flap fairings	+204	(+450)
Delete existing spoilers	-245	(-540)
Add new spoilers	+281	(+620)
Add suction system	+472	(+1 040)
Add cleaning system (not including fluid)	+147	(+325)
Delete wing anti-icing	-27	(-60)
Add new anti-icing system	+75	(+165)
Add electrical supply power system	+181	(+400)
Miscellaneous	+9	(+20)
New HLFC Configuration I	59 363	(130 870)
Cleaning system fluid (expendable)	113	(250)

108

empty weight but as an expendable because the cleaning system is used only from takeoff to 1524m (5000 ft) altitude. The anti-icing fluid is carried in the operational empty weight because it normally is not expended in flight.

The electrical system has one 120-kVA samarium-cobalt generator per engine. The generator requires an oil cooling system along with attachment pads and wiring disconnects. *Contradiction from pg. 101, 6.1.3.4.*

6.2.1.4 Operating Empty Weight—Table 13 provides a weight summary for the principal components and systems of the airplane OEW. The center-of-gravity position moved forward one-half of one percent with the HLFC modifications added to the 757-200. No new operational restrictions are needed with the HLFC airplane. It can operate within the existing 757-200 center-of-gravity limits.

Table 13. System Component Weights—HLFC Configuration I

Item	kg	(lb)
Suction system	472	(1040)
Channel collector duct	116	(255)
Suction channels	11	(25)
Collector duct	93	(205)
Compressor	75	(165)
Exit duct	23	(50)
Motor	54	(120)
Installation clamps and supports	100	(220)
Cleaning system	260	(575)
Storage tank	14	(30)
Fluid	113	(250)
Distribution lines	9	(20)
Feeder lines, valve, and control	4	(10)
Manifold and porous media	68	(150)
Installation and supports	52	(115)
Anti-icing system	74	(165)
Storage tank	2	(5)
Fluid	64	(140)
Lines, valve and control	4	(10)
Manifold and porous media (in cleaning system)		
Installation and supports	4	(10)
Electrical system	181	(400)
Generators	84	(185)
Remote and quick disconnects	16	(35)
Bearings and mounting	9	(20)
Oil cooling system	27	(60)
Wiring	45	(100)

6.2.2 Performance Evaluation

The mission rules used to compute performance conform to the same U.S. domestic conditions as used for the baseline in section 4.3. In computing the fuel used for the "reserve" segments of the profile, no credit was taken for HLFC drag reduction, and no penalty was assessed for power to drive the suction compresssors. (An alternative reserve requirement, consisting of the excess fuel required to fly from the midpoint of the cruise segment to the destination with HLFC inoperative plus 15 min thereafter, also was examined. It was found to be much less conservative and was not considered further.) Standard day conditions with operation from sea level have been assumed. Power extraction for the HLFC system is 103 kW (138 hp) per engine and results in an SFC penalty of 1% while the system is operating. The OEW increased by 0.83%.

The final HLFC airplane performance is representative of an "uncycled" configuration, incremented from the baseline turbulent airplane. That is, the favorable impact (in OEW) of reducing takeoff gross weight has not been factored into the results. The mission summary is presented in Table 14. The HLFC system is activated in climb at 3048m (10 000 ft) and operates through the cruise phase. All other segments, including reserves, are based on the airplane performance with HLFC inoperative. The 113 kg (250 lb) of washing fluid is assumed to have been expended by the time 1524m (5000 ft) altitude is reached.

The characteristics and performance of the HLFC airplane are compared to those of the baseline in Tables 15 and 16.

Block fuel is reduced by 1510 kg (3330 lb), 8.1% less than the turbulent airplane fuel burned. The resultant reduction in takeoff gross weight is 739 kg (1630 lb). The increment between takeoff gross weight and maximum landing weight is the same as the baseline, so the HLFC airplane has a maximum landing weight of 89 072 kg (196 370 lb). (The 2% difference in SFC indicated in the configuration characteristics chart results from a reduction of the engine cruise operating point from 2971-kg [6550-lb] thrust per engine to 2631-kg [5800-lb] for the HLFC airplane. HLFC airplane cruise at minimum SFC and near maximum L/D could be attained by reducing engine size and would thus permit matched airframe-engine operation. This resizing has not been performed. The incremental block fuel benefit for resized engines would be about 1%, for a total of 9% improvement over the turbulent airplane.)

110

Table 14. Mission Summary—HLFC Configuration I

Mission segments	Fuel burn, kg (lb)	Fuel remain, kg (lb)	End segment weight, kg (lb)	Time, hr	Distance, km (nmi)
① Taxi out, 9 min	184 (405)	22 888 (50 460)	99 051 (218 370)	0.150[a]	—
② Takeoff, sea-level climb to 457m (1500 ft)	376 (828)	22 513 (49 632)	98 675 (217 542)	0.033	8.2 (4.4)
③ Climb to 10 668m (35 000 ft), accelerate to M = 0.8	2 234 (4 926)[d]	20 279 (44 708)	96 327 (212 366)[c]	0.318	223.0 (120.4)
④ Cruise M = 0.8, 10 668m (35 000 ft) to 11 887m (39 000 ft)	13 784 (30 389)[d]	6 494 (14 317)	82 543 (181 977)	4.097	3489.5 (1884.2)
⑤ Descend to 457m (1500 ft)	249 (549)	6 245 (13 768)	82 294 (181 428)	0.315	205.6 (111.0)
⑥ Approach and land	227 (500)	6 018 (13 268)	82 067 (180 928)	0.083	—
⑦ Taxi in, 5 min	102 (225)[a]	—	—	0.083[a]	—
Total mission	17 156 (37 822)	17 054 (37 597)	—	4.85[b]	3926 (2120)
⑧ Total reserves	6 018 (13 268)	—	—	—	—

[a] Not included in total mission fuel or trip airtime.
 Taxi time included in block time.
 Taxi-in fuel (from reserves) included in block fuel.

[b] Trip air time.

[c] Includes expenditure of 113 kg (250 lb) glycol/water washing fluid.

[d] Based on HLFC active in climb above 3048m (10 000 ft) and entire cruise.
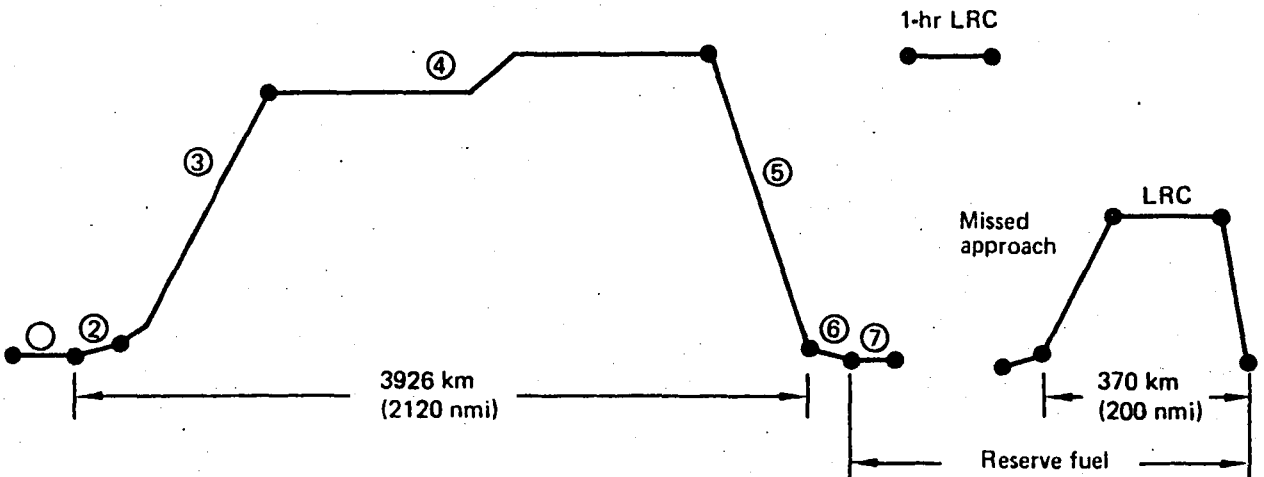
Table 15. Comparison of Characteristics—757-200 Versus HLFC Configuration I

● 3928 km (2120 nmi) range

Item	757-200		HLFC configuration I	
Takeoff gross weight, kg (lb)	99 790	(220 000)	99 051	(218 370)[a]
Operating empty weight, kg (lb)	59 402	(130 960)	59 901	(132 060)
Block fuel, kg (lb)	18 665	(41 150)	17 156	(37 822)[b]
Reserves, kg (lb)	5 860	(12 920)	6 018	(13 268)
Maximum landing weight, kg (lb)	89 811	(198 000)	89 072	(196 370)
Passengers	178			
Wing				
Area, m^2 (ft^2)	181.25 (1951)			
Aspect ratio	7.95			
Sweepback, deg	25.0			
Thickness ratio, %	10.3			
Engines				
Type	(2) Rolls-Royce RB211-535C			
SL static thrust, N (lb)	166 355 (37 400)			
Cruise Mach number	0.80		0.80	
Initial cruise range factor, km (nmi)	20 880	(11 268)	23 066	(12 448)
Initial cruise TSFC, kg/N-hr (lb/lb-hr)	0.0682	(0.669)	0.0696	(0.682)
Initial cruise lift-to-drag ratio	16.34		18.40	
Wing loading, kg/m^2 (lb/ft^2)	550.7	(112.8)	546.5	(111.9)
Thrust/weight, N/kg (lb/lb)	3.33	(0.340)	3.37	(0.343)
Approach speed (MLW), km/hr (kn)	250	(135)	272	(147)[c]

[a]Includes 113 kg (250 lb) glycol/water washing fluid.

[b]Based on HLFC active in climb above 3048m (10 000 ft) and washing fluid expended at 1524m (5000 ft).

[c]FAR stall C_L = 2.33 at maximum landing weight.

Table 16. Comparison of Performance—757-200 Versus HLFC Configuration I

Item	757-200	HLFC configuration 1
Taxi weight, kg (lb)	99 974 (220 405)	99 235 (218 775)
Takeoff gross weight, kg (lb)	99 790 (220 000)	99 051 (218 370)[b]
Payload, kg (lb)	16 148 (35 600)	16 148 (35 600)[a]
Operating empty weight, kg (lb)	59 402 (130 960)	59 901 (132 060)
Fuel load, kg (lb)	24 424 (53 845)	23 472 (50 865)
Range, km (nmi)	3928 (2120)	
Cruise Mach number	0.80	
Cruise altitude, m (ft)	10 668/11 887 (35 000/39 000) step	
Block time, hr	5.08	
Block fuel, kg (lb)	18 665 (41 150)	17 156 (37 822)[c]
Percent reduction of block fuel	(ref.)	8.1

[a]178 mixed class passengers at 91 kg (200 lb) each.

[b]Includes 113 kg (250 lb) glycol/water washing fluid.

[c]Based on HLFC active in climb above 3048m (10 000 ft).
and washing fluid expended by 1524m (5000 ft).

113
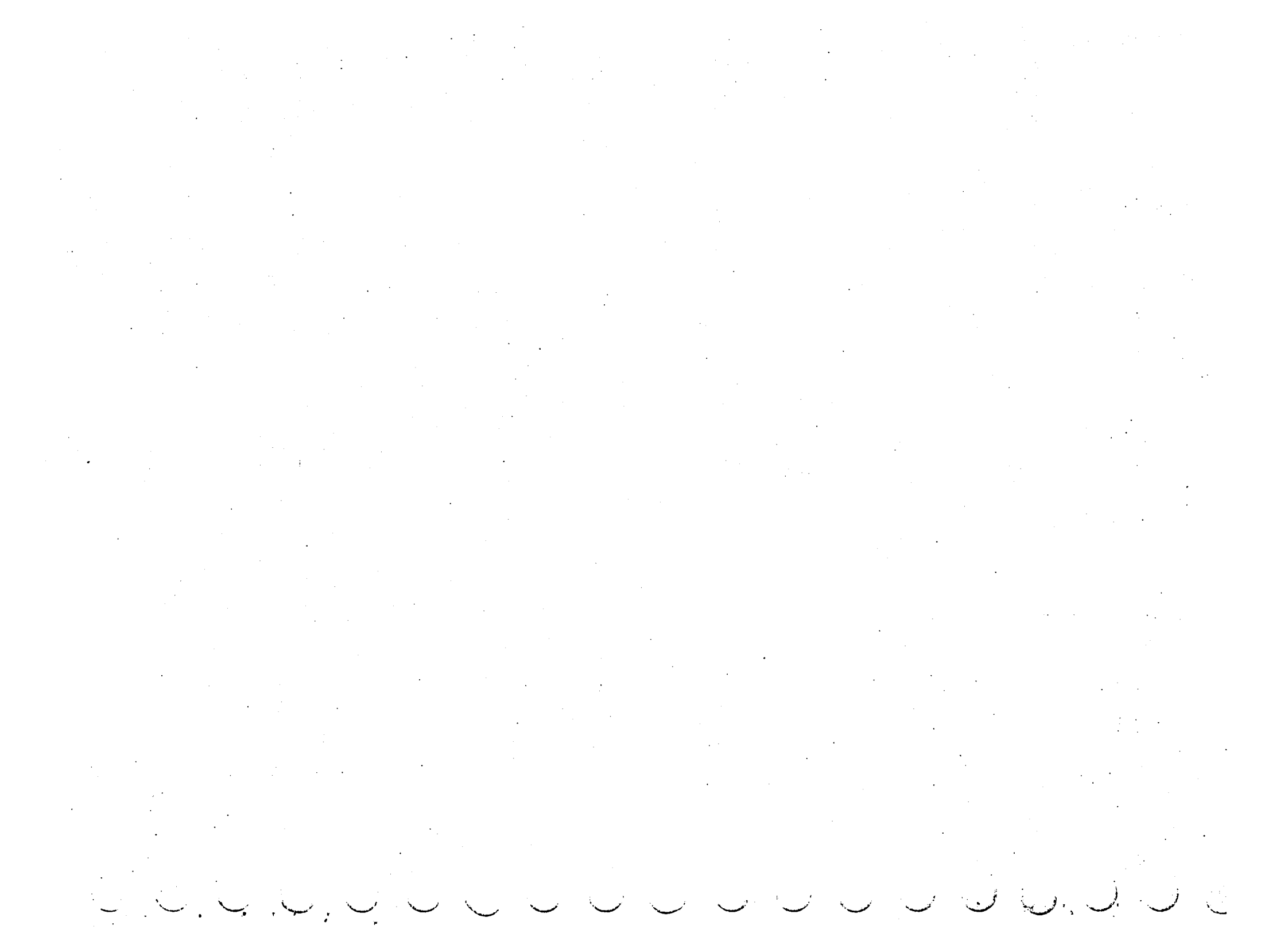
7.0 CONCLUSIONS AND RECOMMENDATIONS

7.1 CONCLUSIONS

The primary conclusion of this study is that hybrid laminar flow control (HLFC) is feasible for an airplane of the 757 class and size, with the same reservations that apply to the feasibility of any laminar flow control (LFC) airplane; i.e., the economic aspects depend on manufacturing and operational data that are not available. The study shows that approximately 60% of the wing upper surface and 40% of the lower surface can be laminarized in cruise by providing boundary layer suction only in the leading-edge region. For the airplane considered here, an 8% block fuel savings was realized. Although not studied in detail, the further gain attainable with the application of HLFC to the empennage and adjustment of cruise altitude was estimated, indicating that the fuel savings would be increased to 12%.

The study airplane was severely constrained to retain the 757 cruise altitude and Mach number and wing planform, thickness, and area. It was not possible within the scope of this contract to reoptimize these variables to obtain the best possible fuel savings. Reoptimization should yield a significant increase in fuel savings.

A 10% chord trailing-edge flap will provide pressure distribution control that permits laminar flow to be maintained over a range of cruise lift coefficients and cruise Mach numbers comparable to that required by current-day transports to accommodate altitude and air traffic restrictions. This flap also provides enough pressure distribution control to permit partial laminarization during climb and descent.

As a by-product of this study, a parametric map (fig. 26) has been prepared showing the Reynolds number and sweep boundaries within which both HLFC and natural laminar flow (NLF) can be expected. It was shown that the HLFC greatly increases the available envelope as compared with the NLF designs. It also was shown, however, that appreciable runs of NLF should be attainable for 100- to 150-passenger airplanes with sweep angles of 15 to 20 deg.

All of the results of this study are contingent on a transition criterion that had to be selected on the basis of limited experimental data. A sensitivity study was made, however, that shows that the main conclusions will stand even for large variations of the transition criterion.

7.2 RECOMMENDATIONS

As a result of the HLFC study, the following recommendations are made:

● Research should be conducted to improve the definition of the transition criterion for mixed Tollmien-Schlichting (T-S) and crossflow (C-F) instabilities. Data will become available for this criterion from the NASA-Dryden NLF Glove Flight experiments and from the NASA-Langley LFC experiments in the 2.44m (8 ft) pressure wind tunnel. A considerable amount of data for a variety of pressure distributions will be required, however, before it can be established that the criterion is not dependent upon secondary variables. Theoretical studies of the combined T-S and C-F instabilities would be valuable for the interpretation of the experimental data and should be done.

- The best configuration for an HLFC airplane depends significantly on the degree of leading-edge high-lift protection that will be required. Three studies should be made regarding this question: (1) to define the limits and trades for wings without leading-edge devices but considering the cruise requirements for HLFC, (2) to determine the acceptable size of surface discontinuities, considering application of locally increased suction, and (3) to determine the achievable smoothness of variable geometry leading edges.

- The severity of the insect contamination problem should be better defined. In the present study, it was assumed that protection will be required leading to penalties of weight and mechanical complexity. The wind tunnel test referenced in the report showed that insect contamination can exceed the allowable roughness for laminar flow. However, the actual magnitude of this problem under operational conditions is not clear. The X-21 airplane achieved full chord laminarization many times without any leading-edge insect protection, and recent flight experience on general aviation aircraft have shown less sensitivity than expected (ref. 28). The LFC leading-edge flight test (LEFT) planned for 1983 will provide vital data on insect contamination and the effectiveness of two different approaches to protecting leading edges against insect contamination.

- Integration of the cruise flap and the wing control surfaces should be investigated. The present cruise flap study considered only the section characteristics. The integration of those into a three-dimensional wing, considering the need for aileron control, has not been considered.

- An extension of the parametric study conducted under this contract should be made to identify the lift limitations of HLFC and NLF airfoils. The conflicting requirements of high lift coefficient, zero or accelerating velocity gradients, and weak terminating shocks tend to place an upper limit on the useful lift coefficient for HLFC/NLF airfoils. These limits could be determined by an extension of the parametric study made under this contract. (These calculations need not wait on additional data for the transition criterion. Because the stability calculations would not have to be repeated, the analysis could easily be modified if the criterion were changed.)

- Following the research program outlined above, further HLFC airplane studies should be conducted. The current study has shown that even without changing the major variables of the 757 configuration, a significant fuel savings can be obtained. An extension of this study to allow optimization should lead to significantly larger fuel improvements.

8.0 REFERENCES

1. Whites, R. C., Sudderth, R. W., and Wheldon, W. G., Laminar Flow Control on the X-21, *Aeronautics and Astronautics*, Vol. 4, pp. 38-43, July 1966.

2. Boeing Commercial Airplane Company, Evaluation of Laminar Flow Control System Concepts for Subsonic Commercial Transport Aircraft, NASA CR-158976, December 1978.

3. Lockheed-Georgia Company, Evaluation of Laminar Flow Control System Concepts for Subsonic Commercial Transport Aircraft, NASA CR-159254, September 1980.

4. Boeing Commercial Airplane Company, Natural Laminar Flow Airfoil Analysis and Trade Studies, NASA CR-159029, May 1979.

5. Runyan, L. J. and Steers, Louis L., "Boundary Layer Stability Analysis of a Natural Laminar Flow Glove on the F-111 TACT Airplane," *Viscous Flow Drag Reduction, Progress in Astronautics and Aeronautics*," Vol. 72, edited by Gary R. Hough, AIAA, 1980.

6. Montoya, Lawrence C., Steers, Louis L., Christopher, David, and Trujillo, Bianca, "F-111 TACT Natural Laminar Flow Glove Flight Results," ACEE Oral Status Review, NASA-Dryden Flight Research Center, September 1981.

7. Mack, L. M., "Computation of the Stability of the Laminar Compressible Boundary Layer," *Methods in Computational Physics*, edited by B. Adler, Academic Press, N.Y., pp. 247-299, 1965.

8. Pfenninger, W., "Flow Problems of Swept Low-Drag Suction Wings of Practical Construction at High Reynolds Numbers," *Annals of the N.Y. Academy of Sciences*, Vol. 154, Art. 2, pp. 672-703, November 1968.

9. Mack, L. M., "On the Stability of the Boundary Layer on a Transonic Swept Wing," AIAA 17th Aerospace Sciences Meeting Paper 79-0264, New Orleans, La., January 15-17, 1979.

10. Jaffe, N. A., Okamura, T. T., and Smith, A. M. O., "Determination of Amplification Factors and Their Application to Predicting Transition," *AIAA Journal*, Vol. 8, pp. 301-308, February 1970.

11. Srokowski, A. J. and Orsag, S. A., "Mass Flow Requirements for LFC Wing Design," AIAA Aircraft Systems and Technology Meeting Paper 77-1222, Seattle, Wash., August 22-24, 1977.

12. Runyan, L. J. and George-Falvy, D., "Amplification Factors at Transition on an Unswept Wing in Free Flight and on a Swept Wing in Wind Tunnel," AIAA 17th Aerospace Sciences Meeting Paper 79-0267, New Orleans, La., January 15-17, 1979.

13. Hefner, Jerry N. and Bushnell, Dennis N., "Status of Linear Boundary Layer Stability Theory and the e^n Method, with Emphasis on Swept Wing Applications," NASA TP-1645, 1980.

14. Bushnell, Dennis N. and Tuttle, Marie H., "Survey and Bibliography on Attainment of Laminar Flow Control in Air Using Pressure Gradient and Suction," Vol. 1, NASA RP-1035, 1979.

15. Bauer, F., Garabedian, P., Korn, D., and Jameson, A., "Supercritical Wing Section II," COSMIC Report LAR-12265, University of Georgia, 1977.

16. Northrop Report NOR 67-136, "Final Report on LFC Aircraft Design Data, Laminar Flow Control Demonstration Program," *X-21A Engineering Section*, June 1967.

17. Tani, I., Effect of Two-Dimensional and Isolated Roughness on Laminar Flow," edited by G. V. Lachman, *Boundary Layer Control*, Vol. 2, Pergamon Press, 1961.

18. Von Doenhoff, A. E. and Braslow, A. L., "The Effect of Distributed Surface Roughness on Laminar Flow," edited by G. V. Lachman, *Boundary Layer Control*, Vol. 2, Pergamon Press, 1961.

19. Hahn, M. and Pfenninger, W., "Prevention of Transition over a Backward Step by Suction," *Journal of Aircraft*, Vol. 10, No. 10, October 1973.

20. Coleman, W. S., "Roughness Due to Insects," *Boundary Layer and Flow Control*, edited by G. V. Lachman, Pergamon Press, Vol. 2, pp. 682-747, 1961.

21. Gregory, N., "Research on Suction Surfaces of Laminar Flow," *Boundary Layer and Flow Control*, edited by G. V. Lachman, Pergamon Press, pp. 924-960, 1961.

22. "Leading Edge Glove Flight Test Article Development," Douglas Aircraft Company Oral Review presented at NASA-Dryden Flight Research Center, ACEE-21-PM-1632, Contract NAS1-16220, September 1981.

23. Squire, H. B. and Young, A. D., "Calculation of the Profile Drag of Airfoils," RAE R&M 1838, 1937.

24. Balje, O. E., "A Study on Design Criteria and Matching of Turbomachines, Part A and Part B," *Journal of Engineering for Power*, January 1962.

25. Whitney, A. E. et al., "Development of Integral Environmental Control System Designs for Aircraft," AFFDL-TR-72-9, Vol. III, May 1972.

26. Boldt, T. R. et al., "Airplane Actuation Trade Study, Phase II," Air Force Contract F33615-79-C-3630, December 1981.

27. Kohlman, D. L. et al., "Icing Tunnel Tests of a Glycol-Exuding Porous Leading Edge Ice Protection System on a General Aviation Airfoil," AIAA Paper 81-0405, January 1981.

28. North, David M., "Laminar Flow Tests Pass Expectations," *Aviation Week and Space Technology*, p. 56, June 21, 1982.

APPENDIX A

AIRFOIL PARAMETRIC STUDY–DISCUSSION

OF INDIVIDUAL CASES

FIGURES

A.1 EFFECT OF MIDCHORD UPPER SURFACE GRADIENT

Figures A-1 through A-4 show the effect of leading-edge sweep angle on the transition location for cases 1-1 through 1-4. They show that without suction, case 1-2 has the most laminar flow at all sweep angles. With suction, case 1-4 has the most laminar flow at all sweep angles at Reynolds numbers of 15×10^6 and 30×10^6, and case 1-3 is best at all sweep angles at a Reynolds number of 45×10^6. The figures also show that case 1-3, with suction, is not affected by the sweep angle. This is because sweep has a much larger influence on the growth of crossflow disturbances than on the growth of Tollmien-Schlichting (T-S) disturbances. The suction in case 1-3 completely damps out the forward crossflow disturbances, and the absence of a pressure gradient prevents growth of crossflow downstream. Therefore, the transition location is entirely determined by the T-S disturbance envelope, which is little affected by sweep. Case 1-4 also is little affected by the sweep angle for the same reasons.

The compressible stability envelopes for each case are shown in Figures A-5 through A-8. These envelopes together with the transition criteria shown in Figure 5.1-2 were used to determine the transition locations for each case. If the transition criteria were changed, these same disturbance envelopes could be used to determine transition locations corresponding to the new criteria.

The following discussion summarizes the results shown in Figures A-5 through A-8. Each case is compared with the baseline, case 1-1.

A.1.1 Case 1-2

Without suction, the forward parts of the crossflow (C-F) stability envelopes were not as highly amplified as case 1-1. The aft parts of the C-F stability envelopes, however, were more highly amplified than case 1-1. This is a result of the reduced extent of pressure drop in the forward region and the larger pressure gradient in the aft region of case 1-2 relative to case 1-1.

The T-S disturbances showed a slightly reduced envelope level for most conditions. Overall, case 1-2 showed an increase in the extent of laminar flow over case 1-1 and was best for this group without suction. With suction, however, where the aft C-F envelope plays the major roll, case 1-2 had less laminar flow than case 1-1 and was the worst overall.

A.1.2 Case 1-3

Without suction, the forward C-F disturbances were more highly amplified, and the aft C-F disturbances were suppressed relative to case 1-1. This resulted in C-F stability envelopes characterized by a large initial peak that is reduced further aft. T-S disturbances were more highly amplified in the aft region. As a result, case 1-3 showed reduced amounts of laminar flow, without suction, relative to case 1-1 and was one of the worst overall. With suction, however, C-F disturbances become negligible and even though T-S disturbances were more highly amplified than for case 1-1, the net result was a substantial increase in laminar flow. Case 1-3 rates as one of the best overall and had more laminar flow than any other case at a Reynolds number of 45×10^6.

A.1.3 Case 1-4

This case varied slightly from the other three in the group. The initial pressure gradient was slightly greater, and the pressure recovery started further aft with a slightly different aft slope.

Without suction, the larger initial gradient and peak pressure resulted in C-F disturbances that were more highly amplified than for case 1-1, in a similar manner to case 1-3. The adverse gradient aft of the peak pressure tended to reduce C-F amplification factors at a faster rate than for case 1-3. The favorable gradient that starts again at s/c = 0.3, however, caused C-F disturbances to be amplified aft of that point.

T-S disturbances, as a result of the adverse gradient aft of the peak pressures, were amplified highly back to s/c = 0.3 where the favorable gradient slowed or stopped T-S growth. As a result, case 1-4 showed poorly without suction and very well with suction similarly to case 1-3. Case 1-4 resulted in the most laminar flow at Reynolds numbers of 15×10^6 and 30×10^6 and was one of the best overall.

A.2 EFFECT OF INITIAL UPPER SURFACE PRESSURE GRADIENT

Figures A-9 and A-10 show the effect of leading-edge sweep angle on the transition location for cases 2-1 and 2-2, respectively. These figures show that, without suction, case 2-1 is more sensitive to sweep than case 2-2. As a result, case 2-1 has more laminar flow than case 1-1 at the lower sweep angles and vice versa at the higher sweep angles, except at a Reynolds number of 15×10^6 where case 2-1 is better at all sweep angles. With suction, case 2-1 shows more sensitivity to sweep and is, in general, slightly better than case 2-2.

The compressible stability envelopes for cases 2-1 and 2-2 are shown in Figures A-11 and A-12. The following discussion summarizes the results shown in these figures and compares each case with the baseline, case 1-1.

A.2.1 Case 2-1

Without suction, the higher initial pressure gradient caused the C-F disturbances to be more highly amplified ahead of s/c = 0.05 relative to case 1-1. Aft of s/c = 0.05, however, the C-F growth was slowed, resulting in lower C-F envelopes. T-S disturbance envelope levels were just slightly higher than case 1-1. As a result, case 2-1 without suction had more laminar flow than case 1-1, except for the higher leading-edge sweep and Reynolds number combinations where the initial C-F disturbances (ahead of s/c = 0.05) were solely responsible for transition. With suction, the differences in C-F and T-S disturbances were found to be small because the pressure disturbances are identical aft of the location where suction ends (s/c = 0.2).

A.2.2 Case 2-2

Without suction, the decreased initial pressure gradient resulted in lower C-F amplifications ahead of s/c = 0.1 relative to case 1-1. Aft of s/c = 0.1, however, C-F disturbances continued to grow at a faster rate than case 1-1, resulting in higher C-F disturbance envelopes. T-S disturbance envelopes were slightly lower than case 1-1. As a result, case 2-2 had less laminar flow than case 1-1, except for the higher leading-edge sweep and Reynolds number combinations where the initial pressure gradient of case 1-1 was solely responsible for transition. With suction, case 2-2 showed only minor differences from case 1-1, as was the case with case 2-1.

A.3 EFFECT OF MIDCHORD SHAPE

Figures A-13 and A-14 show the effect of leading-edge sweep angle on the transition location for cases 3-1 and 3-2, respectively. When these results are compared with the no-suction results for case 1-1 (fig. A-1), it can be seen that the differences between the three cases are generally small.

The compressible stability envelopes for cases 3-1 and 3-2 are shown in Figures A-15 and A-16, respectively. These figures show that even though the transition locations are similar for the two cases, T-S disturbances are more highly amplified for case 3-2 than 3-1 and vice versa in the case of C-F disturbances.

A.4 LOWER SURFACE PRESSURE DISTRIBUTIONS

Figures A-17 through A-20 show the effect of leading-edge sweep angle on the transition location for the four lower surface cases. Without suction, case 4-2 is best at all sweep angles and Reynolds numbers except at a sweep angle of 25 deg and a Reynolds number of 15×10^6, where case 5-1 is best. With suction, case 4-2 shows much less sensitivity to sweep angle than any of the other cases. In general, with suction, case 5-1 has the least amount of laminar flow, and cases 4-2 and 5-2 have the most, with case 5-2 being slightly better for all combinations except at a sweep angle of 25 deg and a Reynolds number of 15×10^6.

The compressible stability envelopes for each of the four cases are shown in Figures A-21 through A-24. The following discussion summarizes the results shown in these figures and compares cases 4-2, 5-1, and 5-2 to the baseline, case 4-1.

It should be noted that the suction distributions were optimized for each Reynolds number for case 5-2. This was the only case in which this was done, and it was done for two reasons: first, to determine how the suction requirements varied with Reynolds number as a result of the second steep pressure rise and second, to try to reduce the high c_{q_N} of 14.1×10^{-5} obtained for the high sweep and high Reynolds number combination, which was the first analyzed.

A.4.1 Case 4-2

Both with and without suction, the C-F stability envelopes are reduced substantially overall, relative to case 4-1, because of the reduced midchord pressure gradient. T-S amplification is increased, but not enough to offset the C-F reduction. The net result is an increased extent of laminar flow relative to case 4-1 for all conditions. With suction, case 4-2 has higher T-S amplification and lower C-F amplification, with the net result an increase in the extent of laminar flow relative to case 4-1.

A.4.2 Case 5-1

Without suction, case 5-1 showed an increase in the extent of laminar flow relative to the baseline (case 4-1) distribution. This improvement is due to the step-function shape of the distribution. By alternating steep gradients, which amplify C-F and suppress T-S disturbances with flat or zero gradients that amplify T-S and suppress C-F disturbances, a seesawing movement of the compressible stability envelopes results that delays transition. With suction, however, this case was the worst of the group because the second steep rise in the pressure distribution occurs immediately after suction ends ($s/c = 0.2$). This results in large C-F disturbance amplification downstream of the end of suction.

A.4.3 Case 5-2

In an attempt to improve the hybrid laminar flow control (suction) characteristics of the case 5-1 pressure distribution, the second steep pressure rise was relocated so that it fell in the suction region. The new distribution resulting from this modification was called case 5-2 and was analyzed with suction only.

The C-F disturbance growth of case 5-2 is greatly reduced relative to case 5-1 and also relative to the baseline, case 4-1. T-S amplification is higher than for cases 5-1 and 4-1. The overall result is that with suction, case 5-2 is much better than case 5-1. At all Reynolds numbers except 15×10^6 at the high sweep angle of 25 deg, case 5-2 is the best of the four cases analyzed.
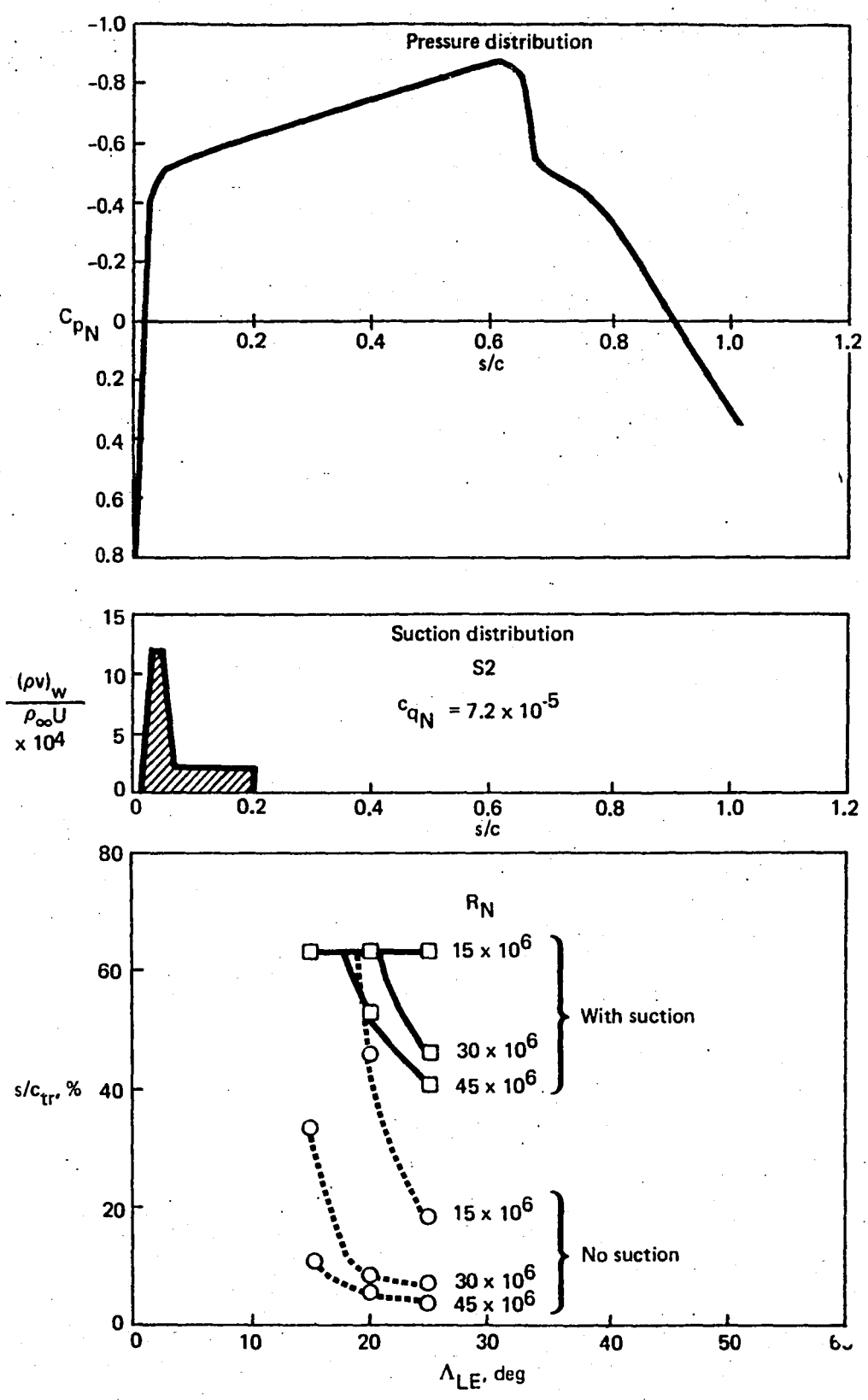
Figure A-1. Transition Data, Case 1-1
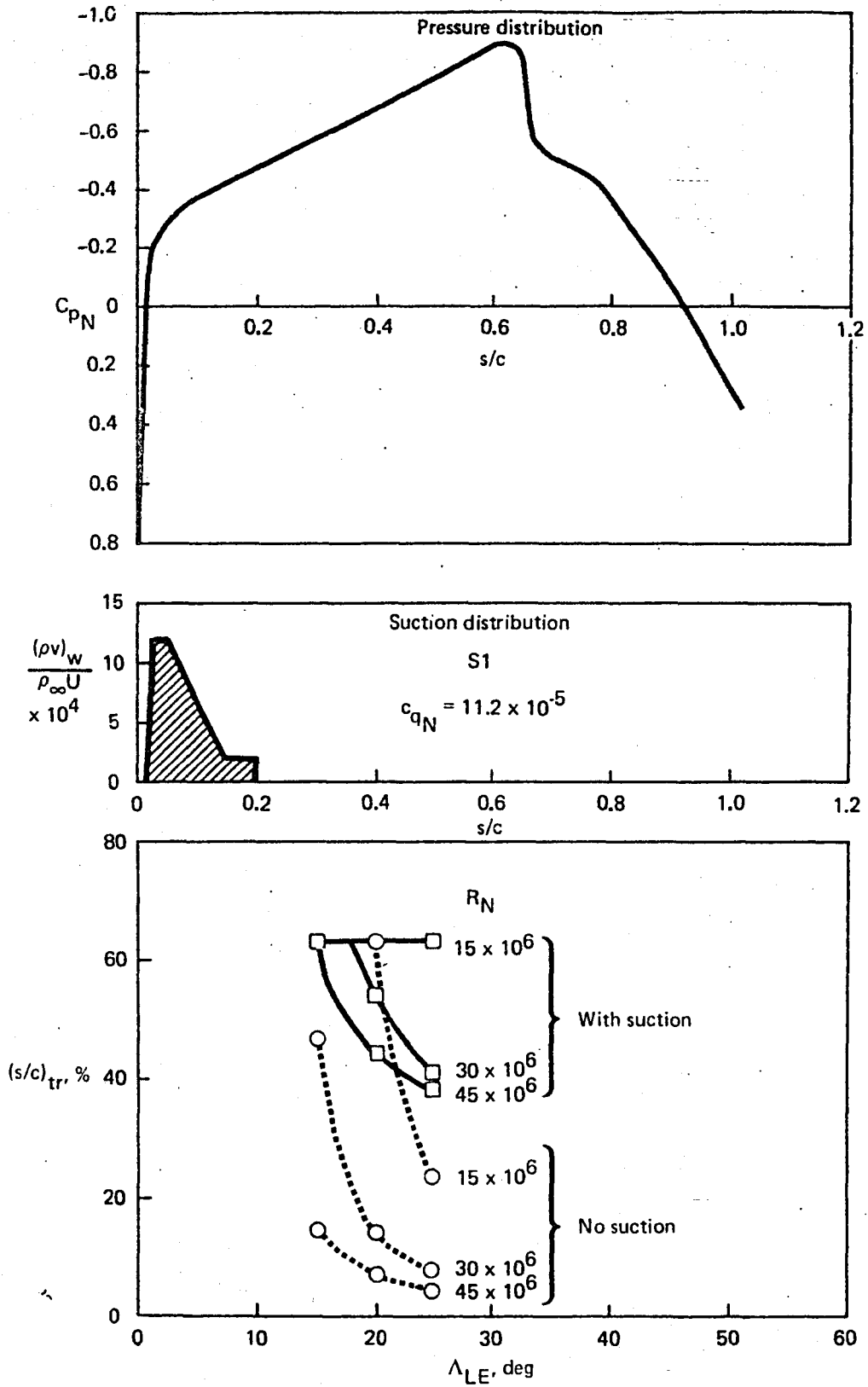
Figure A-2. Transition Data, Case 1-2
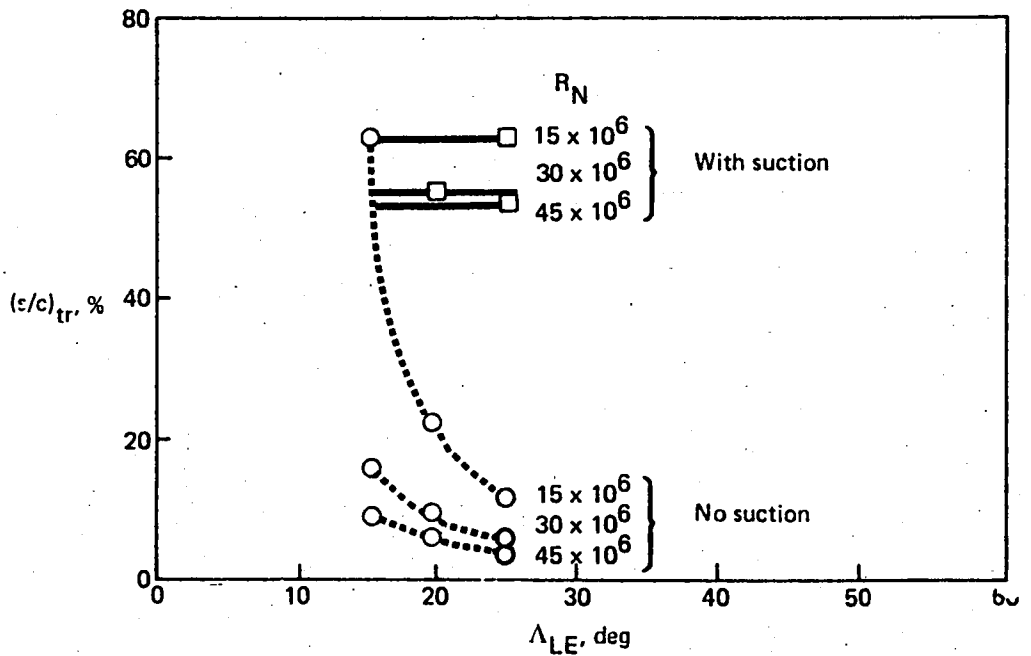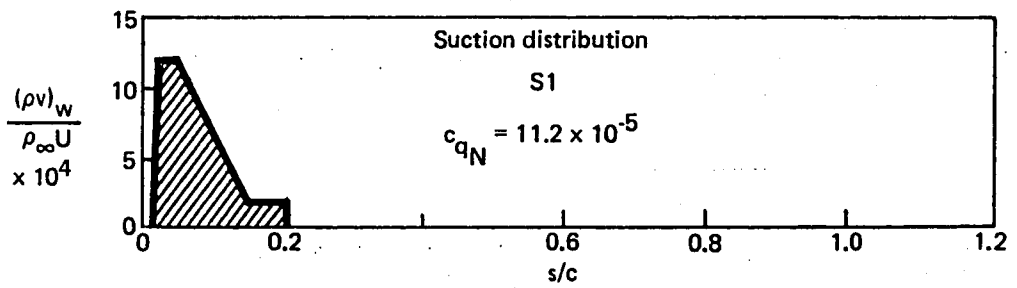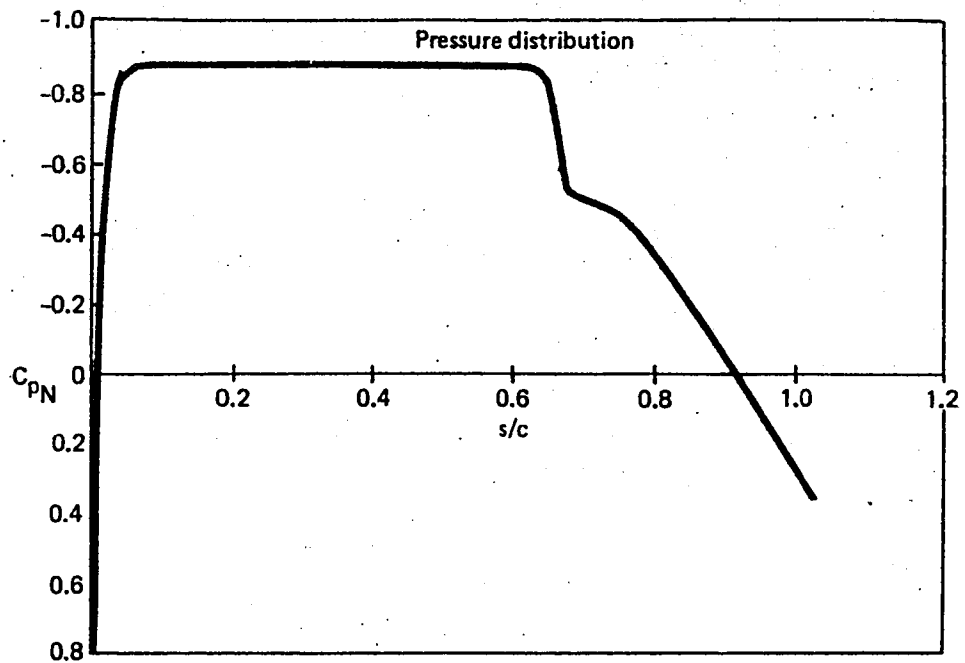
Figure A-3. Transition Data, Case 1-3
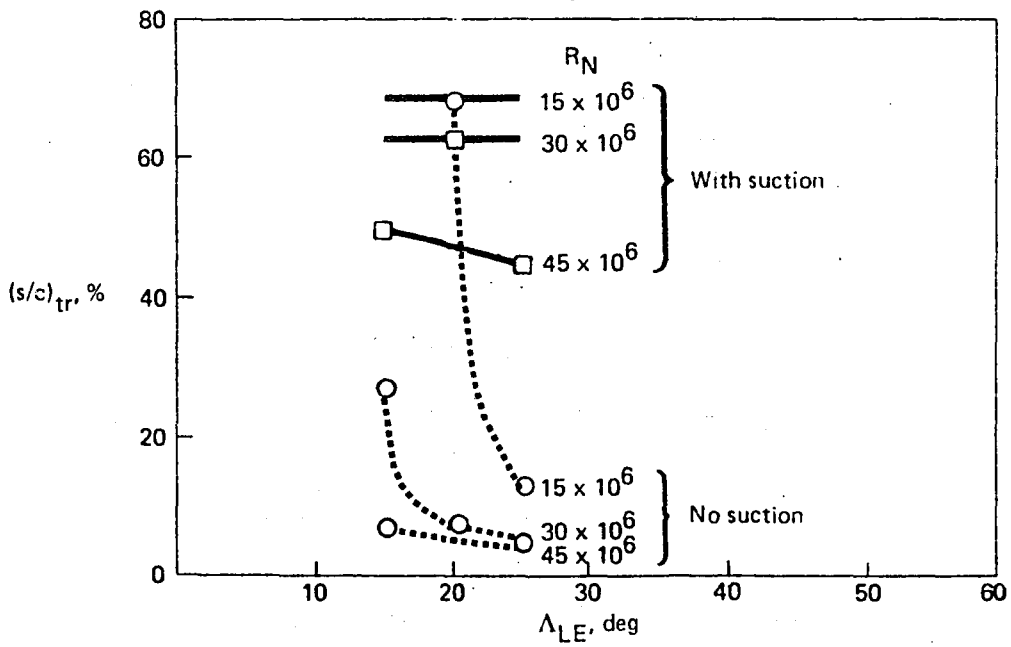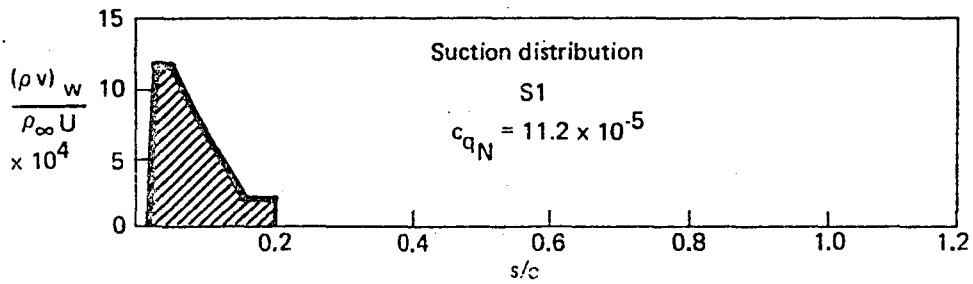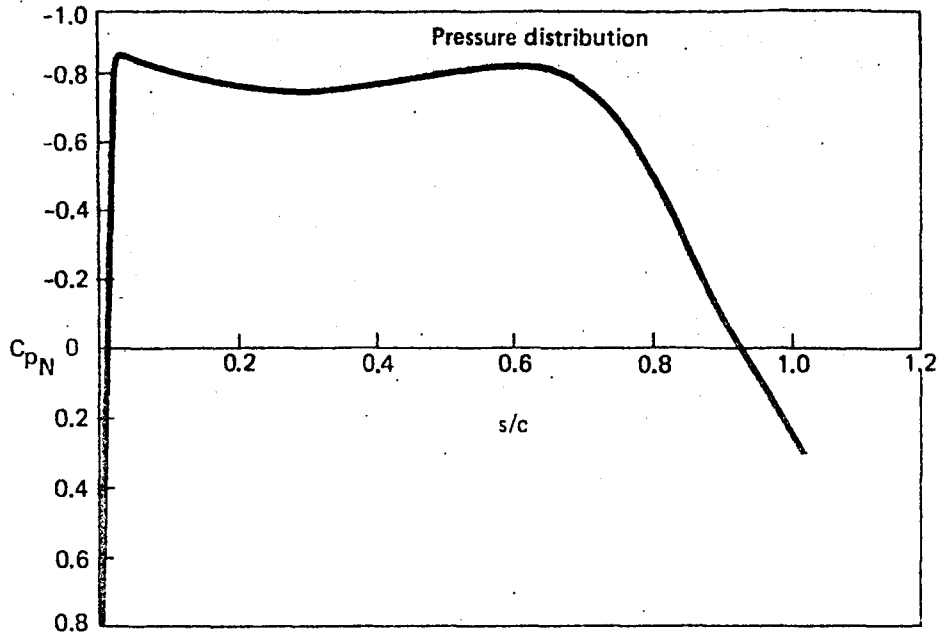
Figure A- 4. Transition Data, Case 1-4
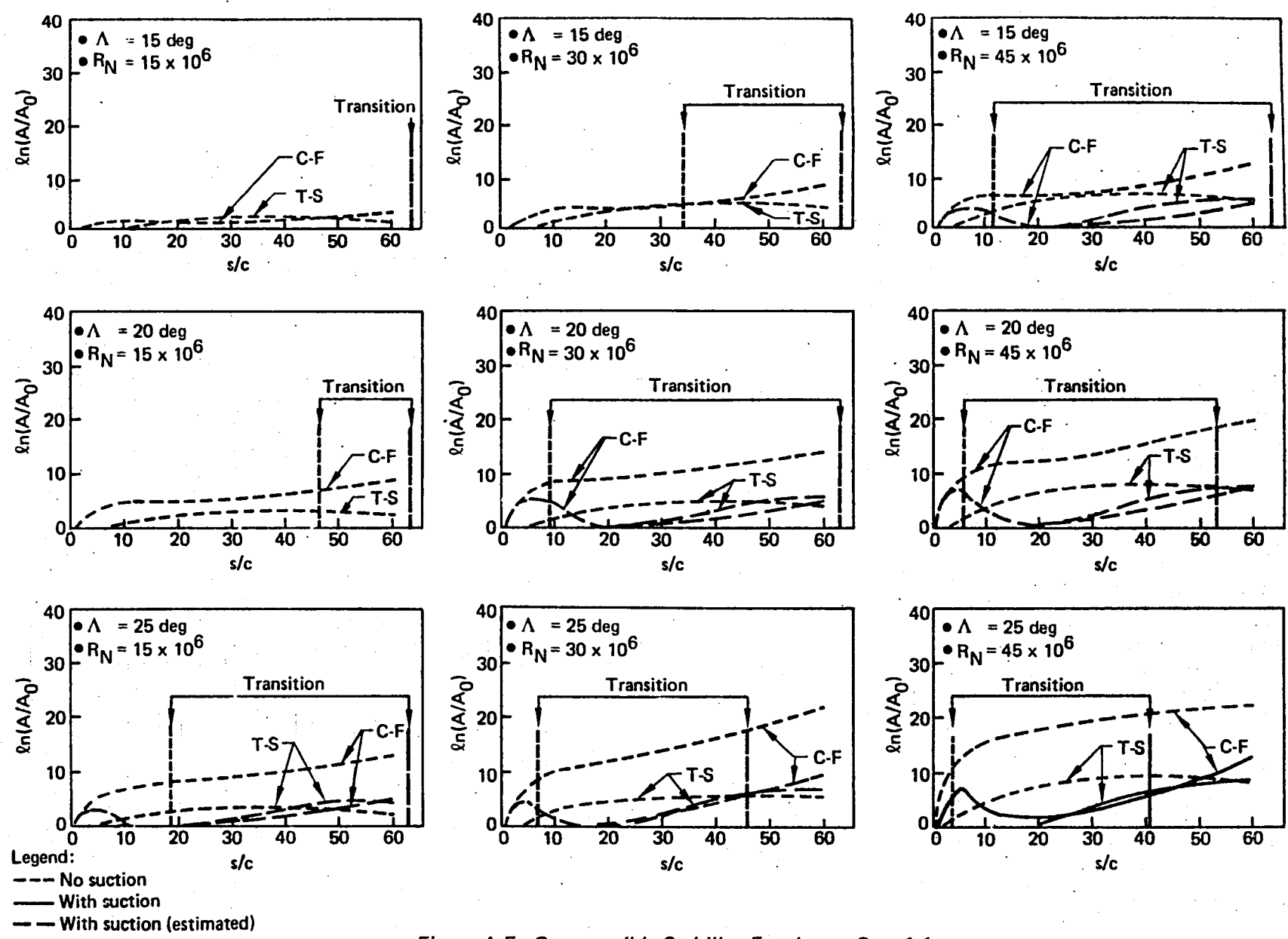
Figure A-5. Compressible Stability Envelopes, Case 1-1

Legend:
- - - No suction
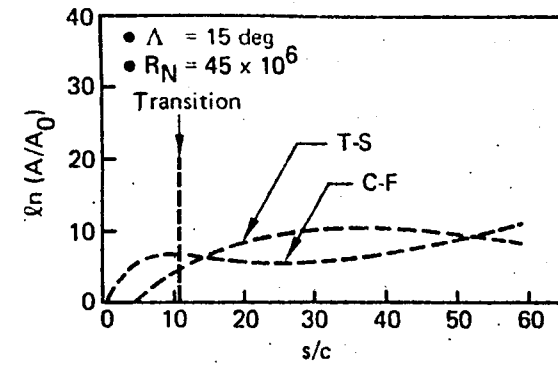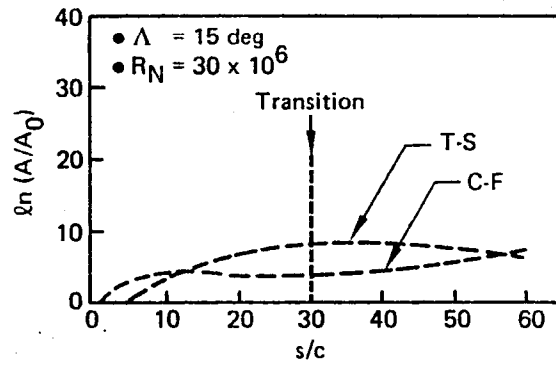——— With suction
— — With suction (estimated)

A-11
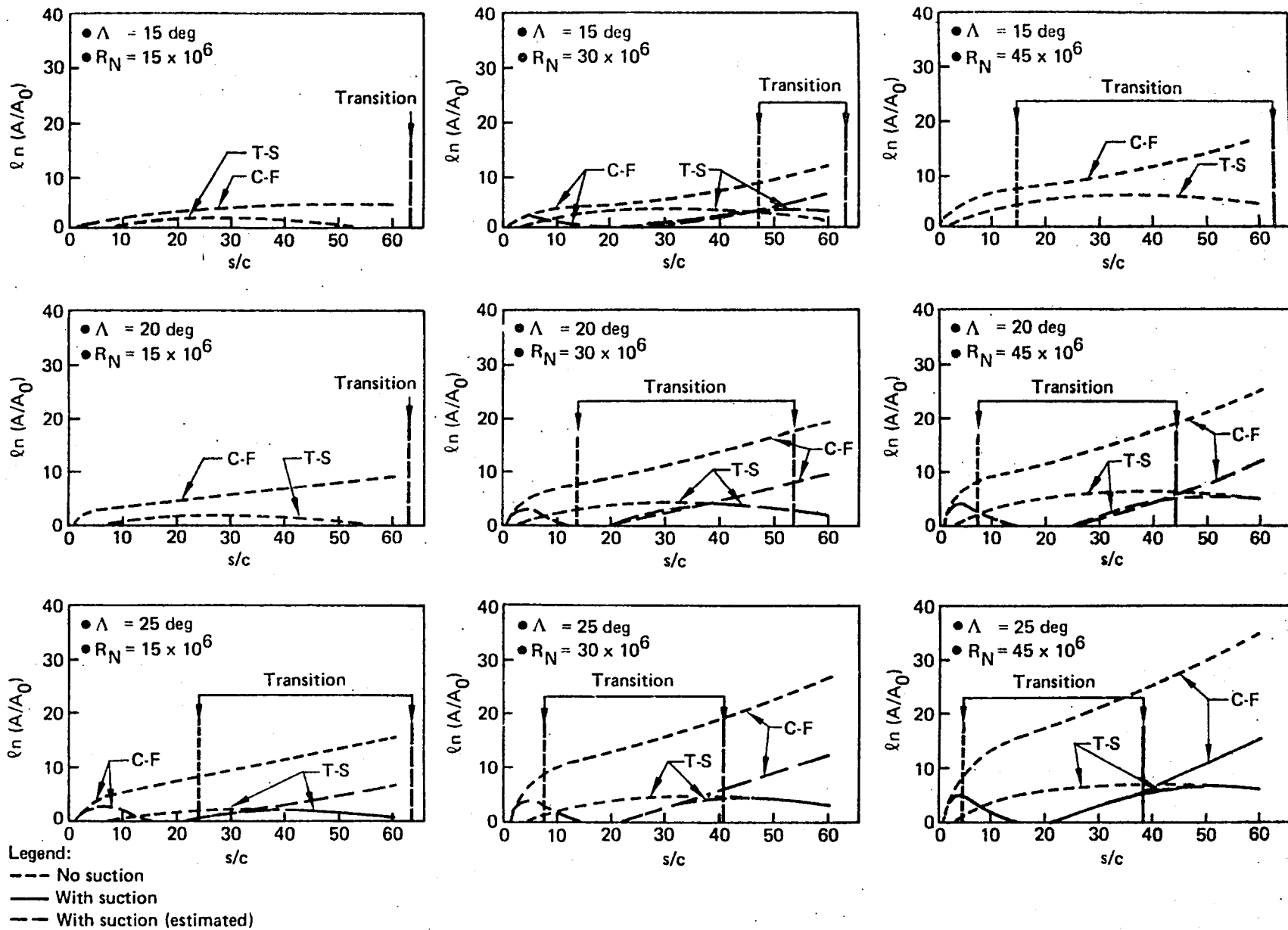
Figure A-6. Compressible Stability Envelopes, Case 1-2
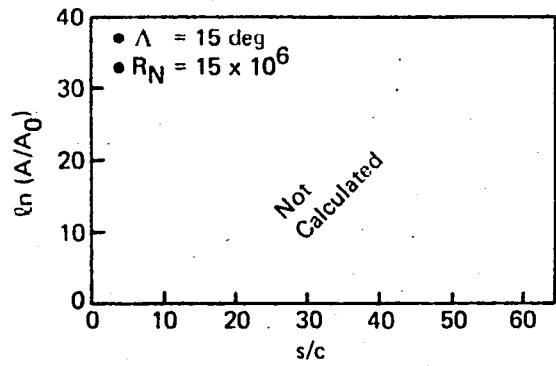
Legend:
--- No suction
— With suction
-- With suction (estimated)
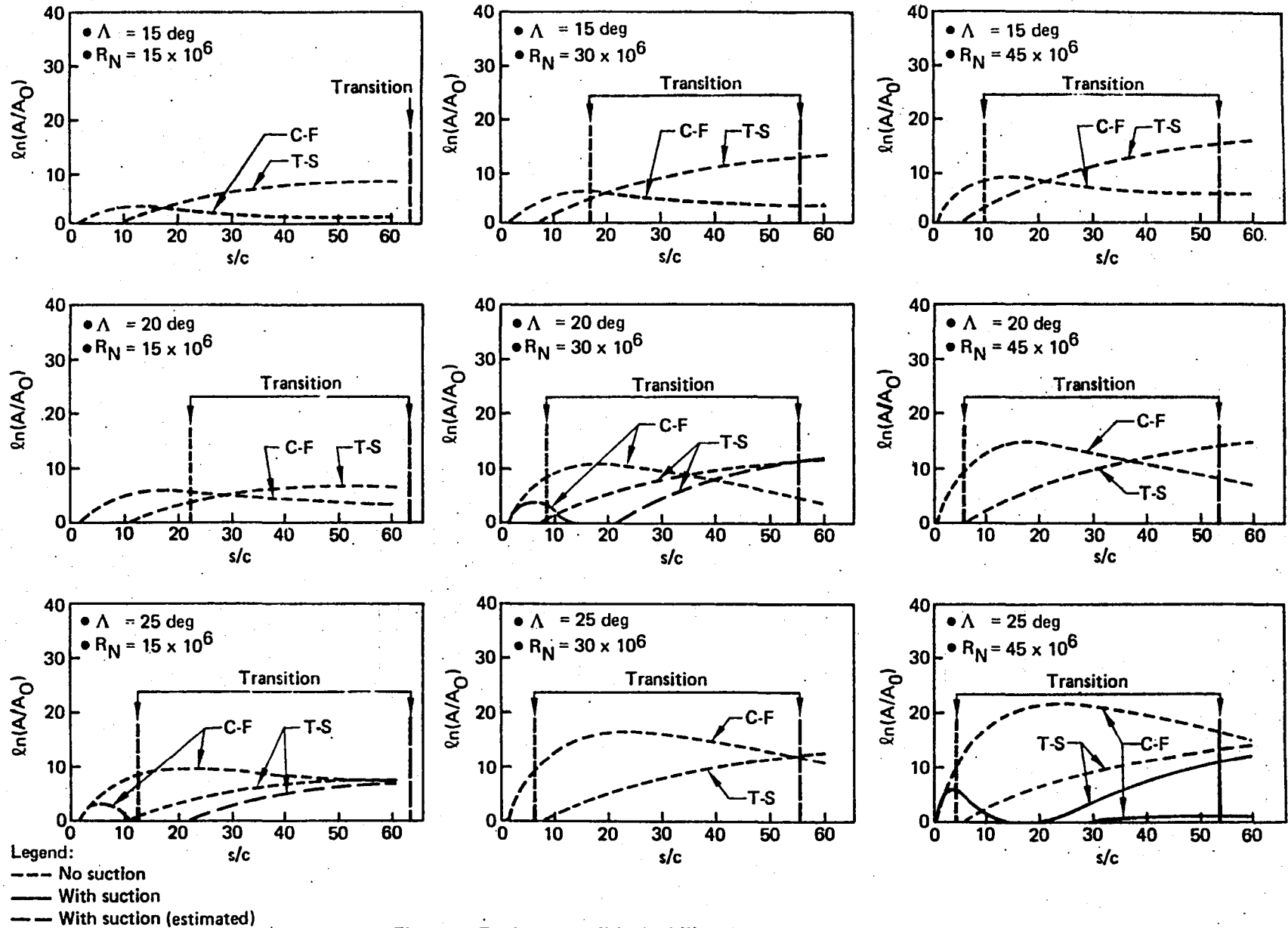
Figure A-7. Compressible Stability Envelopes, Case 1-3

Legend:
- - - - No suction
───── With suction
── ── With suction (estimated)

A-13
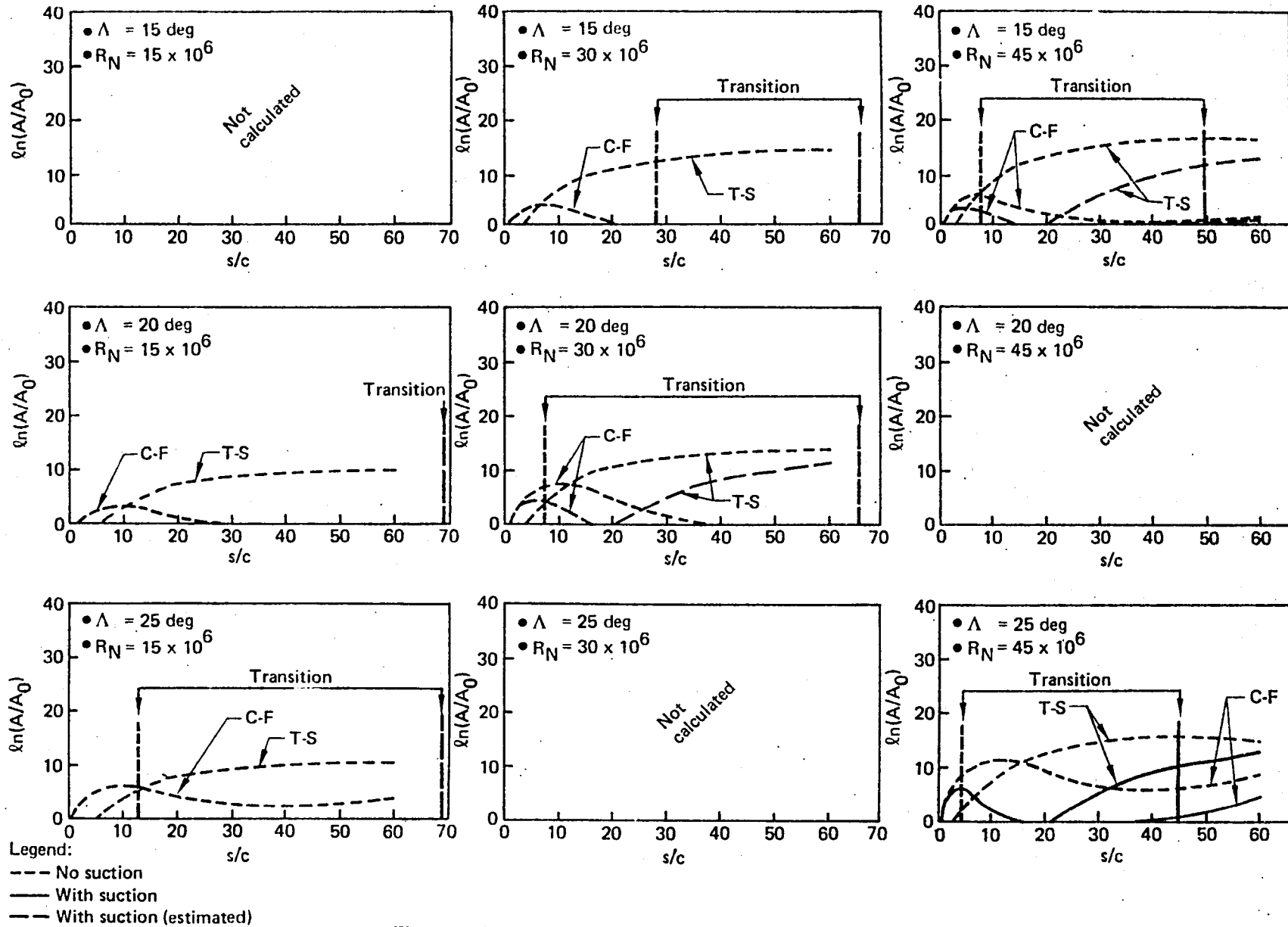
Figure A-8. Compressible Stability Envelopes, Case 1-4

Legend:

- - - No suction
——— With suction
— — With suction (estimated)

A-14
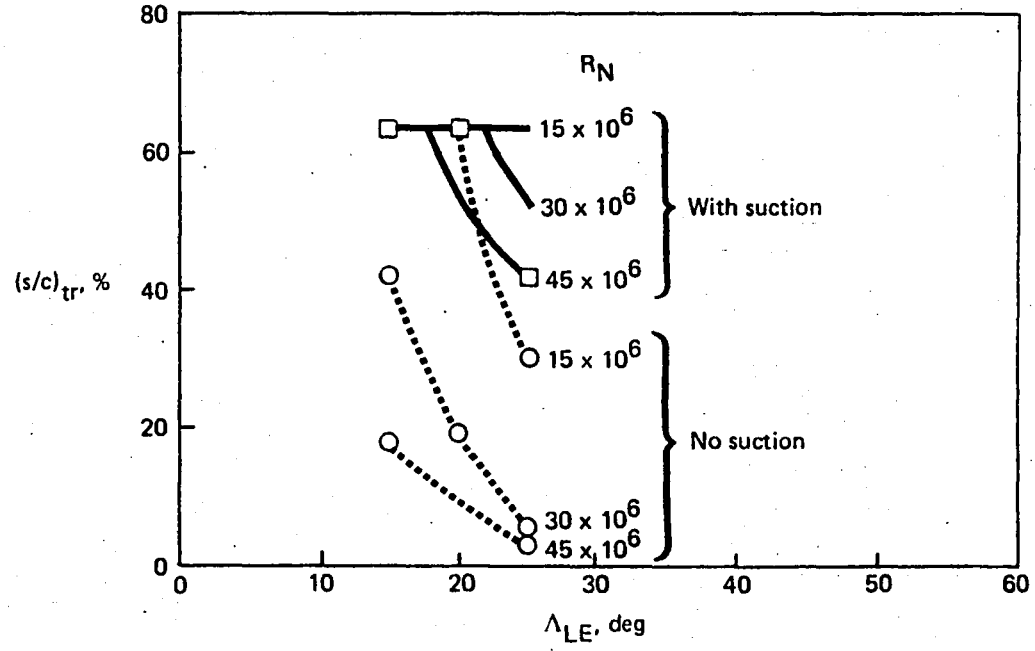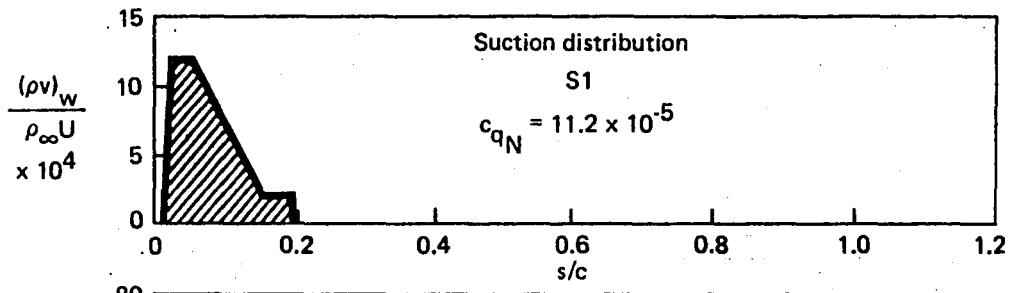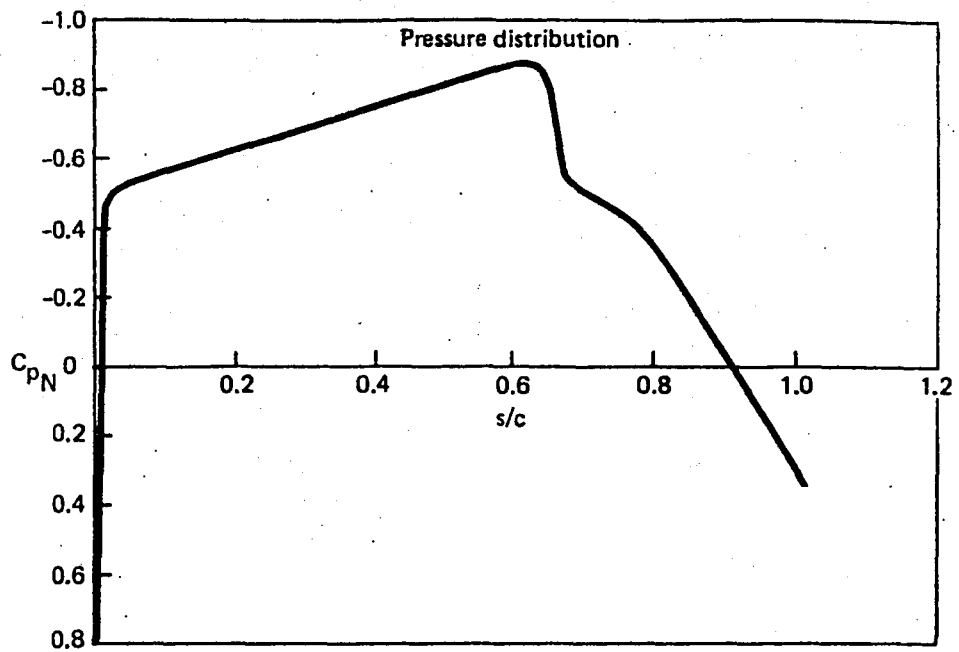
Figure A-9. Transition Data, Case 2-1
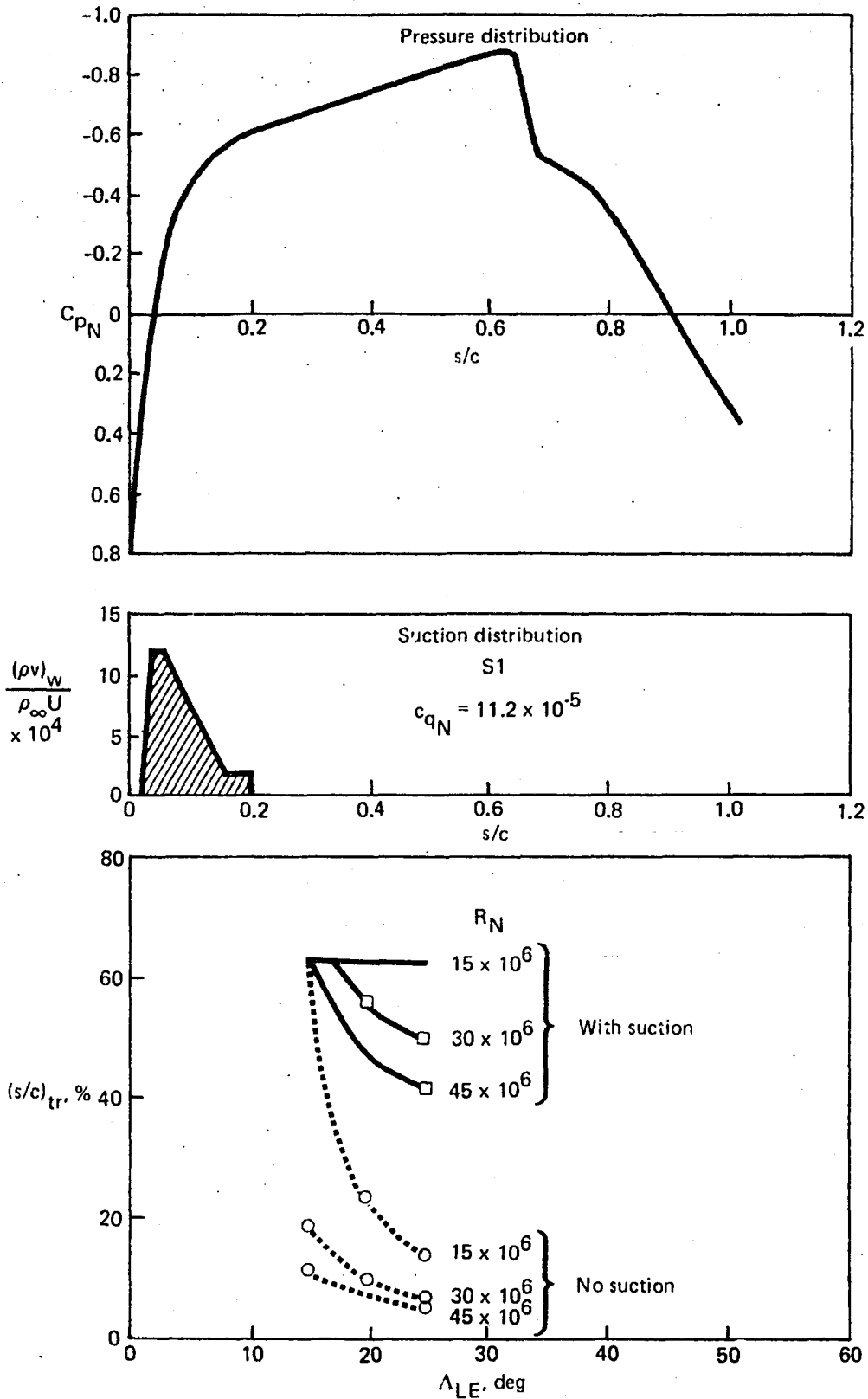
Figure A-10. Transition Data, Case 2-2

Figure A-11. Compressible Stability Envelopes, Case 2-1

Legend:
- – – No suction
- ——— With suction
- ——— With suction (estimated)

A-17
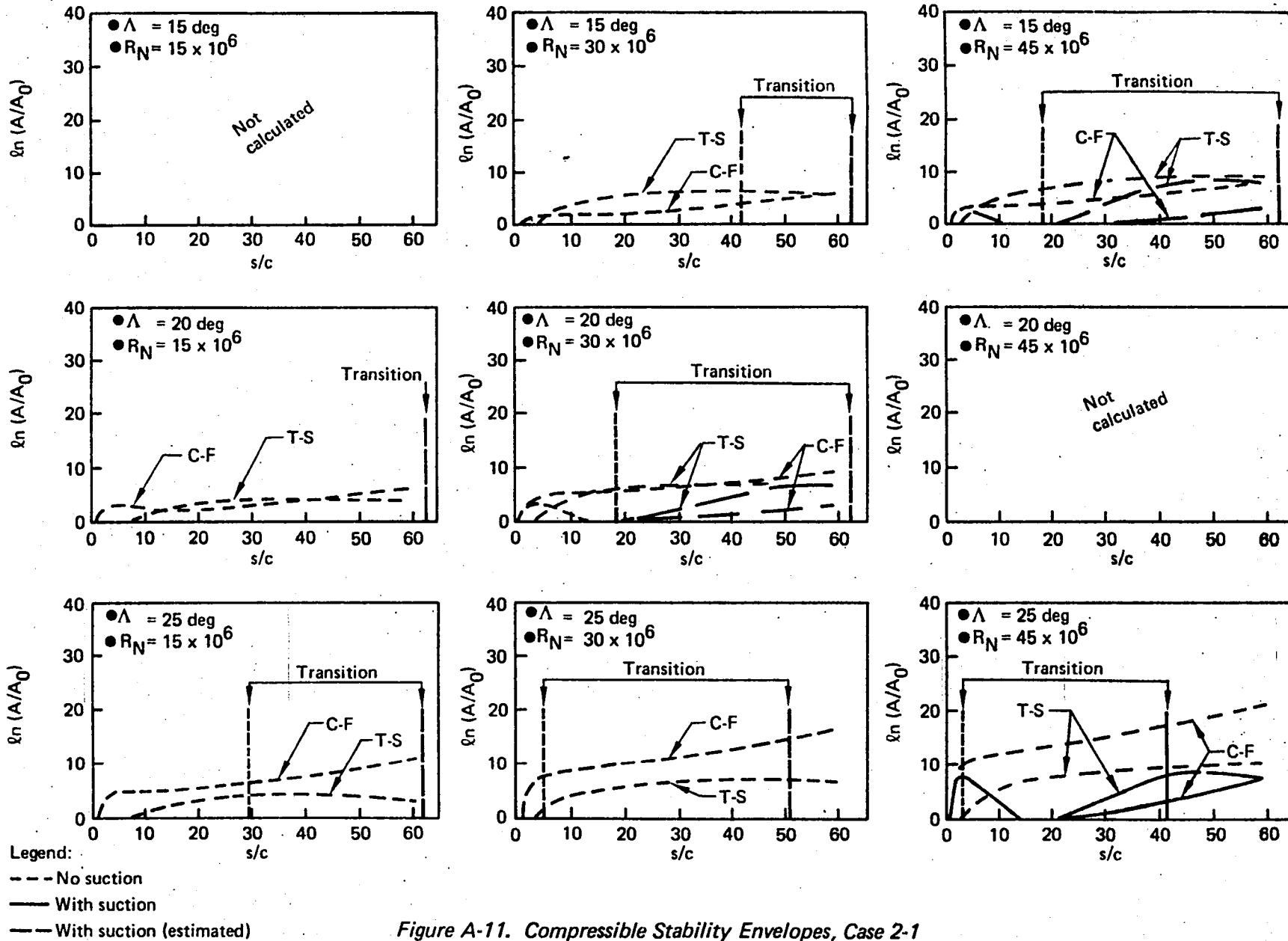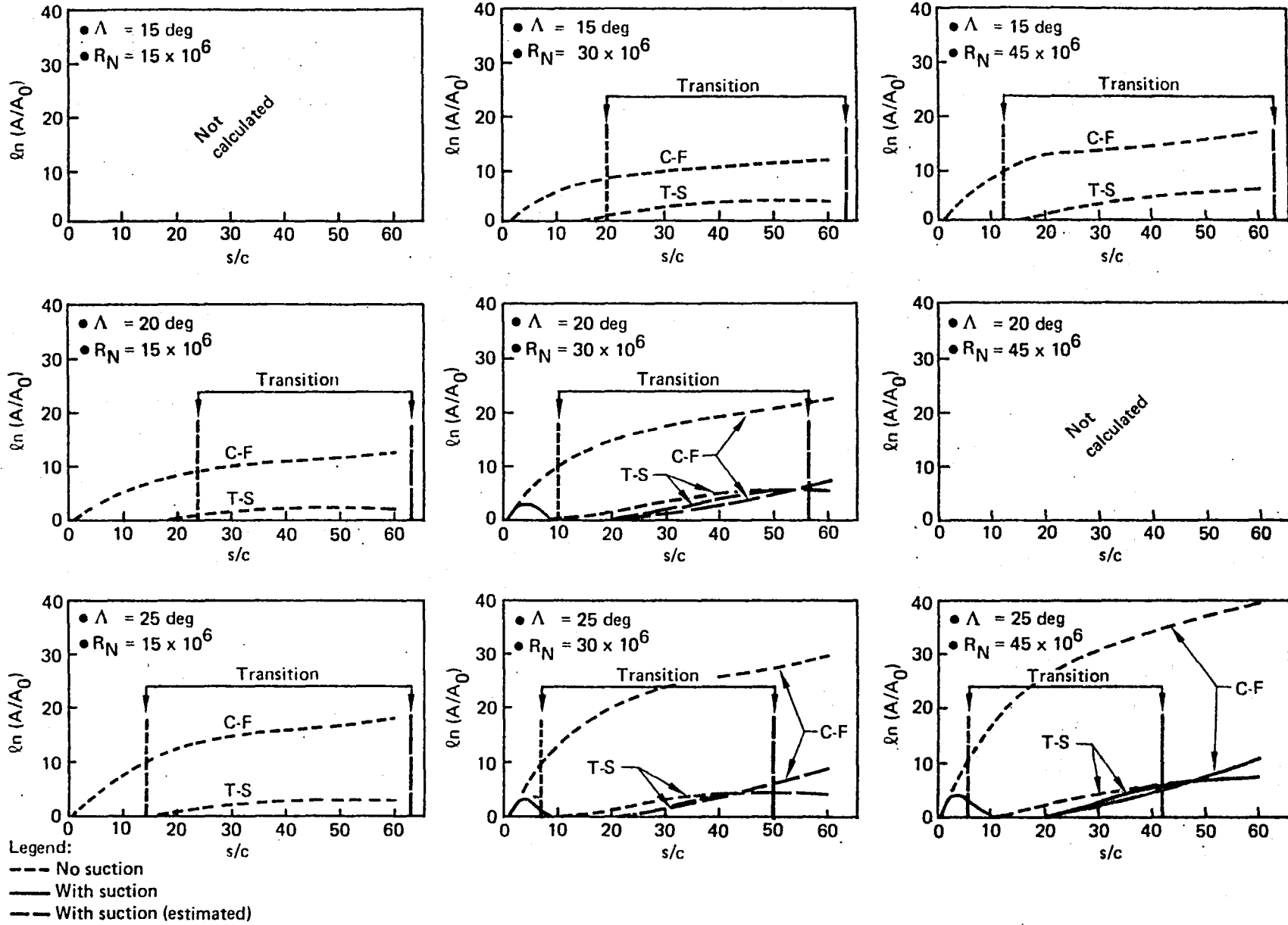
Figure A-12. Compressible Stability Envelopes, Case 2-2

Legend:
- - - No suction
——— With suction
— — With suction (estimated)

A-18
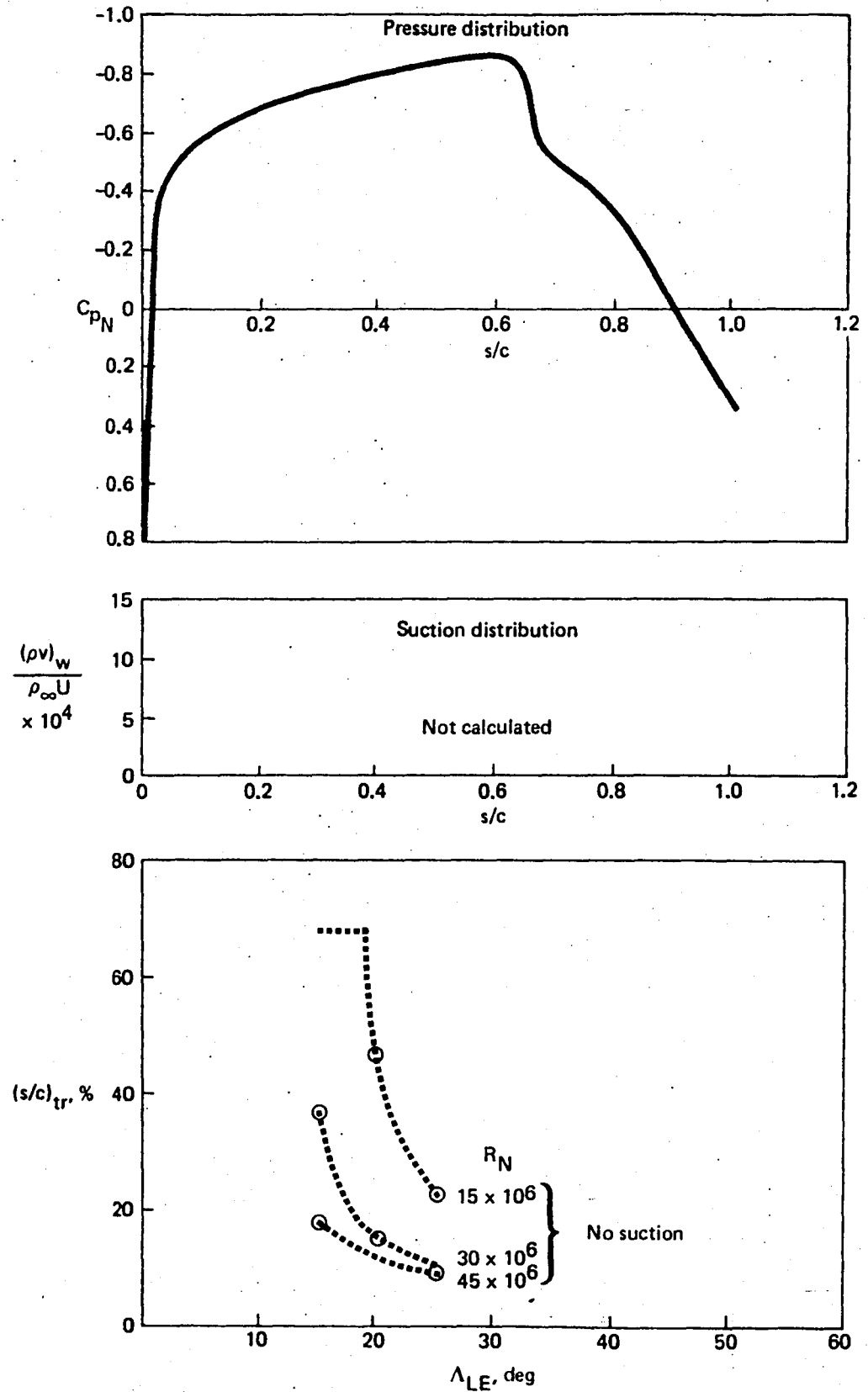
Figure A-13. Transition Data, Case 3-1

A-19
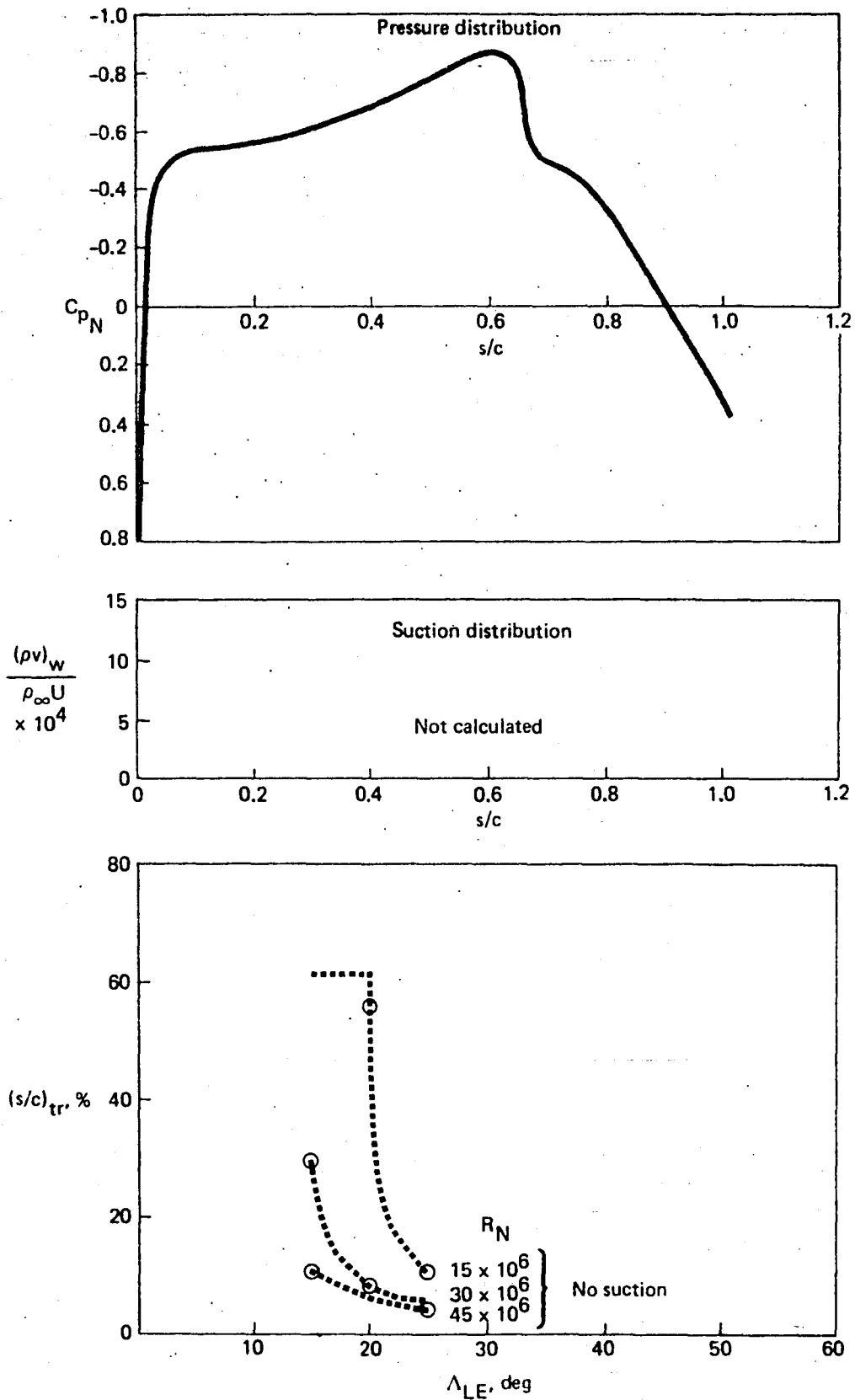
Figure A-14. Transition Data, Case 3-2

Figure A-15. Compressible Stability Envelopes, Case 3-1

A-22

Figure A-16. Compressible Stability Envelopes, Case 3-2
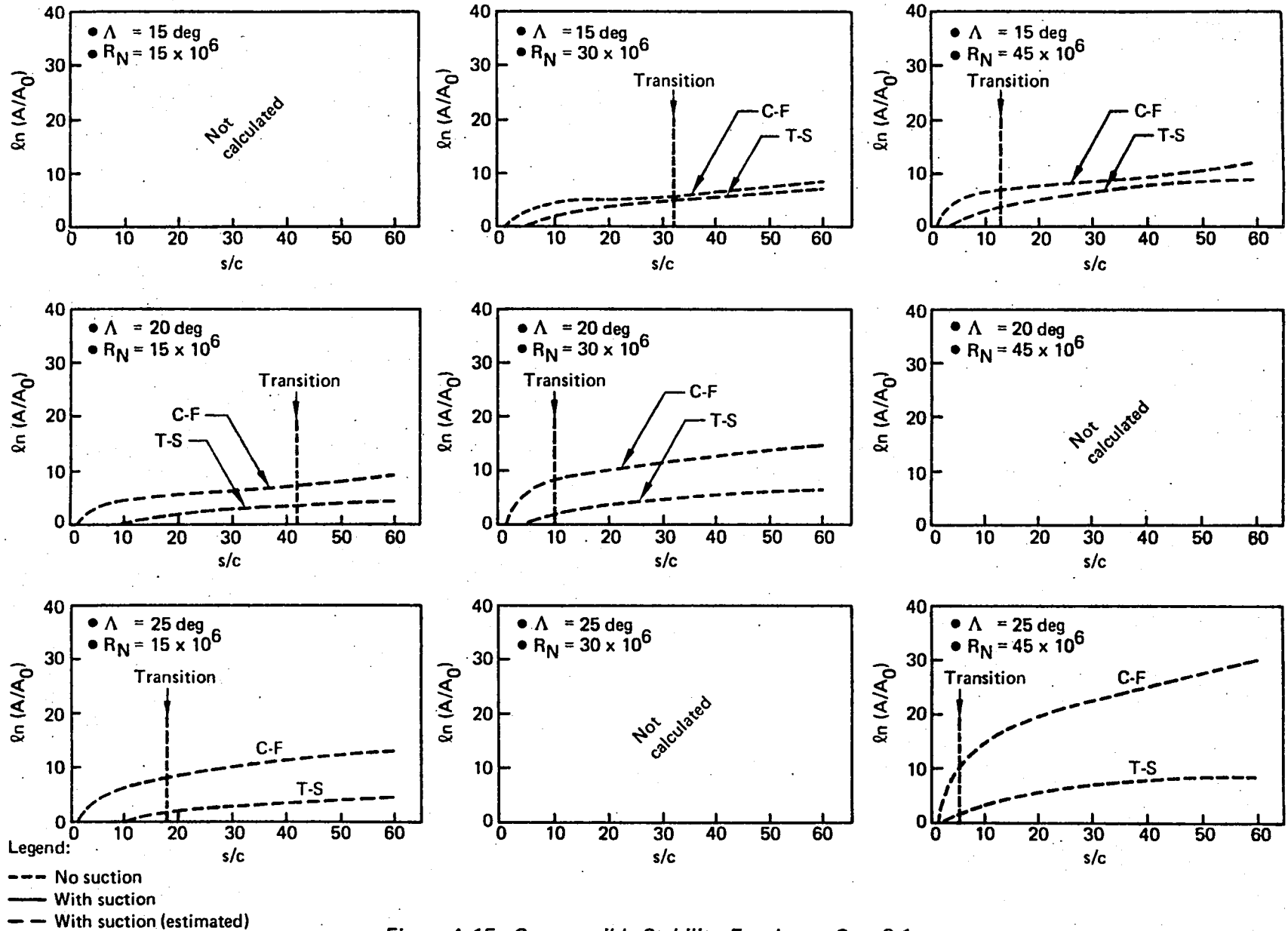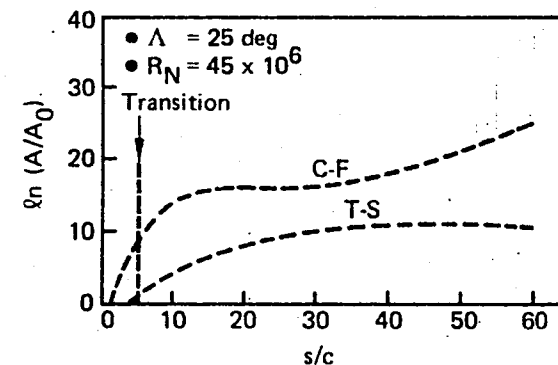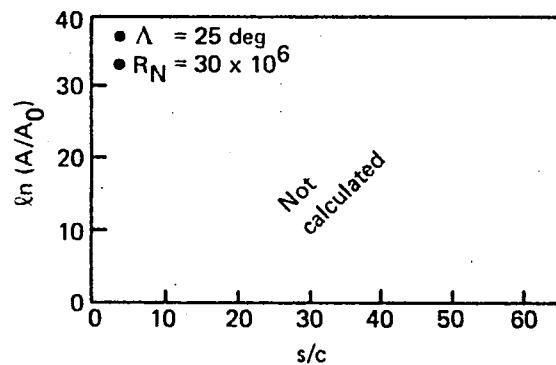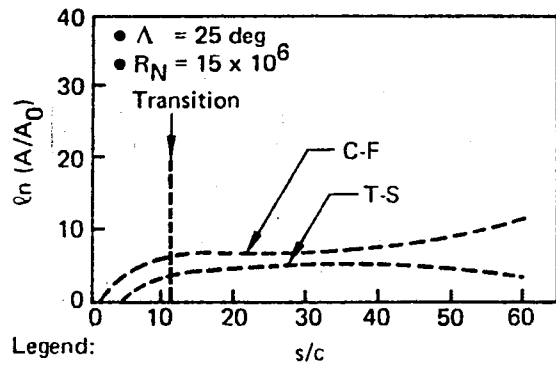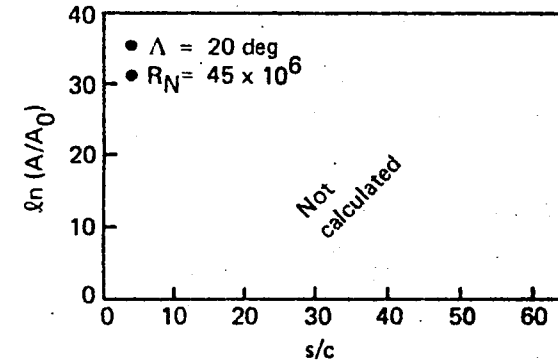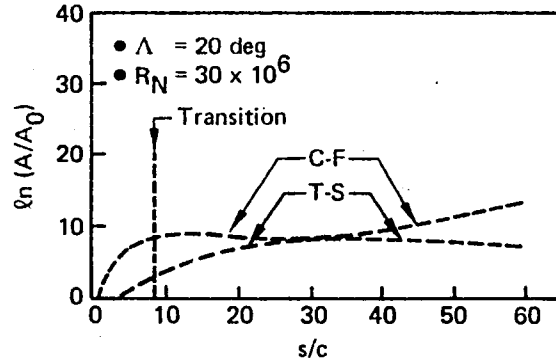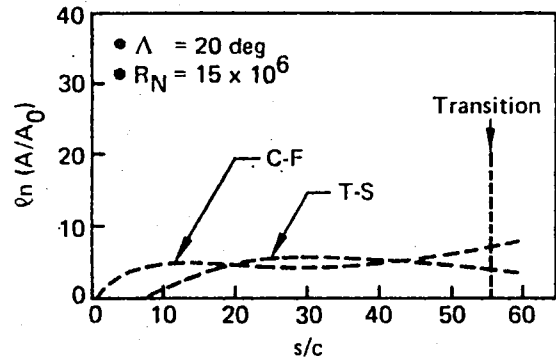
Legend:
--- No suction
— With suction
-- With suction (estimated)
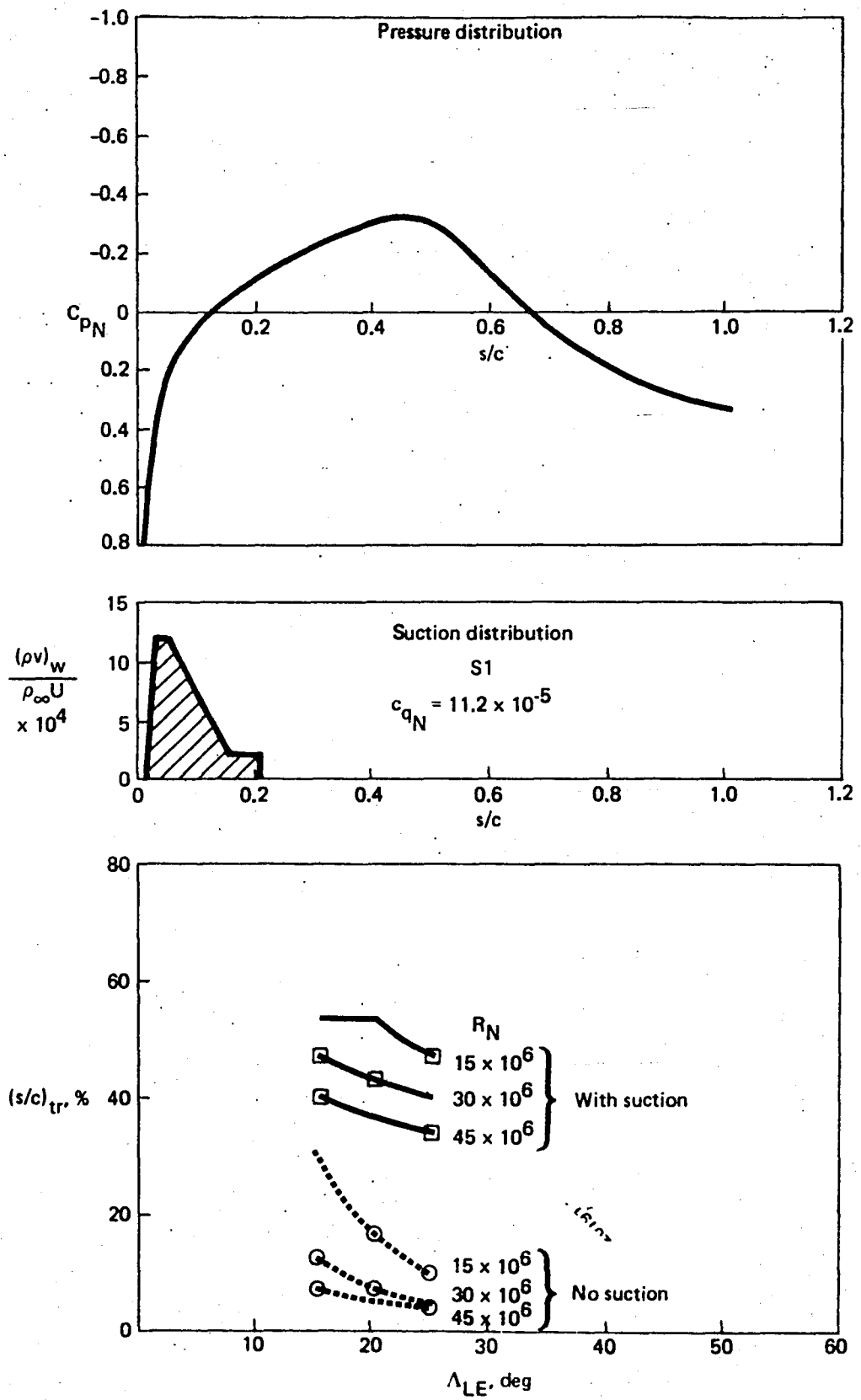
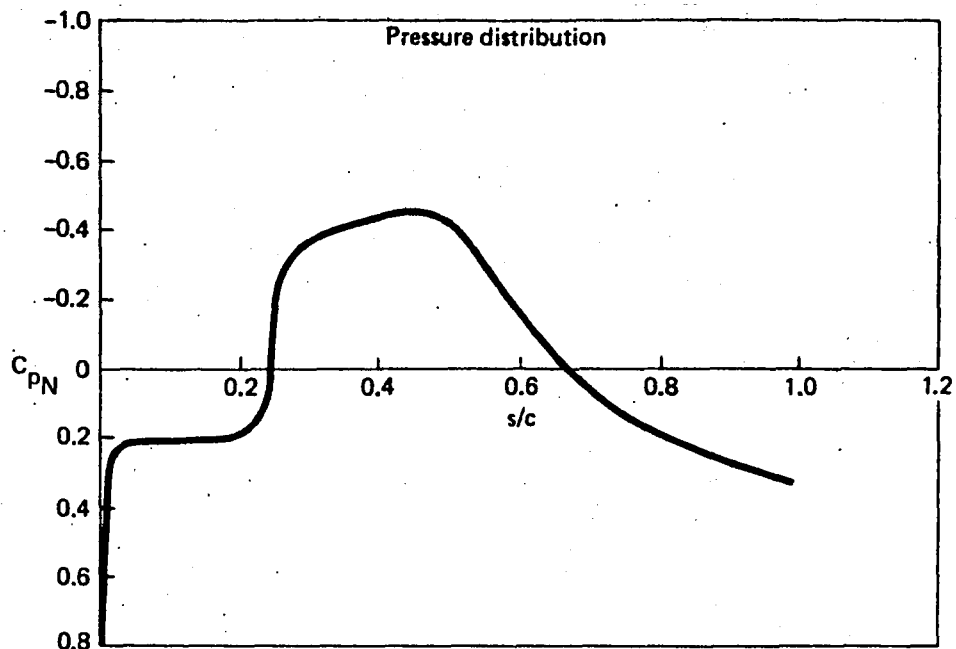Figure A-17. Transition Data, Case 4-1
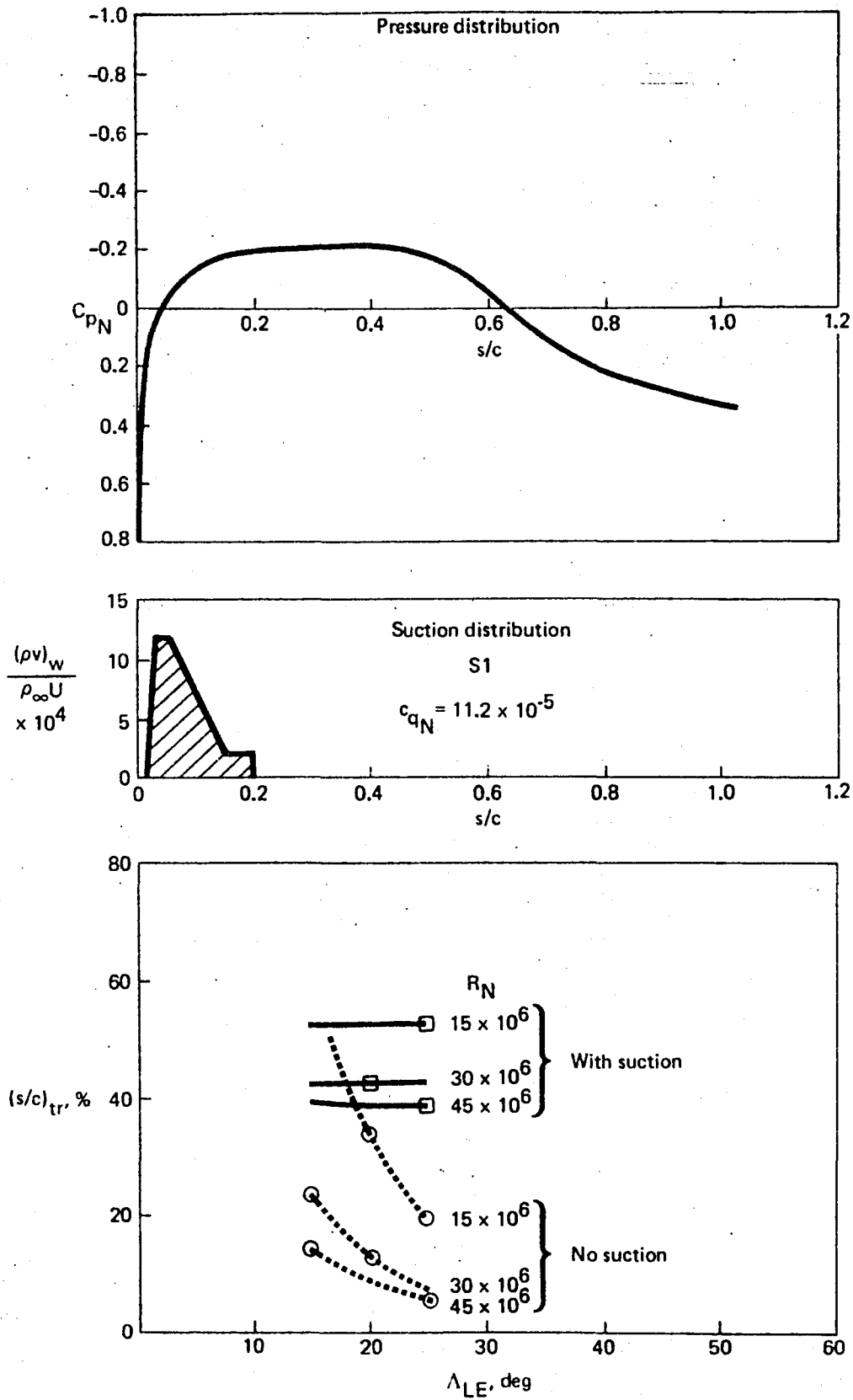
Figure A-18. Transition Data, Case 4-2
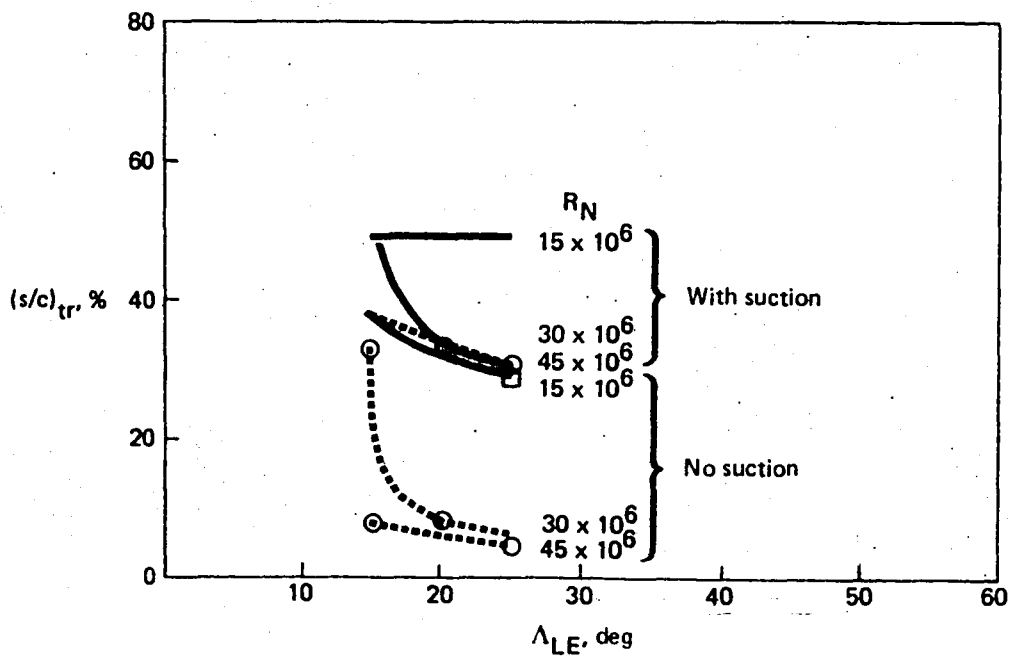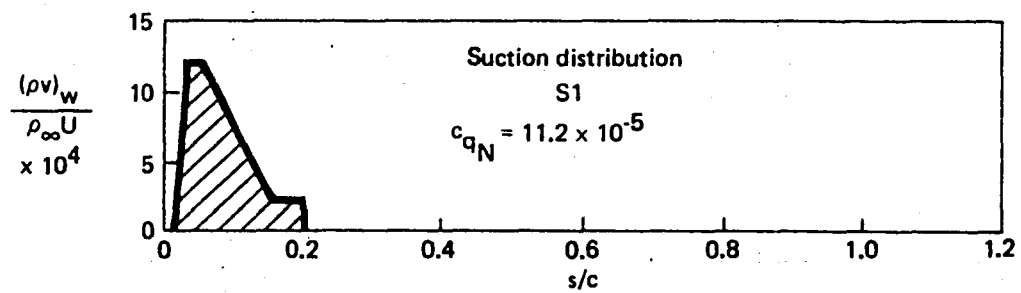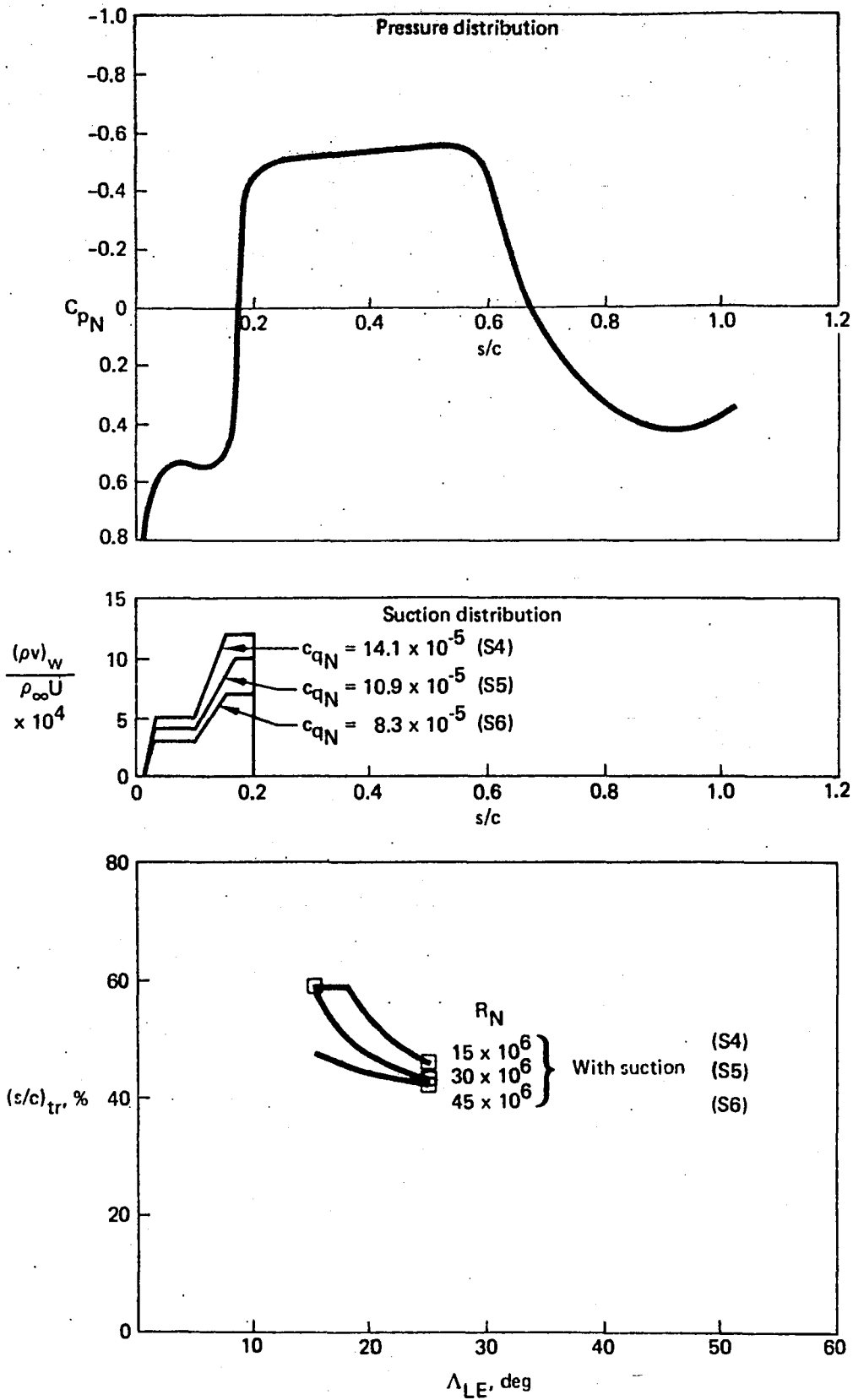
Figure A-19. Transition Data, Case 5-1
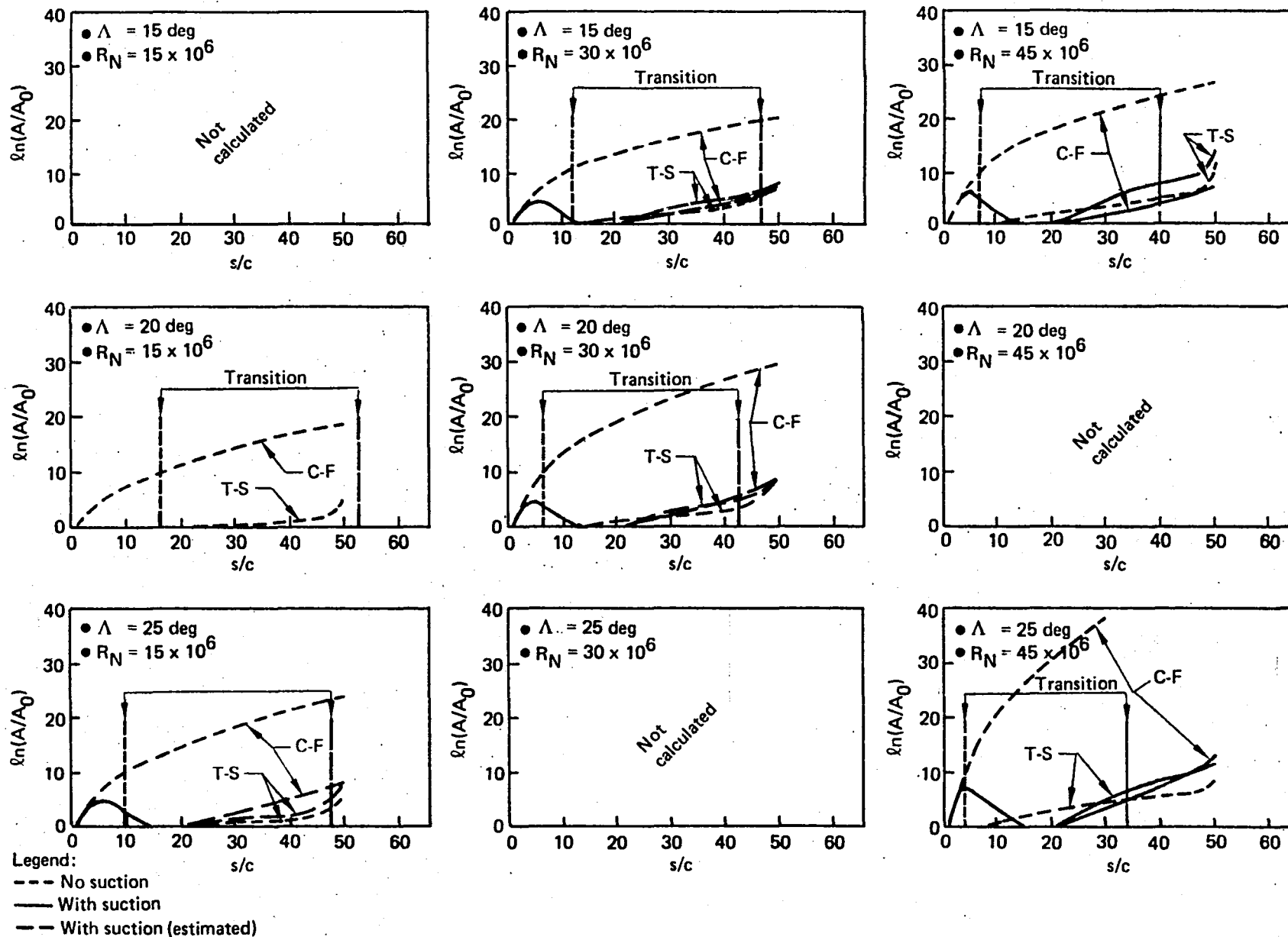
Figure A-20. Transition Data, Case 5-2
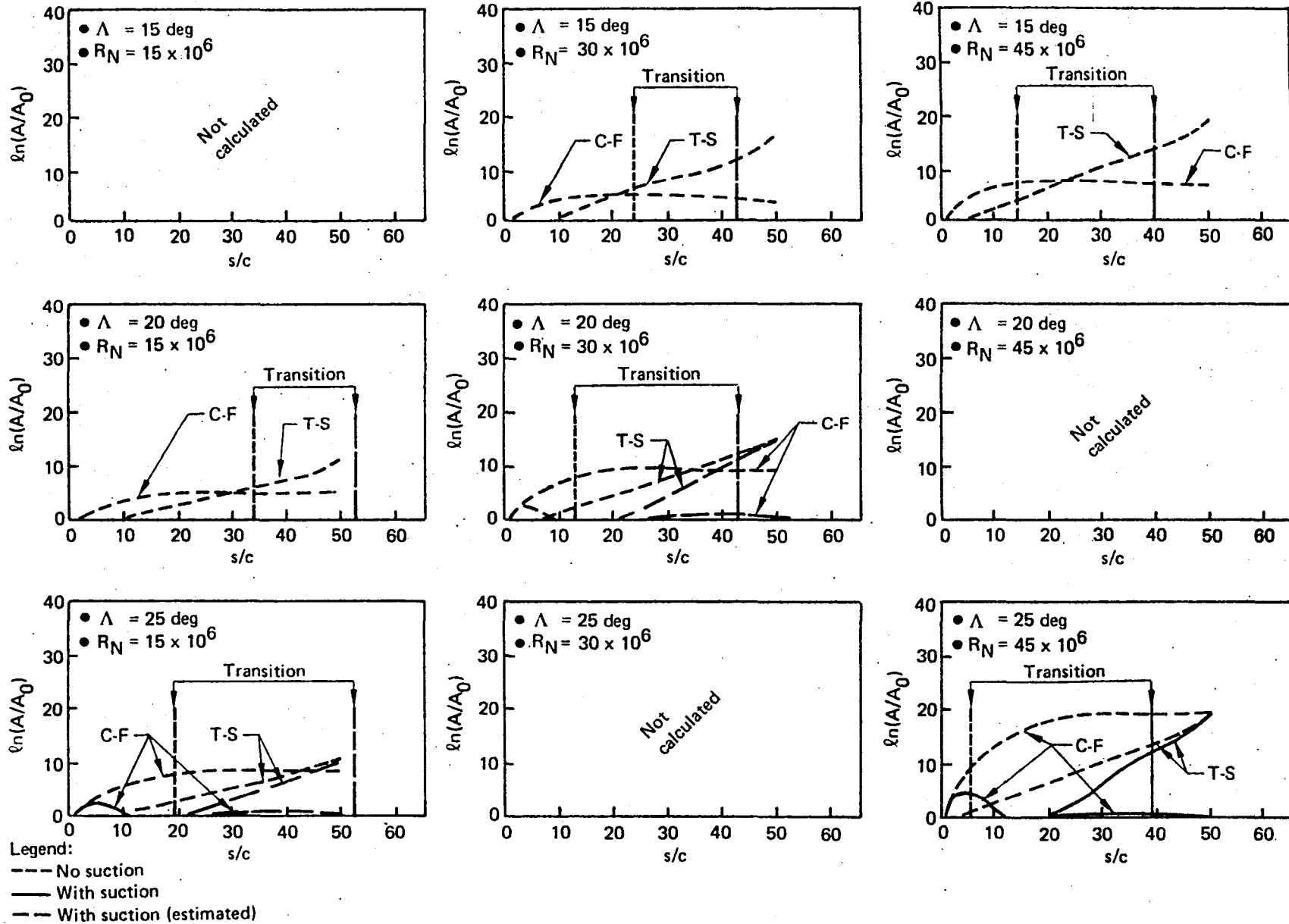
Figure A-21. Compressible Stability Envelopes, Case 4-1

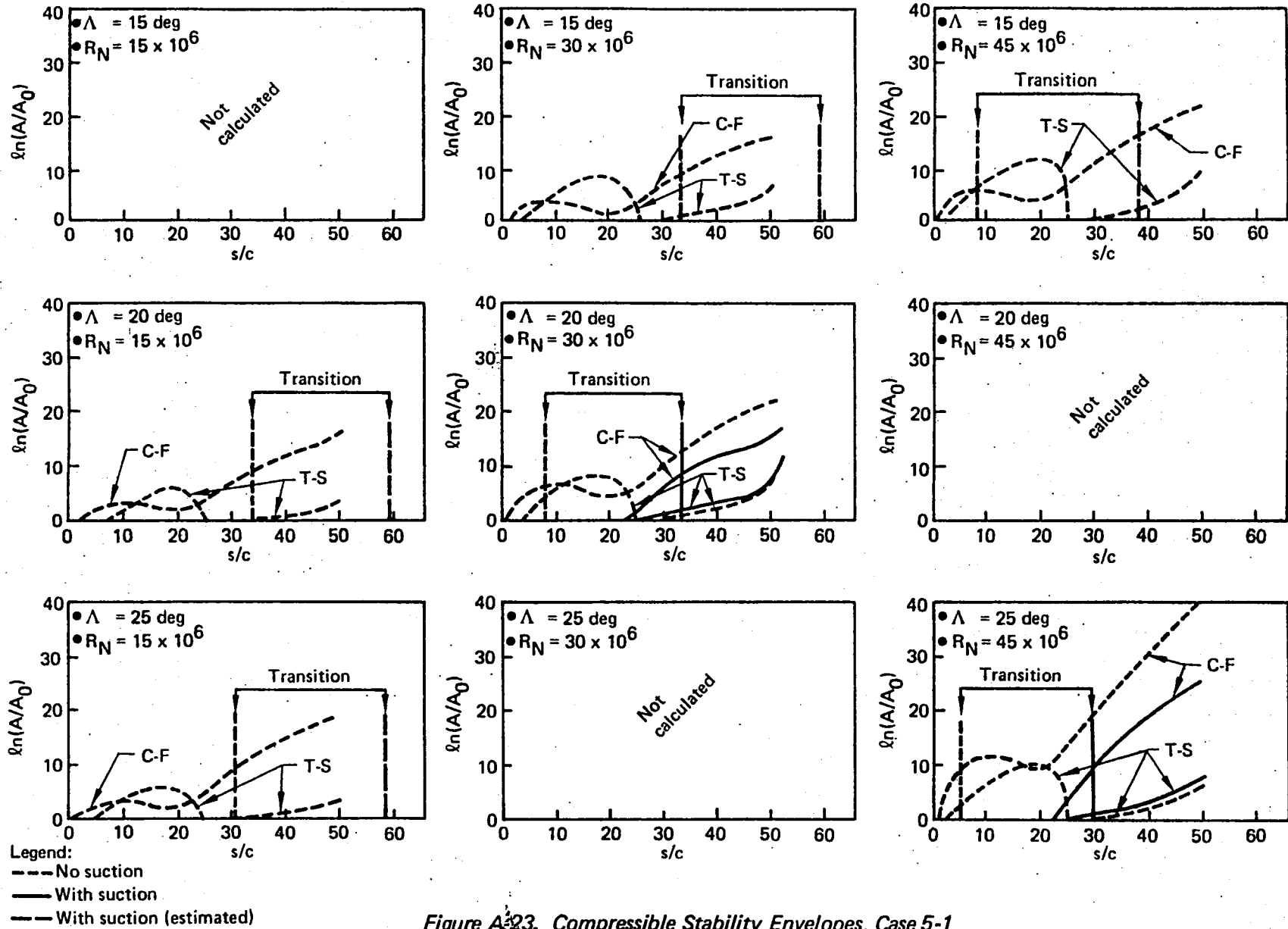Figure A-22. Compressible Stability Envelopes, Case 4-2

A-28

Legend:
- - - No suction
——— With suction
— — With suction (estimated)

Figure A-23. Compressible Stability Envelopes, Case 5-1

Legend:
- - - No suction
——— With suction
— — With suction (estimated)

A-29
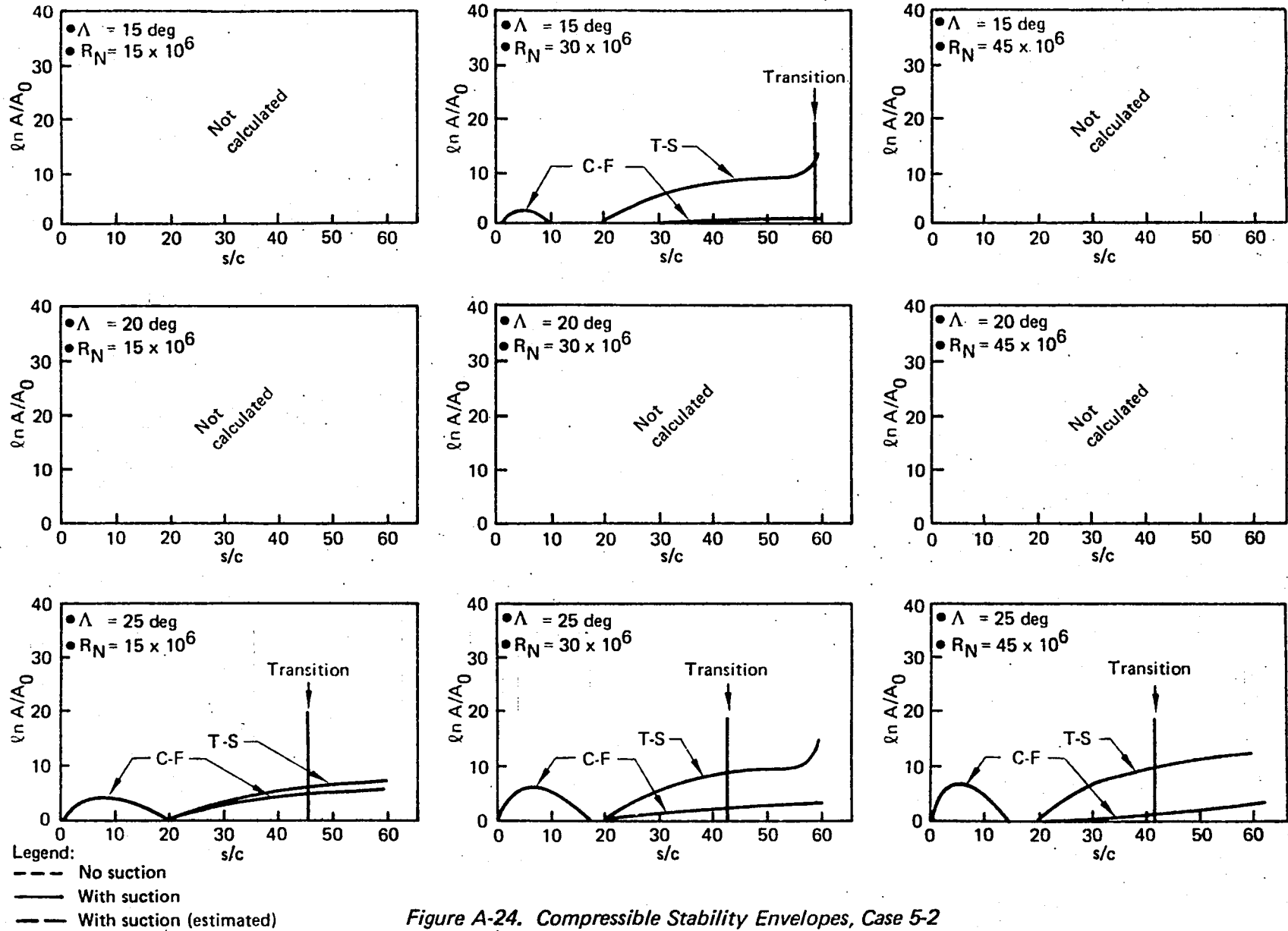
Figure A-24. Compressible Stability Envelopes, Case 5-2

Legend:
- - - - No suction
- ——— With suction
- —— With suction (estimated)

APPENDIX B

STABILITY CALCULATIONS FOR

FINAL WING DESIGN

FIGURES

B.1 OFF-DESIGN

Figures B-1 through B-6 show the pressure distribution, suction distribution, and stability characteristics at three spanwise locations on the upper and lower wing surfaces at an altitude of 9144m (30 000 ft) and normal Mach number of 0.744. The method of analysis is described in section 5.2.3.1. The suction distributions were optimized for this condition.

B.2 CRUISE

Figures B-7 through B-10 show the pressure distribution, suction distribution, and stability characteristics at two spanwise locations on the upper and lower wing surface at an altitude of 10 688m (35 000 ft) and normal Mach number of 0.744. The stability characteristics at = 0.75 were not calculated at this condition because it was apparent, based upon the stability results at 9144m (30 000 ft), that laminar flow at this lower Reynolds number would be maintained back to just slightly beyond the minimum pressure point. The suction distributions are the same as those optimized at the off-design condition. It also should be noted that disturbance envelopes were computed only downstream of the end of suction location. The previous analyses at the off-design condition showed that the forward disturbance envelopes peaked at a level too low to cause transition, and the peak levels would be even lower at this condition.

The suction distributions shown here differ slightly from the final suction distributions shown in section 5.2.3.1. The total suction is the same at a given spanwise location in both cases, but the final suction distributions start right at the leading edge and have lower peaks. The start of suction location was moved forward from that used in the stability calculations in order to prevent leading-edge attachment line contamination problems. The stability calculations were not revised to reflect this change, because total suction was kept fixed and shifting the suction forward usually has a beneficial effect on stability.

Figure B-1. HLFC Off-Design Stability Results—Upper Root

$\bullet R_N = 50 \times 10^6$ $\bullet M_N = 0.744$ $\bullet$ Altitude = 9 144m (30 000 ft) $\bullet \eta = 0.10$

Pressure distribution

C_{p_N}

s/c, %

Suction distribution

$\dfrac{(\rho v)_w}{\rho_\infty U} \times 10^4$

$c_{q_N} = 11.08 \times 10^{-5}$

s/c, %

Compressible stability
T-S envelope

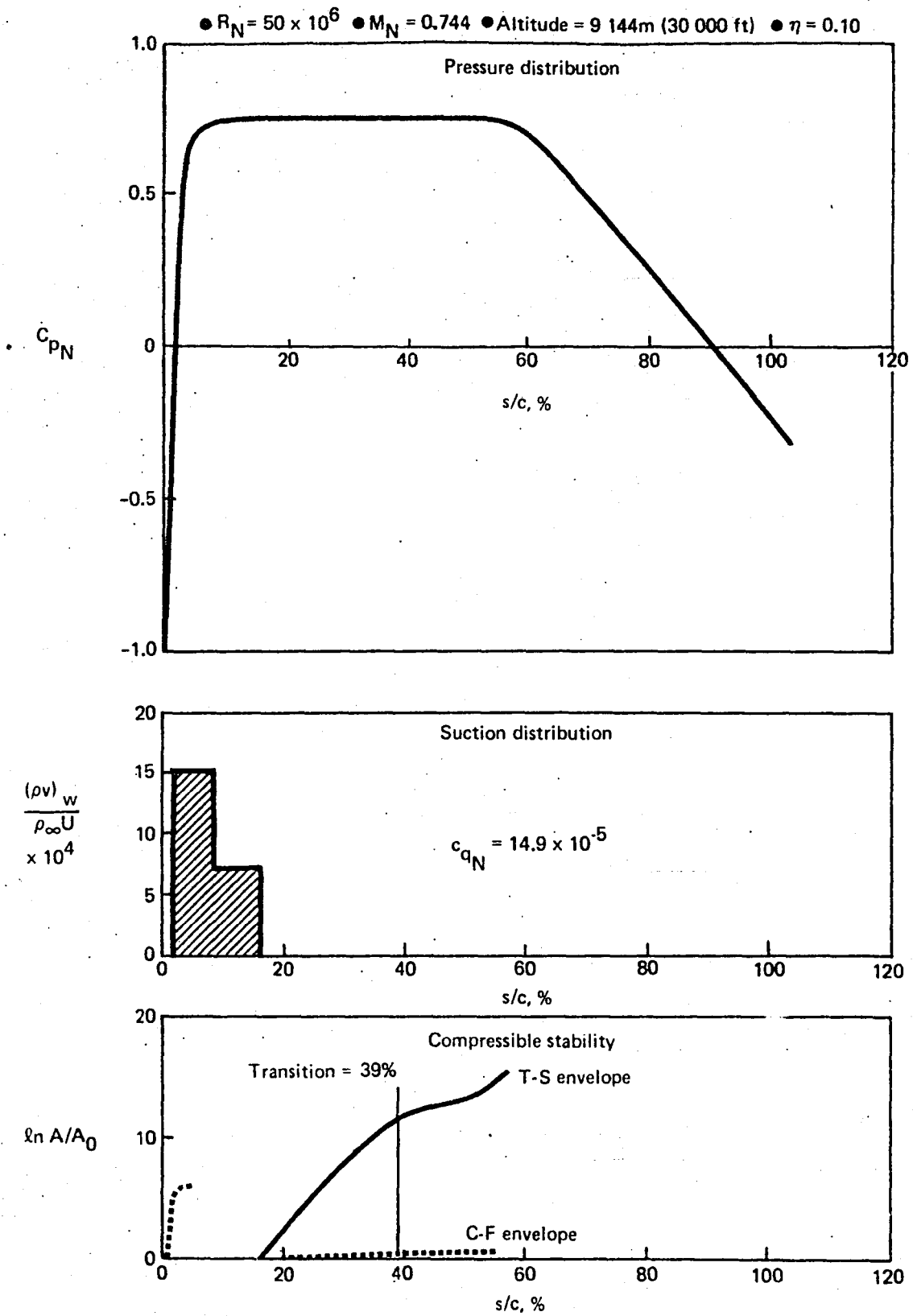Transition = 33%

$\ell n\ A/A_0$

C-F envelope

s/c, %

Figure B-2. HLFC Off-Design Stability Results—Lower Root

● $R_N = 33 \times 10^6$ ● $M_N = 0.744$ ● Altitude = 9 144m (30 000 ft) ● $\eta = 0.40$

Pressure distribution

Suction distribution

S2

$c_{q_N} = 11.94 \times 10^{-5}$

Compressible stability

Transition = 49%

T-S envelope

C-F envelope

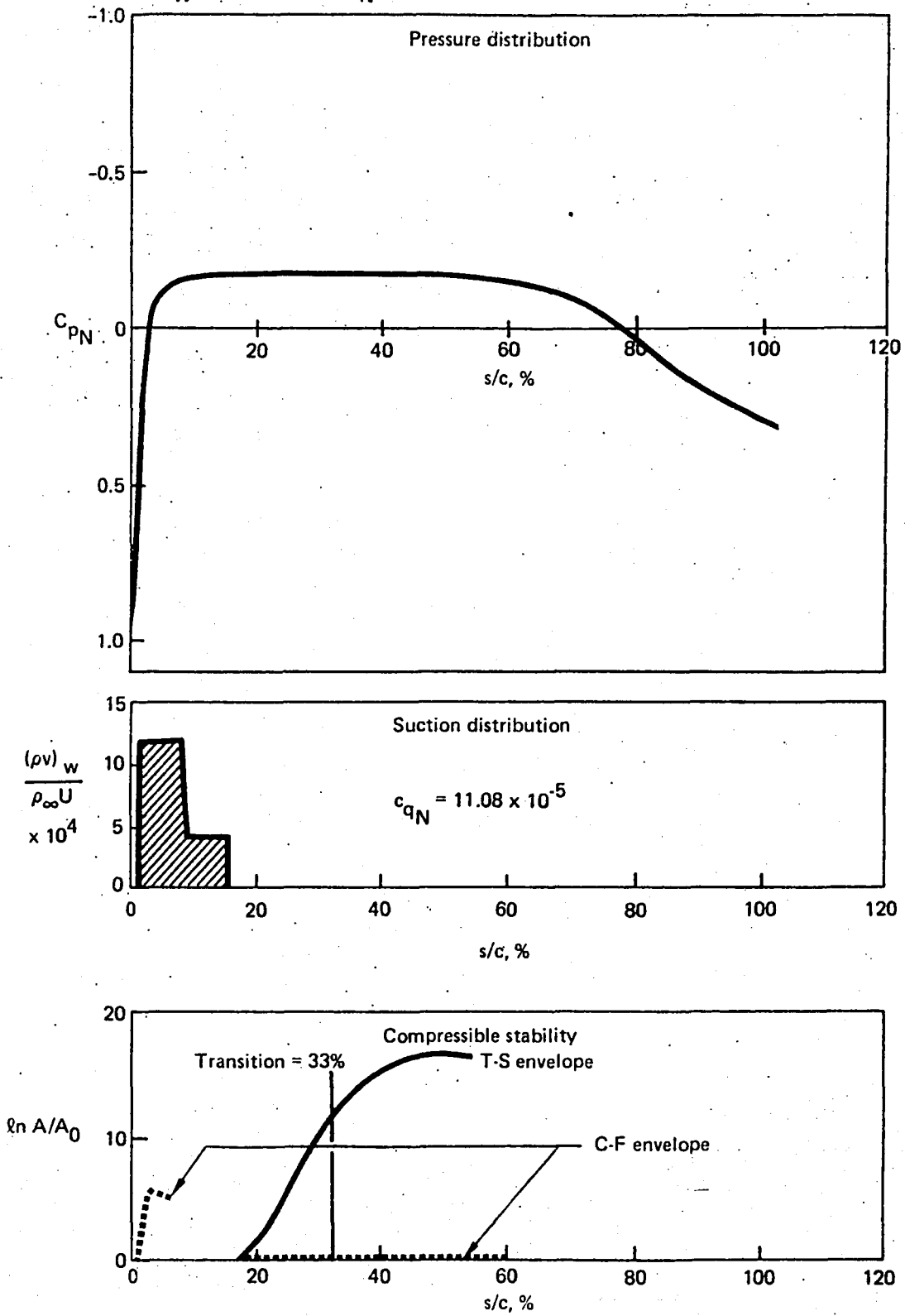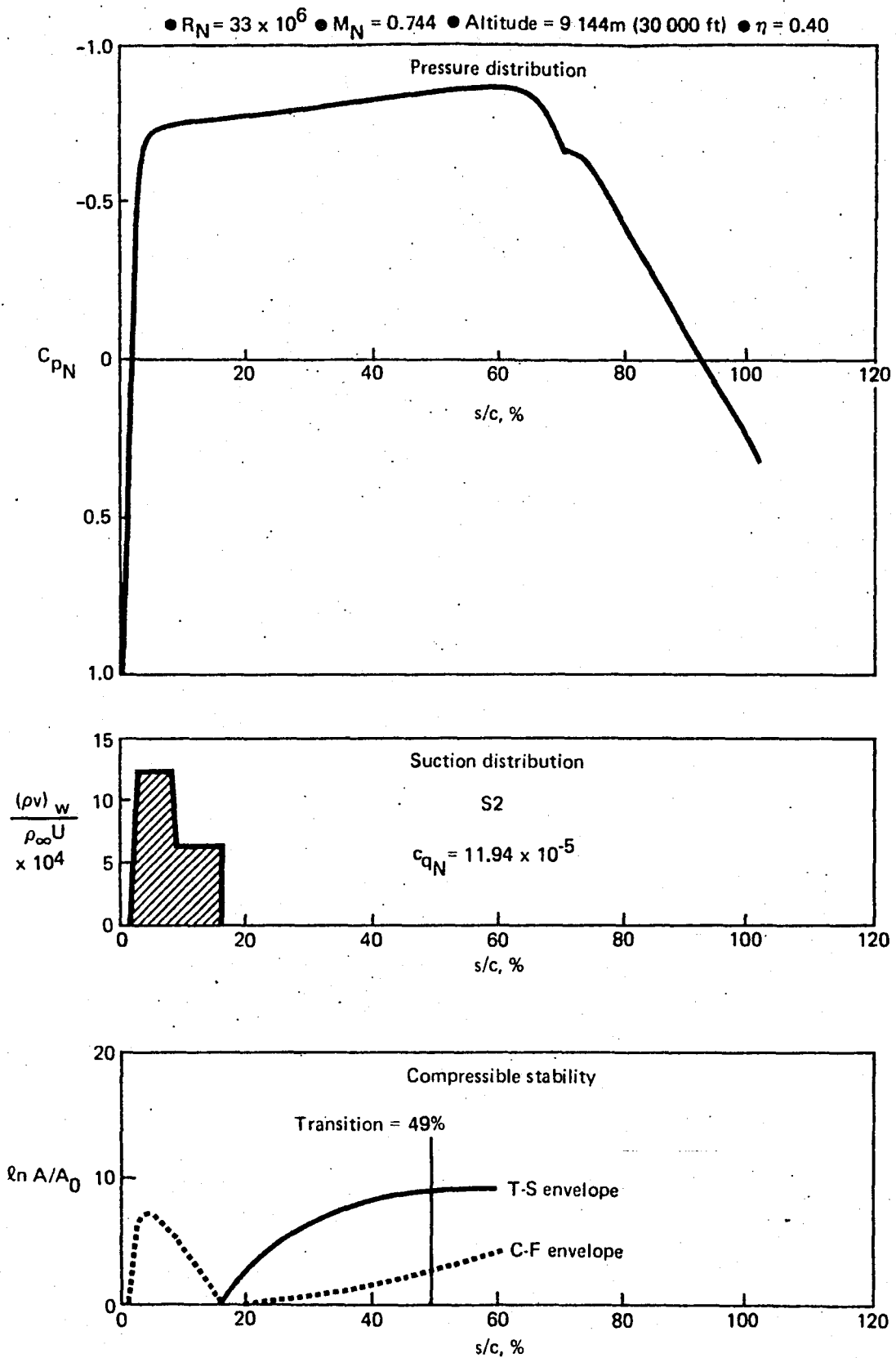Figure B-3. HLFC Off-Design Stability Results—Upper Midspan
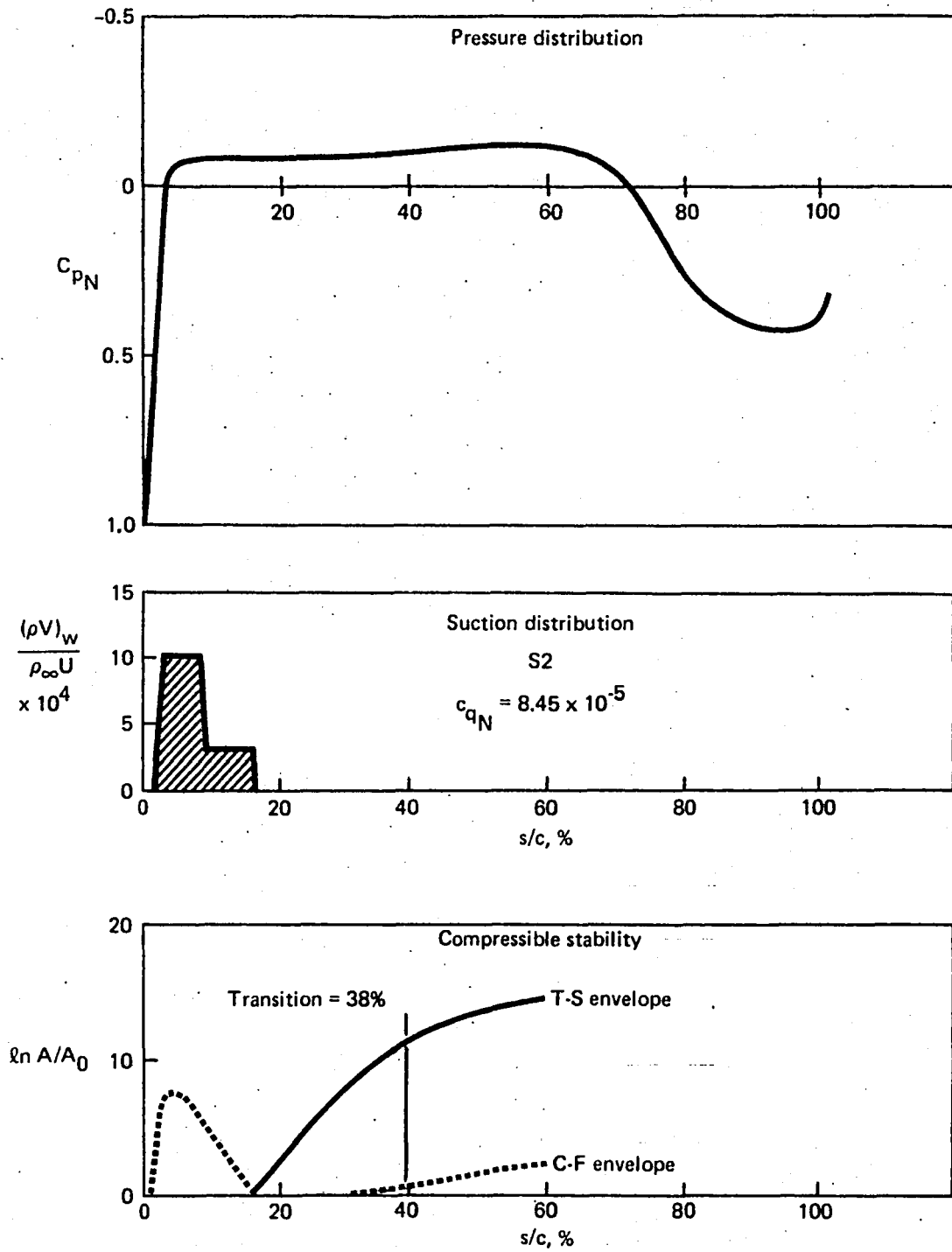
Figure B-4. HLFC Off-Design Stability Results—Lower Midspan
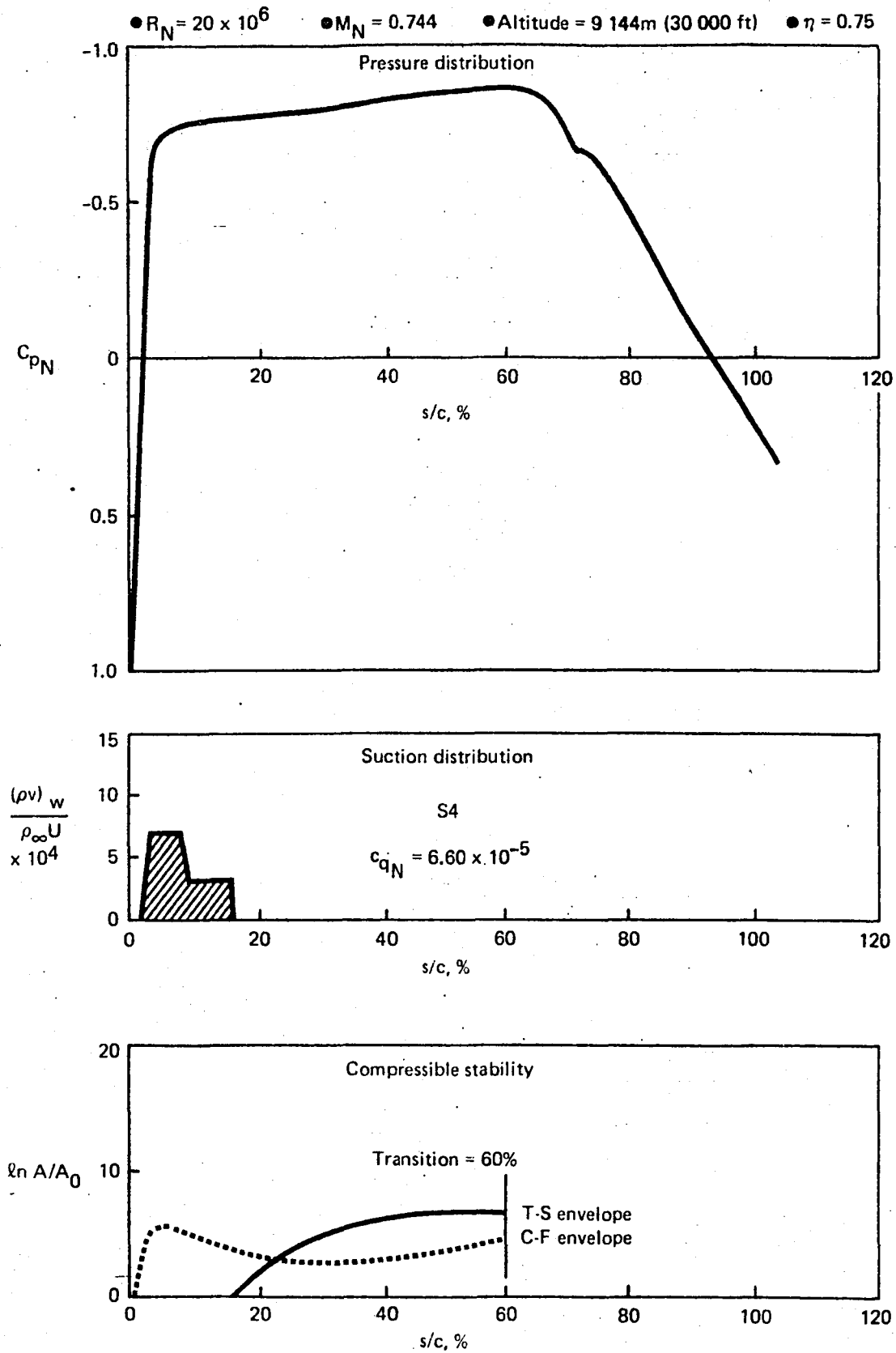
Figure B-5. HLFC Off-Design Stability Results—Upper Tip

$\bullet \ R_N = 20 \times 10^6$ $\bullet \ M_N = 0.744$ $\bullet$ Altitude = 9 144m (30 000 ft) $\bullet \ \eta = 0.75$

Pressure distribution

C_{p_N}

s/c, %

Suction distribution

S2

$c_{q_N} = 7.83 \times 10^{-5}$

$\dfrac{(\rho v)_w}{\rho_\infty U} \times 10^4$

s/c, %

Compressible stability

Transition = 56%

T-S envelope

C-F envelope

$\ln A/A_0$

s/c, %
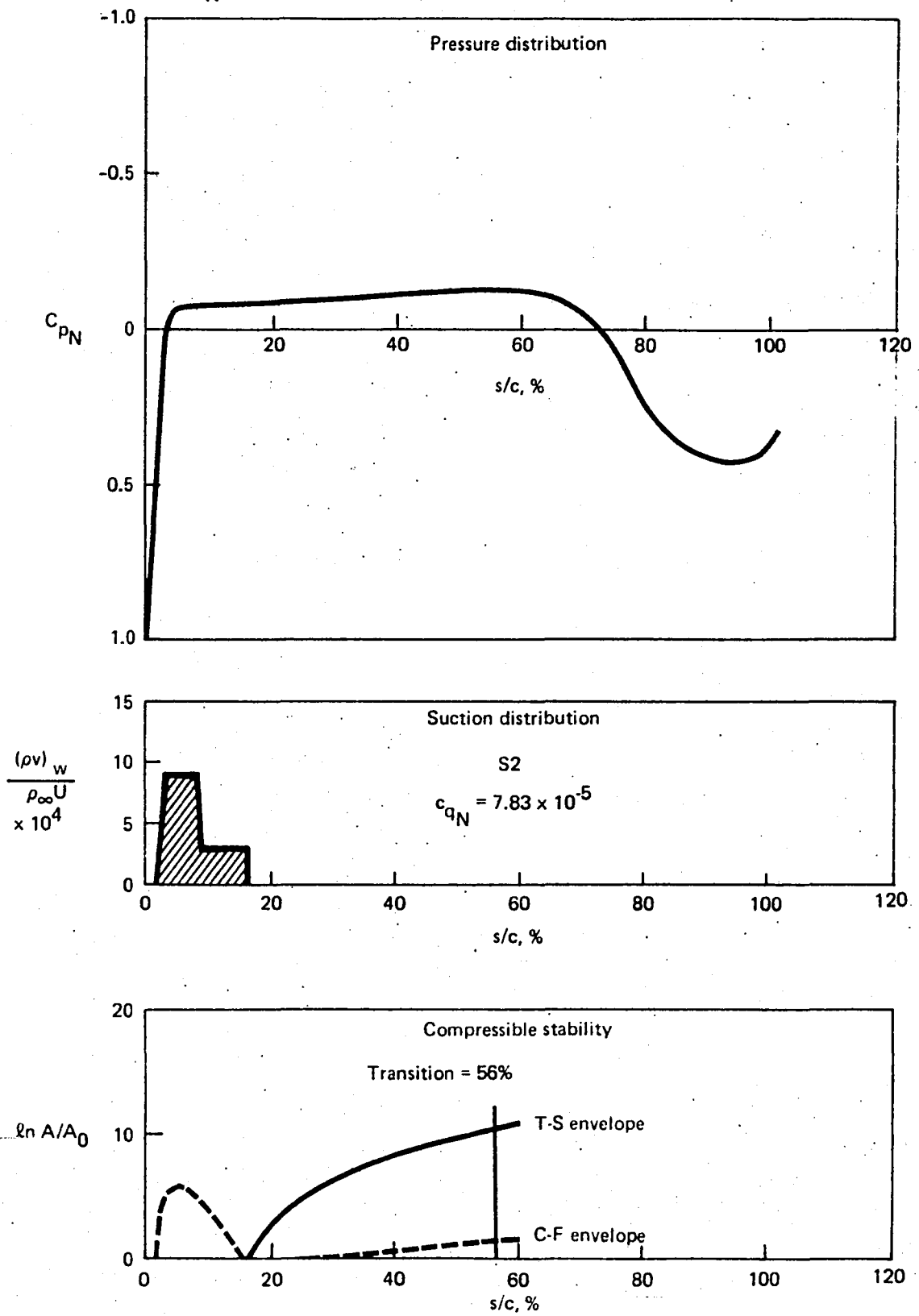
Figure B-6. HLFC Off-Design Stability Results—Lower Tip

B-9

$\bullet R_N = 42 \times 10^6$ $\bullet M_N = 0.744$ $\bullet$ Altitude = 10 688m (35 000 ft) $\bullet \eta = 0.10$

Pressure distribution

C_{p_N}

s/c, %

Suction distribution

$\dfrac{(\rho v)_w}{\rho_\infty U} \times 10^4$

$c_{q_N} = 14.9 \times 10^{-5}$

s/c, %

Compressible stability

Transition = 51%

$\ell n \ A/A_0$

T-S envelope

C-F envelope

s/c, %
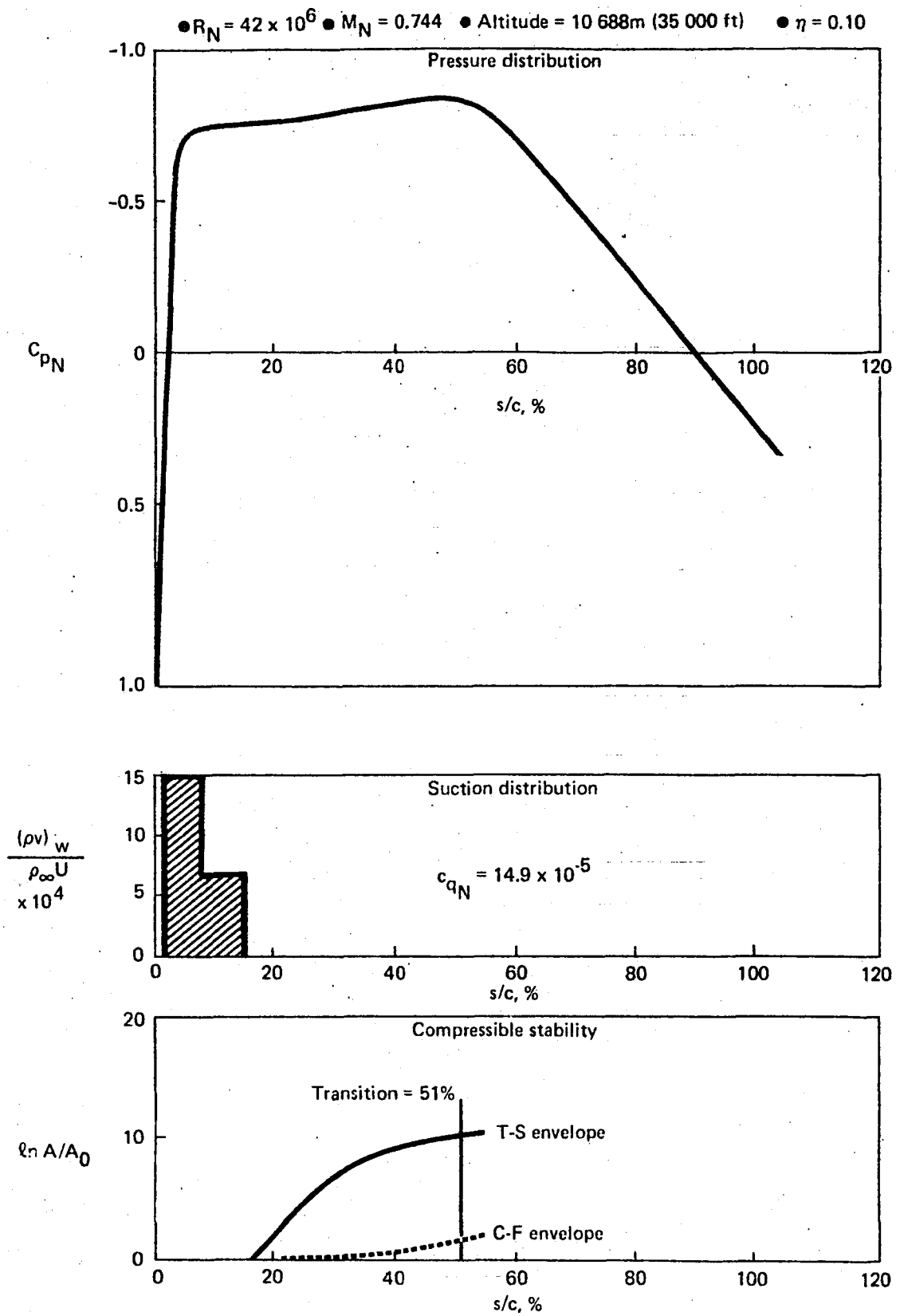
Figure B-7. HLFC Cruise Condition Stability Result—Upper Root

B-10

$R_N = 42 \times 10^6$ ● $M_N = 0.744$ ● Altitude = 10 668m (35 000 ft) ● $\eta = 0.10$

Pressure distribution

C_{p_N}

Suction distribution

$\dfrac{(\rho v)_w}{\rho_\infty U} \times 10^4$

$c_{q_N} = 11.08 \times 10^{-5}$

Compressible stability

Transition = 37%
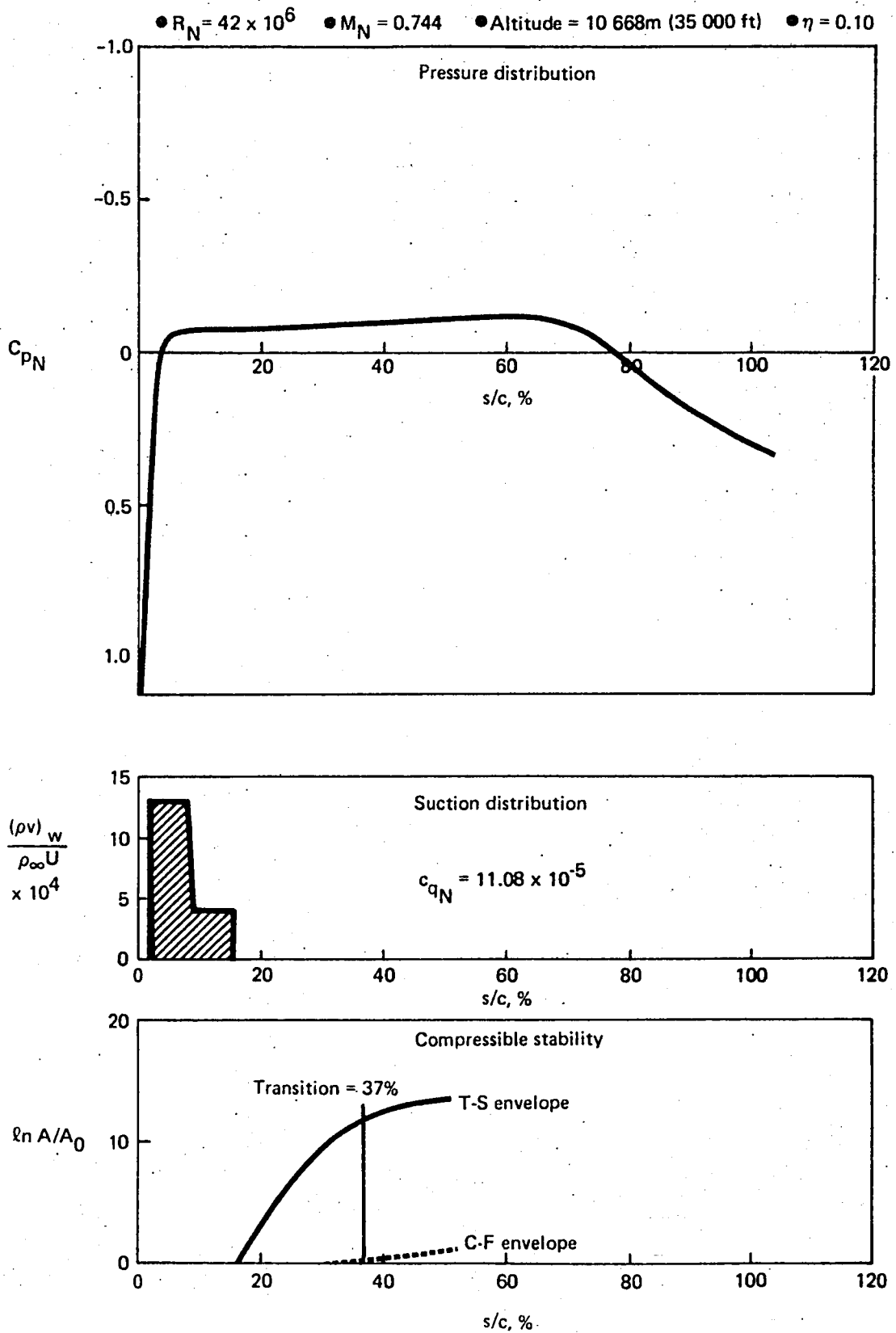
T-S envelope

$\ell n\, A/A_0$

C-F envelope

Figure B-8. HLFC Cruise Condition Stability Results—Lower Root
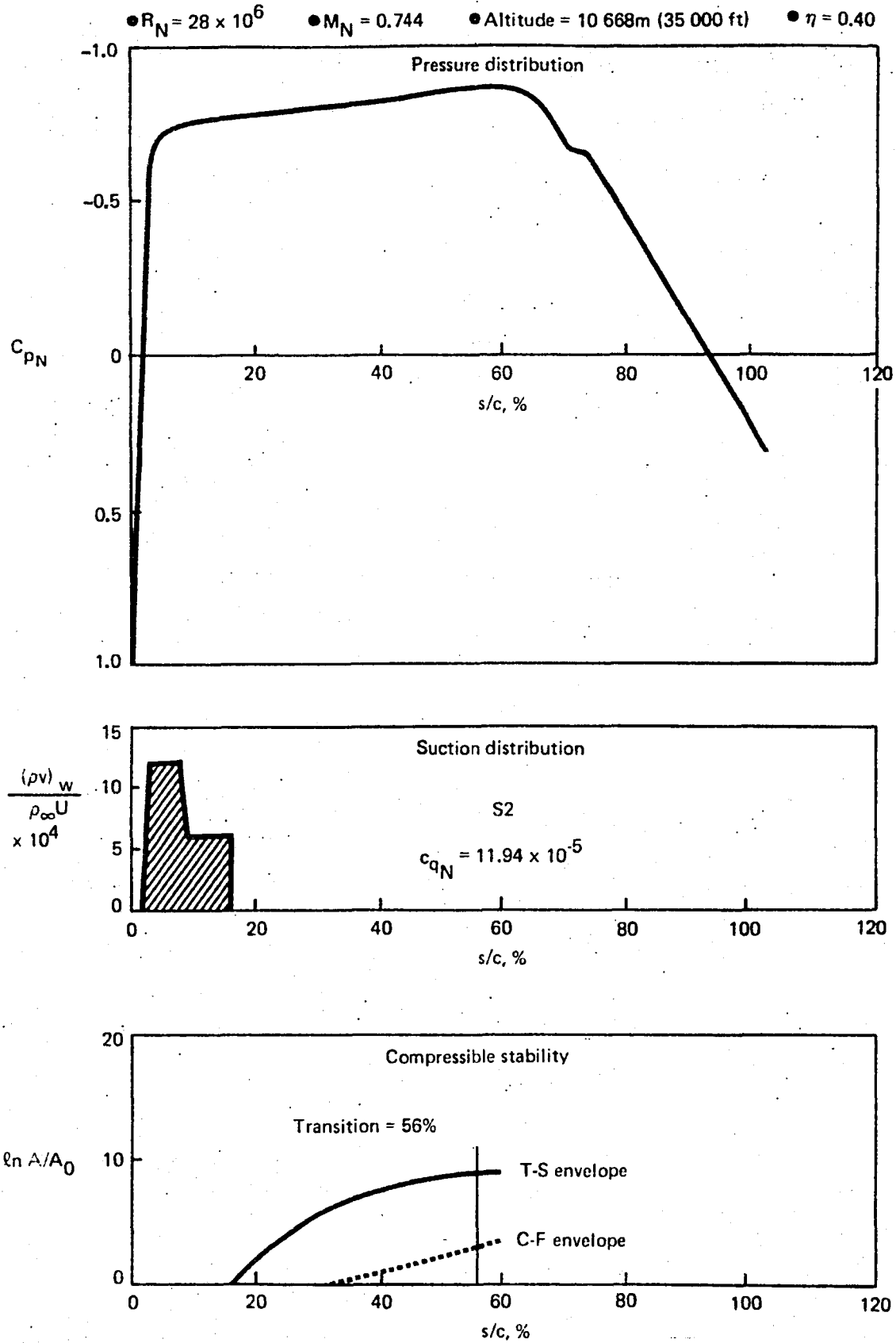
Figure B-9. HLFC Cruise Condition Stability Results—Upper Midspan

B-12

● $R_N = 28 \times 10^6$　　● $M_N = 0.744$　　● Altitude = 10 668m (35 000 ft)　　● $\eta = 0.40$

Pressure distribution

C_{p_N}

s/c, %

Suction distribution

S2

$c_{q_N} = 8.45 \times 10^{-5}$

$\dfrac{(\rho v)_w}{\rho_\infty U} \times 10^4$

s/c, %

Compressible stability

Transition = 42%

T-S envelope

C-F envelope

$\ell n \, A/A_0$

s/c, %
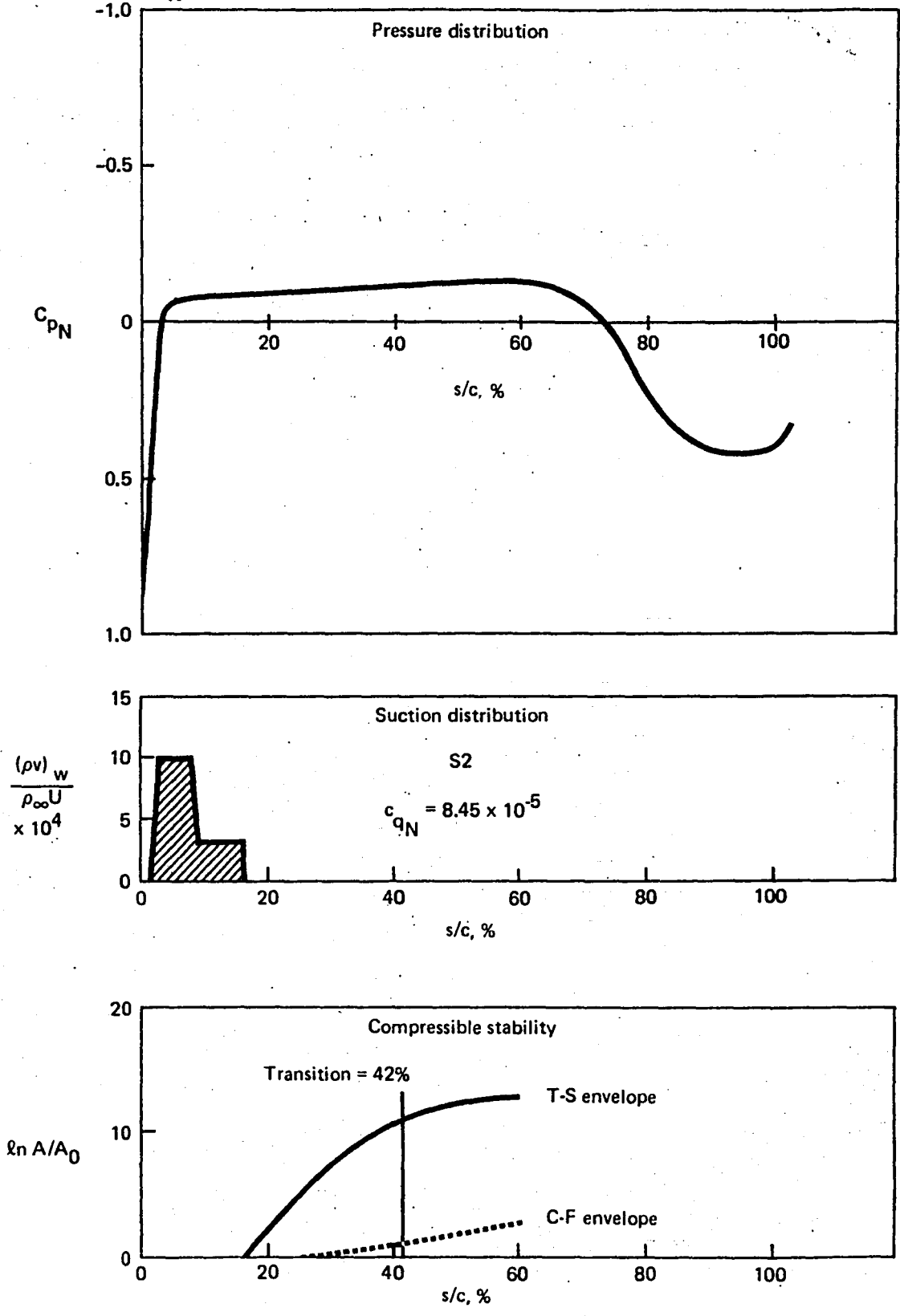
Figure B-10. HLFC Cruise Condition Stability Results—Lower Midspan

1. Report No.	2. Government Accession No.	3. Recipient's Catalog No.
NASA CR 165930		

4. Title and Subtitle	5. Report Date
Hybrid Laminar Flow Control Study, Final Technical Report	October 1982
	6. Performing Organization Code
	534-02-13-30

7. Author(s)	8. Performing Organization Report No.
Preliminary Design Department Boeing Commercial Airplane Company (BCAC)	D6-49359
	10. Work Unit No.
9. Performing Organization Name and Address	NAS1-15325
Boeing Commercial Airplane Company P. O. Box 3707 Seattle, WA 98124	11. Contract or Grant No.
	Contractor report
	13. Type of Report and Period Covered
12. Sponsoring Agency Name and Address	
National Aeronautics and Space Administration Washington, D.C. 20546	14. Sponsoring Agency Code

15. Supplementary Notes

Technical monitor: D. B. Middleton
NASA—Langley Research Center

16. Abstract

The hybrid laminar flow control (HLFC) concept was examined in which leading-edge suction is used in conjunction with wing pressure distribution tailoring to postpone boundary layer transition and reduce friction drag. A parametric study was conducted to determine airfoil design characteristics required for laminar flow control (LFC). The aerodynamic design of an HLFC wing for a 178-passenger commercial turbofan transport was developed, and a drag estimate was made. Systems changes required to install HLFC were defined, and weights and fuel economy were estimated. The potential for 9% fuel reduction for a 3926-km (2120-nmi) mission was identified.

17. Key Words (Suggested by Author(s))	18. Distribution Statement
Laminar flow control Energy efficiency Fuel economy	FEDD distribution Subject category 05

19. Security Classif. (of this report)	20. Security Classif. (of this page)	21. No. of Pages	22. Price
Unclassified	Unclassified	175	

Available: NASA's Industrial Applications Centers

N-305

End of Document